ISOTROPIC COMPRESSION OF MIXTURES OF HARD AND SOFT SPHERES

Leon Mark Toland BEng ARSM

DOCTOR OF PHILOSOPHY

THE UNIVERSITY OF ASTON IN BIRMINGHAM

July 1996

The University of Aston in Birmingham
ISOTROPIC COMPRESSION OF MIXTUR
OF HARD AND SOFT SPHERES
Leon Mark Toland BEng ARSM
Thesis submitted for the degree of Doctor of Ph
1996

SUMMARY

The compaction behaviour of powders with soft and har particular interest to the paint processing industry. Unfortu time, very little is known about the internal mechanisms with therefore suitable tests are required to help in the interpretati

The TRUBAL, Distinct Element Method (D.E.M) program investigation used in this study. Steel (hard) and rubber (soft) p the randomly-generated, binary assemblies because they provi in physical properties. For reasons of simplicity, isotropic dimensional assemblies was also initially considered. The a subject to quasi-static compaction, in order to define th *equilibrium* conditions. The stress-strain behaviour of the a conditions was found to be adequately described by a sec expansion. The structural evolution of the simulation assemb to that observed for real powder systems. Further simulati out to investigate the effects of particle size on the compact two-dimensional, binary assemblies. Later work focused compaction behaviour of three-dimensional assemblies, beca more realistic particle systems.

The compaction behaviour of the assemblies during the si was considered in terms of percolation theory concepts, as v macroscopic and microstructural parameters. Percolation theor ideas from statistical physics, has been found to be useful in the mechanical behaviour of simple, elastic lattices. However, this study, percolation theory is also able to offer a us compaction behaviour of more realistic particle assemblies.

KEY WORDS:

COMPUTER SIMULATED EXPERIMENTATION
ISOTROPIC COMPRESSION
HARD AND SOFT PARTICLES
BINARY PARTICULATE ASSEMBLIES
PERCOLATION THEORY

To those long summer days, when there is either too much or too little for you do to keep your sanity!

Acknowledgements

I am extremely grateful to my research supervisor, Dr C. Thornton, for his support, guidance, insight and continual optimism throughout the duration of the research project. I am also very grateful for his diligence in correction of the script and the checking of equations.

I would like to acknowledge the financial support provided by Imperial Chemical Industries PLc, which allowed me to participate in the Interdisciplinary Higher Degree scheme. I would also like to thank the Engineering and Physical Sciences Research Council for their generous financial support during the research programme.

I sincerely appreciate the help and advice provided by Dr David Kafui in the setting up of computer facilities and software and the supply of programming hints.

I would also like to acknowledge the support and encouragement of Teo Ciomocos, Dr Guoping Lian, Dr Zemin Ning and Dr Gexin Sun who were all involved in the application of TRUBAL to other aspects of particulate material research.

Finally, special thanks to the CEAC 'mafia' for being sociable bastards, all the members of Vauxhall 16/26 (1993-96) for putting up with me, especially Mike, Phil, Fred, Joe, Rob, Colin, Matt and Graham, Louise for her carnal knowledge, Emma for being my little 'sis', Glenn for keeping me going in the first few months, Teo for his fellow suffering and Dr Mark Smith for being a good mate and fellow club lunatic!

Table of Contents

Appendices

List of Figures

List of Tables

Chapter 1

Introduction

1.1 Object and scope of the investigation

The pharmaceutical, foodstuffs, ceramic, polymer and metals industries use compaction techniques like extrusion or die pressing during the processing of granular media. If the ceramics industry is taken as an example, then die pressing of an originally loose, ceramic powder is used to produce a green compact before further processing by sintering. Die pressing means that, the compaction of a powder is accomplished by placing it in a die and applying pressure via a punch to achieve the desired degree of compaction. Isotropic compression, where a particle system is uniformly compacted in all three co-ordinate directions, is another popular compaction technique and is used in processes such as Hot Isotropic Pressing (H.I.P.) to produce 'near net shapes' for powder products. The advantage of such 'near net shape forming' is that it eliminates the need for post-processing operations like milling to produce the desired final product shape and size. A large number of the experimental investigations of such compaction processes only consider single-component powder systems. However, the majority of useful particulate materials have more than one constituent, since even apparently pure, single component powders still contain impurities. Other areas of materials science and technology, like polymeric composites, indicate that the mechanical behaviour of binary mixtures is completely different to that encountered with single component systems. Binary mixtures of 'hard' and 'soft' spheres include such industrially important materials as paint powders. Therefore, a more realistic view of the mechanical behaviour of these granular systems during isotropic compaction is highly desirable on both a theoretical and practical level.

It is now widely recognised that the mechanical properties of granular media depend inherently upon the microstructure of the material. This feature is also observed for the majority of engineering, solid materials such as steel. To date, no entirely satisfactory constitutive model for even single-component particulate material, such as sand, exists. This is mainly due to the complex macroscopic behaviour of granular material; which is the result of its internal discrete nature. Resolution of the difficulties associated with prediction of the behaviour of different granular materials appears to require joint micro-mechanical, macromechanical and continuum mechanical studies.

Traditional laboratory tests on granular material do not provide sufficient information regarding the internal deformation processes. Elementary parameters like the components of stress, for example, must be predicted from boundary measurements. New experimental techniques, however, are being developed that can detect internal deformation patterns within a particulate medium. Examples include high resolution X-ray Computerized Tomography (CT), Lee and Dass, 1993, Positron Emission Particle Tracking (PEPT), which utilises positron emitting radionuclide tracers, Beynon *et al*, 1993, and infra-red thermography, Luong, 1993. None of these techniques though, is capable of describing the microscopic particle interactions in granular media, which generally occur in the submicron range of resolution. It is this problem of experimental measurement that has resulted in the investigation of much simpler systems of particles. The use of such idealised, granular material allows the microscopic particle forces and displacements to be either calculated or measured. Experimentation into idealised particle assemblies can be undertaken by the employment of computer simulation techniques. Cundall and Strack (1979a) have developed such a technique, known as the Distinct Element Method (DEM), which is incorporated in the TRUBAL computer program. Numerical simulation using a modified version of the TRUBAL program has been adopted as the method of investigation in this project. More information about the TRUBAL program and the DEM approach used at Aston is provided in chapter 4 of this text. The TRUBAL program is a very powerful research tool since, by using simple assumptions regarding interparticle contacts, computer algorithms can be created and these algorithms will then allow the program to model the extremely complex behaviour of compacted, granular assemblies. Computer experimentation using such a system allows the use of hypothetical laws. Tests can also be repeated from initial or earlier points in the test with an artificial change in parameters such as the density or coefficient of friction values for the particles.

The primary objective of this project was the investigation of the bulk, mechanical properties of binary, particulate materials during compaction. The work involved the use of computer simulation experiments, for the reasons described earlier. In a similar approach to that adopted by workers such as Cundall *et al*, 1989, and Jenkins *et al*, 1989, the interpretation of macroscopic and microstructural parameters was used in the development of a constitutive model of the isotropic compaction. Theoretical concepts from the statistical physics field of percolation theory were however, also used to aid the interpretation of the macroscopic behaviour of such assemblies.

The different aspects of this interpretative process required modifications to be made to the TRUBAL program which are described in more detail in chapter 4 of the text. Percolation theory can be used as an investigative tool because some of the concepts from this area were found to be useful in the practical investigation of systems of elastic, particle assemblies reviewed in chapter 3. The use of such percolation theory concepts therefore, allows the macroscopic compaction behaviour of the simulation assemblies to be viewed in an alternative manner to the usual micromechanical approach.

The first practical objective for the simulation work was the completion and interpretation of isotropic compression experiments, which considered two-dimensional (2D), binary assemblies of 'hard' and 'soft' spheres. Although particulate materials are three-dimensional (3D) in nature, it is far easier to initially visualise the complicated behaviour of binary, granular mixtures in two dimensions. However, interpretation of the compaction behaviour of three-dimensional assemblies is more useful practically and was, therefore, also undertaken in this study. Further details about the two- and three-dimensional simulation experiments which were performed are provided in section 1.3.

1.2 Terminology used

The conventions of solid mechanics were used in all the calculations performed in the version of TRUBAL program used in this project. However, all the results shown in this text use the normal conventions of soil mechanics. Therefore, compressive stresses or strains are considered to be positive and tensile stresses or strains are considered to be negative in the work presented in this thesis. The use of the terms compaction and compression in an interchangeable manner will also be considered here, since both terms have similar meanings to other workers in this field. The majority of the symbols and terms in this thesis are common to a lot of current particle technology research and so are unambiguous. However, to prevent misinterpretation by other investigators, clarification of any possibly ambiguous terms and definitions of the symbols used will be provided at the relevant points in the text.

One area of potential concern is the definition of the assembly volume V, which is used in the calculation of the mean stress σ_{mean} and volumetric strain ε_v for the two-dimensional assembly. In this case, the volume used is a slice, with a thickness of one mean particle diameter and other dimensions determined by the x- and y- dimensions of the periodic simulation cell specified in the TRUBAL program. Another area of concern involves the use of terms from the statistical physics-based field of percolation theory in the interpretation of the mechanical particle assembly behaviour. The meaning and use of such symbols and terms will however, be examined in more detail in chapter 3.

1.3 Order of presentation

The study which has been undertaken, is presented in the following chapters of the main text. This work can be classified under four general headings. A review of the present work undertaken in the field is provided in chapter 2. The theoretical background and methodology used in the percolation theory and computer simulation models are presented in chapters 3 and 4. Details of the computer simulated experiments and interpretation of the results, which were obtained, are provided in chapters 5, 6, 7 and 8. Finally, concluding remarks and aspects of this study which are worthy of further investigation are presented in chapter 9. A more detailed breakdown of these chapters is given below.

The literature review presented in chapter 2, initially examines previous experimental die compaction studies on single component systems. This work includes the practically important, empirical relationships of Kawakita (1956) and Heckel (1961a). The present knowledge of powder compaction mechanisms is also reviewed. Experimental studies of binary powder systems are examined so that some clues to the observations obtained from the simulation experiments in this study can be provided. The results from photoelastic disc experiments will be reviewed because such disc models are widely used for the modelling of particulate assembly behaviour. The results from other simulation experiments, using both the TRUBAL program employed in this work and different computer models, will also be studied.

An outline of the most important concepts in percolation theory is provided in chapter 3. The use of these concepts in the qualitative description of the mechanical behaviour of elastic particle lattices and the relevance of such concepts to the behaviour of *real* particle systems will also be discussed in this section. Chapter 4 gives details of the DEM and the TRUBAL program used to perform the simulation experiments. This section, therefore, presents information about the logic framework for the computer program and the force-displacement laws used at the particle contacts during a simulated experiment. Control of other experimental aspects such as numerical stability, energy dissipation and deformation of the periodic cell will also be reviewed. Modifications which were made to the original version of the TRUBAL program, to allow more detailed examination of binary systems, are outlined in this chapter.

In chapter 5, the behaviour of both two- and three-dimensional assemblies at the proposed ground state for measurement of results from the simulation experiments i.e. the elastic percolation threshold p_e will be examined. This behaviour will be interpreted in terms of macroscopic, microstructural and percolation-theory based characteristics. The relevance of using p_e as a ground state will also be discussed in this chapter. Chapter 6 presents the results obtained from quasi-static simulation experiments performed on two-dimensional assemblies, which are again interpreted in terms of macroscopic, microstructural and percolation parameters. The effects of mixtures of different particle sizes, in the two-dimensional assemblies, on the quasi-static compaction behaviour are studied in chapter 7. In chapter 8, the quasi-static compaction behaviour of monodisperse, three-dimensional assemblies is examined. This examination shows that the simple theoretical model developed for the two-dimensional systems in chapter 6 is also relevant for the more practically important, three-dimensional assemblies.

Chapter 2

Literature review

2.1 Experimental die compaction studies

Knowledge of previous work on powder compaction is important for placing the work presented in this thesis in context. Research into the mechanism of powder compaction using die compaction techniques has produced empirical relationships which have nevertheless served the process industries reasonably well over the years. Die compaction generally involves uniaxial compaction of a powder loaded into a metal die. The compaction of powders using such a process is taken as an initial step in many powder processing operations, since it offers simplicity, speed and economy of manufacture. A vast amount of literature has been produced on die compaction studies, since isostatic compaction (see section 2.2.2) was until recently of less practical importance. This review will therefore, concentrate on only the most significant work that has been published. The relationship between the packing or compression of particles and their fundamental physical properties is an example of an important physical relationship that has generated empirical formulae. A number of pressure-density and pressure-volume relationships have been proposed over the years for specific powders and on hypothetical grounds. The majority of these formulae however, are not universally applicable, most giving an acceptable relationship only over a limited range of pressures. In this review of the studies carried out on powder die compaction, the experimental relationships will be established first and the theoretical picture of the mechanisms of compaction will be explored in the review's latter stages.

The first serious attempts made at studying the relationship between the applied pressure and powder deformation were produced by workers in the 1920's such as Walker (1923) and Shaxby (1923). Walker analysed the compression of powders by static loading of ammonium nitrate and sodium chloride in a die at pressures around 390 MPa. The load-volume curves for the two materials were found to be different. Walker related the difference in these load-volume curves to the compression process within the material. Compression of ammonium nitrate took place by deformation of the particles, whilst compression of sodium chloride involved disintegration of the particles. Shaxby (1923) analysed the variation of vertical pressure p_v, in the range 13 MPa to 30 MPa, with depth z in columns of sand. He found an exponential increase of p_v with z i.e. the general form of the pressure-depth curve agreed well with the equation:

$$p_v = p_m\left[1 - C\exp(-kz)\right] \tag{2.1}$$

The maximum pressure being p_m and C and k are constants. Athy (1930) looked at the related problem of depth of burial and the density, porosity and compaction of different types of sedimentary rocks. From his results, Athy developed a porosity-depth relationship,

$$n = n_0\exp(-bz) \tag{2.2}$$

where n is the porosity, n_0 is the average porosity of surface clays, b is a constant and z is the depth of burial. The first proposition of an equation relating applied pressure to the volume change of a compact was made by Balshin (1938). The object of Balshin's work was to give a physical picture of the processes which take place during pressing and to formulate the basic mathematical laws of pressing. The work involved investigation of the pressure-volume diagrams of steel and copper powders placed in a die compaction apparatus. Balshin found from his results that an increase in the pressure p of the powder compact was related to a decrease in the volume and height of the compact by the relationship,

$$\ln p = C - M_p V_r \tag{2.3}$$

where M_p and C are constants which depend on the type of powders and conditions of pressing and V_r is the relative volume of the compact. The indicated formula was found to be applicable in the pressure range 100 MPa to 500 MPa for ideal cases. In practice the formula was found by Balshin to deviate slightly from linearity, depending on the nature of the powder and the conditions of pressing. The coefficient M_p, which was called the Modulus of Pressing, described the deformation capacity of the powder and was therefore, found to be useful in decoding the properties of the experimental powders. The deviation from linearity of (2.3), for a wide variety of reasons, indicates that Balshin's relationship may not be a fundamental one. The distribution of density in the pressed specimens was also investigated and was found to decrease approximately linearly with distance from the die plunger.

A more satisfactory approach to the general problem of powder compaction was obtained by Shapiro and Kolthoff (1946) who analysed the packing of the particles in silver bromide powders. They argued that as an external pressure is applied to a powder mass in a die, the apparent density of the powder will increase and approach the true density of the solid as a limit. The ease of this density increase was thought to depend upon the material being compressed i.e. its plasticity and surface development. Shapiro and Koltoff suggested that as the powder is compressed, the porosity n of the powder at any pressure p will be related to the porosity n_0 at zero pressure by the relationship,

$$\mathbf{n} = \frac{(\rho_s - \rho_a)}{\rho_s} = \mathbf{n_0} \times \mathbf{f(p)} \tag{2.4}$$

where ρ_a is the apparent density of the powder mass, ρ_s is the true density of the solid material and f(p) can be determined experimentally. Shapiro and Kolthoff also found experimentally that the change in porosity with pressure of the powders could be expressed as:

$$\frac{\mathbf{dn}}{\mathbf{dp}} = -\mathbf{kn} \tag{2.5}$$

where k was called the *coefficient of powder compressibility* and its value was dependent upon the physical characteristics of the powder. Integration of (2.5) gave the following relationship:

$$\mathbf{n = n_0 exp(-kp)} \tag{2.6}$$

This equation is similar to (2.2), which was obtained by Athy (1930). The relationship represented by (2.6) was also a good approximation of the experimental results obtained by Shapiro and Kolthoff in the pressure range 20 to 140 MPa. The behaviour of the silver bromide powders in the pressure range below 20 MPa, which is the region of interest for the simulation work presented in chapters 5 to 9 of this text, was found to deviate significantly from linearity. Shapiro and Kolthoff however, performed little analysis of their data in this region and so they developed no clear picture of low pressure, elastic compaction behaviour. The relationship between degree of compaction and applied compaction pressure i.e. (2.5) developed by Shapiro and Kolthoff is similar to that obtained by Konopicky (1948) and Heckel (1961a), who used different assumptions in their analysis. Konopicky proposed that a proportionality exists between the relative density D of a metal powder compact and the applied pressure p:

$$\ln\left(\frac{D}{1-D}\right) \propto p \qquad (2.7)$$

The relationship represented by (2.7) was found to be valid in the pressure range 175 to 900 MPa from Konopicky's experimental work on copper powders (size 220 μm). The constitutive equation developed by Heckel has proved very useful in quantitatively describing the compaction process, although it is an empirical relationship. The Heckel equation and a rival one put forward by Kawakita (1956) have become generally accepted and are widely used in the powder metallurgy and pharmaceutical industries. A more detailed analysis of these practically important equations will be provided in sections 2.1.1 (for Heckel) and 2.1.2 (for Kawakita).

The compaction behaviour of pharmaceutical powders has been analysed by a number of workers e.g. Leuenberger (1982); Leuenberger *et al.* (1983); Leuenberger and Jetzer (1984). The term *compressibility* in terms of pharmaceutical powders was defined by Leuenberger and Jetzer (1984) as the ability of a powder to decrease in volume under pressure and the term *compactability* was defined by these same workers as the ability of the powdered material to be compressed into a tablet of sufficient strength. The compressibility behaviour of pharmaceutical powders is believed to follow the Kawakita relationship, developed by Kawakita (1956), in the majority of the papers reviewed in this area. Roberts and Rowe (1986) however, used the Heckel relationship (1961a) in order to determine the yield pressure for pharmaceutical powders (size 4 to 60 μm) e.g. sucrose, calcium carbonate. The aim of this work was to obtain a predictive capability for the compaction behaviour of pharmaceutical powder systems. The correlation used by Roberts and Rowe to obtain the powder yield strength i.e. (2.15) has some doubts associated with its use (see section 2.1.1) and this therefore, casts some doubt on the validity of their results.

It is the compactability behaviour e.g. Amidon *et al.* (1981), or deformation hardness, rather than the compressibility characteristics of pharmaceutical powders which is of most interest to the pharmaceutical research community. Pharmaceutical powders are generally produced as tablets and so knowledge of the deformation hardness behaviour is therefore, of more practical importance than development of pressure-density or pressure-volume relationships.

2.1.1 The Heckel pressure-density relationship

The method of obtaining pressure-density relationships used by Heckel (1961a) was designed to eliminate the shortcomings of other techniques, which are reviewed in Heckel (1961b), whilst maintaining equivalent accuracy and precision. The general principle employed was that, the linear movement of the piston during die compaction could be used to calculate the change in volume of the powder as a function of the pressure, if the cross-sectional area of the die was known. The density-pressure relationship could then be calculated from a knowledge of the weight of the powder and the volume-pressure relationship (where the 'density' was the average density of the compact). It is only the change in the volume of the powder that can be obtained as a function of pressure and so the data must be referred to a known powder compact volume. Heckel (1961a) used the *zero die volume*, which corresponded to the readings taken of the volume of the compacted specimen after completion of the compaction operation. The linear movement of the punches during the compaction process was the algebraic sum of the change of height of the compact and of the elastic compressive strains in the punches. The latter changes were measured by Heckel (1961a) experimentally, using a blank pressing operation, in order to separate the two effects. This punch elasticity data was used in the reduction in the value of the linear punch-movement data, to allow calculation of compact density at the applied pressure (known as the *at pressure* density). The densities measured as the compacts were removed from the die were known as the *zero-pressure* densities. Heckel (1961a) found experimentally that, there was little difference between the *at pressure* and *zero pressure* densities for his metal powders, because of their relatively high elastic moduli. The transformation of any experimental data into a form suitable to produce pressure-density curves therefore, required a number of items of information to be obtained, Heckel (1961a). These items included the powder weight in the die, the cross-sectional area of the die cavity, the elastic changes within the die itself as a function of the applied pressure and either the punch-movement data at zero die movement without an applied pressure or the thickness of the powder compact when removed from the die. The accuracy of the analysis was found by Heckel to be unaffected by his assumption that the cross-sectional areas of the die cavity and the compact on removal from the cavity, were equal. This assumption was reasonable since there was only an extremely small difference in the two cross-sectional areas.

Heckel (1961a and 1961b) believed that the compaction of powders could be considered to be analogous to a first-order chemical reaction, the pores in the powder being the *reactant* and the *kinetics* of the process being the densification of the bulk of the mass. The kinetics of the process was assumed by Heckel to be described by a proportionality between the change in powder density and the pore fraction,

$$\frac{dD}{dp} \propto (1 - D) \tag{2.8}$$

or

$$\frac{dD}{dp} = K(1 - D) \tag{2.9}$$

where p is the pressure, $(1-D)$ is the pore fraction in the powder, K is a proportionality constant and D is the relative density of the compact. The relative density is defined as the ratio of the density of the compact ρ to that of the metal without porosity. The above expression can be reduced to a more usable expression by rearrangement:

$$\frac{dD}{(1 - D)} = Kdp \tag{2.10}$$

and integrating:

$$\int_{D_0}^{D} \frac{dD}{(1 - D)} = K\int_{0}^{P} dp \tag{2.11}$$

where Do is the relative density of the loose powder at zero pressure. Thus

$$\ln(1 - D_0) - \ln(1 - D) = Kp \tag{2.12}$$

or

$$\ln\left(\frac{1}{1 - D}\right) = Kp + \ln\left(\frac{1}{1 - D_0}\right) \tag{2.13}$$

The validity of Heckel's analysis was justified by Heckel (1961a) by plotting ln $(1/1-D)$ against p curves for copper, iron, nickel and tungsten powders (in the pressure range 0 to 896 MPa). An example of these results is presented in figure 2.1.

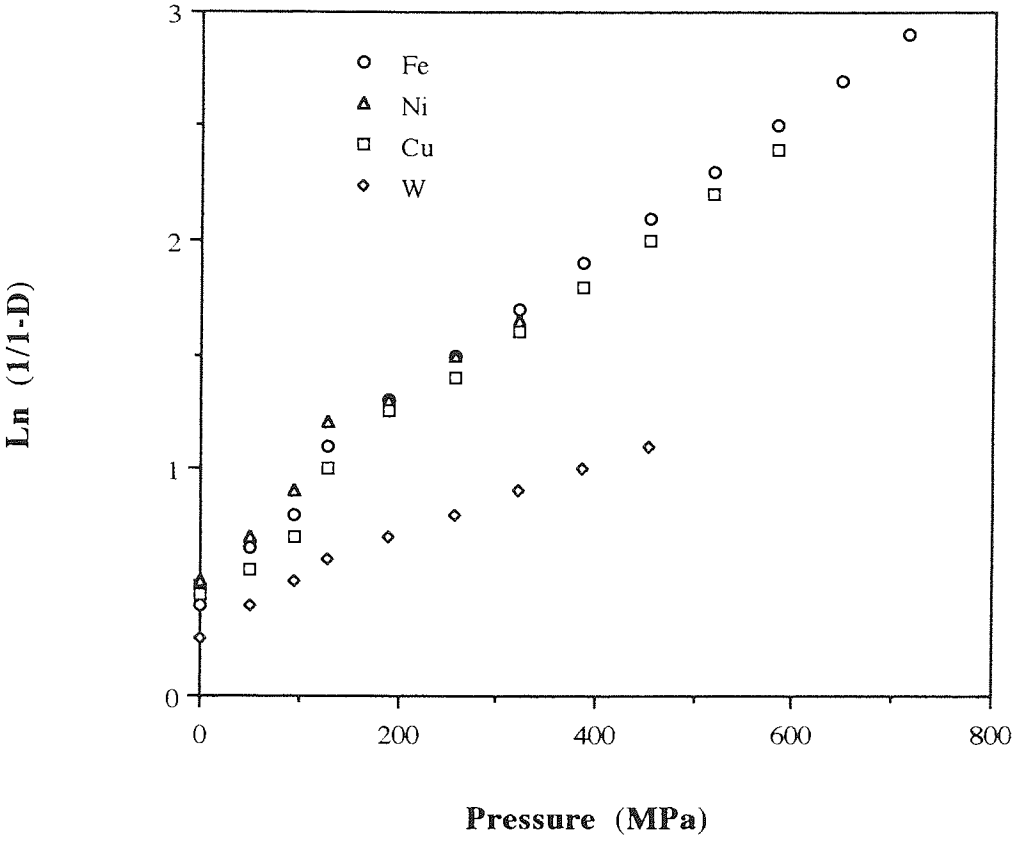

Figure 2.1 Heckel plot for Iron (Fe) - 200 μm, Nickel (Ni) - 250 μm; Copper (Cu) - 150 μm, Tungsten (W) - 15 μm size powders. (After Heckel, 1961a).

Linearity was found by Heckel (1961a) to extend over 65 to 80 percent of the pressure range studied and he believed that extrapolation of these values to even higher pressures could be justified. However, uncertainty about the nature of the compaction mechanisms in even the most frequently studied lower pressure ranges (see section 2.1.3) means that the use of such an extrapolation is in some doubt. Heckel also suggested that the non linearity in the early stages of compaction was probably due to the effect of particle rearrangement processes in the powder, in a manner similar to that proposed by Seelig and Wulff (1946). The general behaviour of the powders in these early stages was also thought (using Seelig and Wulff's theory) to reflect individual particle rather than coherent mass interactions. Similar views on the mechanism of the compaction process are expressed in section 2.1.3.

The curvature expressed in figure 2.1 means that (2.13) will not accurately represent the compaction process in a quantitative sense at low pressures i.e. below 200 MPa. Heckel (1961a) replaced the term $\ln (1/1-D_0)$ in (2.13) with a constant A, to give the following expression:

$$\ln\left(\frac{1}{1-D}\right) = Kp + A \tag{2.14}$$

The expression (2.14) was found by Heckel (1961a) to be quantitatively valid for his experimental powders, except at pressures below 100 MPa, where Heckel urged caution in the use of his relationship. This caution is only partially justified because very little experimental data was obtained from this low pressure region by Heckel. Heckel (1961b) also analysed the microstructure of the compact particles using microscopy, in an attempt to produce an association between the macroscopic mechanical behaviour and the micromechanical processes occurring within the powder systems. Heckel (1961a) concluded from this analysis that the curved region present in figure 2.1 was associated with densification which took place by a mechanism of individual particle movement. Heckel (1961a) also found from his experimental results, that the transition from curved to linear behaviour visible in figure 2.1 corresponded closely with the minimum pressure necessary to form a coherent compact. Heckel (1961b) suggested that the linear region of figure 2.1 was associated with plastic deformation of the compact, since this is the region of proportionality between the degree of densification and the void fraction (given by (2.9)) but offered no experimental evidence to support his ideas. Heckel (1961b) also viewed K in (2.14), as a material constant and believed that K represented a measure of the ability of the compact to deform. This belief may be a reasonable and valid one, but Heckel's assertion in Heckel (1961b) that a correlation can be produced between K and the yield strength of a material σ_y i.e.

$$K \cong \frac{1}{3\sigma_y} \tag{2.15}$$

is not, for a number of reasons. The correlation relationship in (2.15) was produced from limited experimental data in Heckel (1961b), and was only at best, a reasonable curve fit to the data. The justification for a plastically deforming mechanism in this linear region of the Heckel pressure-density curve has also still not been experimentally confirmed.

Donachie and Burr (1963) doubted that a simple correlation such as (2.15) between σ_y and K could be obtained. They argued that the yield strength is a defined parameter and the values observed vary with the definition and sensitivity of the experimental technique used to observe the yield behaviour. The values of K, A and D were also observed by Heckel (1961b) to vary according to the conditions of compaction, and that this created difficulties in the development of quantitative relationships involving these parameters.

2.1.2 The Kawakita pressure-density relationship

The Kawakita equation was developed from an observed relationship between pressure and volume during powder compression and is widely used in the fields of powder metallurgy and pharmaceutics. The equation was introduced by Kawakita (1956) and not, as is often wrongly stated in the literature, to have been developed by Kawakita and Tsutsumi (1966). Kawakita (1956) studied the behaviour of copper and iron powders (size 100 to 300 μm) subject to die compaction up to 150 MPa and assumed that, the degree of volume reduction of the compact C was proportional to the applied compaction pressure p. Kawakita in the same paper, also suggested the following empirical equation, which provided a good fit to his experimental data ,

$$C = \frac{V_0 - V}{V_0} = \frac{abp}{1+bp} \tag{2.16}$$

where V_o is the initial apparent volume of the powder mass (assumed to be the volume of the die before compaction begins), V is the volume of the compact under the applied pressure p (calculated from the cross-sectional area of the die and the length of travel of the die piston) and a, b are constants, characteristic of the powder . Rearrangement of (2.16) gives the more useful relationship,

$$\frac{p}{C} = \frac{1}{ab} + \frac{p}{a} \tag{2.17}$$

The linear relationship between p/C and p allows the values of the constants a, b to be evaluated graphically. This linear relationship was found to hold for soft and medical powders in Kawakita (1963), but particular attention had to be paid to the experimental measurement of the initial volume of the powder V_0 in (2.16).

It was necessary to measure V_0 in order to apply (2.16) and deviations from this relationship were found to be related to fluctuations in the measured value of V_0 (Kawakita, 1966). The constant a was thought by Kawakita (1966), to correspond to the limiting value of the relative reduction of the volume by the compaction process. The value of a was therefore, considered to be equal to the initial porosity of the powder mass n_0 and a relationship was developed,

$$a = \frac{V_0 - V_\infty}{V_0} \tag{2.18}$$

where V_∞ was the net volume of the powder (the volume difference between the initial powder volume and the volume reduction, at any stage, due to the compaction process). Examination of (2.18) indicates that a cannot be n_0, which is described by the relationship,

$$n_0 = \frac{V_p}{V_0} \tag{2.19}$$

where V_p is the initial volume of pores within the powder. Thus the statements made by Kawakita (1966) about the nature of a are incorrect. Kawakita and Ludde (1970) believed that, there was some correlation between the constant a and the physical properties of the powders i.e. a was the reciprocal of the gradient of the p/C Vs p curves and was found to alter in value with different powder materials. However, these workers were unable to find a clear relationship between the constants a and b and the physical properties of a powder. James (1972) suggested that these findings undermine the development of relationships between a, b and powder material properties such as yield stress by Kawakita.

Kawakita's equation for die compaction (2.17) has also been developed for tapping compaction and vertical vibrating compaction by Kawakita and Ludde (1970). The compaction pressure p in these cases was replaced by the tapping number N and the vibrating time t (for vibrating compaction). Kawakita's equation for die compaction is represented graphically in figure 2.2 from results obtained by Sheinberg (1967). Sheinberg reported that he obtained linearity using the Kawakita relationship in the die compression of stainless steel (100 μm) and copper oxide (150 μm) powders up to a pressure of 220 MPa.

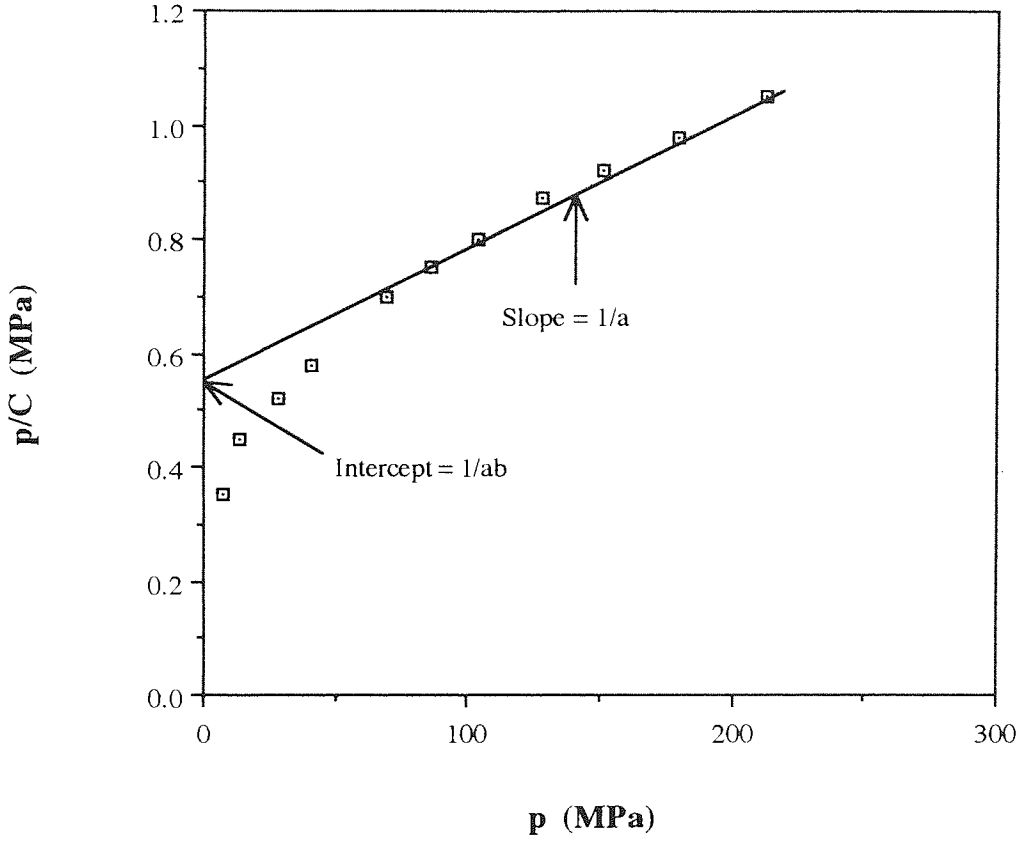

Figure 2.2 Kawakita plot for stainless steel powder (100 μm). (After Sheinberg, 1967).

Figure 2.2 however, does indicate that Sheinberg's assertion of linearity is subjective and definitely does not apply in the early stages of compaction, when the applied pressure is below 60 MPa. Kawakita's equation (2.17) has proved useful in quantitatively describing the compaction process and allowing comparative experiments to be carried out. However, Sarumi and Al-Hassini (1991) found that the equation was only useful over the limited pressure range between 40 and 250 MPa and for strain rates between 10^{-3} s^{-1} and 10 s^{-1}. Kawakita's relationship was also derived from curve fitting in Kawakita (1956), rather than considerations about the underlying physical principles of compaction and it has been suggested by Bockstiegel (1966b) that this model does not provide a satisfactory description of the "reality of powder die compaction".

James (1972) suggested that an improvement on Kawakita's equation would have to involve the process of pore closure within the compact. The stress distribution around pores is complex but it is a reasonable assumption that pore closure will be influenced by the stress required for particle deformation which will in turn be determined by the external compaction pressure (see section 2.1.3.).

2.1.3 Mechanisms of powder compaction

A review of the present theoretical knowledge of the mechanisms of compaction, as related to general powder systems will be presented in this section. An appreciation of the stages undergone during powder compression is important since this should lead to a better understanding of the individual mechanisms of compaction experienced by the powder particles which in turn should enable better correlations to be made between the mechanical behaviour and the porosity and structure of powders.

Many authors have suggested that the die pressing of metal, ceramic and pharmaceutical powders should be regarded as a multi-stage process e.g. Seelig and Wulff (1946); Cooper and Eaton (1962); Leuenberger (1982). The development of these concepts for compaction of metallic powders has been reviewed by James (1972) and Bockstiegel and Hewing (1965). They suggest that the first stage would involve slippage of the particles without excessive deformation. This stage was also referred to as *transitional restacking* by James. The effect in this early stage of compaction would be that, the bulk material would become denser with the particles sliding and re-arranging themselves according to the force exerted on them and no reduction of the particles' size would occur, though some fragmentation may be involved during the re-arrangement process. The densification associated with this stage was found to be a few per cent from experimental work on ductile powders of relatively smooth shape, performed by Donachie and Burr (1963), Bockstiegel (1966a). The restacking effect was found to be larger for irregularly shaped particles and for powders which were difficult to deform in Kostelnik *et al.* (1968). If the compaction pressure is increased then the next stage in James' model is believed to be the elastic compression of the particle-particle contact points. The simulation work presented later in this thesis is restricted to considerations of particle rearrangement and elastic compression.

However, if the compaction pressure is increased above this point, then it is believed that plastic deformation at these contact points would proceed simultaneously with a diminishing amount of sliding (or non-radial particle motion). James suggested that further compression would result in growth of these contact areas via plastic deformation and breakage. Fragmentation of particles was assumed to occur at the stage of plastic deformation by Bockstiegel and Hewing (1965). It was also suggested by these workers that, the external compressive forces would eventually reach values sufficient to cause massive deformation of the particles. Friction, plastic deformation and cold welding (at the particle contacts) would therefore, lock the particles into pseudo-rigid arrangements, to form what may be described as a particulate solid or powder compact. These final stages in pressing could be regarded as a form of bulk compression, where plastic compression of the mass tending towards final elimination of pores and ultimate densification, terminates with the subsequent elastic (recoverable) compression of the compact. Little experimental evidence concerning the stages involving plastic deformation has been presented and the work that has been performed is inconclusive, James (1972); Hewitt (1974). However, particle sliding is often invoked to explain observed peculiarities of pressure-density relationships, James (1977); Donachie and Burr (1963);Heckel (1961b).

The development of particle contact areas during compaction is an important field of study, since it is the geometrical arrangement of particle contact surfaces that has been found by some workers e.g. Fischmeister *et al* (1978), Oda (1972a,b), James (1977) and Nystrom and Karehill (1986), to affect the bulk compaction behaviour of powder systems. Fischmeister *et al* (1978) used quantitative metallographic techniques and scanning electron microscopy in an attempt to reliably analyse contact facet development between spherical bronze powders (particle size 100 μm) compacted up to 1 GPa. The results of this experimental work convinced Fischmeister *et al* to suggest that, for the experimental powders studied, non-radial particle motion (sliding) proceeded well into the expected, although not reliably confirmed, 'plastic' stage of densification. Fischmeister *et al* also found that the stage of transitional restacking present in the model of James (1972), appeared to be very limited in extent for a real system. These workers therefore, proposed that deformation and sliding of particles may occur right from the beginning of compaction. However, Fischmeister *et al* admitted they had made no attempt to test the generality of their observations for different types of powder.

Ceramics differ fundamentally from metals largely by their atomic bond characteristics, which in turn account for the basic brittleness and tendency to fragmentation of ceramics compared to the ductility and cold working characteristics of metals. Ceramic systems therefore exhibit different behavioural patterns to metallic systems when under pressure.

The die compaction behaviour of ceramic systems has been investigated by Cooper and Eaton (1962) and their view of the compaction mechanism for ceramic powders has been widely accepted in the ceramics processing industry. They also regarded compaction as a multi-stage process, involving two distributed processes. The first was the filling of voids within the powder system of the same order of size as the original particles (before compaction). The process was said to occur primarily by particles sliding past one another, which may require plastic deformation or even slight fracturing or plastic flow of the particles. This step was said to be distinguished by the voids being filled by particles from the original size distribution with only slight modification by fracture or by plastic deformation. This first stage can be said to resemble the features of the transitional restacking stage present in metallic compaction, which was discussed earlier. The second process in ceramic powder compaction was then believed to be associated with the filling of voids that are substantially smaller than the original particles. These can be filled only by plastic flow or by fragmentation. Plastic flow is more efficient than fragmentation because material is always forced into the voids. This model of the later stages of compaction is comparable with the idea of the elimination of pores proposed by James (1972) and Bockstiegel and Hewing (1965) in their work. Cooper and Eaton (1962) performed experimental work on the compaction behaviour of four ceramic powders of different hardness values but of essentially the same particle-size fraction (44 to 62 μm). Fractional volume compaction-pressure curves produced from these experiments revealed the inadequacy of using a single mechanism to account for the compaction behaviour. Cooper and Eaton used their theory of compaction and considered the two processes mentioned above i.e. the filling of large holes and the filling of small pores, to act as largely independent probabilistic processes. Using this approach they developed an expression for the fractional volume compaction V^*, in terms of the applied pressure p,

$$V^* = a_1 \exp^{-\left(\frac{k_1}{p}\right)} + a_2 \exp^{-\left(\frac{k_2}{p}\right)} \qquad (2.20)$$

where a_1 and a_2 are dimensionless coefficients that indicate the fraction of theoretical compaction that would be achieved at infinite pressure by each particular process. The total $(a_1 + a_2)$ equals unity when compaction can be completely described in terms of two separate processes. If $(a_1 + a_2)$ is less than unity, it is an indication that other processes must become operative before complete compaction is achieved. Cooper and Eaton (1962) suggest that, the coefficients k_1 and k_2 (units of pressure) represent the magnitude of the compaction pressure where the particular process has the greatest probability density. The whole compaction process at compaction pressures below 172 MPa was assumed to be attributed to the filling of large voids. Cooper and Eaton believed that, the compaction behaviour of their experimental powder systems could be accurately described by the combined action of the two processes described earlier, at higher pressures. They also suggested that their relationship produced a good fit with the results obtained from their experimental powders. A number of approximations however, were used in the development of the compaction relationship. The value of the coefficients a_1 and a_2 for example, were determined by extrapolating the data to infinite pressure. The domination of a single compaction process (filling of large voids) at low pressures (below 100 MPa) could also not be assured since Cooper and Eaton did not accurately study this pressure region.

The work performed by Van der Zwan and Siskens (1982) suggests that the compaction of agglomerated, ceramic powders is much more complex than that shown for the powders containing discrete particles examined by Cooper and Eaton (1962). An agglomerate in ceramics technology is defined by Onoda and Hench (1978), as a small mass of particles, which are bonded together by surface forces and/or solid bridges, having a network of interconnective pores. Van der Zwan and Siskens studied ferrite agglomerates (diameter 100 to 320 μm) subject to uniaxial compaction up to 80 MPa and proposed an extension of Cooper and Eaton's two stage compaction process to a four stage process for agglomerated materials. Although such work is useful in the study of powder agglomerate compaction behaviour, it is much less relevant in the study of the simpler, discrete powder systems reported in this thesis.

Torre (1948) initially proposed the idea that, the compaction of powders composed of discrete particles could be considered in terms of a hollow sphere subjected to a uniform external hydrostatic pressure. This theoretical concept was used to model the pore behaviour during the compaction process. The concept was used to give theoretical support to the formula proposed by Konopicky (1948) i.e. (2.7). Torre derived a theoretical formula as a result of his ideas:

$$\mathbf{p} = \frac{2}{3}\sigma_y \mathbf{Ln}\left(\frac{\mathbf{r_a}}{\mathbf{r_i}}\right)^3 \tag{2.21}$$

where σ_y is the yield stress in tension and r_i, r_a are the inner and outer radii of the hollow sphere respectively. Heckel (1961a) tried to give experimental evidence for Torre's correlation. However, a critical analysis performed by Bockstiegel (1966a), revealed that Torre's formula could not be the correct yielding criterion for a hollow metal sphere because of mistakes in Torre's calculations, which involved unsound assumptions about the theory of elasticity. Torre's basic idea of the relation of the compaction behaviour of a porous body to the shrinkage behaviour of individual pores under a surrounding stress field was however, considered to be worthy of further attention. Bockstiegel therefore, recalculated this hollow sphere model in a manner more strictly related to principles known from the theory of elasticity in Bockstiegel (1966a). Bockstiegel found from this analysis that a hollow metal sphere cannot yield unless the external pressure exceeds a certain threshold, p_{min}, which is larger, the smaller the volume of the hole becomes in relation to the volume of the solid metal. A formula was therefore developed:

$$\mathbf{p_{min}} = \frac{2}{3}\sigma_0 \frac{\mathbf{r_a}^3 - \mathbf{r_i}^3}{\mathbf{r_i}^3} \tag{2.22}$$

where σ_0 is the upper yield stress of the metal in tension, r_a is the outer radius and r_i the inner radius of the hollow sphere. The above yielding criterion can be used to explain quantitatively why, on average, larger pores disappear at lower pressures than smaller ones. However, (2.22) should strictly be viewed under conditions of elastic behaviour and as measurable deformation continues into the plastic region modification of this equation is necessary, due to the fact that Hooke's law on which it is based, no longer applies. Bockstiegel (1966a) provided experimental evidence for his assertion that large pores shrink first, from die compaction studies of iron powders (size 100 μm) compacted up to 150 MPa.

Stanley-Wood and Johansson (1980) provided further experimental evidence that, a reasonable qualitative picture was provided by Bockstiegel's model. These workers studied the variation of inter- and intra-particle porosity of dicalcium phosphate and magnesium trisilicate powders (size 15 μm) die compacted up to a pressure of 250 MPa, by means of mercury intrusion and nitrogen adsorption techniques and also found that large pores shrunk first followed sequentially by smaller pores as the compaction pressure increased. Palmer and Rowe (1974) used similar experimental techniques on polyvinyl chloride polymer powders (size 75 to 90 μm) subject to die compaction up to pressures of 220 MPa. They found that the pore structure of a polymer compact was also dependent upon the initial morphology of the particles and the mechanism of compaction.

Sundstrom and Fischmeister (1973) argued that the models of Bockstiegel and Hewing (1965) and Bockstiegel (1966b) did not take into account the actual shapes of the pores in the powder compact (the pores were usually assumed to be spherical) or the interaction between adjacent pores. These workers performed die compaction experiments on two-dimensional lead plate models (particle size 10 mm) up to a pressure of 1 GPa. The pore shapes specified in these models were either tetracuspid or 'diamond', in an attempt to represent the pore shape encountered in a regular array of equally-sized spheres. Sundstrom and Fischmeister found that the pore shape remained rather unchanged during compaction, in a manner similar to the model of Torre (1948). The deformation of the 'diamond' pore model was calculated using finite element analysis and the results of this analysis indicated that, the nearly hydrostatic character of the stress field around the pores was responsible for the limited pore shape-change during compaction. Stress-strain data from these compaction experiments persuaded Sundstrom and Fischmeister that the stress required for densification was influenced less by work hardening of the material (in the plastic region) and more by the change in the particle geometry. A two stage mechanism for compaction was presented by these workers as a description of the compaction process. The early stages of compaction were suggested, from the evidence of the finite element analysis, to involve pore closure and the latter stages were said to be controlled by plastic deformation of the bulk powder mass, although no experimental evidence was presented for this latter statement.

Most models of the densification behaviour of powders subject to pressure obtain the degree of particle shrinkage from the linear densification between two spherical particles in a regular packing e.g. Sundstrom and Fischmeister (1973).

Artz (1982) however, developed a model that considered the densification of spherical powders in three-dimensional cold compaction, to be described in terms of the shrinkage of the Voronoi cells associated with the initial packing of the powder particles. The Voronoi cell or polyhedron of a particle in a packing is the set of all points in space which are closer to the particle's centre than to any other particle centre. Densification of the packing within Arzt's model is modelled as concentric growth of the particle (see figure 2.3), beyond the stationary walls of its cell (new radius R'). The excess volume outside the polyhedron (the shaded area in figure 2.3b) is redistributed evenly over the free surface of the sphere (in the case of cold compaction) to produce the truncated sphere visible in figure 2.3c. Artz believed that the advantage of this approach lay in its ability to quantitatively explain the increase in particle co-ordination during compaction (increase in new neighbours). The precise prediction of particle geometry during densification via cold compaction using Arzt's method however, depends upon the assumption of plastic flow as the dominant densification mechanism.

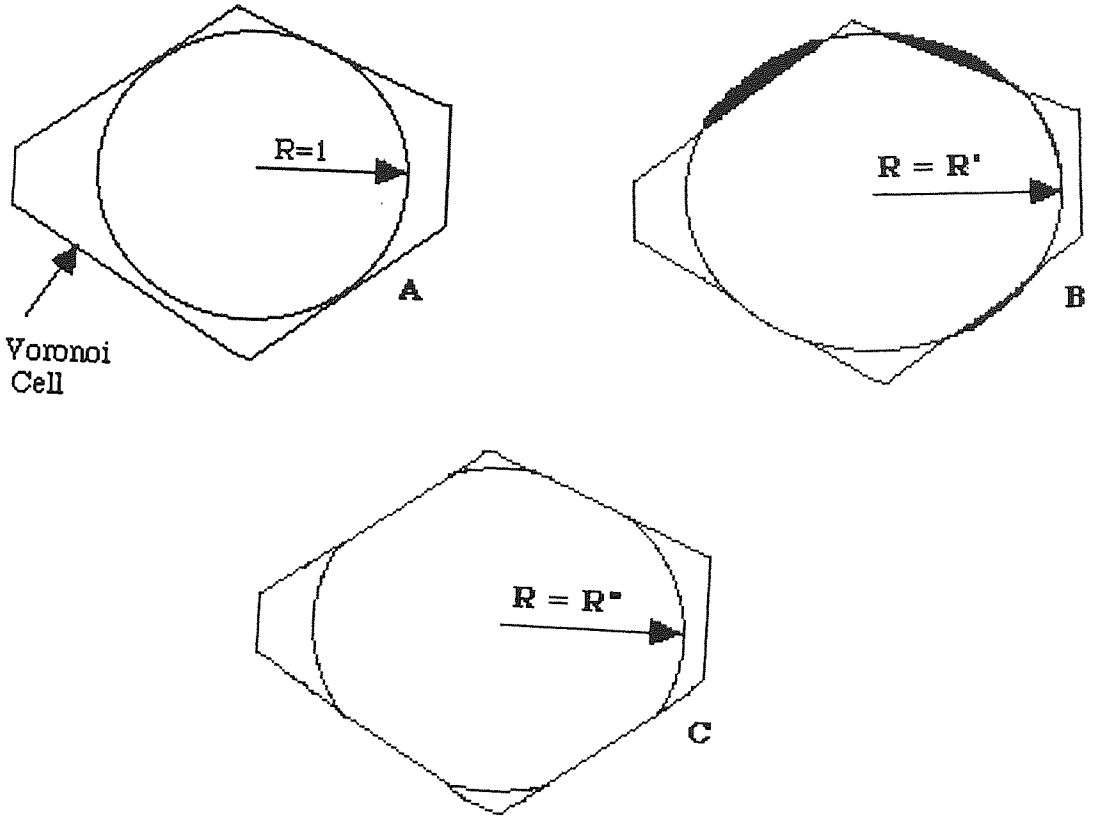

Figure 2.3 **A:** Average Voronoi cell (particle radius R = 1)
B: Concentric growth of particle beyond cell walls (new particle radius R = R'). **C:** Redistribution of excess particle volume as truncated sphere of radius R".
Excess particle volume - shaded] (After Arzt, 1982)

The mechanisms of die compaction can only be truly understood if the knowledge of the transmission of forces through the compacting mass is clarified. Analysis of the nature of the force transmission through a powder mass in a die during compaction has been studied by a number of workers. Train (1956 and 1957) used a system of manganin resistance gauges embedded in a magnesium carbonate powder mass to record the pressure response of the mass during compaction (up to 181 MPa). A complex stress pattern was found to develop in the mass during the compaction process. When the compaction pressure was low (below 3 MPa), a resisting pressure built up in the powder, especially in the zone where the face of the moving punch met the die wall, and there was a pressure gradient from the top corners towards the top centre and towards the bottom of the pressing.

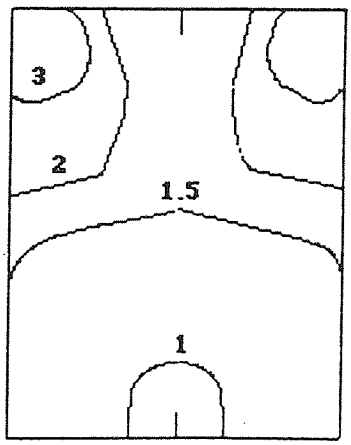

Figure 2.4 Vertical pressure distribution in magnesium carbonate compact at 3 MPa - [Contour levels in MPa]. (After Train, 1957)

The internal pressure distribution pattern changed as the applied pressure was increased, until at pressures > 55 MPa, a relatively constant pattern was obtained. The pressure distribution at this stage now exhibited wedge-shaped high pressure zones in the top corners, joined by ridges of slightly lower intensity to another high pressure region in the mid-lower centre position of the compact. Low pressure zones were found to occur in a zone close to the centre of the upper punch and also in the regions near the bottom corners of the die (see figure 2.5).

A detailed explanation of these observed pressure patterns is presented in Train (1957). Train, in the same paper, found that the most efficient bonding of the particles in the powder mass and highest powder strength resulted from subjection of the particles to shear as well as to compressive forces. Train (1957) also discovered a good correlation, over the range of pressures observed (from 3 MPa to 1 GPa), between the local pressure developed in a compact and the apparent density produced at the same point. Train believed that this correlation, from the evidence of his experimental results, was observed in all sections of the compact. The pressure distribution patterns obtained by Train were in accord with those published by Kamm *et al* (1947) who analysed compaction of a copper powder up to 466 MPa. Ünckel (1945) who worked with iron powders compacted up to 588 MPa, detected the low intensity zone in the compact centre, under the top punch, but did not demonstrate the presence of a high intensity area beneath this zone.

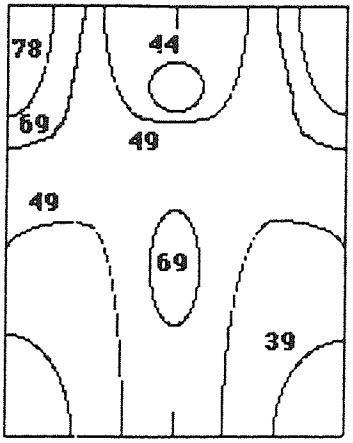

Figure 2.5 Vertical pressure distribution in magnesium carbonate compact at 65 MPa - [Contour levels in MPa]. (After Train, 1957)

Macleod and Marshall (1977) also obtained similar density distribution results to those of Train in their die compaction studies (up to 500 MPa) of uranium dioxide powders (size 600-900 μm). These workers used the technique of autoradiography, where the sample material contains a radioisotope which allows the concentration of material at a point to be accurately determined. The occurrence of the density patterns were explained by these workers in terms of die wall frictional effects, which were found to be the largest single contributors to the density distribution and relative volume changes within the compact.

Kunin and Yurchenko (1968) developed a formula taking account of the effect of die-wall friction on the calculation of the net compaction pressure. These workers carried out work on tin, copper and aluminium powders (size 200 μm) subject to die compaction in the pressure range 0 to 150 MPa. These workers believed that the overall compaction pressure p was balanced by the pressure required for powder densification p_n and the friction of the powder against the die walls, p_f i.e.:

$$p = p_n + p_f \tag{2.23}$$

Theoretical analysis by Kunin and Yurchenko allowed the development of a formula for the calculation of the net pressure for compaction σ_n:

$$\sigma_n = \left(1 - \frac{16 m \mu K}{\pi d^3 \gamma}\right)\sigma \tag{2.24}$$

where m is the compact weight (kg), μ is the coefficient of wall friction, K the coefficient of lateral pressure, d the die-opening diameter, γ the density and σ the applied compaction pressure. Van Groenou (1981) also analysed the effect of die-wall friction on die compaction of iron oxide samples (size 200 μm) up to 100 MPa and found that the friction coefficient was some unique function of the ratio of particle size to wall roughness. However, Van Groenou admits that this functional relationship was a simplification of a more complex situation and further analysis was required.

A significant percentage of the powders used in the ceramic, polymeric and food processing industries are composed of agglomerated powders. Therefore, the effects of die wall friction on the internal mechanisms of compaction during the compression of such powders are industrially important. Isherwood (1987) developed simple models of the frictional effects in agglomerated powders during uniaxial compaction and compared the predictions from theses models with experimental results from uniaxial compaction of polymers (polypropylene agglomerates) up to 25 MPa. This comparison indicated that a power law relationship provided a good fit to the compaction data:

$$\left[\left(\frac{\Delta H}{\theta_0 H_0}\right)\right]_t = B p_A^{\,n} \tag{2.25}$$

where n is the exponent for the relationship, $\Delta H = H_0 - H$ is the change in compact height, H_0 is the compact height before compaction and H is the compact height during compaction, θ_0 is the initial porosity, the subscript t denotes friction, p_A is the applied pressure and the constant B is given by:

$$B = - \frac{1 - a^n}{n \ln a} C \qquad (2.26)$$

where $a = p_T/p_A$, p_T is the pressure transmitted through the powder compact and p_A is the external pressure applied to the powder during uniaxial compaction. A power law representation like (2.25) may have been quantitatively useful in the relatively, low pressure range studied by Isherwood, but little evidence of its qualitative significance was presented. Therefore, such a relationship does not help in the understanding of the physical processes responsible for the compaction behaviour of agglomerated powders. Briscoe and Evans (1991) looked at uniaxial die compaction (up to 160 MPa) of zirconia and alumina, ceramic powders which were agglomerated with water-soluble polymer binders to form granules in the size range 250 to 280 μm. This paper extended and drew upon reported studies by Briscoe *et al* (1987) on the action of frictional effects during the extrusion of food (maize) powders and showed a means of modelling wall friction on a discrete particle-wall interaction basis. The friction at the die wall during compaction experiments in Briscoe and Evans' work was deduced and these values compared with data obtained from a number of other compaction experiments. This comparison was made by assuming a model of friction which was an extension of the adhesion model of friction proposed by Briscoe (1981). Therefore, in the model proposed by Briscoe and Evans (1991), it was assumed that frictional work was dissipated at the walls in the binder material and friction arose from interface shear at real areas of contact in the ceramic powder. These workers found that if the data obtained from the various experiments was compared in terms of their model, then reasonably self-consistent behaviour was observed. Briscoe *et al* (1994) incorporated die wall friction effects in their die compaction study (0 to 700 MPa) of alumina powders (mean size 1.3 μm). They found that a simple empirical equation could represent the relationship between compact density and compaction pressure (range 35 to 700 MPa) produced from their experimental work:

$$\rho = A + B \ln(\sigma) \qquad (2.27)$$

where ρ is the percentile relative green density with respect to the theoretical density of alumina (3980 kg/m^3), σ is the compaction pressure and A, B are experimental parameters. Although (2.27) was quantitatively useful, no qualitative arguments were put forward by these workers to explain its significance. Adams and McKeown (1995) did however, develop a micromechanical model of uniaxial powder compaction for beds of agglomerates called the lumped-parameter relationship. This model apparently provided a good fit to the bed compaction data for a number of different agglomerates e.g. sand, lead, up to a pressure of 20 MPa. However, the lumped-parameter relationship assumed the agglomerates were subject to plastic deformation and it is therefore, not qualitatively useful for the simulation work presented in this thesis. Adams and McKeown also tried to validate their model by claiming that it lead to an explicit form of the Kawakita relationship presented in (2.17). However, the problems with the qualitative interpretation provided by Kawakita's model, which were reviewed in more detail in section 2.1.2, mean that this validation is not certain.

2.2 Experimental studies of binary systems

The pressure-density relationships reviewed in section 2.1 were only proposed for single component powder systems covering a relatively narrow range of particle sizes. A number of compaction studies however have been performed on binary systems, mostly using the Hot Isostatic Pressing (HIP) technique. A selection of the more important work published on compaction of binary mixtures of powders will be considered in this section.

2.2.1 Uniaxial compaction studies

Kurup and Pilpel (1978) analysed the pressure-density relationships of mixtures of the type normally employed in pharmaceutical tablets, Esezebo and Pilpel (1976) e.g. starch and polyvinylpyrrolidone (particle size 4 to 10 μm). The experimental work involved die compaction at pressures up to 300 MPa. The results were then analysed in terms of the equation of Heckel (2.14). The Heckel equation was rewritten in this situation as:

$$\ln\left[\frac{1}{(1-\rho_f)}\right] = K_H p + A_H \qquad (2.28)$$

where ρ_F is the packing fraction of the pharmaceutical tablet, p is the applied pressure and K_H, A_H are constants, determined from the slope and intercept respectively of the extrapolated linear portion of the plot of $\ln[1/(1-\rho_F)]$ against p. Kurup and Pilpel claimed that the Heckel plots for the mixtures examined were characterised by an initial curved section up to a pressure limit of 200 MPa followed by a linear section. Figure 2.6 however, indicates that such a statement is very subjective. The possible mechanisms responsible for the observed mechanical behaviour are discussed in section 2.1.3. Kurup and Pilpel suggested that Heckel's relationship was sensitive enough to distinguish between the various stages of the compaction process for the composite materials investigated. The results indicated that the value of K_H increased and the value of A_H decreased as the amount of the softer (minor) component e.g. starch, in the binary powders was increased. Kurup and Pilpel used the unproved assertion of Heckel (1961b), that K_H is the reciprocal of a material's mean yield stress in the analysis of their results. However, it is possible that K_H is a material constant since the results showed that the softer, more ductile binary systems had higher K_H values than the harder powders. It can be concluded from the work of Kurup and Pilpel that correlations can be established between the composition of the formulated powder mixtures and the values of the Heckel parameters.

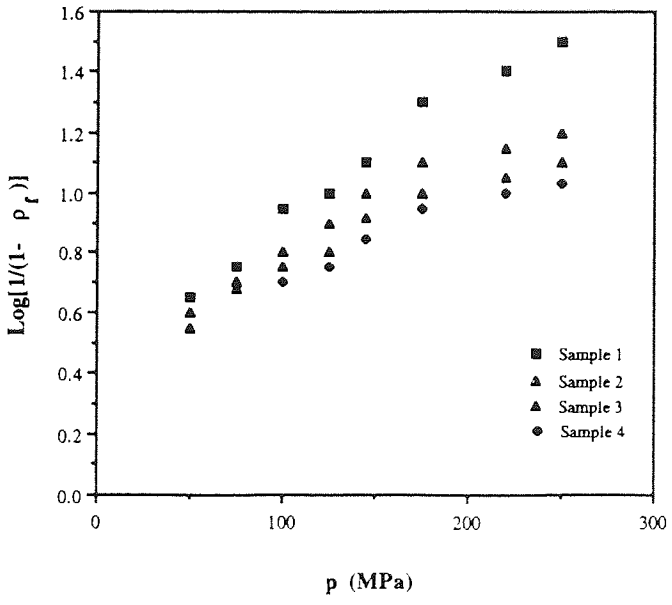

Figure 2.6 Heckel plots for binary mixture samples of starch and polyvinylpyrrolidone. (After Kurup and Pilpel, 1978)

Lange *et al* (1991) performed uniaxial die compaction experiments (at room temperature) for aluminium and tin powders (size 0.2 mm and 1 mm respectively) containing various amounts of spherical (size 1.2 mm) steel inclusions. The aluminium and tin powders were regarded by Lange *et al* as the 'soft' component and the steel inclusions as the 'hard' component, of the binary mixtures. The compaction studies were carried out in the applied pressure range 0 to 450 MPa and the results illustrated that the 'hard' inclusion phase offered little constraint to matrix deformation at volume fractions < 0.20, but produced a rapidly increasing constraint at larger volume fractions. Microstructural observations (using SEM) showed that in order to achieve full density, the matrix particles in contact with the steel inclusions had to deform more than those particles located away from the inclusions. The increased amount of deformation was due to the excluded volume associated with the packing of particles and inclusions of different sizes. The use of SEM techniques by Lange *et al.* revealed that the hard inclusions were able to form a continuous touching network from observation of the deformation flattening of the steel spheres during compaction. These SEM observations however, did not provide conclusive evidence for their proposal that the inclusion network supported a substantial portion of the applied pressure, particularly at low inclusion volume fractions.

Lange *et al.* (1991) also performed computer simulations to model *site percolation* (see section 3.1) via random filling of sites on a face-centred cubic lattice and to determine the extent of site percolation across the model. This computer modelling suggested that the continuous inclusion network was expected to span the composite system at the percolation threshold, corresponding to an inclusion solid fraction $\phi_i \approx 0.16$ and that $> 95\,\%$ of the inclusions would be part of the same network when $\phi_i > 0.20$. The percolating network of hard inclusions was believed to support a portion of the applied stress and thus, partially 'shield' the deformable phase e.g. the aluminium or lead powders, from the total applied compaction pressure. Lange *et al* also evaluated this stress protection role by comparing the applied stress required to achieve a prescribed 'corrected' matrix density within the composite (σ_c^*) to the stress required to achieve the same density in the matrix material alone (σ_o). The stress supported by the inclusion network σ_n was then estimated by:

$$\sigma_n = \sigma_c^* - \sigma_0 \qquad (2.29)$$

The constraint (of densification) ratio due to the presence of the inclusion network was estimated by the ratio σ_c^*/σ_o according to these workers. A major criticism of this work is that Lange *et al* did not have a clear idea of how to separate the various contributions to the retardation in densification, as measured by the constraint ratio. Thus analytical estimates of the magnitude of the network stress and the other stress values provided by (2.29) need to be examined in more detail. Lange *et al* also suggested that the inclusion network released its elastic strain in a non-linear manner because of the Hertzian contact phenomenon (Johnson, 1985). The suggestion was said to be justified by the theoretical work of Walton (1987), which predicted that the stress-strain behaviour of a powder compact composed of spherical particles could be described by $\sigma = A\varepsilon^{3/2}$, where A was a function of the elastic constants of the particles and the relative density of the compact. The recovery strain for the inclusion network could therefore be quite significant due this non-linear elastic behaviour.

Lange *et al* also believed that soft matrix material would exhibit linear stress-strain behaviour but provides no justification of this statement from analysis of particle-particle contact behaviour. Experimental evidence provided by these workers did however, indicate that compacts with a large percentage of inclusions spontaneously broke apart on removal. This may provide some justification for the presence of differential strain recovery phenomenon (due to linear and non-linear contact behaviour in the two components) and the associated residual stresses described above, but it is not conclusive evidence.

2.2.2 Hot Isostatic Pressing (HIP) studies

Isostatic pressing involves the application of equal pressure in all directions during the compaction of a powder. The aim of this process is to attempt to ensure the uniformity of powder density during compaction (up to 200 MPa) and limit post-compaction processing of the product. The isostatic pressing is *hot* because complete densification of the ceramic and metallic systems processed using HIP requires elevated temperatures (> 1800 K). These high temperatures are due to the material properties of the powder systems. Cold Isostatic Pressing (CIP) would be of more relevance to the work presented in this thesis but no papers have been published, according to the author's knowledge, on CIP of binary powder systems.

Fischmeister *et al* (1978) did however study CIP (up to 250 MPa) of bronze powders (size 100 μm) and suggested that the process involved less sliding and more deformation of the particles (from SEM evidence and co-ordination number data) than occurred in uniaxial compaction.

Modelling and experimental work on the HIP process has often involved the assumption or use of a monodisperse, spherical powder. Funkenbusch and Li (1991) however, investigated the effects of binary powder mixes on initial powder packing and subsequent HIP behaviour. The experimental studies involved compaction of stainless steel powders (using particle sizes in the range 40 to 250 μm and compositions ranging from 0 to 100% of the larger particles) at 840 °C, up to a pressure of 44.3 MPa. Funkenbusch and Li suggested, from their experimental results, that the behaviour of the bimodal powders (size ratio 2:1, 4:1) was similar to that seen in the monodisperse mix and that the role of particle rearrangement during densification of the bimodal powders was of no greater significance than in the case of a monodisperse system which was studied. The bimodal powder mixes were also found to densify more slowly than the monosized system. The nature of the compaction mechanisms within the experimental system was however, prone to potential misunderstanding due to the lack of continuous data monitoring and also a lack of detailed microstructural analysis of such mechanisms. Funkebusch and Li also attempted to model the HIP process, based on the assumption of uniform contraction of particles during the compaction process. The modelling work undertaken by these workers was found to produce results for the stainless steel systems that were comparable with their experimental work. Funkebusch and Li however, do mention in their paper that the modelling work assumed a uniform distribution of contact deformation between all the particles. Modifications to this model would therefore, be required for hard/soft particle system analysis, since the hard components should offer a greater resistance to compaction than the soft components of the system.

Lafer *et al* (1991) looked at the role of hard inclusions (150 μm alumina particles) in the compaction process of powder composite systems (18 and 35% volume fraction of inclusions). These systems also had a nickel base superalloy as the matrix powder (particle size 150 μm) and were subject to HIP up to a pressure of 200 MPa, at a temperature of 1000°C. These workers suggested that their macroscopic and microscopic results agreed with the work of Lange *et al* (1991), even though the nature of the compaction processes was very different.

Lange *et al*'s idea of the formation of a continuous network of hard inclusions, supporting part of the applied pressure was suggested by Lafer *et al* as the explanation for the retardation of densification for the 35% inclusion system. The experimental evidence presented for this case, broken alumina particles visible in all samples of this system using SEM, is however inconclusive, since thermal stresses may be responsible for such behaviour.

Bordia and Raj (1988) attempted to prove that HIP of ceramic/ceramic composites could be performed at pressures > 10 MPa to produce dense and reliable products. The experimental systems (3,9 and 15% alumina) of Bordia and Raj consisted of *hard* alumina inclusions (size 20 to 37 μm) present in a titania matrix (size 20 to 37 μm) subject to a temperature of 1273 K. The experiments however, were conducted under uniaxial rather than isostatic compression and therefore, cannot be strictly classified as HIP experiments. The thermal effects e.g. creep associated with the high temperatures used in HIP studies will also affect the compaction behaviour of the powder particles in these experiments.

2.3 Photoelastic disc experiments

Common laboratory tests do not give sufficient information on the mechanical behaviour of granular material because elementary parameters of the granular assembly, such as the components of internal stress and strain, cannot easily be measured during complex loading. Therefore, models such as those of Heckel and Kawakita (see section 2.1) have limited applicability to general powder systems, as indicated earlier. If photoelastic material however, is used to model the powder, direct measurement of internal contact stresses and strains can be achieved via a variety of photoelasic techniques.

Schneebeli (1956) first developed a two-dimensional analogue of a granular material using an assembly of 100 metal rods (radius 0.25 mm, length 40 mm). In Schneebeli's test set-up only the displacements of the rods could be observed and the internal stress distribution within the assembly was not analysed. Tests executed with the Schneebeli model, in terms of general assembly mechanical behaviour, have been reported by De Josselin de Jong (1959) and Drescher *et al* (1967). De Josselin de Jong (1959) performed tests in simple shear on a Schneebeli model of Plexiglas rods (length 5 cm, radius 1.5 mm).

Drescher *et al* (1967) looked at the plane motion of both a Schneebeli model of Plexiglas cylinders (10 cm long, radius 1.2 to 1.9 mm) and a sand system (particle size 0.5 to 2 mm) subject to the indentation of a rigid wedge. The experimental results were found to be in reasonably good agreement with Drescher *et al*'s theoretical prediction of the indentation force based on the theory of perfect plasticity. The interpretation of tests results using the Schneebeli model however, is not totally satisfactory, because the force distribution in the interior of the model has to be inferred from the boundary conditions. Dantu (1957) therefore, suggested the use of optically-sensitive material for the rods or discs in a Schneebeli-like model in order that the forces in the discs could be determined. Dantu's study aimed to produce a very basic understanding of the mechanism of stress transmission within a granular medium subject to uniaxial compaction (up to 70 MPa). The granular medium used was a two-dimensional cohesionless ensemble formed from Plexiglas cylinders (length 2 cm, radius 1 to 3 mm). Stress transmission lines inside the assembly were clearly obtained by Dantu but no quantitative analysis of the stress distribution pattern was performed.

Wakabayshi (1957) used Plexiglas photoelastic discs (radius 0.5 mm) in two-dimensional stress distribution studies of uniaxial compaction (up to 50 MPa). Wakabayshi was able to observe parallel lines in the direction of the principal stresses within the assembly ('isochromatic principal stress lines') due to the optical properties of the discs. Wakabayshi (1959) performed further uniaxial compaction studies and experiments involving indentation by a rigid wedge on the same granular system. The constructive use of photoelastic techniques by Wakabayshi allowed him to measure the forces in the interior of the disc assembly, which was not performed by Dantu (1957), without using the unsatisfactory procedure of determining the stress state from the boundaries. However, attempts by Wakabayshi (1959) to evaluate the magnitude of the principal stresses did not yield satisfactory results. Wakabayshi (1957,1959) also did not attempt to analyse the interactions of the individual system components and only considered the general stress distribution within the granular system. The application of the techniques of Dantu and Wakabayshi has however, been used by several investigators to investigate the fundamental behaviour of granular material at the grain scale.

Drescher and de Josselin de Jong (1972) used the optically-sensitive particle approach developed by Dantu (1957) and Wakabayshi (1957), to study the flow rules for two-dimensional granular assemblies subject to shear testing.

The experimental assembly used by these workers consisted of 1200 discs of CR-39 co-polymer (radius 4 to 10 mm) enclosed in a wedge-shaped area of 1755 cm^2 between 6 mm thick glass plates that prevented the stack from buckling sideways. The assembly was subject to shearing and viewed in circularly polarised light, which allowed evaluation of the forces acting between discs. The experimental approach and assembly was based on that adopted by de Josselin de Jong and Verruijt (1969). Drescher and de Josselin de Jong calculated the ensemble average stress tensor by averaging the contact forces over a region in the interior of the assembly. Photographs of successive stages during a deformation cycle allowed these workers to determine the relative displacements of the individual discs. An average velocity-gradient tensor was then deduced for the same assembly region for which the average stress tensor was determined. The most important results produced by Drescher and de Josselin de Jong in terms of the experimental work presented in chapters 5 to 9, involved qualitative analysis of the contact force distribution network within their experimental assembly. A discrete distribution of contact forces was observed in the test assembly (see figure 2.7). Drescher and de Josselin de Jong believed that the forces transmitted through the disc contact areas depended on the geometrical distribution of the contacts between adjacent particles. Chains of aligned contact points were also thought to form rigid columns of particles, which attracted large forces because of their relative rigidity with respect to the surrounding particle groups. Drescher and de Josselin de Jong put forward the reasonable suggestion that since the columns of discs were created in a random fashion and the probability of producing a chain of aligned particles was small, a discrete contact force distribution (as observed in figure 2.7) was likely.

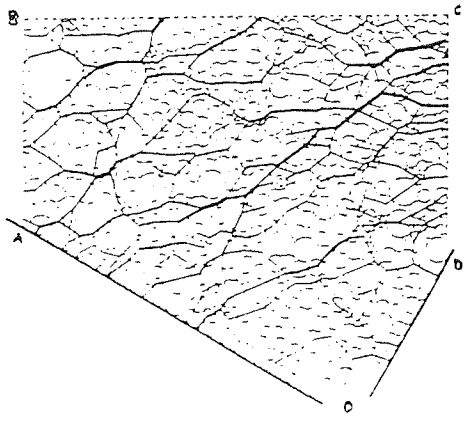

Figure 2.7 A network of contact forces [Thickness of lines proportional to the magnitude of the transmitted forces]. (After Drescher and de Josselin de Jong, 1972)

The idea of an arrangement of discrete particle forces in an assembly is however, very different to the more familiar concept of a continuous distribution of forces inherent in the continuum concept of stress.

Oda and Konishi (1974) also performed work on two-dimensional, random assemblies of photoelastic, epoxy resin cylinders (length 1.9 cm, radius 0.3 to 0.5 mm) subject to simple shear. Oda and Konishi reported in this paper that their two-dimensional model tended to show the same macroscopic deformation and strength characteristics as that obtained in tests on sand by Oda (1972a,b). The number of sliding contacts during shearing in their cylinder assembly was found to be small and confined to some preferred contact orientations. Oda and Konishi (1974a) suggested that this limited number of sliding contacts was probably due to the nature of the assembly deformation mechanism. They also thought that, deformation of the assembly involved relative motion between instantaneously rigid groups of particles and this suggested little particle sliding. This 'rigid groups of particles' idea seems to be akin to the particle 'columns' suggestion of Drescher and de Josselin de Jong (1972) as a qualitative microscopic model of particle behaviour. Konishi *et al* (1982) employed the technique of Oda and Konishi (1974a) and used similar tests, but with oval shaped particles, to investigate the effects of inherent assembly anisotropy due particle deposition.

Drescher (1976) and Allersma (1982) conducted shear experiments on optically sensitive crushed glass (particle size 1 to 3 mm), since they believed that such material resembled a real granular material more closely than assemblies of rods and discs, as spherical particles are quite rare in nature. A system of crushed glass particles is entirely opaque, because of the reflection and diffraction at the particle faces. However, both Drescher and Allersma ensured that the particle pores were fully saturated with a liquid having the same refractive index as the particles, so that light traversing the masses was not deflected and their systems became transparent to light. If external loads were applied to the assembly, the interaction between particles in contact produced a stress state within each particle. The stress state resulted in an optical effect visible in polarised light, because of the birefringent property of the glass. This optical effect was also produced in the photoelastic rod and disc assemblies which were mentioned earlier in this section. The subjective nature of the analysis of these birefringence patterns casts some doubt on the assembly principal stress directions determined in the tests performed by Wakabayshi (1957,1959), Drescher and de Josselin de Jong (1972) and Oda and Konishi (1974a), who all followed Wakabayshi's (1957) simple analytical approach.

The investigation of Drescher (1976) which aimed to compare the principal directions of the stress and strain-increment tensors during shear testing also required knowledge of the stress trajectories in the crushed glass assembly and again used Wakabayshi's analytical approach. Drescher's results were found to be quantitatively similar to those obtained by Drescher and de Josselin de Jong (1972). Allersma (1982) developed a technique to optically measure the local stress tensor within a specimen during his shear tests. He found from using such crushed glass material that it was not possible to determine the microscopic quantities associated with individual particles or particle contacts. This drawback was due to the invisible nature of the actual particles and hence it was not possible to make any reference to structure or the microscopic mechanisms of deformation.

Properties of granular media have been found to depend not only on their geometrical structure and intrinsic properties of the constitutive grains, but also, often crucially, on the nature of the contacts between grains (Travers *et al* (1986)). In an experimental photoelastic assembly, transmission of forces takes place only through contacts and therefore, the nature of the contacts is important in influencing the macroscopic mechanical behaviour of the assembly. Travers *et al* (1987, 1989) studied uniaxial compaction of two-dimensional ordered packings of parallel horizontal Plexiglas cylinders (length 2.5 cm, radius 2 mm). The system was composed of 2136 cylinders i.e. 48 layers of (alternatively) 44 and 45 cylinders. It was assumed by Travers *et al* that all the geometrical defects in the cylinders e.g. deformation along their axis, could be described as diameter fluctuations and therefore, the diameter of the cylinders was chosen to be 4 ± 0.1 mm. These geometrical defects were believed to responsible for the heterogeneity of the stress network in the assembly. The macroscopic stress-strain law for the assembly was found to be strongly non-linear and was written as:

$$\frac{\mathbf{F}}{\mathbf{F_0}} = \left(\frac{\Delta \mathbf{h}}{\mathbf{h_0}}\right)^{\mathbf{m}} \tag{2.30}$$

where F is the macroscopic force, h_0 the initial height of the packing and Δh its decrement when force F is applied, F_0 is a prefactor and m is the experimental macroscopic exponent. The value of m was found to be $m = 3.9 \pm 0.3$ from Travers *et als'* (1987,1989) results. The discrepancy between this macroscopic value of m and the microscopic value of $m = 3/2$ from Hertz's law (see Johnson, 1985) was thought by Travers *et al* to be attributed to geometrical heterogeneities of the cylinders in the assembly.

This idea may be acceptable, since Travers *et al* (1989) performed further experiments on their Plexiglas cylinder assembly and found that a better surface state on a second assembly of Plexiglas cylinders gave a value of $m = 3.5 \pm 0.4$, closer to the Hertz exponent value. In an assembly of rubber cylinders, where the deformation of the cylinders was much larger than the scale of the inhomogeneities, the measured exponent $m = 1.4 \pm 0.1$ was compatible with the Hertz exponent. The work of Drescher and de Josselin de Jong (1972) indicated that the strongest stresses in the assembly formed links which are more or less connected. Travers *et al* aimed to show in their work that the macroscopic stress-strain law represented by (2.30) was very sensitive to the strongest-stressed network visualised in previous photoelastic work.

Travers *et al* (1987) found that they could create lattice vacancies, by random removal of cylinders under compression, and the neighbouring cylinders would still remain in equilibrium. These workers believed that such behaviour was observed because the assembly was almost ordered and the inter-grain friction was not negligible. Therefore, they created successively three kinds of vacancies in their assembly to show the geometrical sensitivity of the macroscopic stress-strain law. The mechanical behaviour of these systems is shown in figure 2.8. The first vacancy type were *bright* vacancies i.e. the cylinders removed were the nodes of the strongest-stressed network as seen in photoelastic analysis.

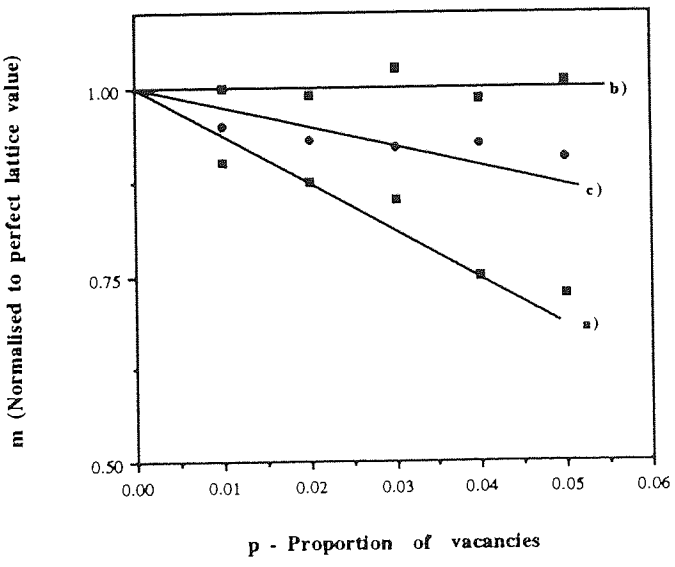

Figure 2.8 The relationship between the exponent m and the Plexiglas composition of the assembly p for three vacancy cases: a) *bright* vacancies b) *dark* vacancies c) *pseudo random* vacancies (After Travers *et al*, 1987)

The second type were *dark* vacancies i.e. the cylinders removed were not part of the strongest-stressed network. The final type were *pseudo-random* vacancies, where the site of the vacancy was determined from a random number program, irrespective of the contact force. However, direct visual observation by Travers *et al* of systems generated with any of these three types of vacancy indicated little difference between the systems. In the assembly with *bright* vacancies m shows a strong variation with vacancy concentration, which indicates that the strongest-stressed network is mechanically important. Travers *et als'* work also showed the importance of the heterogeneity of the spatial distribution of stresses between the grains. These workers suggested that the lack of influence of dark vacancies in the stress-strain law (see figure (2.8)) strengthens the concept of *mechanical porosity* as opposed to *geometrical porosity* (ratio of the assembly void volume to the total volume) in determination of the mechanical behaviour. Mechanical porosity was considered by Travers *et al* to take account of the volume of cylinders not involved in the assembly stress network i.e. those cylinders not transmitting stresses. Travers *et al* (1989) also found that besides this contact disorder, orientational order affected the mechanical behaviour of their experimental systems. The use of such studies on regularly packed, homogeneously elastic experimental assemblies in describing the mechanical behaviour of real, heterogeneous, randomly packed real particle systems must however be treated with caution.

The concepts of percolation theory (reviewed in chapter 3) have been used by a number of workers in the analysis of the heterogeneity of contacts in two-dimensional experimental assemblies of elastic discs and cylinders. Geometrical heterogeneities in elastic assemblies were investigated by Travers *et al* (1987, 1989) in terms of the concepts of normal macroscopic mechanical analysis. Travers *et al* (1986) however, looked at the effect of compositional heterogeneities arising from two-dimensional Schneebeli models consisting of binary mixtures of hard and soft cylinders, in terms of percolation concepts. The mixtures studied were composed of Plexiglas (proportion p) and rubber (proportion $1-p$) cylinders (diameter 4 ± 0.1 mm, length 2.5 cm). The ratio between the bulk Young moduli was $\sim$ 2000, the rubber selected being hard enough to avoid initial strains under gravity and the Plexiglas being selected for its photoelastic properties. The assembly packing structure and size was the same as that used in Travers *et al* (1987, 1989). The experiments involved low speed uniaxial compaction ($\dot{\varepsilon} = 4.5 \times 10^{-8}$). A vertical displacement Δh was imposed on the assembly and the corresponding compressive force F (0 to 2000 N) was measured. Several pressure cycles were performed until reproducible results were obtained.

The force-displacement relationship for the compression of the assemblies, when reproducibility of results was attained, was found by Travers *et al* (1986) to be that expressed by (2.30). The values of m and F_0 in (2.30) were found to be $m \sim 1.4 \pm 0.1$ and $F_0 \sim 4 \times 10^4$ N for an assembly where $p = 0$ (pure rubber) and $m \sim 3.9 \pm 0.3$ and $F_0 \sim 10^{11}$ N for a pure Plexiglas assembly ($p = 1$). The externally applied cylinder deformation was much larger than the scale of the geometrical inhomogenciticS for the rubber cylinders and Travers *et al* (1986) believed that this geometrical inhomogeneity was responsible for the value of m close to the Hertzian exponent when $p = 0$. The force-displacement relationships for these assemblies are presented in figure 2.9.

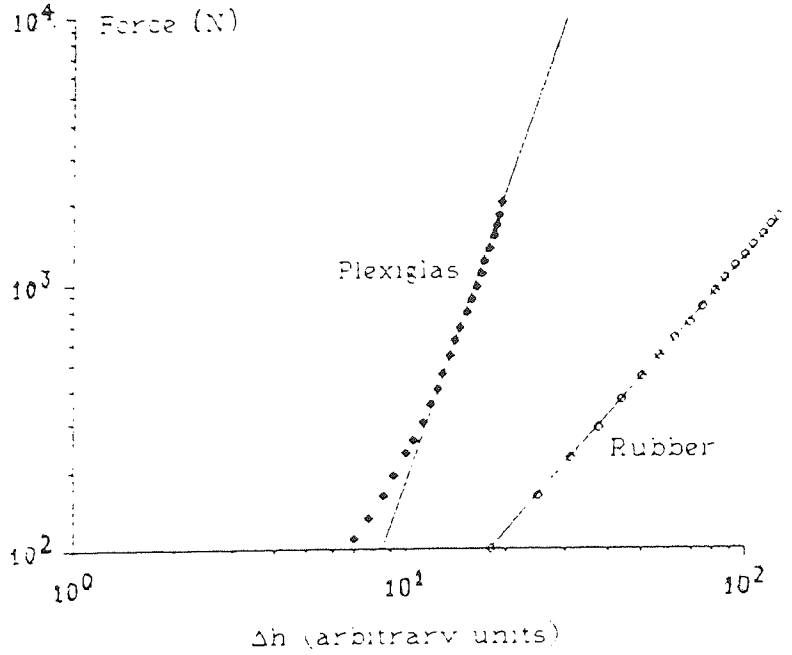

Figure 2.9 Force-displacement (log-log scale) for packings of 48 x 44 Plexiglas or rubber cylinders. (After Travers *et al*, 1986)

Travers *et al* (1986) observed a power law dependence represented by (2.30) for all the mixtures studied ($0 \leq p \leq 1$). The variation of the two quantities m and F_0 with composition p were also examined and are presented in figures 2.10 and 2.11 respectively.

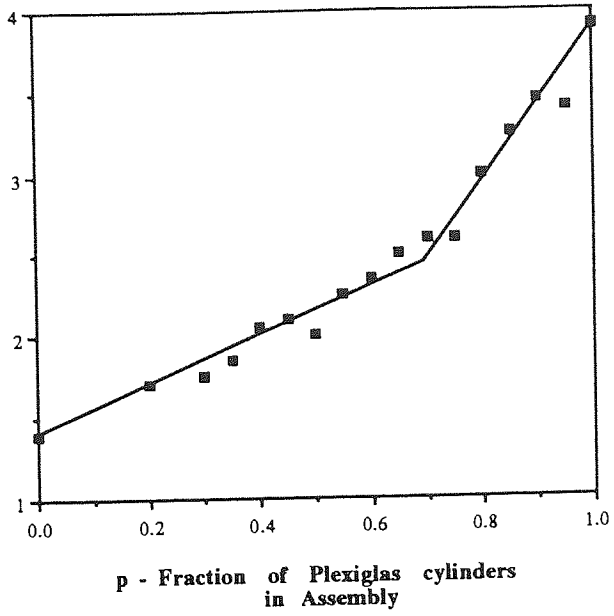

Figure 2.10 Relationship between the exponent *m* and the proportion of hard cylinders in the assembly. (After Travers *et al* , 1986)

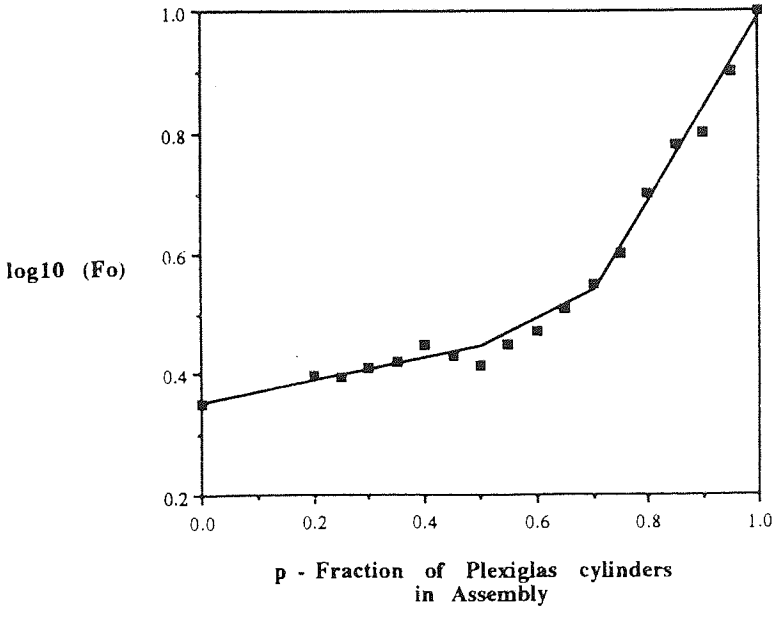

Figure 2.11 Relationship between the prefactor F_0 ($\log_{10}$ values) and the proportion of hard cylinders in the assembly. (After Travers *et al*, 1986)

The values of m and $\log_{10}(F_0)$ used were average values obtained from measurements on at least three separate samples. Figure 2.10 shows a break in the slope at $p = 0.7$ whilst figure 2.11 shows a weak break at $p = 0.5$ and a stronger one at $p = 0.7$. It should be noted that, the interpretation of a change in the slope of both figures 2.10 and 2.11 at particular value of p by Travers *et al* is very subjective. Troadec *et al* (1991) and Oger *et al* (1991) however, claim similar results in virtual copies of Travers *et als'* (1987) experiment. Travers *et al* (1986) suggest that this apparent difference in mechanical behaviour above and below $p \sim 0.7$ can be explained by a percolation-type transition (see chapter 3). This value of p is said to correspond to a rigidity threshold p_r where the assembly is stable against the macroscopic external force. Travers *et al* claimed that the value of p_r is comparable with the central-force elastic percolation threshold $p_{cen} = 0.65 \pm 0.005$ obtained by Lemieux *et al* (1985) on a triangular elastic lattice (see section 3.5), as a justification for the location of this transition point. Troadec *et al* (1991) claimed that the weak break in the slope of figure 2.11 at $p = 0.5$ corresponded to the geometric percolation threshold (see chapter 3). This threshold is a connectivity threshold and would represent the point where an infinite cluster of cylinders carrying stresses first spans the dimensions of the assembly. Further experimental results are required however, before the location of such connectivity and rigidity transition points can be quantitatively and qualitatively confirmed. Travers *et al* (1986) and Troadec *et al* (1991) believed that the strongest-stressed network of particles suggested by Drescher and de Josselin de Jong (1972) was represented by an 'infinite' percolating cluster of purely hard cylinders from photoelastic analysis of various assemblies and that this cluster supports the externally applied force. However, it was not possible to analyse the stress network in the soft cylinders using photoelastic techniques, which suggests that Troadec *et al* and Travers *et al's* conclusion may be incorrect.

Roux (1991) performed a theoretical analysis of the work of Travers *et al* (1986), Troadec *et al* (1991) and Oger *et al* (1991) in terms of percolation theory. He suggested that, since the structure of the contact networks at the supposed critical points was denser than a single path (observed from the photoelastic analysis undertaken by these workers), then the distribution of contact deformation would be expected to be multifractal (see section 3.4). This suggestion however, has not been tested numerically or experimentally. He also believed that in three dimensions, random close packing would be the most probable packing structure, if no long range interactions affected the construction of the stress-carrying network.

Roux believed that the same qualitative behaviour i.e. a critical point but with different critical exponents (see section 3.2), would be observed if a three-dimensional version of Travers *et als'* (1986) two-dimensional assembly was tested. No experimental evidence however, was offered to justify such a belief.

The use of percolation concepts in analysing the heterogeneity of contacts has also been employed in the study of the electrical conductivity of conducting grains. Packings of such conducting grains may be poorly conducting (or insulating) because of an insufficient number or quality of contacts. Percolation theory can provide an approximate criterion of continuity and by using random binary mixtures of conducting and insulating spheres workers such as Clerc *et al* (1980), Oger *et al* (1986) and Ammi *et al* (1988) have investigated this criterion more precisely. These workers discovered that there was a non-linear macroscopic response for the dependence of conductivity with pressure. The response was believed to correspond to a continuous increase in the average number of 'good' electrical contacts as the pressure applied to the granular system was increased. The definition of 'active' contacts in this case however, may be different from the mechanical one since a finite pressure may be required to break the insulating layers between grains before conduction can occur. The interpretation of mechanical (or electrical) experiments using relatively small assemblies of cylinders or spheres, in terms of the behaviour of real granular systems containing millions of particles, must be viewed with some caution. Finite size effects and wall effects may be present at the same time e.g. Ammi *et al* (1988). The relative importance of such effects will however depend on the global configuration of the cylinder or disc packing.

2.4 Computer simulation

Computer simulation techniques involving numerical models of assemblies of discs and spheres are now widely used in the analysis of the internal stresses and strains in granular media. Numerical modelling is more flexible than analytical modelling and has the advantage over physical modelling (described in section 2.3) in that any data is accessible at any stage of a test. The flexibility of numerical modelling extends to different loading configurations, particle sizes, size distributions and physical properties of the particles.

Bouvard and Lange (1991) used a computer model based on the work of Auvinet (1972) to study the affect of inclusion connectivity on the densification behaviour of a matrix powder in three dimensions. Differentiation between matrix and inclusion particles was achieved via a *size difference*. A minimum size ratio of 1:3 (matrix particle: inclusion) was selected to achieve a significant number of large particles at small volume fractions of large particles. This work was stimulated by the experimental studies of Lange *et al* (1991) and Lafer *et al* (1991) on the affects of *hard* inclusions on the densification behaviour of real particle systems (see section 2.2). Bouvard and Lange found from their simulation experiments that the critical volume fraction of inclusions required to form the first percolative cluster strongly depended on the inclusion to matrix size ratio (see figure 2.12).

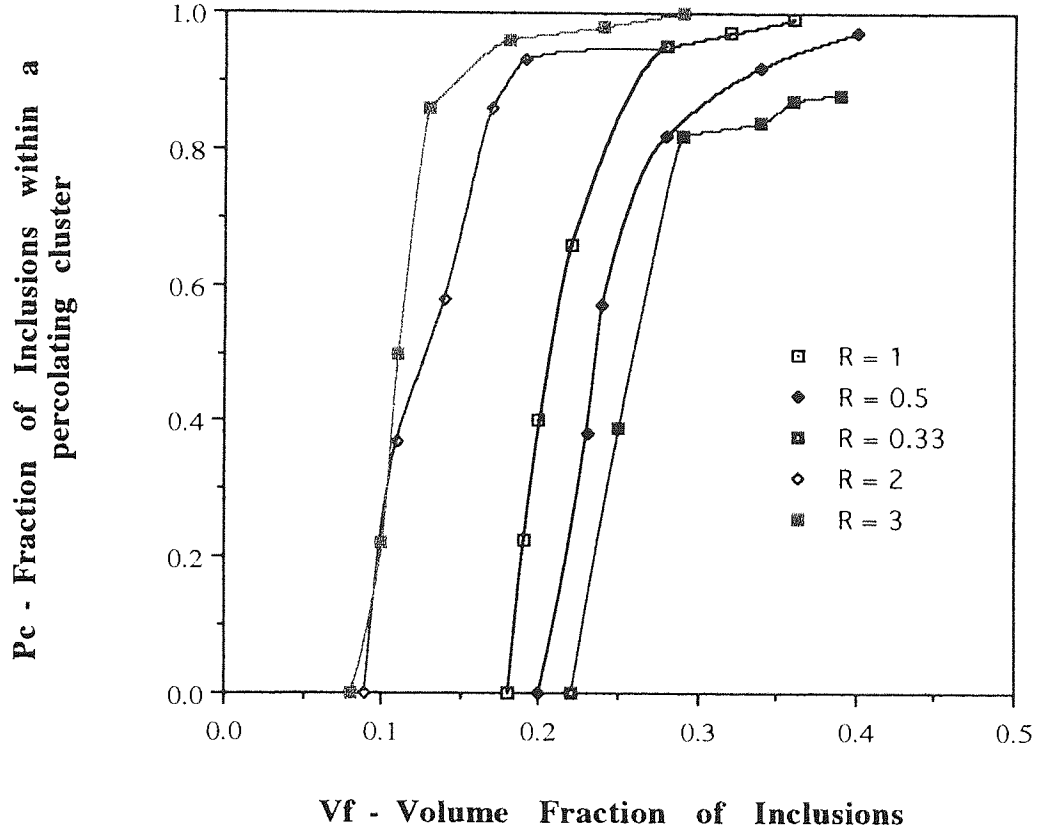

Figure 2.12 Relationship between the fraction of inclusions in a percolating cluster and the volume fraction of inclusions in the assembly (After Bouvard and Lange, 1991)

The parameter R in figure 2.12 is the ratio of the matrix particle radius r_m to the inclusion particle radius r_i i.e. $R = r_m / r_i$.

Bouvard and Lange, using the suggestions of Lange *et al* and Lafer *et al*, stated that it was the inclusion percolative network that supported an increasing fraction of the applied pressure as the volume fraction of inclusions in the assembly was increased. Bouvard and Lange however, performed simulation studies on particle systems without the contrast in matrix/inclusion particle material properties used by these experimental workers and they offered no conclusive evidence, from their computer simulation studies, to justify such a statement. Bouvard and Lange found a more useful way of representing their data in terms of composite processing by plotting P_c, the fraction of inclusions within a percolative cluster (obtained from the computer model) as a function of inclusion connectivity expressed as Z_{ii}, the average co-ordination number for inclusions touching one another (also obtained from the model). A plot of P_c against Z_{ii} reduces all the data to one master curve independent of size ratio R, and this curve is shown in figure 2.13. The figure indicates that a percolation-type threshold corresponds to $Z_{ii} \approx 2$ and $Z_{ii} \approx 4$ characterises the complete connectivity of all inclusions ($P_c = 1$). The position of the percolation threshold supports Bouvard and Lange's theoretical argument that, when one of a number of clusters first spans the simulation volume, Z_{ii} is expected to have an average value of 2. However, these workers used numerically simulated samples of limited size and therefore, found it difficult to identify the position of the percolation threshold with any precision.

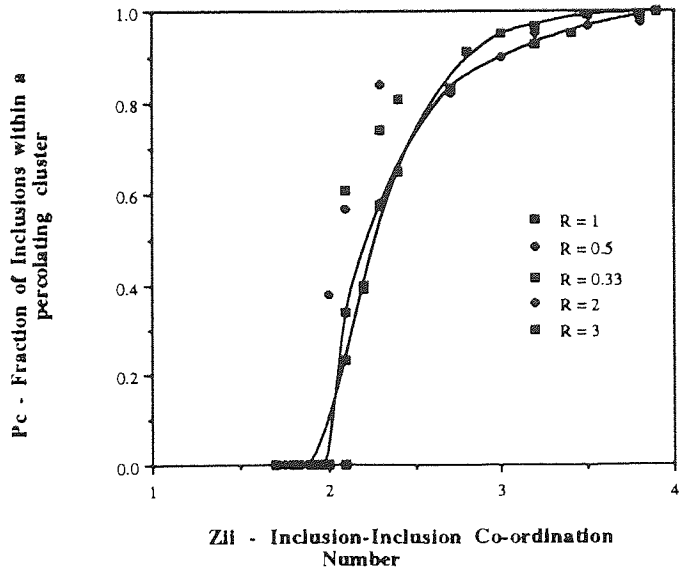

Figure 2.13 The relationship between the fraction of inclusions in the percolating cluster and the inclusion-inclusion co-ordination number. (After Bouvard and Lange, 1991)

Bouvard and Lange (1991) claimed that their computer model was designed to simulate the random packing of spherical particles, with any given size distribution, inside a cube. A number of conditions however, were imposed on the particle generation routine e.g. each generated particle had to have three particle contacts with previously packed particles before it was considered to be stable. The use of such conditions suggests that the use of the term *random* generation is incorrect. The model used by Bouvard and Lange also incorporated the use of walls and therefore, wall effects would affect the simulation results. The use of a periodic solution-space (see section 4.1) in the numerical experiments presented in this thesis eliminates such wall effect problems. Bouvard and Lange also mentioned that the restricted range in size ratio ($0.33 < R < 3$) used in their study (due to computer capability) may limit the practical application of their work. Their work is however, useful in providing an initial qualitative and quantitative approach to the percolation-based study of binary powder systems.

Sintered bodies often consist of a composite of sintering particles and non sintering *hard* inclusions. Although sintering is a thermally-based deformation process it is still useful to study the application of percolation-based techniques in computer simulation studies of this area. This is because the transition-like mechanical behaviour observed in a binary particle assembly as the composition is altered during uniform sintering e.g. Jagota and Scherer (1993) may, to a certain extent, be qualitatively akin to the behaviour of a binary system subject to deformation during isotropic compaction. Jagota and Scherer (1993) looked at the effective sintering rates and viscosities of two-dimensional granular composites using discrete computational models. The composites studied consisted of randomly mixed *hard* and *soft* spheres on a triangular lattice. Conceptually, the computational models consisted of replacing the packing of particles by a network of links (interparticle contacts) and nodes (particles). The deformation of the particle packing was computed by imposing requirements of quasi-static equilibrium on the particles. Two distinct models were employed: the *truss* model in which only force equilibrium was enforced for each particle and the *beam* model in which force and moment equilibrium are enforced for each particle. The composites are obtained by starting with a triangular lattice fully occupied by soft spheres. These spheres were then replaced randomly by hard spheres and the effective uniaxial viscosities and sintering rates $\dot{\mathbf{s}}$ of the composite were computed as a site fraction v_f of the hard spheres. The effective uniaxial viscosities were determined in the computational model by simulating compression of the packing along the z axis and setting $\dot{\mathbf{s}} = 0$ for all spheres.

Two types of hard-hard particle interactions were studied: *bonded* and *sliding*. The bonded case was intended to correspond to sintering inclusions and the sliding case to non-sintering inclusions. In both cases hard-hard contacts were specified in the computer models of Jagota and Scherer to be far more resistant to deformation along the contact normal compared to soft-soft contacts and the ratio of the contact viscosities was set as:

$$\frac{\mu_n^{hh}}{\mu_n^{ss}} = 1 \times 10^{12} \tag{2.31}$$

where μ_n^{hh} and μ_n^{ss} are the contact viscosities between hard-hard and soft-soft spheres respectively in the normal direction. The following relationship was also developed by Jagota and Scherer to determine μ_n^{ss}:

$$\mu_n^{ss} = 3\eta\pi R^2\sqrt{\alpha} \tag{2.32}$$

where η is the viscosity of the soft particles themselves, α is the normalised contact area $\alpha = r_c^2/R^2$, r_c is the contact radius and R is the particle radius. Jagota and Scherer also used the following relationship in their computer model:

$$\mu_t^{ss} = \frac{\mu_n^{ss}}{3} \tag{2.33}$$

where μ_t^{ss} is the tangential viscosity between soft-soft contacts. In the *bonded* case the tangential viscosity between hard-hard contacts μ_t^{hh} was large i.e. larger than μ_t^{ss} by a factor of 10^{12}. This high value of μ_t^{hh} allowed the hard-hard contacts to resist sliding and rotational deformation. However, in the *sliding* case this ratio between μ_t^{hh} and μ_t^{ss} was low i.e. a value of 1.0, to allow such sliding deformation to occur. Jagota and Scherer (1993) stated that contacts between hard and soft spheres were assigned viscosities by the computer model which were a series combination of the hard-hard and soft-soft viscosities, but did not provide any values in their paper.

Simulations were conducted for different sized packings i.e. from (20×20 particles) to (80×80 particles). These simulations were used to compute the effect of increasing fractions of hard inclusions. Jagota and Scherer found that the effective properties of their two-dimensional composite packings were characterised chiefly by the occurrence of a rigidity threshold.

The effective viscosities were found to scale with the viscosity of the soft particles for fractions of hard particles less than the threshold (see figure 2.14). The viscosities shown in figures 2.14 and 2.15 were normalised to the uniaxial viscosity of the packing with zero fraction of hard spheres.

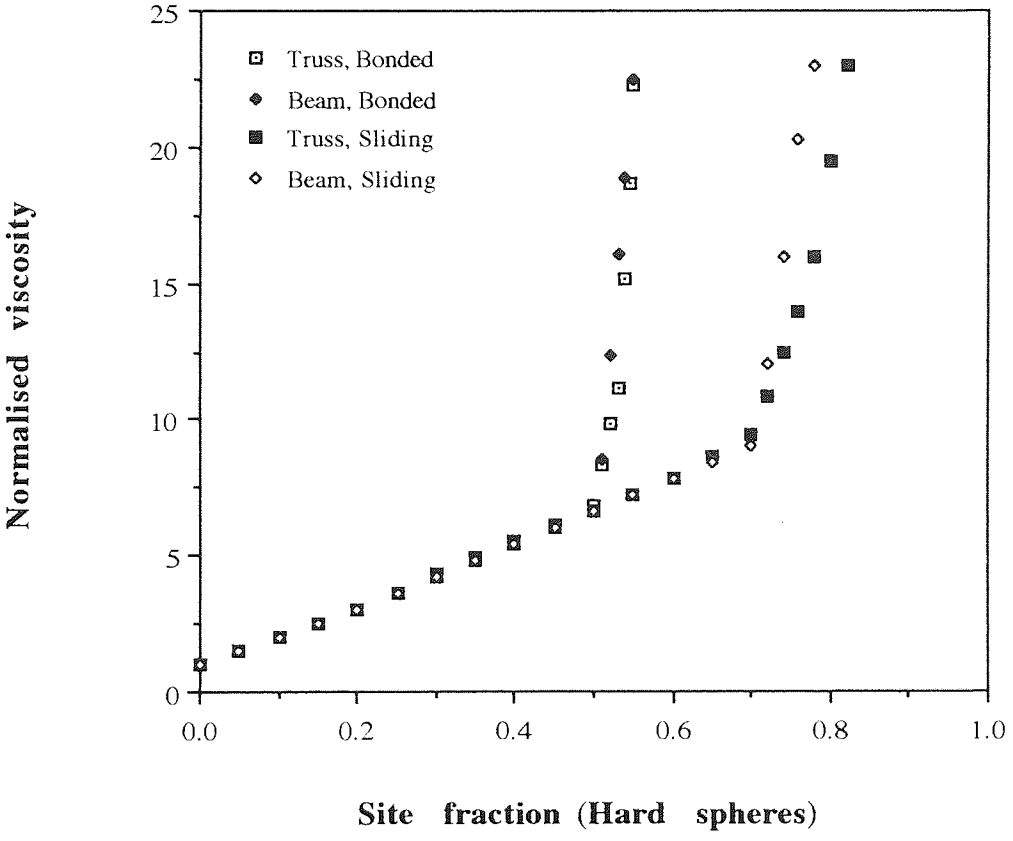

Figure 2.14 The relationship between the effective uniaxial viscosity and the site fraction of hard spheres *below* the rigidity thresholds for the different assembly models.
(After Jagota and Scherer, 1991)

When the hard-hard contacts were bonded, the rigidity threshold was found to correspond with the site percolation threshold on a triangular lattice i.e. a site fraction of 0.5 (see Stauffer, 1992). In this bonded case, before the hard spheres have percolated, the hard spheres exist in clusters completely surrounded by soft spheres and therefore, the effective properties of the composite are controlled by the soft phase. After the hard spheres have percolated, there exists a continuous cluster of hard spheres that transmits the load and at this point, the effective properties of the particle assembly are governed by the hard phase. Therefore, site percolation (see section 3.1) is necessary for rigidity and it would be expected that the two thresholds are close.

However, in the experimental work of Lange *et al* (1991), where the relatively rigid steel particles were presumably not bonded, the rigidity threshold was not found to occur at the site percolation threshold.

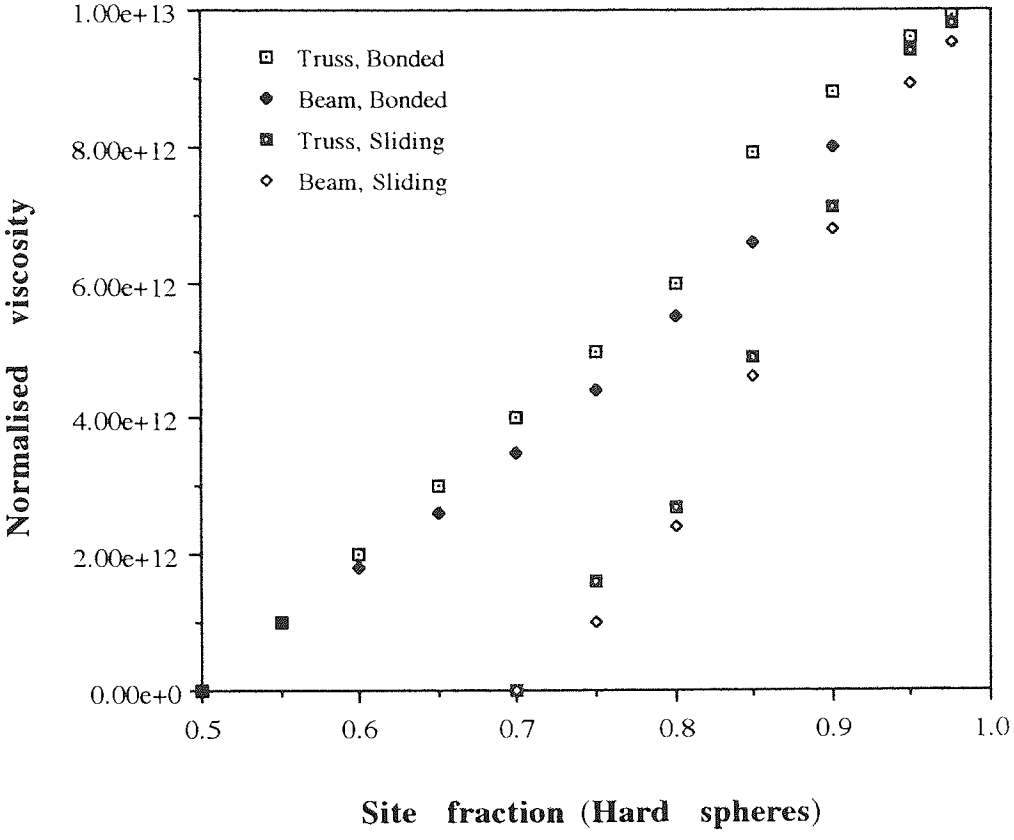

Figure 2.15 The relationship between the effective uniaxial viscosity and the site fraction of hard spheres *above* the rigidity thresholds for the different assembly models.
(After Jagota and Scherer, 1993)

When the hard-hard contacts were sliding, the rigidity threshold was found to occur at a high volume fraction i.e. the site fraction value was now ≈ 0.7, which closely matched the value obtained in the photoelastic work of Troadec *et al* (1991). It can be argued that rigidity would only precede the geometrical event in finite lattices, because of the extra constraints provided by the edges of the lattices. However, because rigidity came after the associated percolation event, in the case of sliding contacts, the correlation between the two thresholds may not be exact.

Jagota (1993) developed the two-dimensional model of Jagota and Scherer (1993) to study the sintering behaviour of three-dimensional monosized binary assemblies of hard and soft spheres. Jagota used a computer-generated random packing of 1146 spheres and adopted the simulation procedure used in the two-dimensional situation outlined in Jagota and Scherer (1993). In all this three-dimensional, simulation work, Jagota found soft-to-hard transitions in behaviour qualitatively similar to his two-dimensional studies presented earlier. The quantitative nature of the transitions however varied from the two-dimensional case, due largely to the change in dimension i.e. in the bonded case the threshold value of v_f was now $\approx$ 0.32 and in the sliding case the transition was much higher ($v_f \approx 1$). The values of v_f indicate when the generated assembly first becomes mechanically stable. The value of v_f close to unity, obtained in the sliding case, indicates a probable break down in the computer model used by Jagota. This unity value for v_f would suggest that the randomly generated packing was unstable and that the indication of rigidity was only detected because of the physical constraints provided by the vertical faces of the assembly on the assembly particles.

Jagota and Scherer suggest that their results, in both two and three-dimensions, apply equally well to a composite of elastic spheres with linear springs representing the contacts, because of the mathematical analogy between linear viscous and linear elastic deformations. They also suggest that similar problems have been solved for the effective elastic properties of percolating clusters e.g. Feng and Sen (1984) although the emphasis there is usually on bond (or link) percolation (see section 3.5).They therefore, believe that their results can be applied to the study of elastic percolating networks. Jagota and Scherer however, admit that the quantitative nature of the thresholds obtained for their work are different from those obtained by bond percolation studies.

A number of other numerical models have been developed to describe granular systems e.g. Auvinet (1972), Powell (1980), Suzuki and Oshima (1983), Pflueger (1988), but it is the distinct element method (DEM) originated by Cundall (1971) that is now widely used in numerical simulation studies. Cundall (1971) initially developed the distinct element method to analyse rock mechanics problems i.e. the progressive failure of rock slopes by simulating a discrete system of two-dimensional rigid blocks. The DEM computer algorithms used by Cundall were then developed further, Cundall and Strack (1979a), to allow modelling of a two-dimensional system of discs using the BALL program.

The validation of BALL was provided in Cundall and Strack (1979b), where the force vector diagrams determined numerically, closely resembled those obtained photoelastically by de Josselin de Jong and Verruijt (1969). The aim behind the BALL program was to allow observation of the microfeatures of idealised granular assemblies, in order to aid development of a general constitutive model e.g. Cundall *et al* (1982), Cundall and Strack (1983). Modified versions of BALL were used for the same purpose by Thornton and Barnes (1986), Thornton (1987) and Bathurst and Rothenburg (1989) amongst others. The BALL program formed the basis of the TRUBAL program developed by Cundall and Strack (1979a). TRUBAL was designed to model the mechanical behaviour of three-dimensional (3D) assemblies of spheres. The present nature of the TRUBAL program will be examined in chapter 4 and it should be noted that a two-dimensional (2D) mode of operation is available for use in simulation work. Validation of the TRUBAL code was reported by Cundall (1988) and Zhang and Cundall (1989). Cundall (1988) for example, performed several three-dimensional numerical triaxial compression experiments on glass particle assemblies (54 spheres) consisting of two sizes (0.1825 mm and 0.1075 mm). In general Cundall found that his numerical results qualitatively agreed with physical results obtained by Chen *et al* (1988), who performed physical experiments using similar assemblies and conditions.

Gherbi *et al* (1993) used an apparently unmodified version of Cundall's 1979 TRUBAL code to perform 2D numerical experiments on a Schneebeli assembly of 1000 P.V.C. cylinders (radius 1 to 2 mm) subject to isotropic compression (up to 41 kPa). The aim of this work was to reproduce the distribution of average contact force per particle observed by experiment, using a similar Schneebeli assembly and conditions. Gherbi *et al* claimed that their numerical and experimental results agreed both with each other and with a gamma distribution (see Burr, 1974) to a reasonable extent. No detailed statistical analysis of the contact force distributions was, however, presented by these workers. Modified versions of TRUBAL in 2D have also been utilised in the work of Trent (1988), Cundall (1989a) and Ng and Dobry (1992).

A modified version of the TRUBAL code (see chapter 4) has been used at Aston for simulation work on a variety of particle system problems. The areas of investigation have included the identification of fracture and fragmentation processes during the computer simulated impact of agglomerates, Kafui and Thornton (1993), and a study of the elastic-plastic impact of fine particles with a surface, by Ning and Thornton (1993).

Studies using the Aston version of TRUBAL also included, the modelling of *wet* particle systems in agglomerate collisions, Lian *et al* (1993) and three-dimensional computer simulated axisymmetric compression of 3620 sphere systems composed of five different sizes, by Thornton and Sun (1993). A modified version of Thornton and Suns' particle assembly, to represent a binary system of hard and soft spheres, was used in the simulation work described in chapter 9. After initial generation, this assembly was subjected to isotropic compression ($\dot{\varepsilon} = 10^{-4}$) and a servo-control (see section 4.8.2) was periodically introduced to maintain a desired stress level of 100kPa until the solid fraction and co-ordination number had attained constant values and a quasi-equilibrium state had been achieved. Shear tests on both dense (initial solid fraction 0.660) and loose systems (initial solid fraction 0.618) were then performed by Thornton and Sun at a stress level of $\sigma = 100$ kPa and compared with real experiments. These workers found that the stress-strain relationship obtained from the equilibrium states, produced using the servo-control, was a power law with an exponent of 3/2. The value of this exponent was also the same as that predicted by the theoretical Hertzian normal force-displacement law at the contacts (see Johnson, 1985).

Chapter 3

Percolation concepts

3.1 Introduction

Percolation theory is a development from the field of statistical physics and is used in the representation of simple models of disordered systems. The work is therefore of use in the qualitative analysis of the disordered systems represented by random packings of granular materials. The initial idea of percolation was presented by Broadbent and Hammersley (1957), who considered the general situation of random spreading of a 'fluid' through a 'medium'. The interpretation of the terms 'fluid' and 'medium' are dependent on the context of the situation. The randomness of the spreading was of two types. The first type involved familiar diffusion processes where the randomness evolved from the random walks of the 'fluid' particles. The other type involves randomness frozen into the 'medium' itself e.g. the geometrical structure of a random particle packing and this was termed a *percolating* process by Hammersley. A diffusing particle may eventually reach any position in the 'medium'. Percolation processes differ from diffusion processes because the process is confined to a finite region before a threshold concentration is reached (the *percolation threshold* or *critical concentration*).

The percolation problem can be most readily illustrated using two-dimensional percolation on a square lattice. All the sites on the lattice can be occupied randomly with a probability p or can be empty with a probability $1\text{-}p$. The occupied and empty sites may stand for very different physical properties. A simple physical assumption could be that the occupied sites are conductors, the empty sites are insulators and that electrical current can flow only between nearest neighbour conduction sites. If the value of p is low, the conductor sites are isolated or form small clusters of nearest neighbour sites (see figure 3.1a). Two conductors belong to the same cluster if they are connected by a path of nearest neighbour conductor sites and a current can flow between the two sites. At low p values the mixture is an insulator, since a conducting path connecting opposite edges of the lattice does not exist. At large p values however there are many conduction paths between opposite edges of the lattice existing where electrical current can flow and the mixture is thus a conductor. At a concentration in between these values a threshold concentration p_c may therefore exist, where for the first time electrical current can percolate from one lattice edge to the other (see figure 3.1b). Above p_c we have an conductor, below p_c we have an insulator.

This threshold concentration can be considered to be the percolation threshold for the system.

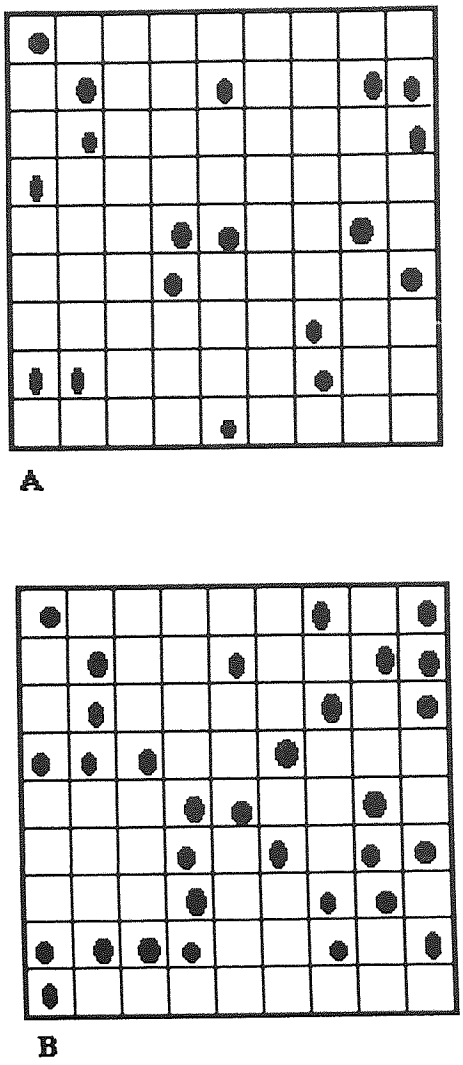

Figure 3.1 A two-dimensional square lattice showing occupation of lattice sites by conductors (black dots): **A**) View of lattice at value of p below p_c **B**) View of lattice at value of p above p_c

The example presented above relates to *site percolation* where the sites of a lattice have been randomly occupied. *Bond percolation* refers to the situation when the bonds between the sites are randomly occupied (see Stauffer, 1992).The definitions of site and bond percolation on a square lattice have been generalised to any lattice in d-dimensions. Two occupied bonds belong to the same cluster if they are connected by a path of occupied bonds. The critical concentration of bonds separates a phase of finite clusters of bonds from a phase with an infinite cluster (see figure 3.2). An example of *bond percolation* in a physical system is a *random resistor network*, where the metallic wires in a regular network are cut randomly with a probability $q \equiv 1\text{-}p$. The threshold probability q_c separates a conductive phase at low q from an insulating phase at large q.

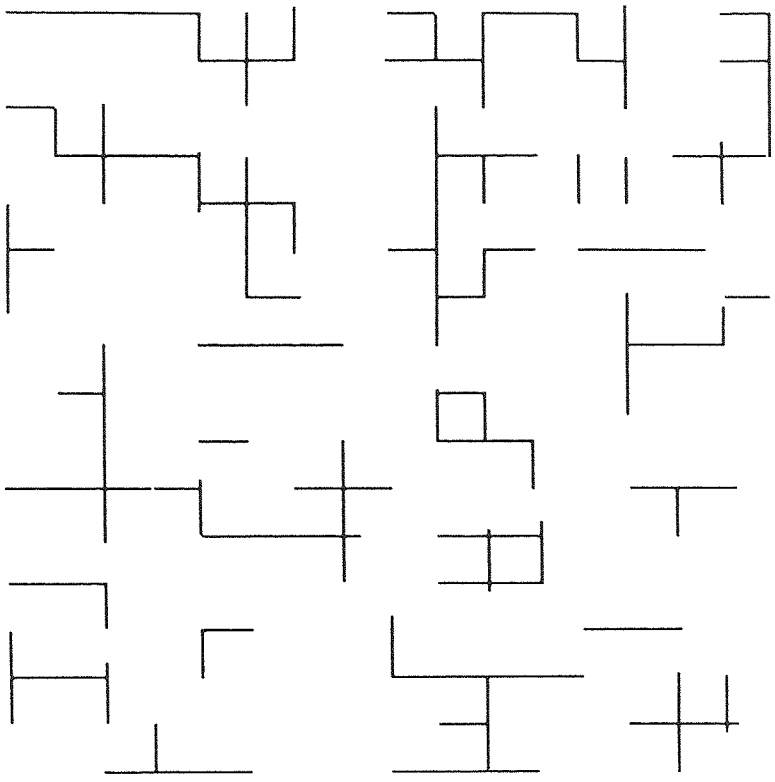

Figure 3.2 Random resistor network on a two-dimensional lattice.

Continuum percolation is probably the most natural example of percolation. In this case the positions of the two components of a random mixture are not limited to the discrete sites of a regular lattice. A simple example, continuing the electrical analogy, is a sheet of conductive material which contains circular holes punched randomly into it. The relevant quantity is now the fraction p of remaining conductive material. This model of continuous percolation is called the Swiss cheese model (see Halperin *et al.* 1985), due to its similarity to a Swiss cheese (see figure 3.3). Models to describe sandstone and other porous materials, where the size of the spheres can also vary, use a similar approach (see Elam *et al*, 1984).

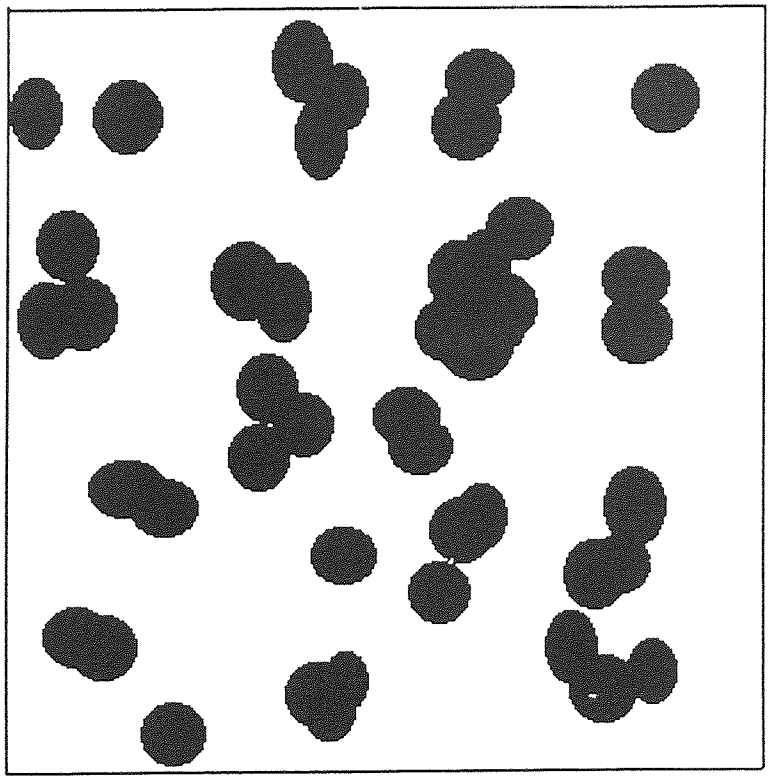

Figure 3.3 Swiss Cheese model of continuum percolation (black regions represent holes).

The concepts of percolation theory can be applied to a wide range of physical systems. An example from biology is the spreading of an infectious disease. In its most simple form, the disease starts with one individual, who can infect his nearest neighbours with probability p in one time step. In the next time step the infected neighbours can infect in turn their (previously) uninfected neighbours, and the process will continue. The critical concentration in this example separates a phase at low p where the disease will not spread after a finite number of time steps from a phase where the disease will spread infinitely. Modelling of forest fires can use the same process where the probability that a burning tree can ignite its nearest neighbour trees in the next time step replaces the infection probability. In the case of granular systems of particles the connectivity of the particles across the particle lattice is the important criterion for percolation. The probability of a particle belonging to a connected cluster of particles in a time step is the required probability. The geometric percolation threshold p_g (see section 3.2) in this case, separates a phase at low p where there are only finite clusters of particles, from a phase at high p where an infinite cluster spans the particle lattice (in theory).

The work presented earlier refers to the structural properties of percolation systems, particularly around the percolation threshold. However, dynamical properties of percolation systems can also be considered. A physical property in this case such as elasticity is assigned to each site or bond in the lattice, which are now considered to act as springs. The elastic properties of this random network of springs, such as the elastic modulus of the percolation network, can then be determined (see Allain *et al.* 1985, Bergman and Kantor, 1984 and Feng, 1984). In the context of a system's elastic response a new threshold point, the elastic percolation threshold p_e, needs to be considered. In a system below p_e the network in the lattice is disconnected and the elastic modulus is zero. If the system is above p_e, opposite faces of the lattice become increasingly connected by springs as p is increased, the network becomes stiffer and the macroscopic elastic modulus E increases as (see de Gennes, 1976),

$$E \approx (p-p_e)^{\mu_e} \tag{3.1}$$

where μ_e is the elasticity exponent (see section 3.5).

In this chapter consideration will be given to both static and dynamical aspects of percolation. A more detailed analysis of the critical nature of percolation thresholds for a system will be provided. The structural properties of percolation clusters will be presented. The basic concepts of fractals will be introduced (see Feder, 1988 and Mandlebrot, 1982) and applied to particle clusters to obtain the important structural property of the cluster fractal dimension. The characteristics of the 'backbone' of a percolating cluster will be highlighted. A large number of 'real' physical systems are multifractal in nature and the nature of multifractality will be briefly explored. An overview of the present understanding of elastic lattice percolation systems will also be provided. Finally the possible relevance of percolation concepts to granular systems will be examined.

The introductory text written by Stauffer (1992) is a good starting point for the reader unfamiliar with percolation theory. Further work on percolation concepts (for the interested reader) is presented in the texts of Bunde and Havlin (1991), Feder (1988), Zallen (1983) and Deutscher *et al.* (1983).

3.2 The percolation threshold

The percolation transition is a simple example of a phase transition phenomenon. A physical example of such a phase transition is a thermal phase transition e.g. a solid/liquid transition, where the solid (ordered) phase changes into a liquid (disordered) phase at a critical temperature T_c. In percolation processes, the concentration of occupied sites or connected bonds p (see section 3.1) plays a similar role to the temperature in thermal phase transitions. In a manner also similar to thermal transitions, long range correlations control the percolation transition p_c and the nature of these correlations around p_c are described by critical exponents and power laws. In terms of percolation on elastic lattices, which are reasonable approximations to granular systems (see section 3.5), there are two types of phase transition. The first is the geometrical phase transition where the critical concentration p_g separates a phase of finite clusters ($p < p_g$) from a phase where an infinite cluster is present ($p > p_g$). The second type is the lattice rigidity transition at the elastic percolation threshold, where the critical concentration p_e separates a phase of 'infinite' rigidity ($p > p_e$) from a phase where the elastic modulus of the lattice is zero ($p < p_e$).

The *critical exponents* associated with percolation describe the critical behaviour of the geometrical properties of the clusters close to p_c. The first important geometrical quantity of the clusters is the probability P_∞ that a site (or bond) belongs to the infinite cluster. P_∞ describes the order in the percolation system and is known as the *order parameter*. If $p < p_c$, only finite clusters exist and $P_\infty = 0$. If $p > p_c$, the value of P_∞ increases with p by a power law relationship,

$$P_\infty \approx (p-p_c)^\beta \tag{3.2}$$

where β is the critical exponent associated with the order parameter. The *correlation length* ξ characterises the linear sizes of the finite clusters, both above and below p_c. The correlation length has been defined (see Stauffer, 1992) as the mean distance between two sites on the same finite cluster. Another power law relationship describes the increase in ξ as p approaches p_c,

$$\xi \approx |p-p_c|^{-\nu} \tag{3.3}$$

The value of the exponent ν is the same both above and below the percolation threshold. The mean number of sites in a cluster (its mass) S is another cluster quantity that diverges at the percolation threshold as,

$$S \approx |p-p_c|^{-\gamma} \tag{3.4}$$

where S is the mean cluster size and the exponent γ has the same value both below and above p_c. The behaviour of P_∞ and S around p_c is illustrated in figure 3.4.

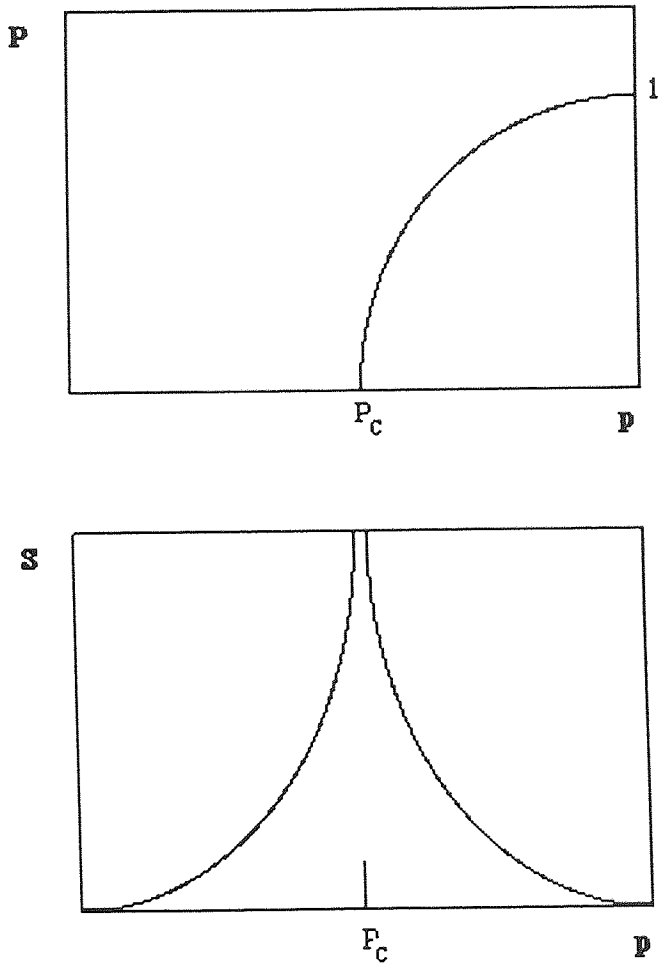

Figure 3.4 Behaviour of P_∞ and S around the percolation threshold.

The exponents β, ν and γ are the critical exponents mentioned previously. These exponents however, are not the only critical exponents characterising the percolation transition.

The exponents α, τ and σ for example, relate to the size distribution of the percolation clusters. Relations between all these exponents exist (see Zallen, 1983) and they can be determined from the knowledge of just two of the exponents' values. The value of the exponents does not depend on the type of percolation (site, bond or continuum) nor on the details of the lattice (e.g. triangular or square), but only on the dimension d of the lattice. Table 3.1 presents the values of the critical exponents β, ν and γ determined by both numerical simulation and theoretical analysis for two and three dimensions. The exponents are said to be universal (see Stauffer, 1992). Phase transitions exhibit this general property of *universality* when the order parameter for the transition vanishes continuously at the critical threshold (known as a second order phase transition). A physical example is the magnetisation transition in all three-dimensional magnetic materials. This transition is described by the same exponent β_m (the magnetism order parameter), irrespective of the type of interactions between the elementary magnetic moments within the magnetic material or the crystalline structure of the material, as long as the magnetic moment interactions are of short range.

Exponent	d = 2	d = 3
Order parameter P: β	5/36[A]	0.417 ± 0.005[B]
Correlation length ξ: ν	4/3 [A]	0.875 ± 0.003[B]
Mean cluster size S: γ	43/18[A]	1.795 ± 0.005[B]

Table 3.1 Critical exponent values for percolation.
[A] Theoretical value (from Nienhuis, 1982).
[B] Simulation value (from Strenski *et al* 1991).

The dynamical properties of percolation systems can also be considered in terms of a system phase transition. The fact that the percolation threshold is a critical phenomenon implies that the transition can be characterised by power laws of $|p - p_c|$. The first empirical evidence for such power law behaviour for dynamical lattice properties was presented by Last and Thoulness (1971). They studied a two-dimensional diluted conducting material and their data suggested that above $p_c \cong 0.6$, in the critical transition region, the conductivity σ_c behaved as,

$$\sigma_c \approx (p - p_c)^{\mu} \tag{3.5}$$

where the exponent $\mu > 1$. There are a number of dynamical exponents which relate to transport properties in percolating systems. The transport behaviour in general two-component systems for example, can be reflected by consideration of a random mixture of two conductors A_{CO} (with concentration p) and B_{CO} (with concentration 1-p) with conductivities σ_{ACO} and σ_{BCO} respectively, where $\sigma_{ACO} >> \sigma_{BCO}$ (see Bunde *et al* 1985). The model describes a random superconductor model in the limit $\sigma_{ACO} \rightarrow \infty$. The conductivity will be infinite above p_C and below p_C there will exist only finite superconducting clusters and the conductivity of the system will be finite. The size of the superconducting clusters increases on approach to p_C and the conductivity will diverge as,

$$\sigma_{co} \approx (p_c - p)^{-s} \tag{3.6}$$

where s is the critical exponent for superconductivity. The exact values for dynamical exponents such as μ, s and μ_e are not yet known for two and three dimensions. Determination of dynamical exponents has been the subject of many years' work (see Stauffer, 1992) but perhaps the most successful conjecture has been that of Alexander and Orbach (1982), which was found to be quite accurate for percolation when $d \geq 2$ (see Stauffer, 1992). The difficulty in determining the dynamical exponents is due to the complex structure of the percolation clusters. The clusters consist of loops, branches and dangling ends on all length scales (see section 3.3.2). The values of the dynamical exponents are therefore, usually estimated using numerical methods such as the Monte Carlo technique e.g. Feng (1985), because of this lack of an exact theory.

The dynamical exponents discussed above have been determined for lattice percolation and are independent of the lattice type. In terms of continuum percolation systems (see section 3.1) the static exponents e.g. β and ν are the same as for lattice percolation. Halperin *et al.* (1985) however, have shown that the dynamical exponents are not the same, from studies of the transport properties of random void or 'Swiss cheese' systems. These workers found that, in continuum percolation the transport exponents depend not only on the way the percolation system is generated but also on the way a random walk through the system is performed. This finding was also demonstrated by Petersen *et al.* (1989). The treatment used by Petersen *et al* (1989) was also found to be capable of extension to continuum models of elastic percolation systems (see section 3.5).

3.3 Structural properties of the percolation cluster

3.3.1 The cluster fractal dimension

The structure of percolation clusters can be well described by the fractal concept as was first noticed by Stanley (1977). Mandlebrot (1986) proposed the following definition of a fractal:

A fractal is a shape made of parts similar to the whole in some way.

A complete and neat characterisation of fractals is still lacking (see Mandlebrot, 1987). The above definition however contains the essential feature that a fractal looks the same whatever the scale. A physical system that exhibits a fractal structure is cumulus weather clouds. The clouds consist of big heaps with small bulges. The small bulges have smaller bumps with bumps on them and so on down to the smallest scale of resolution. A picture therefore only showing the clouds would not allow estimation of the clouds' sizes without additional information. The infinite or *percolation* cluster at the percolation threshold p_c also has a fractal structure. A percolation cluster is said to be *statistically self-similar* on all length scales (larger than the unit size of the cluster and smaller than the lattice size) i.e. it is impossible to tell from pictures of the cluster at what level of magnification the pictures were taken. This self-similarity is illustrated by inserting a scaled version of the lattice into the original lattice (see figure 3.5).

Physical systems in general have a characteristic smallest length scale such as the radius r_o of a molecule or atom. A system of points in a two-dimensional lattice (as displayed in figure 3.1) can be replaced by a plane of monomers or particles. The volume of a theoretical three-dimensional lattice can then be replaced by a packing of spheres. The number of monomers n in a circular disk (of radius r) is given by (see Feder, 1988):

$$\mathbf{n} = \rho_n \left(\frac{\mathbf{r}}{\mathbf{r}_o} \right)^2 \tag{3.7}$$

The number density ρ_n will be $\rho_n = \pi/2\sqrt{3}$ for closely packed spheres in two dimensions. In the three-dimensional situation the value of n for close packings of spherical monomers in a spherical region of radius r is given by:

$$\mathbf{n} = \rho_n \left(\frac{\mathbf{r}}{\mathbf{r}_o} \right)^3 \tag{3.8}$$

where the number density is now $\rho_n = \pi/3\sqrt{2}$.

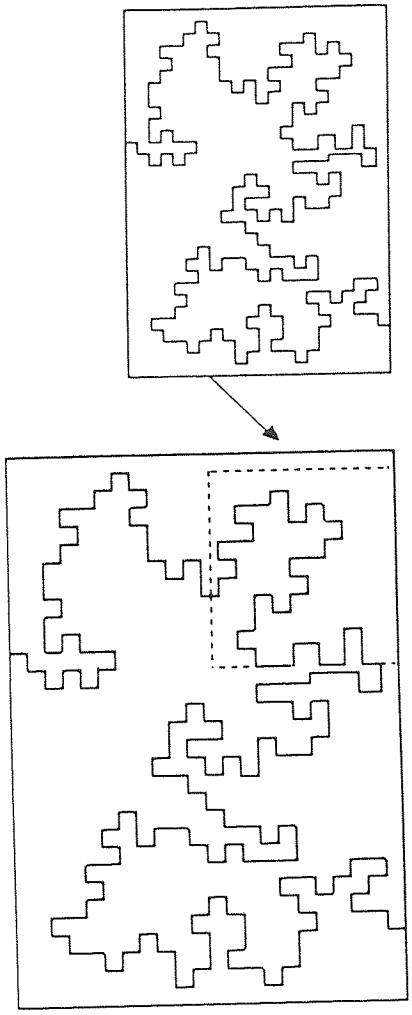

Figure 3.5 Illustration of lattice self-similarity.

The above relations only apply in the limit $r/r_o > 1$, since the spherical surface of the ball and the circular shape of the disk perimeter can only be approximately covered by the monomers. An asymptotic form has been developed in Feder (1988), from the analysis of the examples presented above, for the relation between the number of particles and the 'cluster size' measured from the smallest sphere of radius r containing the cluster:

$$\mathbf{n} = \rho_n \left(\frac{\mathbf{r}}{\mathbf{r}_o} \right)^D \tag{3.9}$$

where D is the *cluster dimension* in this number-radius relation.

If every monomer has the same mass then n can be interpreted as the mass m and ρ_n as the mass density ρ_m. The cluster dimension is therefore often called the mass dimension. The nature of the packing of the monomer and factors associated with the shape of the cluster will determine the density ρ_n. A randomly packed volume of spheres will therefore, cause the value of ρ_n to be reduced from 0.7405 (see above) to 0.637. The value of ρ_n for an ellipsoid of revolution with axial ratio b/a will also differ from that determined from a spherical cluster of a dense packing of spheres i.e. $\rho_n = \text{b/a}\ \pi/3\sqrt{2}$. The value of the cluster dimension D however, does not depend on the shape of the cluster or on the nature of the packing of the monomers. The value of D may also be non-integer i.e. D is a fractal quantity. In general the exponent D in the number-radius relation is called the *cluster fractal dimension*. The fact that a cluster is porous or random does not necessarily imply that the cluster has a fractal dimension D. A fractal cluster has the property that the density decreases as the cluster size increases in a way described by the exponent in the number-radius relationship (see equation 3.9). If a particle density is introduced for the monomers then the density ρ_d at a radius r from the generation point for percolating clusters is given by (see Bunde and Havlin, 1991):

$$\rho_d(r) = r_o^{-D} r^{D-Eu} \tag{3.10}$$

The value of the density is constant only if D the fractal dimension equals E_u the Euclidean dimension of the space in which the cluster is placed. Fractal clusters will therefore, usually have a density that decreases with distance from the origin point of the cluster. The cluster fractal dimension thus determines the spatial occupation properties of the cluster in a quantitative manner (see equation 3.9). The shape of the cluster however, is not described by the cluster fractal dimension.

The value of the cluster fractal dimension for a percolating cluster has been determined in a number of numerical simulations. Grossman and Aharony (1986) performed numerical simulation on the two-dimensional square lattice and found the cluster fractal dimension D to be $D = 1.75$. The variation of the value of D in square lattice simulation work is illustrated by the value of $D = 1.8928$ obtained by Mandlebrot and Given (1982), using a different process of cluster generation. Stanley (1977) looked at computer simulated bond percolation on a three-dimensional square lattice and found that the value of D was now $D = 2.09$.

The results obtained by Stauffer (1992) for site percolation on a two-dimensional triangular lattice (at the percolation threshold), give an estimate for the fractal dimension D consistent with the exact value $D = 91/48$. The numerical value of D is close to that obtained by Mandlebrot and Given (1982). Numerical evidence produced by Sykes and Essam (1964) suggests that values of the fractal dimension D may be accurately determined by simulations on such triangular lattices and can be used as benchmark values for experimental comparison.

3.3.2. Substructures of the percolation cluster

The fractal dimension D is not the only geometrical characteristic of a percolation cluster at p_c. The percolation cluster is also composed of a number of several fractal substructures. If an imaginary voltage difference is applied between the two edges of a lattice containing a conductive percolation cluster then the fractal substructures can be related to physical structures (see Stanley, 1977, Pike and Stanley, 1981). The *backbone* of the cluster consists of those sites (or bonds) which carry the electrical current. The *red bonds* (singly connected bonds) are the bonds that carry the total current (see Stanley, 1977) i.e. if these bonds are cut the current flow stops. The *blobs* are the parts of the backbone that remain after removal of any red bonds. The *dangling ends* finally, are the parts of the cluster which carry no current and are connected to the backbone only by a single site. Pictures of the backbone as presented in Figure 3.6. indicate that, the backbone consists of 'blobs' connected by 'links', which supports the model originally proposed by de Gennes (1976) and Stanley (1977).

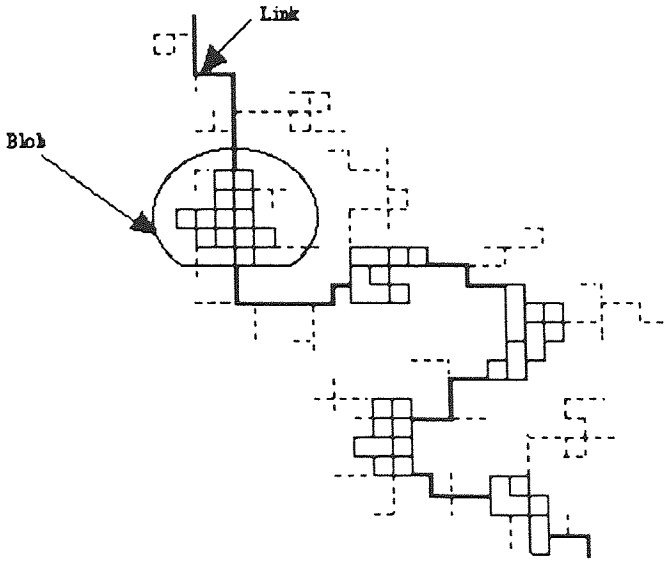

Figure 3.6. 'Blobs - Links' model of a two-dimensional lattice backbone. Dashed lines :- *Dangling Ends* ; Solid Lines : - *Red Bonds*; Light Lines :- *Multi-connected bonds.*

The sites (or bonds) that comprise the backbone form a subset of the sites on the percolation cluster and every site on the percolation cluster is also part of at least one backbone. The percolation cluster is fractal, with a fractal dimension of D = 1.89 (see section 3.2). The backbones on the percolation cluster are therefore, also fractal and the dimension of the backbone D_b is smaller than the fractal dimension of the cluster. This is because most of the percolating cluster's mass is concentrated in the dangling ends. Numerical simulations around p_c by Herrman and Stanley, 1984, Laidlaw *et al.* 1987, have shown that the mass $m_b(L)$ of the backbone connecting the edges of a lattice of size L is given as,

$$m_b(L) \approx L^{D_b} \tag{3.11}$$

The estimates for the value of D_b have been $D_b \cong 1.62 \pm 0.02$ (Herrmann and Stanley, 1984) and $D_b \cong 1.61 \pm 0.01$ from Laidlaw *et al.* (1987).

The set consisting of the red bonds or 'links' forms a subset of the sites on the backbone, according to Pike and Stanley, 1981. These workers also found that the number of these red bonds n_{red} will diverge as the maximum distance between two sites on the ends of the backbone i.e. the lattice dimension L increases, according to the power law:

$$n_{red} \approx L^{D_{red}} \qquad \text{where} \quad D_{red} = \frac{1}{\nu} = \frac{3}{4} \tag{3.12}$$

The above equation indicates that, there is a connection between the fractal dimension of the red bonds D_{red} and the critical exponent ν, related to the correlation length ξ of the cluster (see section 3.2). The majority of mass in the backbone is in the blobs, since the fractal dimension of the red bonds (from equation 3.12) is much less than that of the backbone.

A number of other cluster substructures exist and these are also fractal in nature. The substructures include the *external perimeter* (or *hull*), the *skeleton* and the *elastic backbone*. The hull consists of those cluster sites which are adjacent to empty sites and are connected to the edges of infinite lattice via empty sites. The total external perimeter however, also includes holes within the cluster. The skeleton is defined as the union of all the shortest paths from a specified site in the cluster to all sites at a distance l_{min} corresponding to the minimal path within the percolating cluster (see Herrman and Stanley, 1984).

The elastic backbone is the union of all the shortest paths between two cluster sites (see Herrman *et al.* 1984). The values of the hull fractal dimension D_h, the percolation cluster fractal dimension D and the dimensions of other fractal substructures, in two and three dimensions, are presented in Table 3.2.

Fractal dimensions	d = 2	d = 3
D	91/48[A]	2.524 ± 0.008[B]
D_B	1.62 ± 0.02[C]	1.74 ± 0.04[C]
D_{red}	3/4[D]	1.14 ± 0.01[B]
D_h	7/4[E]	2.548 ± 0.014[B]

Table 3.2. Fractal dimensions of percolation cluster substructures
A - Neinhuis (1982); B - Strenski *et al.* (1991)
C - Herrmann & Stanley (1984); D - Coniglio (1982)
E - Saleur & Duplantier (1987)

3.4 Multifractal behaviour

The electrical conductivity and mechanical properties of percolating systems provide important examples of multifractal behaviour. A simple fractal object e.g. a snowflake, requires a single fractal dimension D (see section 3.3.1) to completely characterise the structure of the object. Multifractal phenomena however, which have become an active area of investigation, require an infinite number of fractal dimensions for their description. Multifractal measures are related to the specification of physical measures on the underlying geometry of the system. This geometry may be the surface of a sphere or a volume, or it could itself be a fractal. (see Bunde and Havlin, 1991). In recent years it has been established that several physical quantities related to random systems do not obey the conventional power laws associated with the threshold condition (see section 3.2). Mandlebrot (1974) first found such multifractality in the context of turbulence. The voltage distribution in random resistor networks is another example (see de Arcangelis et al., 1985), which is more specifically related to the transport properties of percolation systems.

The behaviour of the infinite percolation cluster at the percolation threshold p_c, for a random resistor network can be analysed using a simple lattice model. If a voltage is applied on the two opposite sides of the cluster separated by a distance L, where each bond has unit conductivity, then a voltage drop V_j will occur on each of the lattice bonds j. The distribution of these voltage drops n(V) is of interest but is of a very complex nature, as seen in figure 3.7.

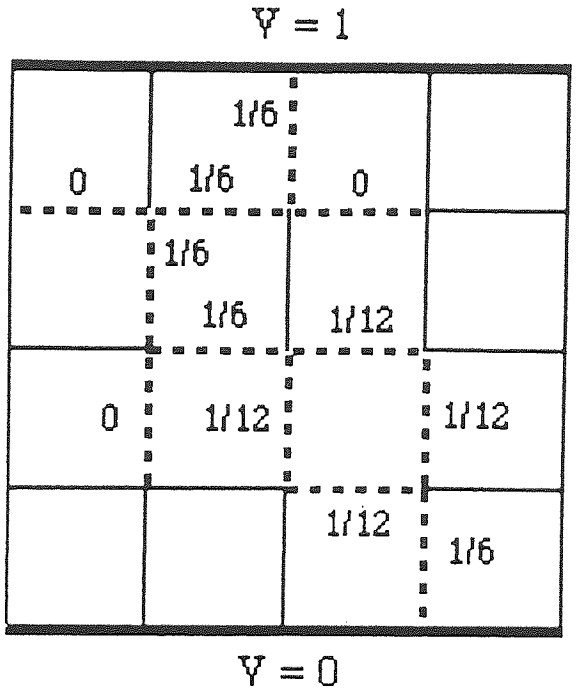

Figure 3.7 Voltage drop distribution in a two-dimensional lattice at the electrical percolation threshold.

Interpretation of figure 3.7 indicates that, some of the bonds carry a large fraction of the total current while others carry only a small fraction. The maximum voltage drop V_{max} will be found on singly connected bonds, carrying the total current I. The external voltage is chosen as one unit for simplicity and assuming unit resistance, then from Ohm's Law $V_{max} = I = \rho^{-1}$. The total resistance of the cluster is ρ. The value of ρ was found to scale with the linear cluster size L (see de Arcangelis et al., 1985) as $\rho \sim L^{\zeta}$. The maximum voltage drop was also found by these workers to scale as,

$$V_{max} \approx L^{-\zeta} \tag{3.13}$$

where ζ is the critical exponent for the system electrical resistance. The voltage range between V_{max} and V_{min} can be of many orders of magnitude. V_{min} is the minimum voltage drop within the percolating system. The wide voltage range indicates that [V_j], the distribution of the voltage drops, is very broad. de Arcangelis *et al.* (1985) obtained a voltage drop distribution from a numerical simulation. The distribution was characterised by a long tail at small voltage drops (see figure 3.8). Multifractality in this case describes the fact that, different voltage ranges in the histogram can be viewed as different fractal sets and a different fractal dimension will characterise each set. In terms of the multifractal mechanical behaviour of a percolating system a complete, continuous distribution of forces could also be obtained (see section 3.5).

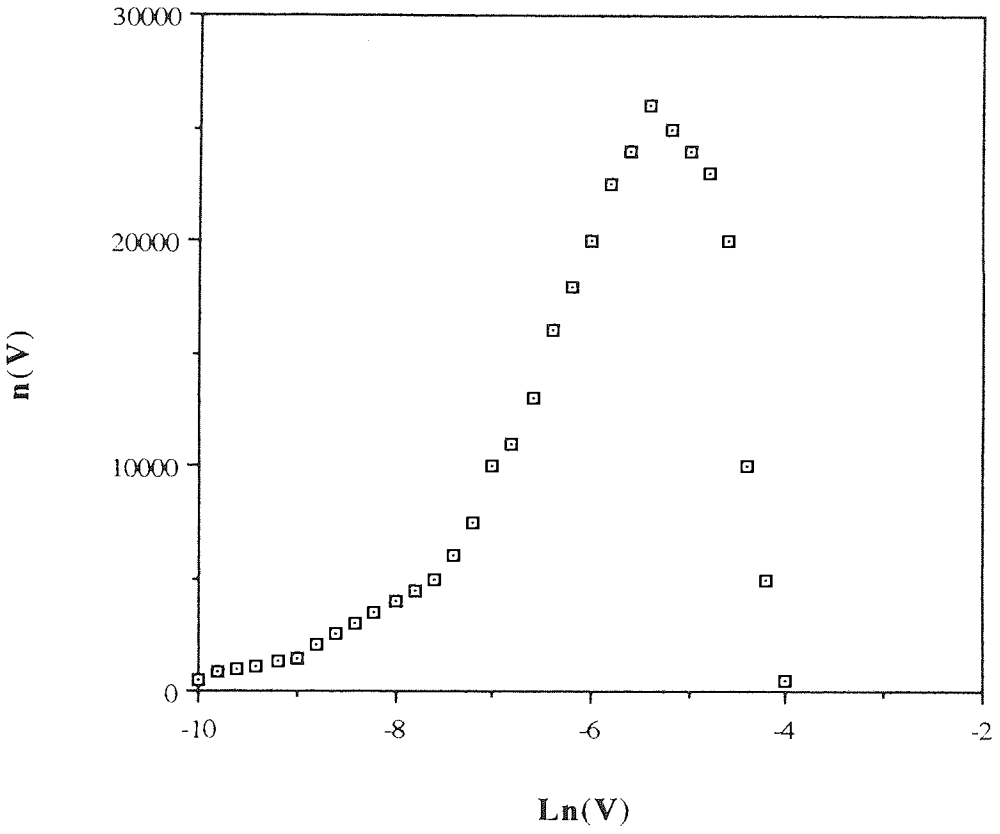

Figure 3.8 Voltage distribution for a percolating cluster at threshold. (After de Arcangelis *et al.*, 1985)

3.5 Elastic percolation lattices

The elastic properties of a percolating lattice can be modelled using a random network of elastic springs. A small constant stress field can be applied at the opposite faces of the elastic network. The network will be expanded due to the stress field. The relative expansion $\Delta L/L$ (where L is the lattice dimension) will be proportional to the strength of the field. The proportionality constant is the elastic coefficient e, which characterises the response of the network to the external stress field. The inverse of the elastic coefficient is the elastic modulus E (see Born and Huang 1954). The problem of elasticity of random percolating networks has been mostly viewed as being analogous to the problem of electrical conductivity of such systems. This analogy was first suggested by de Gennes (1976) in relation to the elasticity of gels. The behaviour of E was also found by Last and Thoulness (1971) to be similar to the behaviour of the dc conductivity within a lattice.

A regular triangular lattice of springs rotating freely at their nodes or the centres of the spheres at which they are attached, can be considered following the work of Feng and Sen (1984). This model known as the *central-force* model, assumes that only central, stretching forces will act on the elements of the lattice. Thus forces are invoked within the lattice structure only when a bond stretches or contracts, just like an ordinary spring. In the simplest case scalar force constants for the springs can be assumed. In the *random dilution* model a proportion $1\text{-}p$ of the randomly distributed bonds is missing while another proportion p is present. Feng and Sen found that the rigidity of the lattice E went to zero, in the limit of an infinite lattice, at a well defined value of the proportion $p = p_e$ (the elastic rigidity threshold) via a power law relationship characterised by a critical exponent μ_e i.e.

$$\mathbf{E} \propto (\mathbf{p}\text{-}\mathbf{p}_e)^{\mu_e} \tag{3.14}$$

The elastic exponent μ_e in this case is comparable to the exponent used in equation (3.1). If scalar force constants are used, then the elasticity exponent μ_e can be shown to be identical to the critical conductivity exponent μ (see de Gennes 1976). However, if the spring force constants are vectorial, Kantor and Webman (1984) showed that μ_e is considerably larger than μ.

Feng and Sen (1984) and Arbabi and Sahimi (1993) have also looked at the corresponding problem of *random reinforcement*. In this case a proportion p of the lattice springs is infinitely rigid while the others have a finite elastic constant. The elastic modulus E of the lattice in the random reinforcement problem will diverge at the critical threshold p_e, as p moves towards p_e from below as,

$$E \propto (p_e - p)^{-g} \tag{3.15}$$

where g is another critical exponent. The value of p_e cannot readily be obtained from simple geometrical arguments. One essential difficulty in this question of the rigidity of the spring lattice structure originates from the incompleteness of the mechanical information transmitted through a single spring. If a displacement is imposed at one site then, one bond away from that site, the displacement is not completely determined and only its component along the bond axis is known. A single connection between a lattice site and a 'fixed' background therefore, does not provide enough information to impose a particular location on the site, but will only restrict the site location to a particular subspace of the lattice. The fact that only partial information is transmitted through each spring (bond) renders the problem of the search for the lattice rigidity *non-local* in nature. It is for this reason and because of the numerical difficulties encountered in this case, that there has been some controversy concerning the value of p_e. The value of the critical exponents dealing with lattice behaviour around p_e have also therefore been the subject of debate (see Bergman, 1985, Feng and Sen, 1984, Bergman and Kantor, 1984). The presence of different thresholds for the connectivity and central-force problems suggest different universality classes i.e. different types of phase transition are observed for these different aspects of percolation behaviour. Hansen and Roux (1988) however, analysed random dilution on a triangular lattice and found the value of p_e to be about 0.642 ± 0.002, which can be compared with their value of the geometric percolation threshold p_g where $p_g = 0.3472$. This similarity in elastic and geometric percolation behaviour was also evident in the backbone structure of the percolating cluster found by Hansen and Roux (1988), which had a fractal dimension D_b identical to that of geometric percolation. Hansen and Roux also found that the complete distribution of forces in the backbone was characterised by a continuous function and not by a single number i.e. the distribution was multifractal in nature (see section 3.4).

Kantor and Webmann (1984) developed another spring-lattice model of depleted elastic materials, known as the *bond-bending* model, where lattice connectivity was equivalent to lattice rigidity. The microscopic elastic behaviour for this model included a bond-energy term. These workers reported that the rigidity threshold p_e of this system was identical to the geometrical threshold p_g. Kantor and Webmann (1984) and Sahimi and Arbabi (1993) also analysed the elastic properties of elements of the infinite percolation cluster and calculated the elastic stiffness critical exponent τ at p_g. It was found that τ was considerably higher than the percolation conductivity exponent t, which indicated the difference in the nature of the types of physical behaviour around the transition point. In the case where lattice connectivity is equal to rigidity then complete information is transmitted through a lattice-spring (bond). The percolation behaviour of such a system is thus well understood.

The situation of rigidity - connectivity equivalence has been obtained in experimental work where particle grains have been soldered at their contact points, using weakly sintered metal grains (Deptuck *et al* 1985). The elastic modulus of randomly diluted lattices in such a model, vanishes for a proportion p of the springs (bonds) present as p approaches p_e (from above) as,

$$\mathbf{E} \propto (\mathbf{p}-\mathbf{p}_e)^{\tau} \tag{3.16}$$

where τ is an elastic critical exponent. In the case of random reinforcement problem (see Bergman 1985) the elastic modulus diverges at p_c as p approaches p_c from below as,

$$\mathbf{E} \propto (\mathbf{p}_c-\mathbf{p})^{-\sigma} \tag{3.17}$$

The value p_c is the percolation connectivity threshold. The elastic critical exponents τ and σ appearing in the above relations have been found by Roux, 1986, to be closely related to the corresponding critical exponents for conductivity in percolating systems.

The granular or 'disc' model is another elastic network model and this model comprises rotationally invariant random elements. This model was first developed by Schwartz *et al* (1984) and used in the study of the vibrational properties of granular rocks e.g. sandstones.

Schwartz *et al* (1984) argued that, a proper description of the vibrational properties of systems of spheres must take account of the rotational motion of the spheres. Feng (1985) and Feng *et al* (1984) used the model of Schwartz *et al.* to analyse the percolation behaviour of two-dimensional elastic networks via numerical simulation and theoretical analysis. Feng *et al* (1984) found a critical elastic exponent τ for the networks which was much higher than the conductivity critical exponent t. This result supports the results obtained from the purely central-force model of Feng and Sen (1984). Feng (1985) obtained a value for the elastic critical exponent τ that was similar to the one obtained from the bond-bending model of Bergman and Kantor, 1984. Feng believes that this equality in the exponent value, supports the view that percolation properties for elastic systems are universal i.e. τ is independent of the microscopic details of the elastic system in question. The requirements for this universal behaviour are rotational invariance and absence of singular bonds in the elastic lattice. Day *et al* (1986) however, showed that the two-dimensional central-force problem belonged to a new class of percolation problems. They found that qualitative and quantitative geometric properties such as the backbone fractal dimension D_b, the correlation length exponent ξ and the connectivity (at percolation) were completely different from those obtained in simple 2D lattices. Explicit calculations of the cluster backbone by Day *et al* (1986) and construction of a computer algorithm which clearly identified the infinite rigid cluster at the percolation threshold, were found to clearly demonstrate the absence of singly connected bonds, the overwhelming importance of the loop structure of the cluster and the long-range nature of the lattice rigidity.

The elastic behaviour of disordered continuum systems or Swiss-cheese models, which may more closely approximate random granular systems, have also been analysed by some workers. Halperin *et al* (1985) used theoretical analysis to estimate critical exponents for the elastic behaviour (in both 2D and 3D) of some Swiss-cheese models. They considered the contribution of the 'singly connected bonds' in a manner similar to the analysis of Kantor and Webman (1984) for the lattice elasticity problem. Halperin *et al* found that the critical elastic exponents were significantly larger than their counterparts in the standard discrete-lattice percolation networks described earlier in the text. Allain *et al* (1985) looked at a bi-dimensional grid Swiss-cheese model and also found that the elastic moduli and the conductivity of the system did not exhibit the same critical behaviour.

Benguigui (1984) analysed the elasticity exponents of a two-dimensional percolating system made of metal and voids. The results obtained from this work (see figure 3.9) were in excellent agreement with the theoretical prediction of Bergman (1985). The critical elastic exponents from Benguigui's work are therefore similar to those obtained from a lattice elastic model. The differences amongst the various continuum models arise from the differences in the probability distribution and geometry of the bonds in the models.

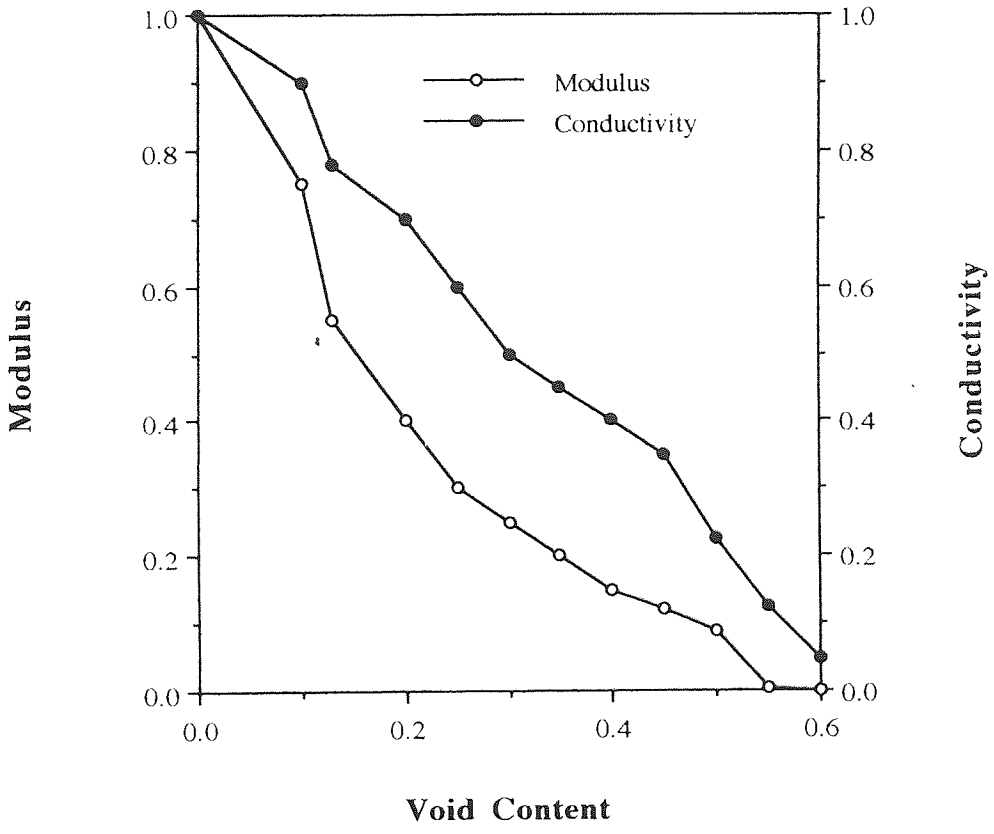

Figure 3.9 Variation of conductivity (σ) and the elastic modulus (E) with void content. (After Benguigui, 1984)

The models outlined above do not reflect the unilateral nature of particle contacts in a real granular assembly. Diode-type models illustrate this global non-linear behaviour which results from the existence of contact forces for only one sign of the interparticle displacement. Diode-type models are so called because of the analogy between the force-displacement relation for an elastic contact and the voltage-current characteristics of a diode in electronics.

Stauffer *et al* (1987) developed such a model, which consisted of a packing of discs with a narrow distribution of radii. The nature of the radii distribution maintained some order in the lattice structure but also introduced some randomness into the contacts. Experimental work on non-linear effects in experimental disc and cylinder arrays was presented in section 2.3.2.

3.6 Relevance of percolation theory to granular systems

Granular arrays in real powder systems e.g. sand, constitute a particular class of heterogeneous material with the co-existence of two phases; the *grains* which form a disordered, amorphous-like phase and the *pores* which are the voids between grains. These two phases have very different physical properties, in spite of the fact that they complement each other in a geometrical sense. The mechanical properties of granular arrays are mostly controlled by behaviour in the region of the intergrain contacts. In a real, random granular array however, a large distribution in the 'quality' e.g. contact force values, of the intergrain contacts will exist. Percolation theory methods allow analysis of the nature of this intergrain contact 'quality' via use of the 'blobs-links' model of a percolating system e.g. determination of the percolating cluster backbone (see section 3.3.2). Modelling of the behaviour of granular arrays via a lattice of elastic springs or bars can be used for such percolation-based analysis (see section 3.5). The lattice *bond-bending* model of Kantor and Webman (1984) is an example. This model provides a good description of the elastic behaviour of a macroscopically inhomogeneous composite material made up of locally rigid regions (akin to grains) and regions that are locally very soft, which in the limiting case are voids. In such a system there is an expectation that the rigidity threshold will be identical to the geometrical percolation threshold of the rigid phase. Near the percolation threshold p_c the macroscopic rigidity of the material will be determined by the elasticity of the long and tortuous thin channels of rigid material which are contained in the backbone of the percolating cluster. The use of a model such as Kantor and Webman's (1984) should yield a correct description of the backbone structure for a continuous inhomogeneous system at the critical region.

A definite answer to the question 'is it reasonable to apply percolation ideas to grain packings?' is not yet forthcoming. However, the general approach provided by percolation ideas may be useful but it needs to be applied with caution in the context of granular assemblies. The main difficulty in applying percolation ideas to real granular systems is the presence of non-linear effects. Although a central-force model as used by Feng and Sen (1984) or a bond-bending model such as Kantor and Webman's (1984), shed some light on the loose packing properties of a granular array, they will miss the strongly non-linear aspect in all contact problems. This non-linear aspect of the contact behaviour arises from the existence of contact forces for only one sign of the interparticle displacement. These local structures can be called *struts*. Another non-linear problem of interest in real granular arrays is that of *buckling*. When the rigidity threshold is reached there will exist long straight lines of bonds which contribute to the rigidity. The structure however, will buckle even under an infinitesimal compressive force because there are no bond-bending restoring forces. These bonds will therefore, no longer ensure rigidity. Such an effect is absent in the 'generic' problem on a central-force lattice. Guyon *et al* (1990) suggest that these non-linear effects may change the universality class of the problem i.e. the nature of the phase transition will be different from that predicted by central-force percolation models. Although quantitative analysis using the percolation approach may be difficult because of such problems, the approach is probably relevant to the qualitative study of grain packings. The use of a critical-phenomenon type treatment rather than providing precise numbers, may present a more detailed picture of the effect of heterogeneities and microstructural features on the behaviour of a granular packing.

In a real granular system the lattice will not be infinite and therefore, finite size effects must be taken into account. If a finite system is considered e.g. a square lattice of L*L sites, then it would be reasonable to expect relevant quantities e.g. the *critical exponents* to depend on the magnitude of L. The characteristic length of a system is the correlation length ξ (which is defined for the infinite system in section 3.2). Different behaviour would therefore be expected for $L/\xi >> 1$ and for $L/\xi << 1$. Scaling functions have been developed to allow determination of critical exponents for computer simulation work on finite lattices by Feder (1988) and Bunde and Havlin (1991). In this way the finite size effects associated with a real granular array can be taken into account by percolation analysis.

The idea of connecting the properties of packings of particles to percolation has been suggested in the past, although only a few quantitative studies have been carried out (see section 2.3). In a real granular system however, the presence of gravity acting on the grains would limit the possibility of the appearance of weakly connected structures i.e. non-percolating particle clusters, on a large and visible scale. The system of grains will stabilise itself at the critical packing value corresponding to a dense array. Filtration cakes or sediments however, which are obtained by letting particles fall under their own weight, are reasonably visible examples of such weak structures. Although the presence of weakly connected structures in real granular systems is difficult to detect, the approach provided by the general use of 'percolation' ideas has some merit in the interpretation of the behaviour of granular assemblies e.g. the development of a percolating 'backbone' of particles in a compacted assembly of particles. A model of *self-organised criticality* at a more general level has been proposed by Bak *et al* (1987). The whole philosophy of this approach is that there exists a dynamic for some critical phenomena e.g. development of lattice rigidity, that causes an attraction towards a critical point. A system may naturally under these circumstances evolve towards and remain at a critical state. This general idea of self-organised criticality is exemplified in many physical situations (see Bak et al, 1989) where the systems are close to a critical point , which should only have a minute chance of occurring in theory, because of the very precise value of the control parameter required for the state.

Chapter 4

DEM computer program TRUBAL

4.1 Introduction

The macroscopic behaviour of granular media is dependent upon the microscopic behaviour of the discrete particles or elements that form the composition of the material. The use of the Distinct Element Method (DEM) technique, in the form of the TRUBAL program, allows consideration of granular media as discontinuua rather than the more conventional continuua assumption. TRUBAL (coded in the FORTRAN language) can therefore be used for modelling of the mechanical behaviour of two and three-dimensional particle systems of elastic spheres. TRUBAL was originally written by Cundall in 1979 and was a development of the earlier BALL program, see Cundall and Strack (1979a). The latest version of Cundall's TRUBAL code was introduced to Aston University in 1988. The 1988 version of the code forms the basic framework for later enhanced versions of the code developed at Aston. In the 1988 version of TRUBAL, particles are randomly generated by the code in a defined cubic space (work space or unit-cell). The work space is considered to have periodic boundaries. The space periodicity is obtained via numerical connection (within the particle mapping scheme) between the opposite faces of the unit-cell, so that particles leaving the cell through one face will re-enter the cell through the opposite face. The progressive movement of each of the constituent particles within the unit-cell is traced via the use of Newton's 2nd Law of Motion in a time-dependent finite difference scheme. In this 1988 version of TRUBAL the theory of Hertz (see Johnson, 1985) is used to model the normal force displacement at particle contacts. The tangential force displacement at the contacts between particles is modelled as linear springs. Supplemental facilities such as servo-control, two-dimensional mode operation and simple 2D graphics are also available in this version of the code.

A number of significant improvements and modifications to the initial modelling system have been made to the Aston version of TRUBAL since 1988. One area of major development has been the implementation of more realistic particle-particle interaction laws. The normal particle contact forces are still modelled by Hertzian theory but the tangential particle contact forces are now modelled according to the work of Mindlin and Deresiewicz (1953) for non-adhesive elastic spheres. Other enhancements that have been made include development of 3D graphics facilities and other forms of particle generation e.g. regular packing structures. New versions of the code are also being developed to account for plastic deformation at particle contacts (Ning 1995) and wet particle systems (Lian 1994).

These improvements mean that a wider range of particle technology problems can now be solved at Aston using TRUBAL e.g. hopper flow, agglomerate impacts and quasi-static deformation.

The rest of this chapter will outline the structure and features of the version of TRUBAL used in the simulation work presented in chapters 5 to 8 of this thesis. The general structure of the program code will be explained and information presented about the main memory map of the program and the nature of the data arrays containing particle, contact and cluster information. Details of the random assembly generation process and the system of particle contact searching will also be explained. An analysis of the evolution of particle displacements and contact forces within the generated system will be undertaken. The details of timestep requirements, the various control modes applied to the generated assembly and methods of energy dissipation within the particle system will also be presented. Finally some details of the output of results both graphically and in the form of data will be given and details of modifications made to the TRUBAL code in these areas will be presented.

4.2 General structure of TRUBAL

4.2.1 The Distinct Element Method

The TRUBAL program simulates the mechanical behaviour of particulate assemblies which consist of spherical particles. The simulation of the progressive movements of particles within an assembly is performed using the Distinct Element Method (DEM). The DEM is a time-dependent finite difference scheme, which is applied to cyclic calculations of incremental contact forces and progressive movements of the spherical particles. In each calculation cycle, the new rotational and translational accelerations of each of the constituent particles are given by Newton's 2nd Law of Motion. If TRUBAL is operating in two-dimensional mode (2D), then the three-dimensional equations of motion are truncated to two dimensions. Numerical integration of these accelerations is then performed over a small time-step, to give updated velocities and displacements for each sphere. The velocities of each particle are then used to obtain the relative approach between contacting particles. The relative velocities between contacting particles are then used to calculate the contact force increments, both normal and tangential, at the contact points, by the use of contact force-displacement laws.

The contact forces are then resolved to obtain any out-of-balance forces on individual particles. These out-of-balance forces are then used to calculate the new accelerations of each particle during the next time-step. The calculation cycle is then repeated for the next time-step. The calculation cycle is illustrated in figure 4.1.

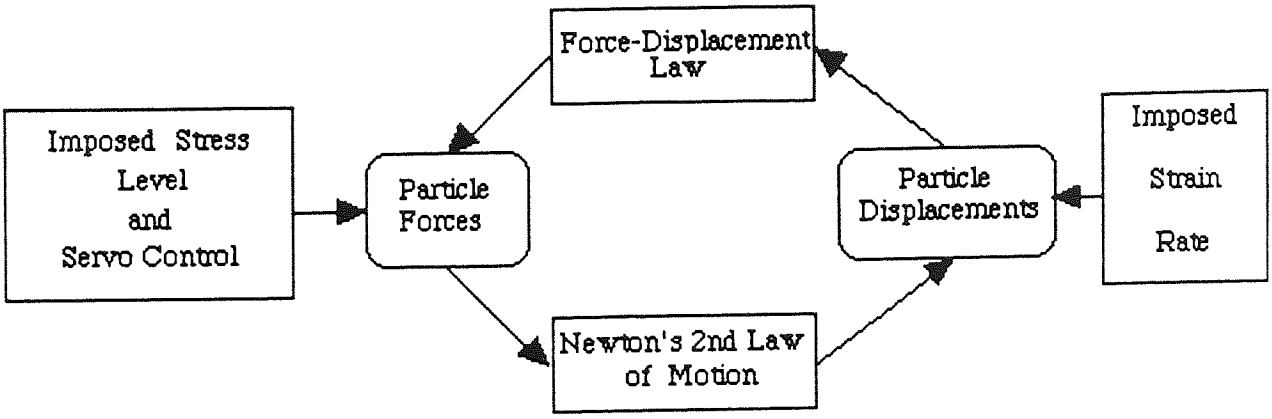

Figure 4.1 The DEM calculation cycle

4.2.2. Outline of program structure

The TRUBAL computer program is written in the FORTRAN language and its basic structure involves four components (as shown in figure 4.2). The first component of the program is the assembly generation module, which is used to generate both random and regular assemblies of particles and to define particle properties. The second and main component of TRUBAL is the cyclic simulation module, in which the Distinct Element Method is used to simulate the evolution of contact forces and particle movements. The third component, the external control module, is included in the TRUBAL code to allow the performance of a wide range of computer simulated experiments e.g. quasi-static deformation and agglomerate collisions. This module also allows the alteration of particle interaction laws and the physical properties of particles. It should be noted that these external control options can be changed or set to a particular value at any time during a simulation.

The final component of the TRUBAL code is the output module, which provides a large selection of graphical and print output options to improve interpretation of any simulation results. Post-processing analysis of data is also carried out in this module e.g. calculation of the assembly stress tensor. The program is also able to save the current state of a simulation via use of the *SAVE* subroutine. The current state of the problem is saved on the file **filename** given in the **SAVe** command line of TRUBAL. A previously-saved problem can then be restored using the **REStart** command line (see Appendix A).

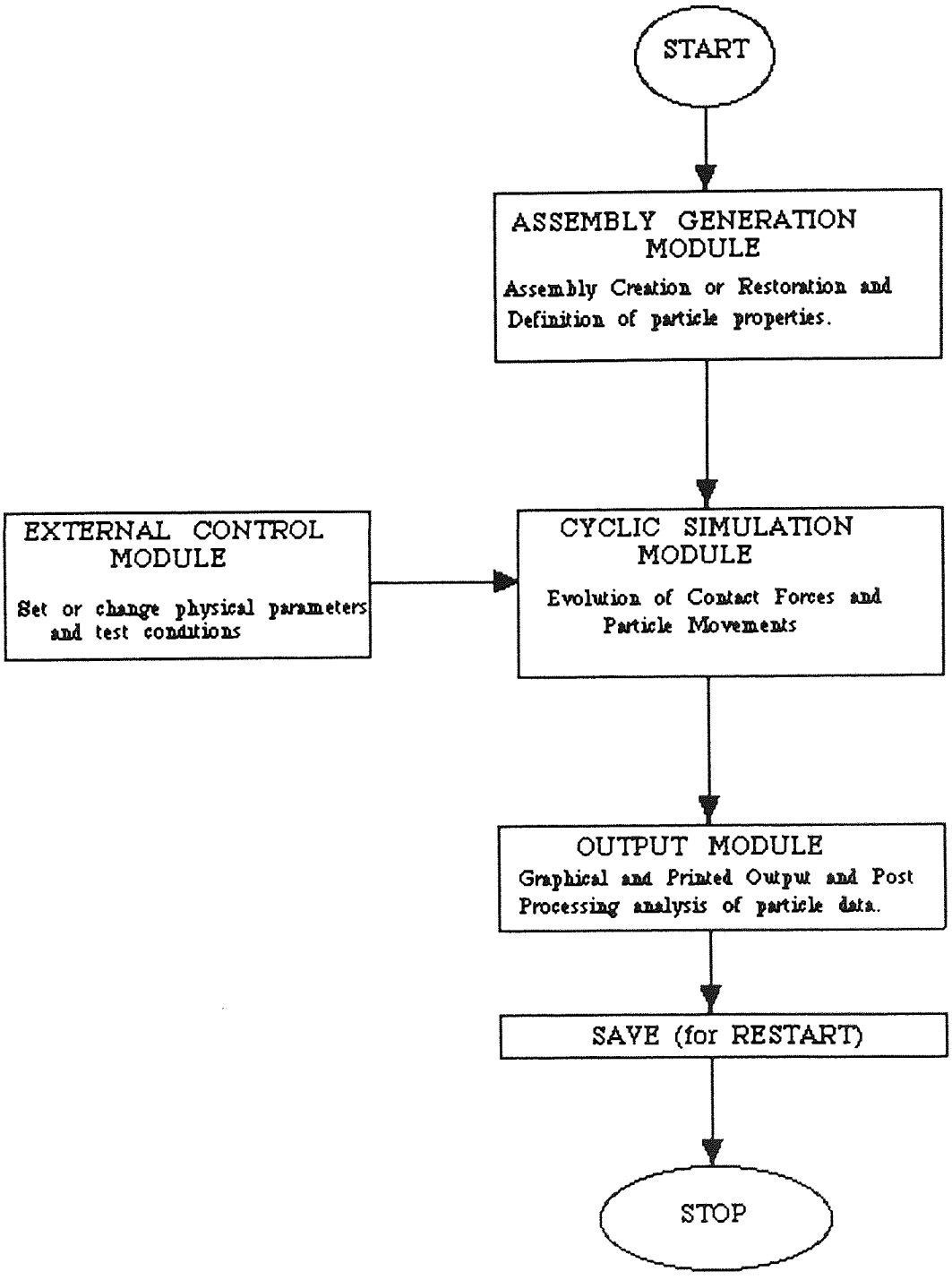

Figure 4.2 The basic structure of the TRUBAL program.

TRUBAL utilises operative commands and these make the code relatively straightforward to use and reduce processing time. An operative command is associated with the computation of one or a number of the basic steps associated with the modelling of particle systems. The operative commands can be considered to be separate modules, which each contain different computer algorithms. The advantages of writing TRUBAL in the FORTRAN language can hence be seen, since FORTRAN was developed to handle a modular program structure. The use of these operative commands permits the application of TRUBAL to different particulate media simulation problems without significant alteration to the existing FORTRAN code of the program. The discrete, modular program structure also allows the enhancement of particular modules or the insertion of new modules to be made, without affecting the other modules. Execution of the TRUBAL program therefore merely requires the user to learn the mnemonic language of the operative commands and to form for a given problem, a specific operative command list. The simulation procedure for a given problem is then controlled by this command list, examples of which are presented in Appendix A.

When TRUBAL is started a computer file called *TRUBAL.DIR* which exists in the users current working directory is interrogated. If this file contains the word BATCH, the program will work in batch mode. The program therefore takes its input from the file *TRUBAL.DAT*, uses the program FORTRAN code stored in the file *TRUBAL.F* and places its output in the file *TRUBAL.OUT*. This is the approach used in the simulation experiments reported in Chapters 5 to 8. It is however possible to insert the word TERM into the file *TRUBAL.DIR*. The program will then expect input from and send any output to specified files.

4.2.3. Main memory map

The memory map holding all the data on particles, boxes, link lists, contacts and walls (if used) is stored within a real array A(I). The array is equivalenced to an integer array IA(I) to allow storage of integer quantities. A(I) is partitioned to store all the arrays of sphere data, wall data, box data, link lists and contact data. These arrays are dimensioned dynamically in response to the maximum number of spheres and walls and the number of boxes requested by the **STArt** command line of the command list for a particular problem (see Appendix A for more details).

The periodic cell used in TRUBAL is divided into boxes, for mapping purposes (see section 4.4). The number of boxes and the size of every box in all the axial directions is the same (Lian 1993). Data elements are allocated dynamically from the main array as required and linked to the data structures by pointers. In this way, data can be retrieved rapidly when it is needed. An outline of the main memory map is presented in figure 4.3.

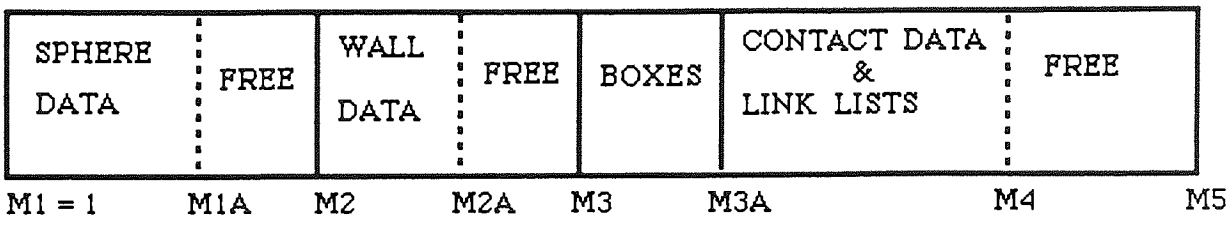

Figure 4.3. The main memory map for the TRUBAL program.

The upper limit address of the main memory is represented by M5 and is declared in the TRUBAL code. The program stops and an error message is printed if the capacity of the main memory is exceeded. This overflow condition indicates that an increase in the main memory limit is required. The upper limits of the arrays of sphere data, wall data and box data are indicated by the dynamic pointers (or addresses) M2, M3 and M3A in array A(I). The values of these addresses are calculated from the following relationships:

$$M2 = M1 + \mathbf{nball}*Nvarb \tag{4.1}$$

$$M3 = M2 + \mathbf{nwall}*Nvarw \tag{4.2}$$

$$M3A = M3 + 2*\mathbf{nbox} \tag{4.3}$$

Nvarb is the number of variables stored in every sphere data array and Nvarw is the number of variables stored in every wall data array. The variables nball, nbox and nwall represent the number of spheres, boxes (subcells) and walls respectively, requested in the initial **STArt** command line for a particular problem.

The memory allocation for sphere data lies between M1 and M2 with the lowest data address at M1. The data related to walls has its lowest address at M2 and is allocated between M2 and M3 in the memory map. The actual number of spheres generated and walls defined however, dynamically determines the actual storage allocated to the sphere data and wall data respectively, within the memory map. The upper addresses of these actual storage allocations are therefore determined according to:

$$M1A = Nball*Nvarb \tag{4.4}$$

$$M2A = M2 + Nwall*Nvarw \tag{4.5}$$

M1A and M2A are the highest addresses in the memory map actually allocated to the sphere and wall data respectively. Nball and Nwall are the actual number of spheres and walls generated by the TRUBAL code for a particular simulation. It should be noted that Nball and Nwall are always less than **nball** and **nwall**; the number of spheres and walls actually specified in the **STArt** command.

Particle contact data and the link lists (see section 4.4) have storage allocations between M3A and M5. The lowest address is at M3A and the highest address, M4, is dynamically determined by the number of links and contacts detected during mapping (see section 4.4). M4 is therefore the only address in the memory map whose value will alter during the course of a particular simulation; as contacts and links are detected and then broken. M4 is specified by the following equation:

$$M4 = M3A + 2*Nlink + Ncont*Nvarc \tag{4.6}$$

Nlink is the number of links detected, Nvarc the number of variables stored in every contact data array C(NVARC) and Ncont the number of contacts detected during mapping (including those contacts which do not currently carry load, see section 4.4).

4.2.4. Sphere data, contact data and cluster data arrays.

The data for generated particles, particle contacts and designated particle clusters within the simulation periodic cell is stored in a number of arrays specified by the TRUBAL program.

The information relating to a generated sphere is stored in the 30 elements of the sphere array B(NVARB). The dimension size of a sphere data array has been set to NVARB=30 in the current version of TRUBAL. The sphere arrays are located between M1 and M1A in the memory map. The contents of the array B(NARVB) are as indicated:

B(1) to B(3): Co-ordinates of the sphere x_x , x_y , x_z

B(4) to B(6): Cumulative linear displacement increments Δx_x , Δx_y , Δx_z

B(7) to B(9): Components of the translational sphere velocity v_x , v_y , v_z

B(10) to B(12): Angular displacements Φ_x , Φ_y , Φ_z

B(13) to B(15): Cumulative angular displacement increments $\Delta\Phi_x$, $\Delta\Phi_y$, $\Delta\Phi_z$

B(16) to B(18): Components of the sphere angular velocity ω_x , ω_y , ω_z

B(19) to B(21): Components of the out-of-balance force F_x , F_y , F_z

B(23) to B(24): Components of the out-of-balance moment M_x , M_y , M_z

B(25): Material type ITYPM and size type ITYPS stored as one item.

B(26) to B(29): Used in original code for specific tests by Cundall - now Free.

B(30): Identifies initial agglomerate to which ball belongs (1 or 2).

The contact data information for every particle-particle contact is stored in the contact data array C(NVARC).The array consists of 23 elements i.e. NVARC = 23 and these elements are shown below:

C(1) to C(3): Components of the tangential force T_x , T_y , T_z

C(4): Normal force N (Hertz theory).

C(5) to C(6): Addresses of the two spheres in contact.

C(7) to C(9): Relative tangential displacement components δ_x , δ_y , δ_z

C(10): Relative tangential displacement δ

C(11): Resultant tangential contact force T

C(12): Unloading point (historical maximum tangential force) T^*

C(13): Reloading point (historical minimum tangential force) T^{**}

C(14): DD - cumulated distance by which the tangential force has fallen short of its equivalent value on an equivalent constant normal force curve, see Thornton and Randall (1988).

C(15): Tangential peeling force for spheres with adhesion T_p

C(16): Value of specific surface energy for spheres with adhesion $\gamma = \Gamma/2$

C(17): Contact area radius a

C(18): Code indicating direction of tangential loading CDF (1 or -1)

C(19): Free

C(20): Used to determine when the work done in breaking the contact is to be calculated.

C(21): Normal stiffness of the contact k_n

C(22): Tangential stiffness of the contact k_t

C(23): Link pointing to the next contact in the list.

The elements that are underlined in the above list are only relevant to contacts between particles with adhesive forces. They are therefore not utilised in the simulation work described in the rest of the thesis. The information pertaining to unique particle clusters within a simulated periodic particle assembly is stored in the array ICARRAY(I,J) specified in the subroutine *CLUSTER* in the TRUBAL code. ICARRAY is shared in common with the subroutine *PCLUST* which plots clusters. The argument I in the array relates to the identity of the sphere in the assembly. The argument J consists of 16 elements outlined below:

J(1) to J(13): Identify the numbers of balls in contact with each ball I

J(14): Label_id of the cluster to which sphere I belongs

J(15): Number of balls in cluster to which ball I belongs

J(16): Indicates whether ball I has been drawn (1) or not drawn (0) in a **PLOt cluster** call (required for use in some TRUBAL post-processing analysis routines).

4.3 Assembly generation

The present version of TRUBAL generates the particles in test assemblies in two different ways. There is a random particle generation method which is used in the simulation work presented in this thesis and involves use of the **RGEnerate** command line (see Appendix A). The option of automatic generation of regular packings is also provided within the TRUBAL code. Random particle generation allows the particles of a simulated assembly to be generated over the entire region of the periodic working space. The generation of a random particle, requires three random numbers to be chosen in the closed intervals $[0,l_x]$, $[0,l_y]$ and $[0,l_z]$. l_x, l_y and l_z are the maximum specified x, y and z dimensions of the working space. These numbers are then designated as the co-ordinates of the centre of the particle.In the two-dimensional simulation work presented in chapters 5 to 7, this random generation routine sets the z co-ordinate of all the particles to the same value; corresponding to the centre of the box volume in the z direction.

If a newly created particle overlaps with a previously generated one then it is rejected. If it does not overlap then the particle is added to the assembly. The process is continued until the required number of particles has been generated. It should be noted that the largest particles in the assembly are generated first, and no effort is made to fit particles into the gaps between other particles. An example of an assembly generation command file is provided in Appendix A.

4.4 Contact searching in the DEM

The use of the Distinct Element Method (DEM) requires cyclic calculation of both the interparticle contact force increments and the particle displacement increments (see section 4.2.1). An efficient searching scheme is required to detect the contacts between particles to allow calculation of the interparticle contact forces. Particles obviously cannot be considered to be in contact if they are remote from each other, thus the principle of the searching scheme involves analysis of particle contacts within the local vicinity of a particle. The contact detection scheme is outlined in this section.

4.4.1 Initial generation of the particles

The use of the Distinct Element Method requires the periodic simulation cell to be divided into **nbox** subcells, where **nbox** is specified by the **STArt** command line (see Appendix A) which initiates every simulation experiment. The value of **nbox** is selected so that the subcell sizes are larger than the diameter of the largest spheres. The efficiency of contact searching however requires this subcell size to be less than twice the largest sphere diameter.

The first step in the contact detection scheme is the formation of link lists (stored between M3A and M5 in the memory map) for every subcell, by mapping of all the constituent particles of the assembly into their appropriate subcells. A spherical particle will be mapped into a subcell if one or more corners of the circumscribing square (in 2D) or circumscribing cube (in 3D) of dimension 2 (R + TOL) enters the subcell box. The maximum radius of the particles R_{max} is limited by the TRUBAL code such that $R_{max} < (DEL/2 + TOL)$. DEL is the dimension of the subcell boxes and TOL is the tolerance set for the sphere mapping.

The maximum number of subcell boxes in which a particle can be entered is four (in 2D) or eight (in 3D). A mapping scheme (in 2D) is shown in figure 4.4.

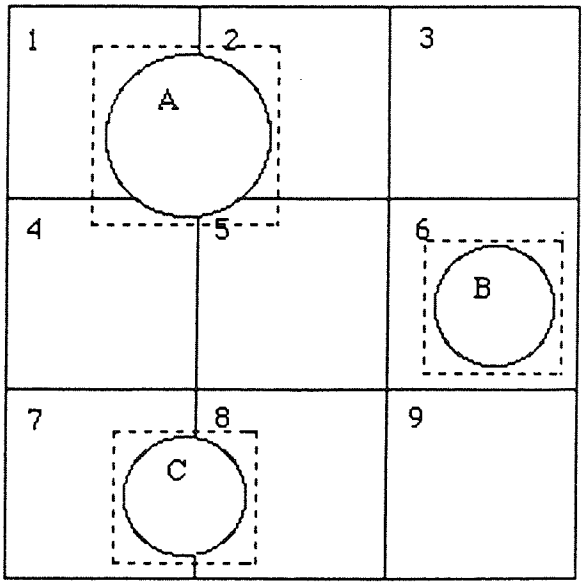

Sphere	Box Entries
A	1, 2, 4, 5
B	6
C	7, 8

Figure 4.4 The particle mapping scheme.

A sphere is in fact mapped twice. The first mapping uses the circumscribing square (in 2D) or circumscribing cube (in 3D) of the same dimension as that of the sphere diameter 2R and the second mapping uses the dimension of 2(R + TOL). The first mapping allows the link lists for each subcell in the periodic cell to be developed. The link list for a particular subcell locates all the addresses of particles that map into that particular subcell. Subcell (box) data is stored in the memory map between M3 and M3A (see section 4.2.3). A subcell address consists of a pair of words. The word lower in memory points to a linked list of sphere entries i.e. each sphere that maps into the subcell accounts for one entry in the linked list attached to the subcell. The start of the particle link list stores the addresses of the first two spheres to be mapped into a particular subcell and the end of the link list stores the addresses of the two spheres that were last to map into that particular subcell. The upper word of the subcell pair points to a linked list of contacts that map into the subcell. The use of link-lists in the program data structure allows the mapping of the spheres and the correct identification of those spheres in close proximity to each other. This is done by allowing each pair of particles in contact within each subcell to be analysed sequentially by the contact detection scheme.

The second step is the contact searching. The existence of possible contacts will only be recorded between those particles which are mapped into the same subcell. Contact searching therefore only needs to be performed between those particles that are held in the link lists of each subcell. The Distinct Element Method allows the contact search to be performed simultaneously with the mapping for formation of the link-lists. When a sphere is mapped into a subcell the spheres that were previously mapped into the same subcell are searched and their distances to the newly mapped sphere calculated. A sphere in the link list lying within a specified gap distance TOL of the newly mapped sphere is regarded as a potential contact. The centre of the gap between the two spheres is defined as the point of contact and this is also mapped into the subcells. The data for a new contact is stored as an array (C(NARVC)) in the main memory map from M4 to M4 + Nvarc (see section 4.2.3). The value of M4 is updated by moving up Nvarc + 1 elements in the array. The contact that first maps into the subcell is stored in the upper word in memory for that subcell (see above). The next contact that maps into that particular subcell is given an address in the last element of the first contact array i.e. C(23) (see section 4.2.4). C(23) acts as a link pointing to the next contact in the list of contacts for the subcell. The contact arrays for each subcell in the periodic cell are thus established using this procedure until no more contacts are mapped into a particular subcell. The storage scheme for link lists and contact arrays is shown in figure 4.5.

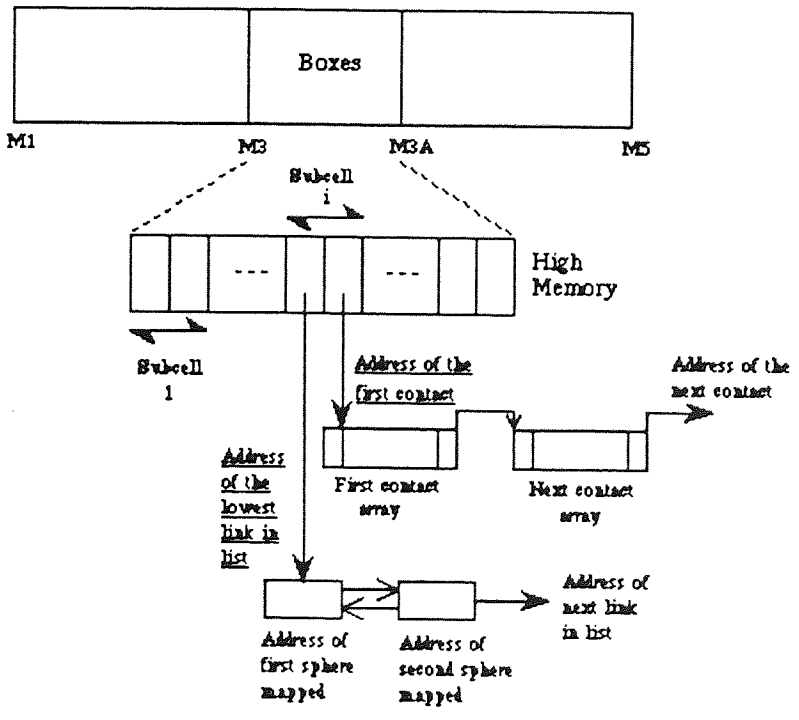

Figure 4.5. The storage scheme for link lists and contact arrays.

If a currently mapped sphere is very close to the border of the mapped subcells it could have potential contacts with spheres that are mapped into neighbouring subcells. This is why a second mapping is performed using a circumscribing square of dimension 2(R + TOL). The second mapping allows such spheres to be mapped into their neighbouring subcells and to detect the spheres (held in the link-lists of the neighbouring cells) that may be in close contact with the currently mapped sphere. The second mapping is also important when retrieval of the old links of a remapped sphere is required, so that deletion of these links can occur when the subcell entries of the remapped sphere are altered.

4.4.2 Remapping of the particles

After the initial establishment of the link-lists and the associated contact arrays, the next search for new particle contacts and remapping is only necessary after several time steps. Remapping only occurs when the maximum accumulated component of the translational displacement increment of any particle exceeds XRES (XRES = TOL/$2\sqrt{3}$). If XRES is not exceeded this implies that the maximum relative movement of the spheres is much less than TOL. If such particles were not detected as potential contacts in the previous mapping, this means that the gaps between them were greater than TOL at that particular timestep. These particles would therefore still not be in contact during the current calculation cycle and would not provide any force contribution until the next contact search. The cyclic calculation of contact force increments is only performed for those contact arrays that were established and allocated previously i.e. before the next sphere mapping and contact searching stage is necessary. The limited sphere mapping and contact searching performed in every timestep therefore helps to save computer time.

When the value of XRES is exceeded the sphere is remapped twice again, using the mapping procedure described previously. Any contact of the remapped sphere with other spheres that is not contained in the corresponding contact arrays is added. Deletion of the old links or contact arrays for a remapped sphere however may be required. This problem arises when the remapped sphere and its contact points moves from one subcell to another. The subcell that the sphere previously mapped is not mapped into again by that sphere during remapping. The links and contact arrays contained in that subcell should therefore be deleted.

The blocks of memory associated with these deleted contacts and links are added to an empty list that strings together all unused memory. Thus when memory is required for new links or contacts detected, this empty list is tried first. This scheme can save computer time and memory requirements. If the links and contact arrays associated with this empty list are not free however, then the free space in the memory map between M4 and M5 will be used in the usual way.

4.5 System evolution

In two-dimensional mode, the force-displacement calculations used in TRUBAL still operate in three dimensions. The equations of motion however are truncated to two dimensions.

4.5.1 Particle displacement evolution

In order to calculate the constituent particle movement, the Distinct Element Method used in TRUBAL at Aston, assumes that the forces and hence the accelerations are constant over a time step interval Δt (see section 4.6). Newton's Second Law of Motion for a sphere can be given, with no global damping (see section 4.8) as:

$$\mathbf{v_i}^{\mathbf{new}} = \mathbf{v_i}^{\mathbf{old}} + \left[\frac{\mathbf{F_i}}{\mathbf{m}} + \mathbf{g_i}\right]\Delta\mathbf{t} \tag{4.7}$$

$$\omega_{\mathbf{i}}^{\mathbf{new}} = \omega_{\mathbf{i}}^{\mathbf{old}} + \left(\frac{\mathbf{M_i}}{\mathbf{I}}\right)\Delta\mathbf{t} \tag{4.8}$$

where i = 1,2,3 are the three components in the *x*-, *y* *and* *z* co-ordinate directions (for 3D simulations) and i = 1,2 for 2D simulations. The mass of the sphere is m, g_i are components of the gravitational acceleration, I is the rotational inertia of the sphere, F_i are the components of the out-of-balance force, M_i are the components of the out-of-balance momentum, v_i^{new} and ω_i^{new} are the updated components of the linear and angular velocities respectively and ω_i^{old}, v_i^{old} are the components of the angular and linear velocities from the previous timestep.

Use of the updated velocity components of each sphere allows the components of the linear and rotational displacement increments in the time step to be calculated from:

$$\Delta \mathbf{x}_i = \mathbf{v}_i^{new} \Delta t \tag{4.9}$$

$$\Delta \Phi_i = \omega_i^{new} \Delta t \tag{4.10}$$

$\Delta\Phi_i$ are the components of the angular displacement increment and Δx_i are the components of the linear displacement increment for a particle. $\Delta\Phi_i$ are added to update the rotational displacements and Δx_i added to update the co-ordinates of each sphere. The co-ordinates of a sphere after a linear translation are determined by the sum of two elements. The first element is the original co-ordinates of the sphere, mapped in the previous timestep. The second element represents the accumulated displacement of the sphere since the previous mapping. Remapping of the particle and resetting of the accumulated displacements to '0' will occur if Δx_i which are added to the accumulated displacement, result in the maximum component of the accumulated displacement exceeding XRES (see section 4.4.2).

4.5.2 Particle contact forces

The interaction force between each pair of contacting spheres is also computed in an incremental way. In the case of two spheres contacting one another, relative movement at the contact has three components. These components are the relative normal approach along the centre line of the two spheres, the relative tangential displacement between the two particle centroids and the relative rotation of the two spheres. The area of contact is very small and therefore the twisting moment at the contact, due to the relative spin about the line joining the centroids of the two spheres is ignored. Thus, only the normal and tangential forces are considered in the present version of TRUBAL.

A contact is only considered to exist between the two spheres in the TRUBAL program if the boundaries overlap i.e. when the relative approach (displacement) α between them, satisfies the condition of:

$$\alpha = \mathbf{R}_A + \mathbf{R}_B - \left\{(x_B - x_A)^2 + (y_B - y_A)^2 + (Z_B - Z_A)^2\right\}^{1/2} > 0 \tag{4.11}$$

where x_i, y_i, z_i (i = A,B) are the co-ordinates of the centres of the two spheres and R_i (i = A,B) are the radii of the two spheres. For a pair of spheres A and B in contact, if the linear and rotational velocities are denoted as v_i^A, v_i^B and ω_i^A, ω_i^B respectively, the relative normal displacement increment at the contact in a time step Δt is calculated as:

$$\Delta\alpha = \left(v_i^B - v_i^A\right) n_i \Delta t \tag{4.12}$$

where i = 1,2,3 are the three co-ordinate directions and n_i is the component of the unit vector normal to the contact plane, directed from sphere A to sphere B. The simple model developed by Hertz (see Johnson, 1985) is used in the TRUBAL code (in subroutine *NHERTZ*) for the calculation of the normal contact force between the two spheres. The normal contact force N is related to the relative approach α of the centres of the spheres by the equation:

$$N = \frac{4}{3}\left[E^* R^{*1/2} \alpha^{3/2}\right] \tag{4.13}$$

Rearranging (4.13) in terms of α:

$$\alpha^3 = \frac{9N^2}{16R^* E^{*2}} \tag{4.14}$$

where

$$\frac{1}{E^*} = \frac{1 - \nu_A^2}{E_A} + \frac{1 - \nu_B^2}{E_B} \tag{4.15}$$

$$\frac{1}{R^*} = \frac{1}{R_A} + \frac{1}{R_B} \tag{4.16}$$

and

$$a^2 = R^* \alpha \tag{4.17}$$

where E_l and ν_l (l = A, B) are the elastic properties of Young's modulus and Poisson's ratio respectively, for the two spheres and a represents the radius of the circular area of contact. Differentiation of (4.13) with respect to $\Delta\alpha$ gives:

$$\frac{\Delta N}{\Delta \alpha} = 2E^* R^{\frac{1}{2}} \alpha^{\frac{1}{2}} \tag{4.18}$$

from which the incremental contact normal stiffness is defined, using (4.16) as:

$$k_n = \frac{\Delta N}{\Delta \alpha} = 2E^* a \tag{4.19}$$

In the phase of initial contact between the spheres i.e. when $a = 0$, it is necessary to use (4.13) with $N = \Delta N$ and $\alpha = \Delta\alpha$:

$$\therefore \quad \Delta N = \frac{4}{3}\left[E^* R^{\frac{1}{2}} \Delta\alpha^{\frac{3}{2}}\right] \tag{4.20}$$

The updated normal force N^{new} at the contact is given by:

$$N^{new} = N^{old} + \Delta N \tag{4.21}$$

where ΔN is the normal force increment determined from the relationship:

$$\Delta N = k_n \Delta\alpha \tag{4.22}$$

The value of k_n is obtained from (4.19) and $\Delta\alpha$ is determined from (4.12). N^{old} in (4.21) is the normal force determined from the previous timestep. The value of N^{new} having been determined, the TRUBAL program then updates the contact radius a, using (4.14) and (4.16)) before considering the tangential behaviour of the spheres.

Computation of the tangential force increment due to the tangential displacement is dependent upon the interaction laws used in the TRUBAL code. The simulation experiments presented in this thesis are concerned with cohesionless spheres. The tangential force T at the contact of the two spheres is therefore given by the partial-slip solution of Mindlin and Deresiewicz (1953). This model predicts that if the two contacting surfaces are subjected to an increased tangential displacement δ, then relative slip is initiated at the perimeter and progresses inwardly over an annular area of the surface. Rigid body sliding will occur when $T=\mu N$ (μ is the coefficient of friction). The calculation of the incremental tangential force ΔT from the incremental tangential displacement $\Delta\delta$ becomes complicated because the force-displacement law is history dependent. The analysis presented here considers the 2D situation. The more complex three-dimensional situation is considered in Lian (1993). An infinite set of geometrically similar force-displacement curves will exist, due to the history-dependence of the loading, each one corresponding to a different value of the normal force N.

Two such force-displacement curves are presented in figure 4.6 which illustrate loading, unloading and reloading conditions applied to the two contacting spheres. Theoretical investigation of the action of varying oblique forces on the behaviour of elastic spheres was undertaken by Mindlin and Deresiewicz (1953). The work identified a general procedural rule, from the analysis of several loading sequences which involved variations in the value of both normal and tangential forces.

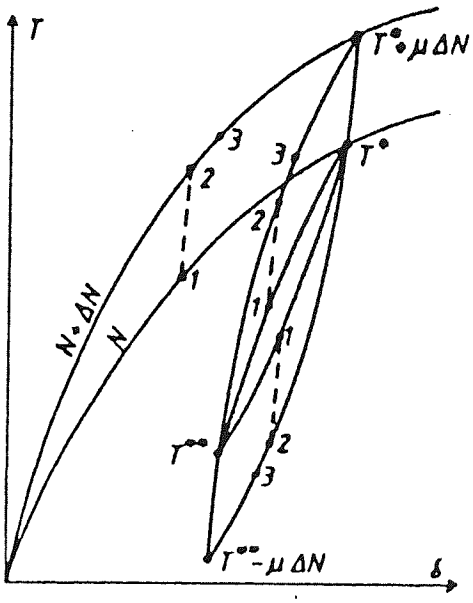

Figure 4.6 Tangential force-displacement relationship. (After Thornton and Randall, 1988)

The procedure, adopting an incremental approach, is to update the normal force N and the radius of the circular area of contact a and then calculate ΔT from the new values of N and a. Thornton and Randall (1988) reconsidered the loading situations analysed by Mindlin and Deresiewicz (1953) and found that the tangential incremental displacement ($\Delta\delta$) for loading, unloading and reloading could be expressed as:

$$\Delta\delta = \left(\frac{1}{8G^{*}a}\right)\left(\pm\mu\Delta N + \left[\frac{(\Delta T \mp \mu\Delta N)}{\theta}\right]\right) \qquad (4.23)$$

This expression does not apply however when (for $\Delta N > 0$),

$$|\Delta\delta| < \left[\frac{\mu\Delta N}{8G^{*}a}\right] \tag{4.24}$$

The rearrangement of (4.23) allows the incremental tangential force (ΔT) to be calculated from:

$$\Delta T = 8G^{*}a\theta\Delta\delta \pm \mu\Delta N(1-\theta) \tag{4.25}$$

The tangential stiffness k_t is defined, from rearrangement of (4.25), as:

$$k_t = \frac{\Delta T}{\Delta\delta} = 8G^{*}\theta a \pm \mu(1-\theta)\frac{\Delta N}{\Delta\delta} \tag{4.26}$$

where

$$\frac{1}{G^{*}} = \frac{2-\nu_A}{G_A} + \frac{2-\nu_B}{G_B} \tag{4.27}$$

$$\theta^3 = 1 - \frac{(T+\mu\Delta N)}{\mu N} \qquad \text{(loading)} \tag{4.28}$$

$$\theta^3 = 1 - \frac{(T-T^{*}+2\mu\Delta N)}{2\mu N} \qquad \text{(unloading)} \tag{4.29}$$

$$\theta^3 = 1 - \frac{(T-T^{**}+2\mu\Delta N)}{2\mu N} \qquad \text{(reloading)} \tag{4.30}$$

where G_A, G_B are the shear modulus values and ν_A, ν_B the values of Poisson's ratio for spheres A and B respectively. The negative sign in (4.25) and (4.26) is only invoked during unloading. The load reversal points are defined by the parameters T* and T** (see figure 4.6). T* is the historical loading force, from which unloading commenced and T** is the historical loading force, from which reloading commenced. The values of these parameters need to be updated ever timestep to take account of the effect of a varying normal force:

$$T^{*} = T^{*} + \mu\Delta N \tag{4.31}$$

$$T^{**} = T^{**} - \mu\Delta N \tag{4.32}$$

For a current state of loading given by point 1 in figure 4.6. (during loading, unloading or reloading), a tangential incremental displacement corresponding to

$$|\Delta\delta| = \left[\frac{\mu\Delta N}{8G^{*}a}\right] \quad \text{with } \Delta N > 0 \tag{4.33}$$

will result in a new state given by point 2 on the curve, corresponding to the new value of N. Larger values of $|\Delta\delta|$ would result in a state further along the curve e.g. point 3. If the conditions given in (4.24) occur, then there is a problem, since point 2 will not be reached and the new state will not lie on the curve corresponding to the new value of N. Szalwinski (1985) considered this case analytically but, by adopting an incremental approach, a satisfactory solution to the problem has been obtained by setting $\theta=1$ in (4.25) within the TRUBAL code. The setting of $\theta=1$ in (4.25) continues until the following condition is satisfied:

$$8G^{*}a\sum|\Delta\delta| > \mu\sum\Delta N \tag{4.34}$$

The tangential force-displacement relationships are calculated in the *TMANDD* subroutine of the TRUBAL code. Implementation of the force-displacement relationships involves the use of the contact data array C(NVARC) (see section 4.2.4). Figure 4.6 indicates that it is necessary to store T* and T** (in elements C(12) and C(13) respectively). Updating of T* and T** using (4.31) and (4.32), after applying (4.25), before the next time-step is also required. The loading history for a pair of contacting spheres during a simulation experiment can be more complex than that indicated in figure 4.6. In order to prevent overloading of the memory map by storage of all the possible load reversal points, the contact behaviour is treated as non-linear elastic, using (4.25) to (4.30), if further load reversals occur in the load range T* to T** during reloading.

In a time step the relative tangential displacement increment at the contact between the two spheres is given by:

$$\Delta\delta = \left[\left(\mathbf{v_i}^{B} - \mathbf{v_i}^{A}\right)\mathbf{m_i} - \left(\omega_i{}^{A}\mathbf{R}_A + \omega_i{}^{B}\mathbf{R}_B\right)\right]\Delta t \tag{4.35}$$

where R_A, R_B are the radii of spheres A, B respectively and m_i is the component of the unit vector parallel to the contact plane. The direction of the resultant tangential force is assumed to be in the direction of the tangential displacement. The updated resultant tangential force T^{new} can be given as:

$$\mathbf{T}^{new} = \mathbf{T}^{old} + \Delta\mathbf{T} \tag{4.36}$$

where ΔT is the tangential force increment and is determined from the relationship:

$$\Delta\mathbf{T} = \mathbf{k}_t \Delta\delta \tag{4.37}$$

where k_t is calculated using (4.26) and $\Delta\delta$ is determined from (4.35). The value of the tangential force determined from the previous timestep is represented by T^{old} in (4.36). The updated normal and tangential contact forces N^{new} and T^{new} respectively, then allow the contribution to the out-of-balance forces and moments on the two spheres to be determined from:

Sphere A

$$\mathbf{F}_i^A = -\mathbf{N}^{new}\mathbf{n}_i - \mathbf{T}_i^{new} \tag{4.38}$$

$$\mathbf{Mo}_i^A = \mathbf{R}_A \mathbf{T}_i^{new} \tag{4.39}$$

Sphere B

$$\mathbf{F}_i^B = \mathbf{N}^{new}\mathbf{n}_i + \mathbf{T}_i^{new} \tag{4.40}$$

$$\mathbf{Mo}_i^B = \mathbf{R}_B \mathbf{T}_i^{new} \tag{4.41}$$

where Mo_i^A and Mo_i^B are respectively the out-of-balance moments for spheres A and B. Moments are taken as positive in the TRUBAL program if they are found to act in the counter-clockwise direction.

4.6 Time step

It is possible to simulate experiments in the Aston version of TRUBAL using real time units. The explicit nature of the finite difference scheme used in TRUBAL means that a time step must be selected which is small enough to make the scheme numerically stable. The dynamic nature of the external loading of an assembly means that we need to consider the time of transfer of load from one particle to another via elastic wave propagation across the particles.

The application of a dynamic load to an elastic sphere produces three types of wave motion (see Johnson 1985). The first two wave types are dilational (pressure) waves and distortional (shear) waves, which travel through the body of a sphere with velocities V_p and V_s respectively:

$$V_p^2 = \frac{2(1-\nu)G}{(1-2\nu)\rho} \tag{4.42}$$

$$V_s^2 = \frac{G}{\rho} \tag{4.43}$$

where G is the shear modulus of the body, ρ is the density of the material and ν is the value of Poisson's ratio for the material. The third type are Rayleigh waves which propagate along the surface of the sphere with a velocity V_r:

$$V_r = \beta\left(\frac{G}{\rho}\right)^{1/2} \tag{4.44}$$

and β is the root of the equation given by Johnson, 1985:

$$\left(2-\beta^2\right)^4 = 16(1-\beta)^2\left[1-\left\{\frac{(1-2\nu)\beta^2}{2(1-\nu)}\right\}\right] \tag{4.45}$$

from which an approximate solution, Randall (1988), has been obtained:

$$\beta = 0.1631\nu + 0.876605 \tag{4.46}$$

It has been shown by Miller and Pursey, see Johnson (1985), that Rayleigh waves account for 67% of the energy radiated by wave motion within a solid compared with 7% for dilational waves and 26% for distortional waves. In the present version of TRUBAL the reasonable assumption that all of the elastic wave energy is transferred via Rayleigh waves has been used.

In an assembly of many spherical particles, assuming identical elastic properties, the highest frequency of Rayleigh wave propagation is assumed to be determined by the smallest sphere (radius R_{min}). The critical time step Δt_c is therefore given by:

$$\Delta t_c = \frac{\pi R_{min}}{V_r} = \frac{\left[\pi R_{min}\left(\frac{\rho}{G}\right)^{1/2}\right]}{\beta} \qquad (4.47)$$

The analysis presented above assumes that all the particles have similar mechanical properties. In the case of binary assemblies of differently composed spheres, the critical timestep value utilised within the TRUBAL code is the minimum value calculated from consideration of the two components' mechanical properties. The use of the above definition of the timestep means that even for millimetre sized particles (used in the simulation experiments described in chapters 5 to 8) the transfer time is in microseconds. Thus one million calculation cycles would be required to span one second of real time. The actual time step used in TRUBAL is a specified fraction (**FRAction**) of the Rayleigh critical time step (see Appendix A and section 6.3.2).

In the simulation experiments reviewed in the later chapters of this text, *density-scaling* is used. The aim of this process is to permit the completion of compaction experiments within a reasonable time frame. Density-scaling can enable experiments to be performed within such time frames, because large particle density values ρ are specified in the **DENs** TRUBAL command line (see Appendix A). A large ρ value in (4.47) produces a value of Δt_c, that is big enough to compensate for the low value of $\dot{\varepsilon}_s$ in the following relationship,

$$n\Delta\varepsilon = n_r \dot{\varepsilon}_r \Delta t_r = n_s \dot{\varepsilon}_s \Delta t_s \qquad (4.48)$$

where n is the number of calculation cycles of the TRUBAL program (see section 4.2.1), $\Delta\varepsilon$ is the change in the volumetric strain of the periodic cell during a calculation cycle, n_r, $\dot{\varepsilon}_r$ and Δt_r are the respective values of number of calculation cycles, strain rate and critical time step when $\dot{\varepsilon}$ = 1.0E2, and n_s, $\dot{\varepsilon}_s$ and Δt_s are the respective values of these quantities for a slower applied strain rate. If a simulation experiment is performed, then it is assumed that the values of n_s and n_r in (4.48) are equal. If $\dot{\varepsilon}_r$ = 1.0E2, Δt_r is calculated to be ~ 1.0E-7 from (4.48) and therefore for a quasi-static experiment where $\dot{\varepsilon}_s$ = 1.0E-7, (4.48) can be written as:

$$X.1 \times 10^{-5} = X.1 \times 10^{-7} \Delta t_s \qquad (4.49)$$

where $X=n_s=n_r$. Re-arrangement of (4.49) will give:

$$\Delta t_s = 100 \tag{4.50}$$

Therefore, when $\dot{\varepsilon}_s$ = 1.0E-7 the critical timestep Δt_c will have to be increased by a factor of 10^9, to allow the faster completion of simulation experiments and this means that,

$$\Delta t^* = 10^9 \Delta t_o \tag{4.51}$$

where Δt^* is the time-step that should be calculated in (4.47) to control the number of calculation cycles required for the quasi-static experiments and Δt_o is the original value of the critical timestep determined from (4.47). If all the other parameters in (4.47) are kept constant, then this relationship will now read:

$$\rho^* = K.\left(10^9\right)^2 \rho = K.10^{18}\rho \tag{4.52}$$

where K is a constant, ρ^* is the particle density value that must be specified in the TRUBAL code (see Appendix A), to allow for faster completion of the quasi-static experiments and ρ is the particle density value originally specified in the code for the simulation experiments. Thus, density values 10^{18} times the original values for both the hard and soft particles must be specified in the TRUBAL code, during quasi-static simulation experiments.

Checks must be made to ensure that the use of density-scaling does not affect the fundamental behaviour of the DEM used in the TRUBAL program (see section 4.2.1). If the scaled particle density ρ^* is 10^{18} times larger for a quasi-static simulation experiment, then the mass of the particles m* is also increased by a factor of 10^{18} from the relationship:

$$m^* = \rho^*.V \tag{4.53}$$

where V is the volume of a particle. The new particle velocity during density-scaling $\dot{x}^*$ is determined by the relationship,

$$\dot{x}^* = \ddot{x}\Delta t^* = \frac{F}{m^*}\Delta t^* \tag{4.54}$$

where $\ddot{x}$ is the particle acceleration and F is the out-of-balance force for the particle. If the value of F is assumed to be kept constant and m* and Δt^* have the values specified for quasi-static compaction. If these values are used, then (4.54) can be re-written as:

$$\dot{x}^* = \frac{1}{10^{18}}.10^9.\dot{x} = 10^{-9}\dot{x} \tag{4.55}$$

where $\dot{x}$ is the original value for the particle velocity. Therefore, the particle velocities are slower by a factor of 10^9 when gravity-scaling is used during a quasi-static experiment. The relationship between the gravity-scaled particle displacement Δx^* and the original particle displacement Δx during a calculation cycle, is determined by the following equation:

$$\Delta x^* = x^* \Delta t^* \equiv x.10^{-9}.\Delta t.10^9 \equiv \dot{x}\Delta t \equiv \Delta x \tag{4.56}$$

Therefore, it can be seen from (4.56), that the particle displacements are unaffected by the use of density-scaling for the particles. The kinetic energy of the particles KE is determined from the following relationship in the TRUBAL program,

$$KE = \frac{1}{2}m\dot{x}^2 \tag{4.57}$$

If density-scaling is used during a quasi-static simulation, then a relationship between the original kinetic energy of a particle KE and its density-scaled value KE* can be determined from the following form of (4.57):

$$KE^* = \frac{1}{2}m^*\dot{x}^{*2} \equiv 10^{18}\left(10^{-9}\right)^2.KE \equiv KE \tag{4.58}$$

Thus, from the evidence of (4.58), the kinetic energy of the particles during a TRUBAL simulation is also unaffected by the presence of density-scaled particles. Density-scaling was also used in the three-dimensional simulation experiments presented in chapter 8.

4.7 Energy dissipation

Particulate systems are not energy conserving. When a strain rate or stress level is applied to a periodic cell, the particle system gains energy from the external applied field. In order for an assembly to reach static equilibrium after some loading period, it is essential that the free energy within the system is dissipated by some damping process. Frictional damping is already incorporated within the TRUBAL code, dissipating energy at particle contacts when any sliding occurs i.e. when $T / N = \mu$. However this form of damping is not capable of dissipating all the system's free energy. The remaining energy exists because of particle oscillations. The oscillations can be split into two types. The first type are the low frequency oscillations of the assembly as a whole and the other type are the high frequency oscillations caused by the relative movement of neighbouring particles. TRUBAL provides two forms of viscous damping to limit these energy gains namely contact damping, to act on the high frequency oscillations and global damping to act on the low frequency oscillations of the assembly particles. The use of damping also minimises the free energy during loading of an assembly. Smooth deformation of the assembly and hence meaningful results can therefore be obtained from a simulation.

Contact damping considers the energy losses during the force transmission through the solid particles. This type of damping is modelled by a dashpot. Once the contact forces have been calculated (in routine *HFORD* of the TRUBAL program) damping forces are then calculated and added to the contact forces, to give the total contributions to the out-of-balance forces of each sphere. The contact damping is important for simulated assemblies to reach quasi-equilibrium, otherwise the contact forces between the particles will continue to oscillate infinitely.

Global damping is a type of mass proportional damping, operating in the form of classical Rayleigh damping and is handled in the TRUBAL subroutine which calculates the motion of each sphere. The mass proportional damping can be envisaged as dashpots that connect all constituent particles to the reference axes of the simulated system. The dashpots operate on the absolute translational and rotational velocity vector components of the spheres and provide a resistance force that is opposite to these vectors. The resistive forces associated with this type of damping therefore need to be included in the equations of motion for particles (see section 4.5.1).

The effect of global damping is similar to immersion of the particles in a viscous fluid. Global damping is a device used to dissipate kinetic energy during the preparation of a simulated system, in order to limit excessive computer time. The global damping should however be switched off before the system is subjected to the desired simulation experiment.

Inertial damping is also used to dissipate the energy used in rotation. If this type of damping is not used excessive rolling may occur between particles in an assembly. The resistive moments offered by this form of damping need to be included in (4.8), which is the equation of motion involving the angular velocity of a particle to give:

$$\omega_i^{new} = \omega_i^{old}\left(1 - D_I\frac{\Delta t}{2}\right) + \frac{\Delta t\left(\frac{M_i}{I}\right)}{\left(1 - D_I\frac{\Delta t}{2}\right)} \tag{4.59}$$

where D_I is the inertial damping coefficient, ω_i^{new} is the angular velocity of a particle subject to this form of damping and ω_i^{old} is the original angular velocity of the same particle.

4.8 Control modes

4.8.1 Strain control mode

When using periodic boundaries, the evolution of the system may be achieved by specifying either a stress control mode or a strain control mode. If the particle assembly is considered to behave as a continuum element, the strain control command superimposes a uniform strain rate tensor for the assembly, such that the incremental displacement of each constituent sphere is given as:

$$\Delta u_i = \varepsilon_{ij} x_j \Delta t \tag{4.60}$$

where ε_{ij} (i,j = 1,2,3) is the specified strain rate tensor and x_j (j = 1,2,3) are the co-ordinates of the centre of the constituent particle. Superimposing the incremental displacements due to the strain rate field on the updated incremental displacement due to the out-of-balance force leads to the total incremental displacement of each sphere as:

$$\Delta u_i^T = \Delta u_i^F + \dot{\varepsilon}_{ij} x_j \Delta t \qquad (4.61)$$

Δu_i^F (i = 1,2,3) represents the updated incremental displacement of each sphere due to the out-of-balance force (see section 4.5.1).

4.8.2 Servo control Mode

In order to apply stress-control to a periodic cell assembly, a numerical servomechanism is implemented by the TRUBAL code. The function of the servo control is to permit any desired stress path to be followed. In the servo control mode the strain rate of the periodic cell is adjusted, so that a measured component of the stress tensor is held constant at a specified level. In all of the simulation experiments presented in this thesis (see chapters 6 to 8) the servo control is used to maintain constant isotropic mean stress σ_0 or σ_{mean} (in 3D or 2D mode respectively). The servo control thus brings the test assembly to the static equilibrium condition under isotropic compression. The servocontrol operates in Mode 1 operation (see Appendix A) as:

$$\text{(3D Mode)} \quad \dot{\varepsilon}_{ij}^{Grid} = \frac{g}{3} \times \left(\sigma_0^{specified} - \sigma_0^{measured} \right) \qquad (4.62)$$

$$\text{(2D Mode)} \quad \dot{\varepsilon}_{ij}^{Grid} = \frac{g}{2} \times \left(\sigma_{mean}^{specified} - \sigma_{mean}^{measured} \right) \qquad (4.63)$$

where g is the specified gain of the servocontrol given in the **GAIN** command line (see Appendix A). The value of g is $\dot{\varepsilon} / \sigma_{error}$ (in Mode 1) where the 'error' is the difference between the specified stress level and the measured value for the assembly of particles and $\dot{\varepsilon}_{ij}^{Grid}$ is the actual strain rate imposed on the periodic cell when the servomechanism is in operation. The choice of the value of the parameter g is critical. If g is too large the servocontrol will become unstable or never reach the specified stress level. If g is too low the servo will be sluggish and the error may be too large. A value of 0.2 for g has been found to be effective (Sun, 1994). In the application of the servo control a limiting maximum strain rate is specified for the simulation. This is necessary when very high velocities are developed, should the measured stress differ greatly from the desired stress. The limit of this maximum allowed strain rate is given by the servo control **GAIN** command line (see Appendix A).

4.9 Output of results

In the current version of TRUBAL, the results of a computer simulated experiment can be either printed out or plotted. The print-out option provides results of sphere data, contact data, energy terms, the stress tensor and other general information. All such data can be printed out at any stage during the simulation. In the graphics plotting option, one can obtain 3D or 2D colour pictures of spheres, contact forces, the contact connection diagram, particle velocities and particle displacements. The graphic package available with TRUBAL is written in FORTRAN using graPHIGS API for IBM RS 6000 workstations. In this section of the chapter, details will be given of the calculations used in producing results for the simulations described in chapters 5 to 8. Information will also be given on the modifications made to both graphical and printed output via alterations to the TRUBAL code.

4.9.1 Standard data output

In order to fully describe the mechanical behaviour of a simulated particle assembly during the isotropic compaction process a number of key parameters are calculated at various stages of an experiment. These parameters include the volumetric strain ε_v, which is calculated from the change in the value of the grid volume of the periodic cell ΔV compared with the initial grid volume V at the start of compaction (the 'ground state' condition):

$$\varepsilon_v = \frac{\Delta V}{V} \tag{4.64}$$

The nature of the selected ground state for the simulations undertaken is considered in more detail in Chapter 5. The stress tensor for an assembly is also calculated during a simulation experiment. If the simulation is two-dimensional, then the isotropic mean stress σ_{mean} is calculated using the values of the stresses σ_{11} and σ_{22} acting in the two perpendicular planes of the 2D assembly, in the following relationship:

$$\sigma_{mean} = 0.5 \times (\sigma_{11} + \sigma_{22}) \tag{4.65}$$

In a three-dimensional simulation the mean stress σ_0 for the particle assembly is dependent upon the individual stresses σ_{11}, σ_{22} and σ_{33} acting in the three co-ordinate directions i.e.

$$\sigma_0 = \frac{(\sigma_{11} + \sigma_{22} + \sigma_{33})}{3} \tag{4.66}$$

The solid fraction of the particles in the assembly ϕ is dependent upon the value of the porosity p calculated by the TRUBAL code i.e.

$$\phi = 1 - p \tag{4.67}$$

The value of the porosity p is calculated as the ratio of the periodic cell volume unoccupied by spheres, or pore volume V_p, to the total volume of the periodic cell at a particular timestep V_T (see chapter 1):

$$p = \frac{V_p}{V_T} = \frac{\left(V_T - \left\lceil \frac{(\Sigma 4\pi R^3/3)}{V_T} \right\rceil \right)}{V_T} \tag{4.68}$$

where the parameter R is the radius of a spherical particle.

The particle co-ordination number is a micromechanical parameter that is used as a general descriptor of assembly behaviour. The apparent co-ordination number for a simulation assembly Z_a is given by:

$$Z_a = \frac{2 \times M}{N} \tag{4.69}$$

where M is the number of particle contacts and N is the number of particles in the assembly. The factor of two is included because each contact involves two particles. The geometric co-ordination number Z_g which indicates the average number of contacts of a particle is calculated as:

$$Z_g = \frac{2 \times M}{(N - N_0)} \tag{4.70}$$

where N_0 is the number of unconnected particles in the assembly.

The value of N_0 is calculated from the histogram of particle contacts. The histogram also indicates the number of particle contacts that involve one particle M_1, how many particles have just one contact N_1 and the number of particles that exhibit more than one contact. This histogram thus allows calculation of the mechanical co-ordination number of the assembly Z_m. The mechanical co-ordination number differs from the geometric version Z_g because all particle contacts that do not contribute to the mechanical strength of the assembly are ignored in the calculation:

$$Z_m = \frac{2M - M_1}{(N - N_0 - N_1)} \tag{4.71}$$

The contact density C is another micromechnical parameter that is used as a general descriptor of granular assembly behaviour:

$$C = \frac{M}{V} \tag{4.72}$$

4.9.2. Modifications to the TRUBAL code

All the modifications described in this section are applicable to two-dimensional simulation experiments. The determination of contact information is also applicable to three-dimensional work but three-dimensional graphical changes are described in more detail in chapter eight. The versions of the TRUBAL code initially available on the IBM RS6000 workstations RS2 and RS1 were not developed for analysis of binary systems of particles. Modifications therefore had to be made to both the graphical and printed output. These enhancements to the program output were designed to allow more detailed analysis of micromechanical parameters and percolation parameters associated with assembly behaviour.

The first modification in the area of micromechanical parameters involved enhancements of the routine *CONDAT* in the TRUBAL code to allow printed output of contact forces, contact areas and mean contact pressures within an assembly. Subrountine *CONDAT* was also amended to identify different contact types i.e. hard-hard particle contacts, soft-soft particle contacts or hard-soft particle contacts. The nature of a particular particle contact type was determined within the subroutine from analysis of the material types **itypm** (see Appendix A) of the particles involved in the contact.

A new routine *CFHIST* was also developed to collect histogram data for plotting contact force, contact area and mean contact pressure distributions, for the assembly system at any desired time during a simulation experiment.

Modifications to the TRUBAL program to allow analysis of percolation parameters were also carried out. The 'backbone' of the percolating cluster within an assembly can be considered to be the component of the cluster that transmits the largest forces from one boundary to another (see section 3.4) . It is this 'major forces' transmission network that is the minimal path for percolation within the random assembly. In order to obtain the 'backbone' for a particular percolating cluster within a two-dimensional assembly various changes were made to the TRUBAL code and a procedure adopted: Using the **PLOT CLUster** command the largest cluster at the 'percolation threshold', whether geometric or elastic (see section 3.3), or at any other point in a simulation experiment is displayed i.e. the 'percolating cluster' (see figure 4.7).

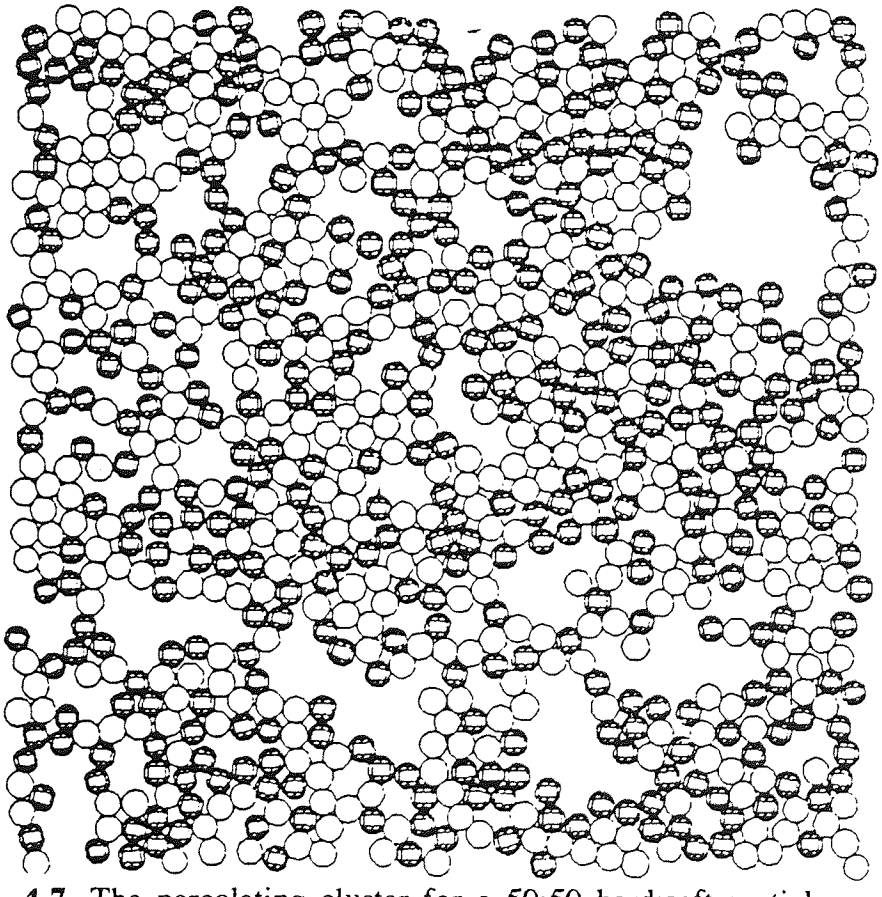

Figure 4.7. The percolating cluster for a 50:50 hard:soft particle assembly at the geometric percolation threshold.

Changes to the *CLUSTER* subroutine within the TRUBAL code eliminate all those particles within the 'percolating cluster' that exhibit contact normal forces below a particular value (initially the mean contact normal force as determined from the contact data).

Using the **PLOT CLUster** command the reduced cluster is then displayed and a check made to ensure that percolation of particles in both directions in 2D is observed. If percolation of particles is not observed then the contact normal force value within the *CLUSTER* subroutine is reduced until percolation is again observed in 2D. The value of the contact normal force at this 'percolation' point is accurate to ± 0.001 N (or 0.007 % of the smallest mean contact normal force of the binary assemblies at the 'geometric percolation threshold' i.e. that observed for the 100% soft particle assembly). If percolation is observed then the contact normal force value within the *CLUSTER* subroutine is increased until a percolating cluster, when displayed, is only just apparent in both directions in the 2D periodic cell. The accuracy of the contact normal force value at this percolation point is again ± 0.001 N. The 'backbone' of the 'percolating cluster' is then displayed graphically, ready for output (see figure 4.8).

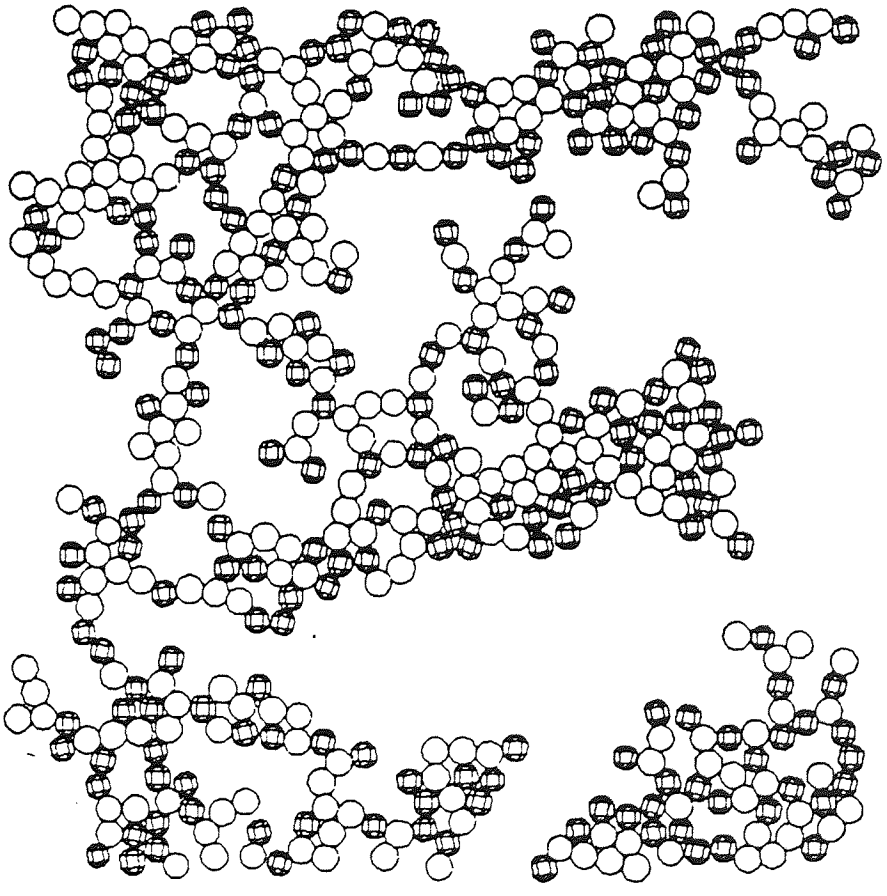

Figure 4.8. The backbone of the percolating cluster for a 50:50 hard:soft assembly at the geometric percolation threshold.

Modifications were also made to the graphical output to allow the generation of nine periodic cells (in 2D) to portray percolation structures in an infinite granular medium (see figure 4.9) of which the graphical information represented in one periodic cell is a small part e.g. figure 4.8.

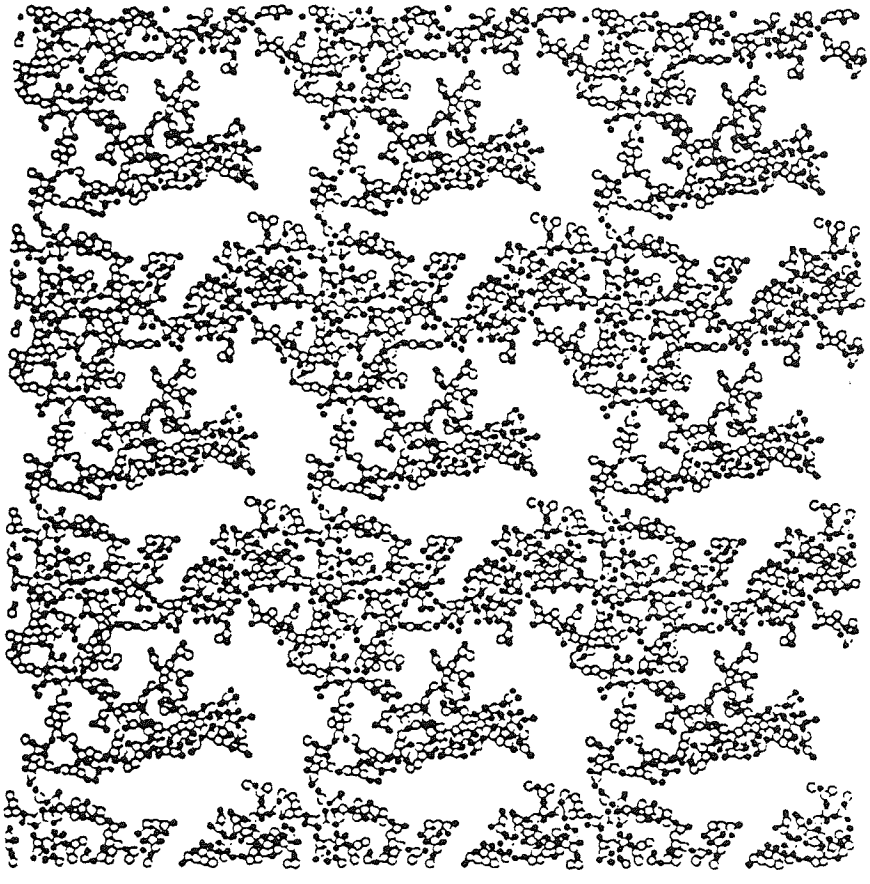

Figure 4.9 Nine periodic-cell view of the percolating cluster backbone for a 50:50 hard:soft assembly at the geometric percolation threshold.

Chapter 5

Percolation threshold behaviour

5.1 Introduction

The simulation experiments presented in chapters 6 to 8 utilise the concept of a percolation threshold in an attempt to specify a rational and unambiguous origin for measurements e.g. volumetric strain. The particle systems considered in this thesis are similar in some respects to the elastic lattices discussed in section 3.5, although the particle interaction laws are more complex e.g. Hertzian (see Johnson, 1985). The use of concepts such as the geometric percolation threshold p_g and the elastic percolation threshold p_e (see section 3.2) is therefore reasonable in the analysis of the simulation data. The quantitative nature of such thresholds will be different from those exhibited by the simple elastic lattices analysed in section 3.5. However, the general approach provided by the idea of a transition in assembly behaviour is useful in determining the *ground state* for the subsequent mechanical response of the assembly. A large number of experiments on elastic lattice systems were performed by statistical physicists in the work reviewed in section 3.5. Statistical averaging techniques were used on the data produced by such experiments, since sufficient results were obtained by these workers. However, only a limited number of experiments are presented in this chapter, because the work reviewed here is supplemental to the main simulation studies presented in chapters 6 to 8. Therefore, this quantitatively-limited data indicates that, further work needs to be performed in this area to allow statistical averaging of the results. Determination of the onset of connectivity across a particle assembly as represented by p_g is useful knowledge, but it is the development of an assembly that can support load, represented by p_e, that is more important in defining the ground state for a system. The nature of both p_g and p_e will be explored in this chapter, for the different types of simulation experiments reported in chapters 6 to 8. It should be noted that the particles in three-dimensional assemblies have greater degrees of freedom than the particles in two-dimensional systems. Therefore, dimensionality should have an important effect on the observed macroscopic behaviour. In all visualisations of the assemblies of mixtures, dark circles or spheres will represent the hard particles.

5.2 Two-dimensional quasi-static compression

Isotropic compression of a two-dimensional assembly using a strain rate of $\dot{\varepsilon}$ = 1.0E-7 and the strain control mode (see section 4.8.1) was performed up to the geometric percolation threshold p_g. The onset of p_g in this two-dimensional case is defined as the presence of a connected, percolating cluster of particles (see chapter 3) stretching across the assembly in both x- and y- directions. The presence of such a connected cluster is identified for the simulated particle assemblies using the assembly connection diagram (see the **PLOt** TRUBAL command line in Appendix A), in which the centres of particles in contact are joined by lines e.g. figure 5.1. This onset of connectivity is accurate to ± 2 calculation cycles (see section 4.5). Examples of 2D percolating clusters at p_g are presented in figures 5.1a to 5.1e for different mixtures.

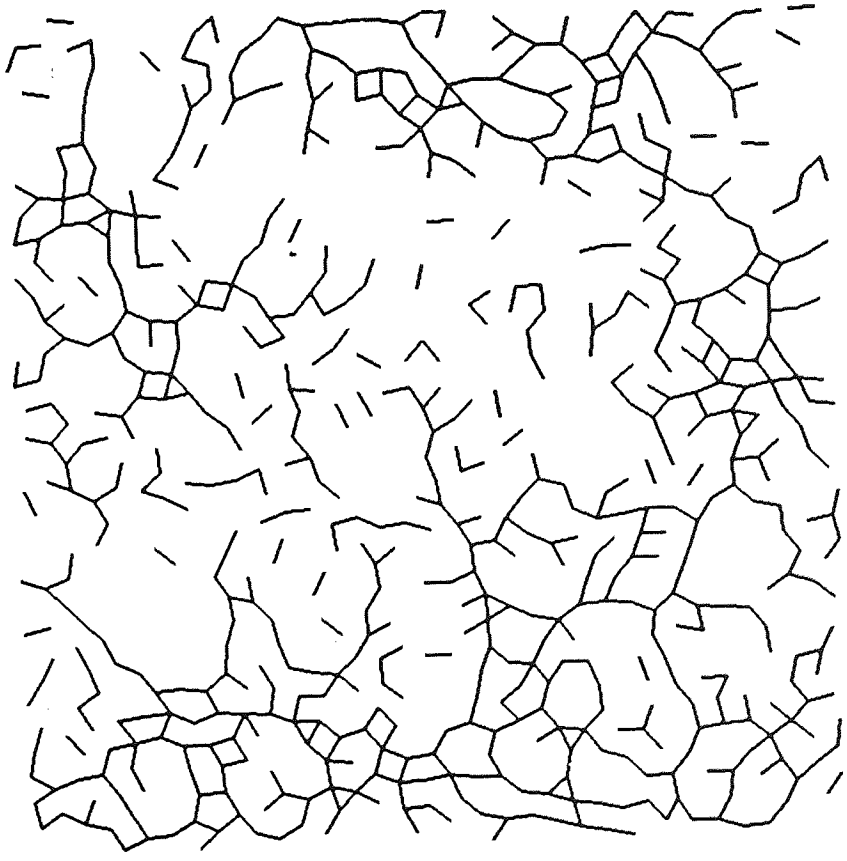

Figure 5.1a Assembly connection diagram for 100% hard assembly at the geometric percolation threshold.

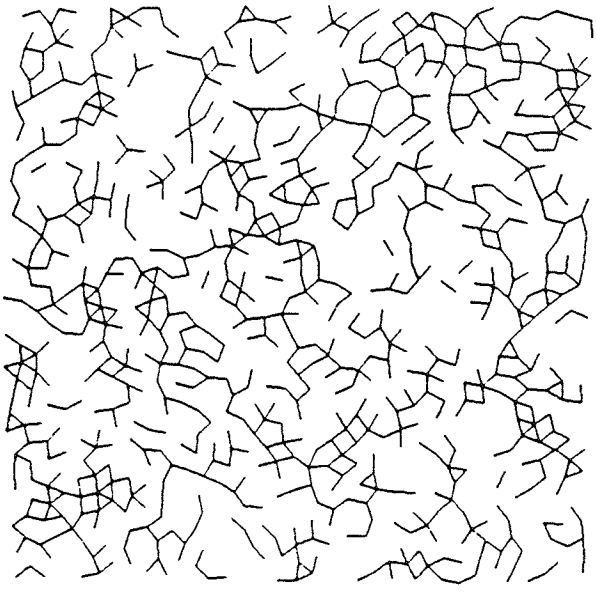

Figure 5.1b Assembly connection diagram for 75/25 assembly at the geometric percolation threshold.

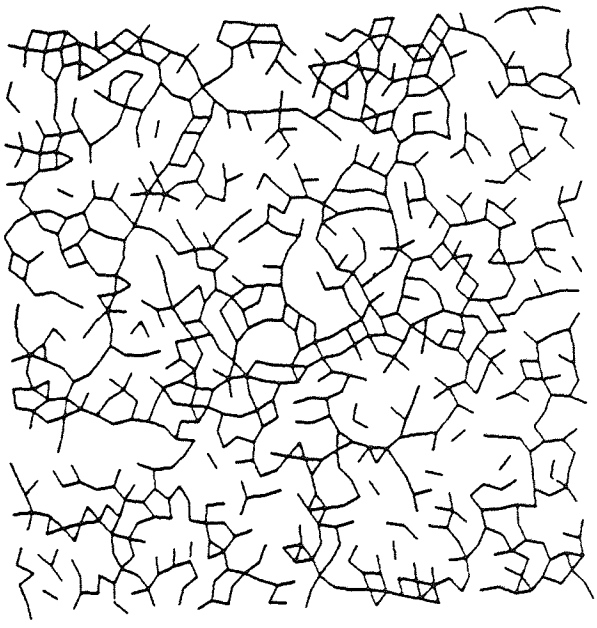

Figure 5.1c Assembly connection diagram for 50/50 assembly at the geometric percolation threshold.

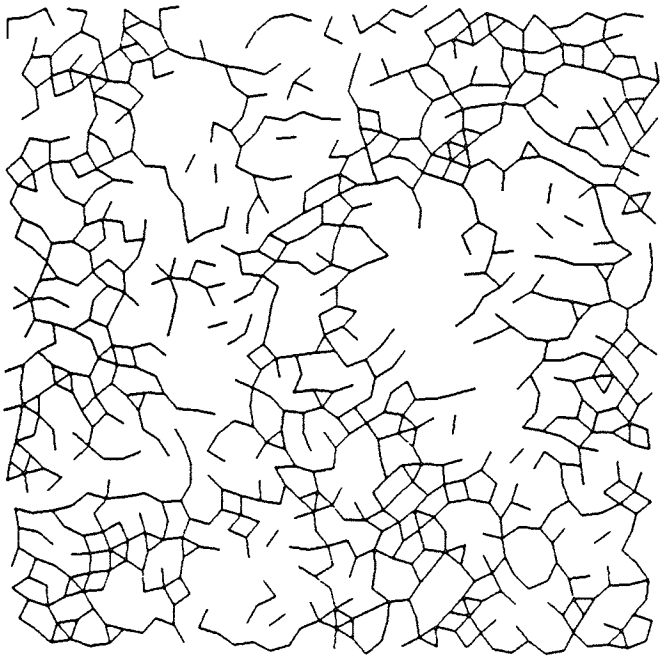

Figure 5.1d Assembly connection diagram for 25/75 assembly at the geometric percolation threshold.

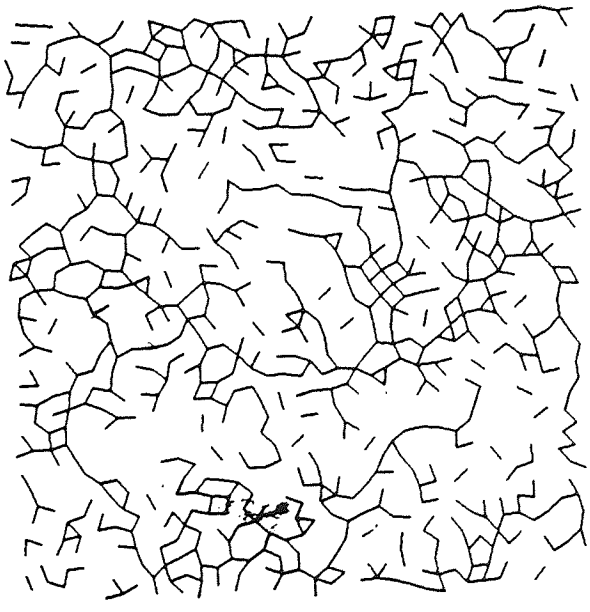

Figure 5.1e Assembly connection diagram for 100% soft assembly at the geometric percolation threshold.

A number of general observations can be made about figures 5.1a to 5.1e. The particle connection diagram for the 100% hard assembly exhibits a very open, *linear* structure, whereas figure 5.1e for the 100% soft assembly shows that extraneous branches to the main percolating pathway are present. Figure 5.1c indicates that the presence of both hard and soft particles in the 50:50 assembly produces a very random diagram with a lot of particle connections and therefore, a simple and direct percolating pathway is not visible. It can also be observed that, the addition of soft particles to a predominately hard particle assembly produces a random connection diagram such as figure 5.1b, whilst the addition of hard particles to a predominately soft particle assembly, results in a relatively ordered structure like figure 5.1d. However, interpretation of these connection diagrams is a subjective process and is therefore open to some argument.

Once p_g was established, the assemblies were then subject to quasi-static isotropic compression (see Appendix A for more details). From the stress-strain curves obtained, the elastic percolation threshold p_e was identified by the point at which appreciable lattice rigidity was first developed i.e. when a rapid increase in the gradient of the stress-strain graph was first visible (see figure 5.2). The assembly connection diagram for the 50:50 assembly at p_e is illustrated in figure 5.3 and indicates that assembly connectivity is more complete at p_e than at p_g (see figure 5.1c).

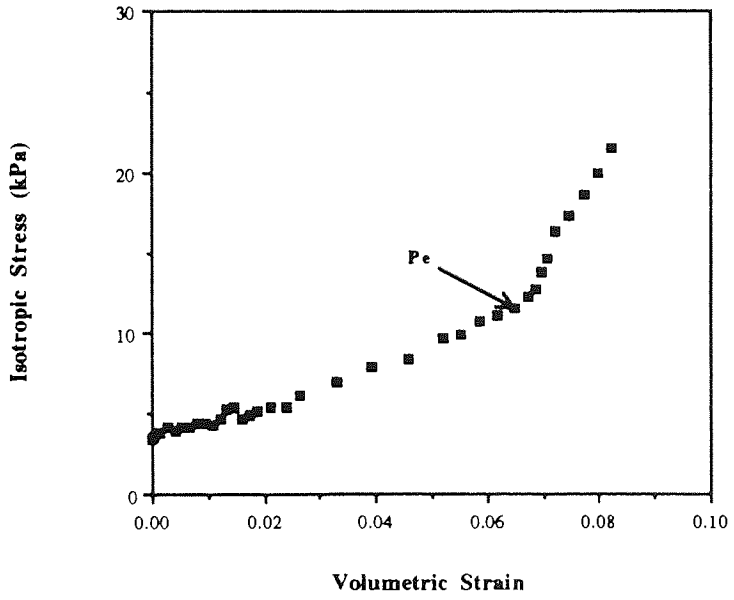

Figure 5.2 Detection of the elastic percolation threshold for the 50/50 assembly.

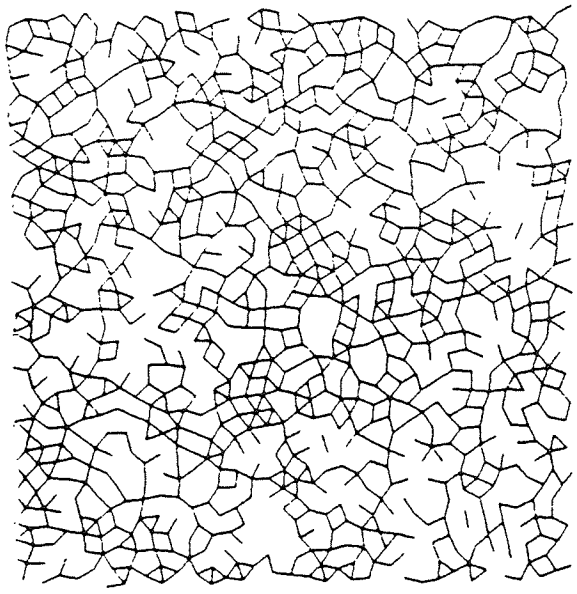

Figure 5.3 Assembly connection diagram for the 50/50 assembly at the elastic percolation threshold.

The isotropic stress levels associated with p_e were determined for the various assembly mixtures from stress tensor information obtained using the **PRInt** command line of the TRUBAL program (see Appendix A). The variation of the stress level at p_e with assembly composition is presented in figure 5.4, which indicates that a transition in behaviour is observed around $p = 0.5$.

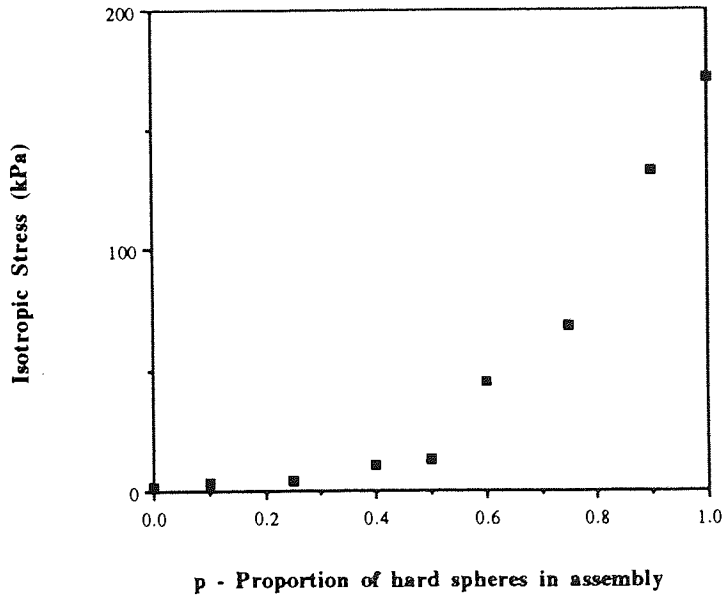

Figure 5.4 Stress level at the elastic percolation threshold against the proportion of hard spheres in the assembly.

For $p < 0.5$, the variation of stress with mixture composition is small and for $p > 0.5$, the stress increases significantly with further increases in the value of p. The idea of a transition in mechanical behaviour for binary assemblies of hard and soft cylinders was also proposed by Travers *et al.* (1986), in the work reviewed in section 2.3. Travers *et al* suggested that, a significant *transition* in assembly load-displacement behaviour was present around $p = 0.7$. However, as mentioned above, a transition in mechanical behaviour for the simulation work is only observed around $p \cong 0.5$. The determination of this transition point is a subjective process and therefore, the quantitative discrepancies between the results from the simulation and experimental studies are probably to be expected.

The data presented in figure 5.4 can be interpreted in terms of more familiar engineering concepts, rather than percolation theory ideas of a transition in mechanical behaviour. Therefore, empirical curve-fitting can be applied to a semi-log plot of the data presented in figure 5.4 and the results of this procedure are shown in figure 5.5.

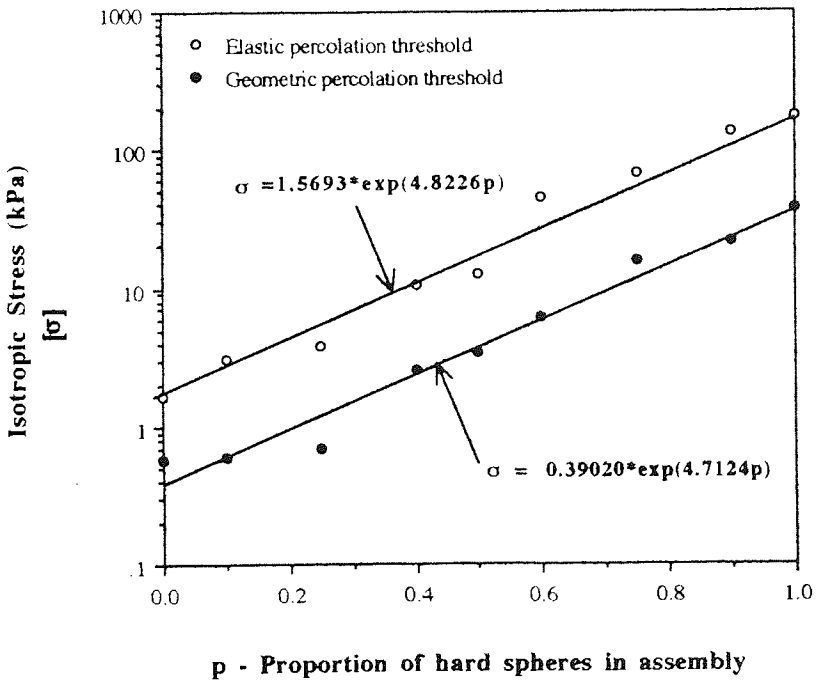

Figure 5.5 Effect of mixture composition on the isotropic stress at the geometric and elastic percolation thresholds.

The best fit lines for the curves in this figure are provided by the exponential relationships:

$$\underline{\text{At } P_g} \qquad \sigma_{pg} = \sigma_{pg}{}^{0}\exp(Ap) \tag{5.1}$$

$$\underline{\text{At } P_e} \qquad \sigma_{Pe} = \sigma_{Pe}{}^{0}\exp(Bp) \tag{5.2}$$

where σ_{pg} is the stress level at p_g, σ_{pe} is the stress level at p_e, $\sigma_{pg}{}^{0}$ and $\sigma_{pe}{}^{0}$ are the stress levels for the 100% soft assembly ($p = 0$) at p_g and p_e respectively, p is the proportion of hard spheres in the assembly and A, B are constants. If log values are considered, then (5.1) and (5.2) can be rewritten in terms of A and B respectively as:

$$A \approx \ln\left(\frac{\sigma_{pg}{}^{1}}{\sigma_{pg}{}^{0}}\right) \tag{5.3}$$

and

$$B \approx \ln\left(\frac{\sigma_{Pe}{}^{1}}{\sigma_{Pe}{}^{0}}\right) \tag{5.4}$$

Therefore, the values of A and B correspond approximately to the slopes of the curves shown in figure 5.5. Further inspection of the values of these constants indicates that, the slopes of the curves for the data obtained from both p_g and p_e are similar. However, if the relationships represented by (5.3) and (5.4) are considered, then it could also be stated that similar ratios between the stress levels for the 100% hard and the 100% soft assemblies are apparently observed at both p_g and p_e.

There are a number of parameters which are general descriptors of the structure of the assembly at the elastic percolation threshold i.e. the solid fraction ϕ, the mechanical co-ordination number Z_m and the geometric co-ordination number Z_g. (see section 4.9.1). The effects of assembly composition on ϕ are presented in figure 5.6. A gradual increase in the value of ϕ up to a maximum value of ϕ = 0.861 at $p = 0.9$, and then a rapid decrease in the value of ϕ when $p > 0.9$, are observed in this figure. The variation of Z_m and Z_g with p is illustrated in figure 5.7, where both curves exhibit the general characteristics of a fairly flat region up to $p = 0.5$, a rapid increase in the values of Z_m and Z_g between $p = 0.5$ and p = 0.75 and then a rapid decrease in these values when $p > 0.75$.

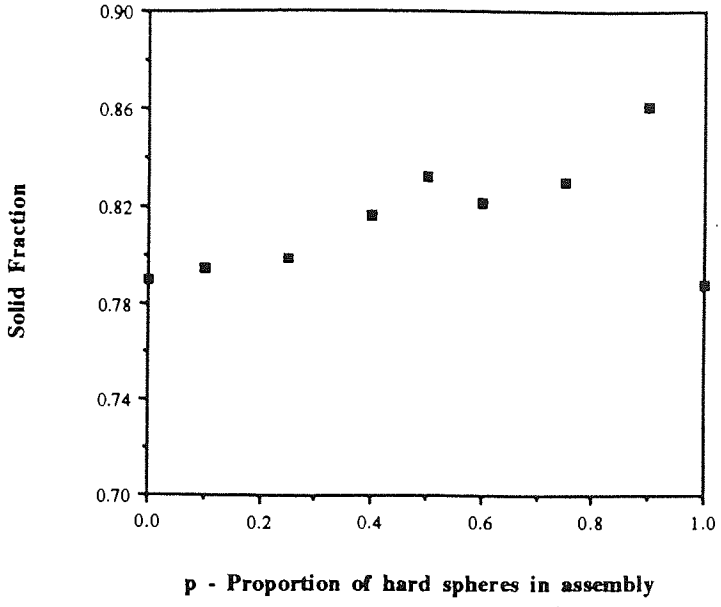

Figure 5.6 Effect of mixture composition on the solid fraction at the elastic percolation threshold.

The values of Z_m reflect the size of the load carrying network within the assemblies (see section 4.9.1) and it can therefore be seen from figure 5.7, that the 75:25 assembly has the largest load-carrying network of particles at p_e..

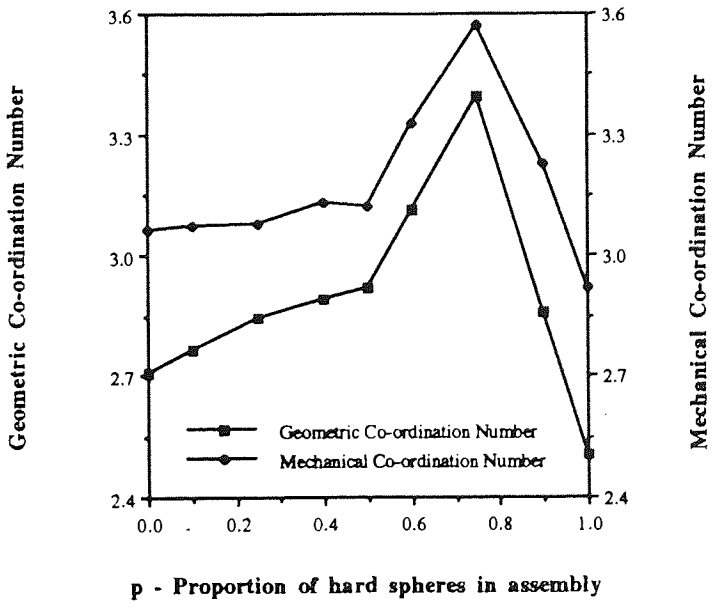

Figure 5.7 Effect of mixture composition on the geometric and mechanical co-ordination numbers at the elastic percolation threshold;

Figure 5.7 also indicates that, when $p > 0.75$ a rapid decrease in the size of the load carrying particle network will result, and below $p = 0.5$ the load carrying network is relatively small. The internal assembly characteristics which may be responsible for this behaviour will be examined later in this section.

In any binary system the distribution of particle-particle contact areas, contact pressures and contact forces are important micromechanical parameters required for a complete description of the state of assemblies at p_e. The contact force, area and pressure data for this assembly at p_e can be analysed using the **PRInt CHD** command line of the TRUBAL program (see Appendix A) and a contact force distribution can be produced. A contact force distribution is shown in figure 5.8 and this diagram indicates that the contact force distribution is approximately exponential. The presence of a strongest stressed network in a particle assembly, which was first suggested by Drescher and de Josselin de Jong (1972), would produce such an exponential distribution. Therefore, figure 5.8 appears to provide evidence of the presence of such a network in the 50:50 assembly at p_e. An exponential distribution is associated with a strongest stressed network because the particles in the assembly carrying the largest forces would be few in number and the majority of particles would only carry small forces, which are typical characteristics of such a network. Exponential distributions were also observed for all the other mixtures at p_e (see Appendix B).

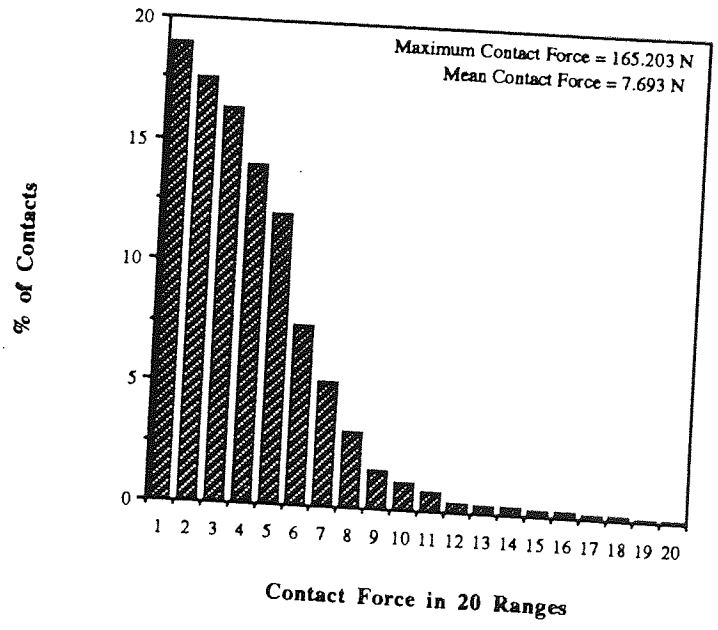

Figure 5.8 Contact force distribution at the elastic percolation threshold for the 50/50 assembly.

Figure 5.9 shows the contact area distribution for the 50:50 assembly. The contact area distributions for the various types of particle contacts i.e. hard-hard, soft-soft and hard-soft contacts are provided in Appendix B, figures B5 - 7. Figure B5 indicates that the hard-hard particle contacts are primarily responsible for the data contained within the first data range of Figure 5.9, because the majority of the hard-hard contacts have small contact areas and experience limited deformation at p_e. The contact area distributions for the hard-soft and soft-soft contacts in figures B6 and B7 are both Gaussian in appearance.

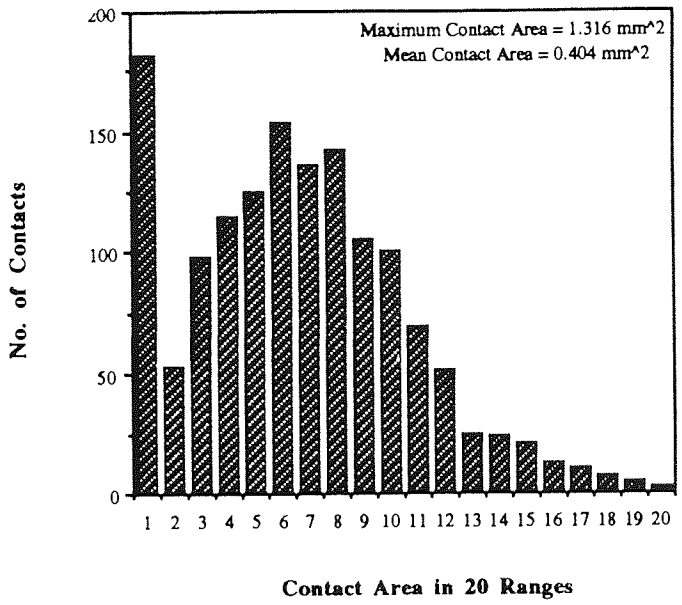

Figure 5.9 Contact area distribution at the elastic percolation threshold for the 50/50 assembly.

The Gaussian distributions show that the external deformation of the assembly is shared amongst all the particle contacts involving soft particles. The contact pressure distribution for the 50:50 assembly is presented in figure 5.10 and this is also found to be Gaussian in appearance. Therefore, a reasonably uniform distribution of contact pressures across the assembly is obtained.

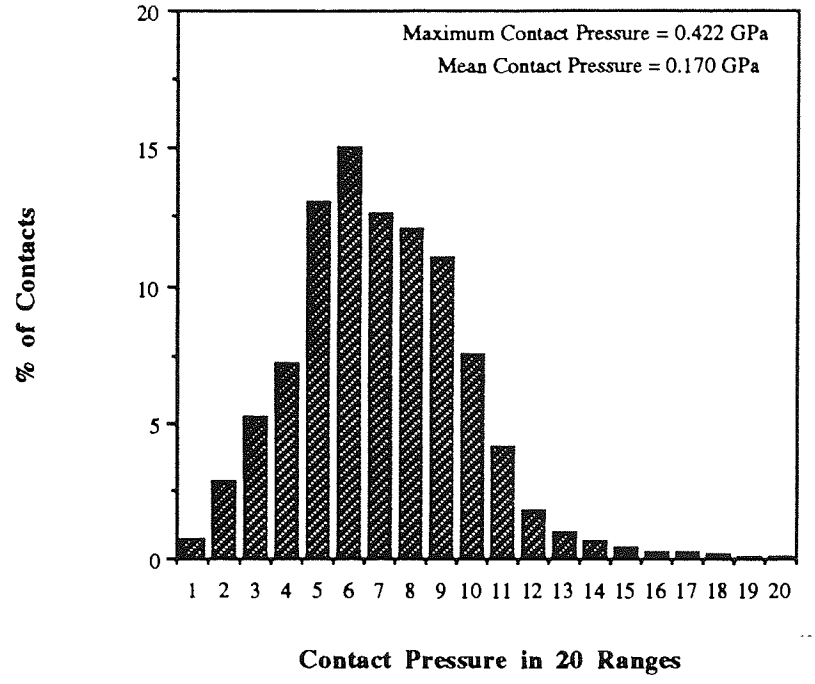

Figure 5.10 Contact pressure distribution at the elastic percolation threshold for the 50/50 hard:soft mix.

The influence of the various contact types on contact pressure distributions for the 50/50 hard/soft assembly is presented in more detail in Appendix B.

The nature of the cluster fractal dimension, which represents the spatial occupation behaviour of a particle cluster, was discussed in section 3.3.1. Calculation of the cluster fractal dimension during the simulation experiments required a modified form of equation 3.9 (see section 3.3.1), to take account of the size of the periodic cell.

$$N = \phi\left(\frac{D}{2r}\right)^{d_f} \tag{5.5}$$

from which

$$d_f = \ln\left(\frac{N/\phi}{D/2r}\right) \tag{5.6}$$

where N is the number of particles in the cluster, ϕ is the assembly solid fraction, D is the size of the periodic cell , r is the average radius of a particle in the assembly and d_f is the cluster fractal dimension. It should be noted that the maximum value for d_f in two-dimensions would be $d_f = 2.00$; indicating complete spatial occupation by a cluster.

The values of d_f at the geometric percolation threshold p_g for the different assemblies are presented in figure 5.11. Specific knowledge of assembly properties at p_g is not important in a practical sense, but a number of general observations can be made from figure 5.11 which will be useful when the data at p_e is analysed. The introduction of particles with different physical properties results in an assembly percolating cluster which occupies more space than that associated with either a 100% soft or 100% hard assembly. As the proportion of hard spheres in the mixture is increased, the fractal dimension of the cluster increases at a decreasing rate for $p < 0.5$. The fractal dimension remains essentially constant for $0.5 < p < 0.75$ but decreases rapidly when $p > 0.75$. The introduction of soft particles into a 100% hard assembly has a more noticeable effect on the value of d_f than the introduction of hard particles to a 100% soft assembly. It should also be noted that from the values of d_f obtained and visual evidence, the size of the percolating cluster associated with the 100% hard assembly is smaller than that associated with the 100% soft assembly.

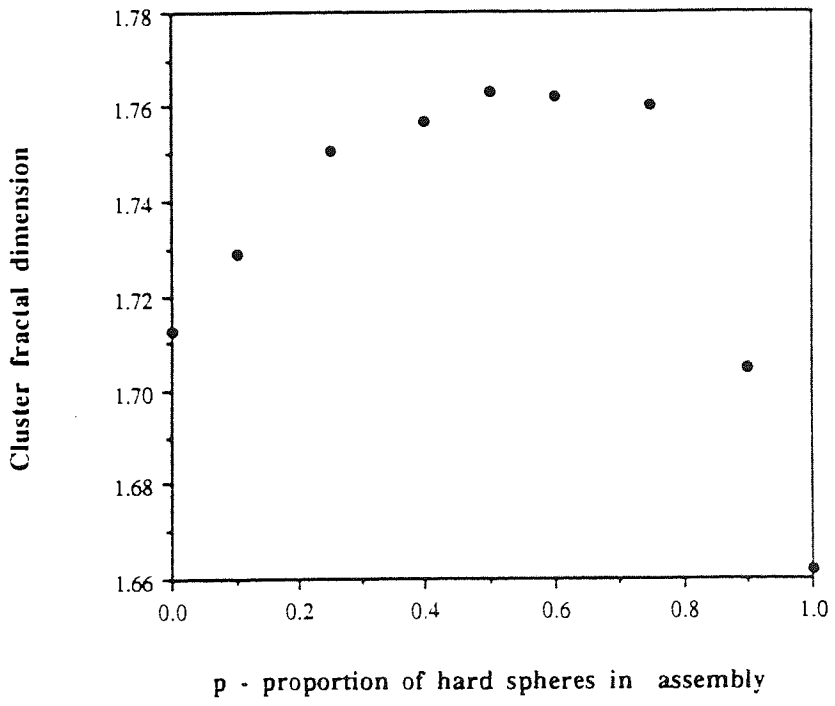

Figure 5.11 Fractal dimension values for the assembly percolating clusters at the geometric percolation threshold.

Plots of the 100% hard and 100% soft assembly percolating clusters (see figures B11 - 14) indicate that a relatively *linear* cluster is observed with the 100% hard assembly but the appearance of the percolating cluster associated with the 100% soft assembly seems to be more consistent with the *blobs-links* model of Stanley (1977) (see section 3.3.2). This blob-links model of the percolating cluster also seems to provide a reasonable accurate portrayal of the random nature of the percolating clusters for other binary assemblies, which are presented in Appendix B. The appreciable contrast in appearance between the percolating clusters for the 75:25 and 100% hard assemblies shown in figures B13 and B14 may provide a reason for the quantitatively significant changes in behaviour observed around p = 0.75, in figure 5.11.

The most important percolation cluster substructure (see section 3.3.2) in terms of the mechanical properties of a particle assembly is the *backbone*, since this represents the 'strongest stresses' network within the assembly. Modifications to the TRUBAL code were made to allow acquisition of the cluster backbone using the *burning* technique (see section 4.9.2) developed by Herrman and Stanley (1984). The backbone for the 50:50 hard:soft assembly at p_e is presented in figure 5.12.

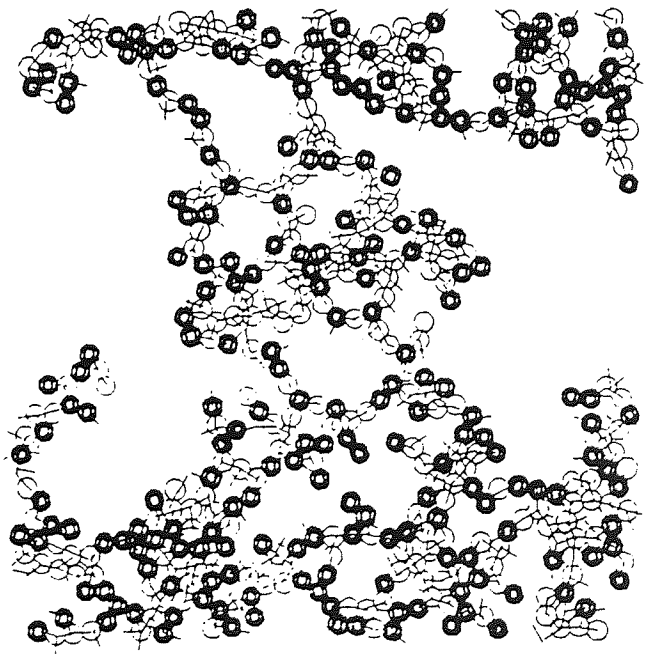

Figure 5.12 Assembly backbone at the elastic percolation threshold for the 50/50 assembly .
[Lines on figure from cluster connection diagram]

The physical size of the backbone for an assembly at p_e, is determined by its fractal dimension value d_f and these values are presented in figure 5.13. Transitions in behaviour around $p = 0.5$ and $p = 0.7$ are observed in this figure, and they may reflect the qualitative changes in behaviour exhibited in figure 5.7. A less *clumped* and more *linear* backbone structure is also observed as the value of p is increased above $p = 0.75$, in the visual evidence presented in Appendix B, figures B15 - B18. Such behaviour does suggest that some kind of physical transition occurs around $p = 0.75$. However, the limited amount of data obtained and the subjective nature of determining a transition point, means that further work is required in this area.

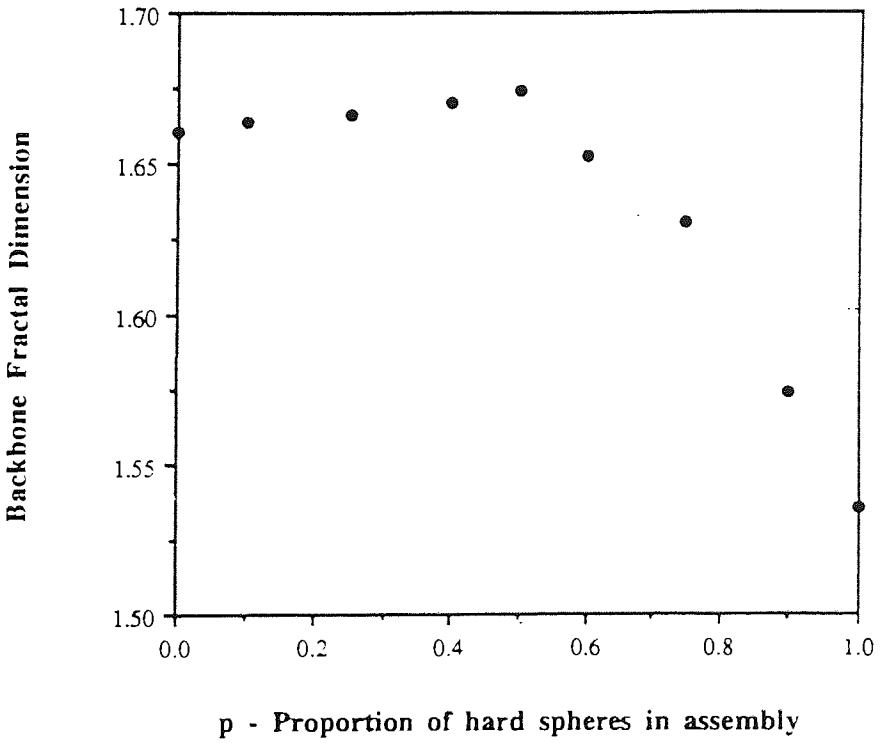

Figure 5.13 Fractal dimensions of assembly backbones at the elastic percolation threshold.

It is not just the fractal dimension of the backbone that is of interest. The composition of the backbone, in terms of particle type, is also useful in a description of the nature of this strongest stressed network within an assembly. Figure 5.14 shows that at p_e., there is a predominance of hard particles in the backbone as the proportion of hard particles p in the assembly is increased. The increasing influence of these hard particles on the stress transmission network above $p = 0.5$ may therefore, be a reason for the observed transition in macroscopic assembly behaviour around this value of p at p_e, discussed earlier in this section.

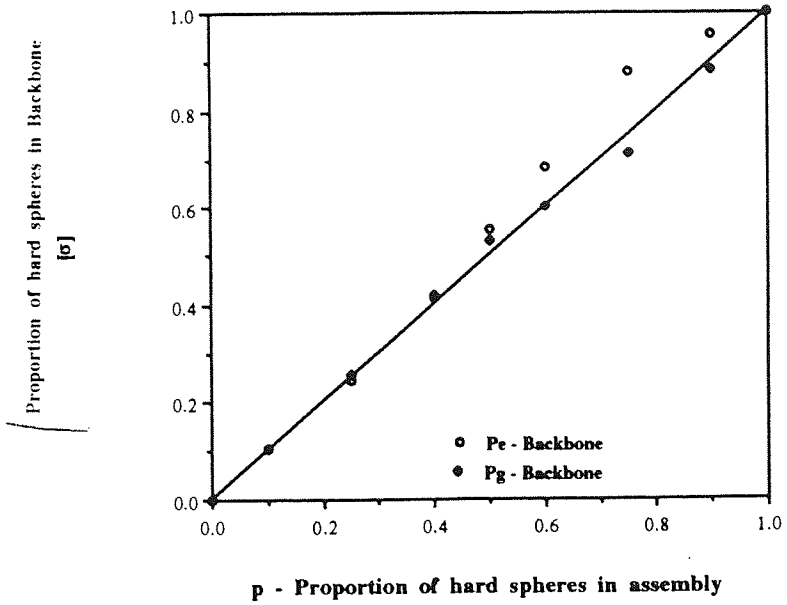

Figure 5.14 Composition of assembly backbones at the geometric and elastic percolation thresholds.

The results presented in figure 5.14 also indicate that the proportion of hard spheres in an assembly backbone at p_g is approximately equal to the proportion of hard spheres in the selected assembly. The behaviour is different to that observed for assemblies at p_e, and suggests that compaction of an assembly must have some the influence on the composition of the backbone structure.

5.3 Quasi-static compaction of 2:1 size ratio assemblies

The effects of changing the size of particles within an assembly, from that of a monodisperse system into a system with a bimodal size ratio, on the behaviour at the geometric and elastic percolation thresholds will be examined in this section. Therefore, consideration will be given to assemblies subject to quasi-static compaction composed of both large hard/small soft and small hard/large soft particles. The 50:50 hard:soft mixture will again be studied and figures 5.15 and 5.16 show the percolating clusters for the 2:1 hard:soft and 2:1 soft:hard size ratio assemblies respectively. The percolating clusters for these assemblies are both formed at the geometric percolation threshold p_g and consist of clumps of particles rather than relatively linear chains.

The stress level associated with p_g for the 2:1 hard:soft size ratio system was σ = 7.402 kPa, which was approximately twice the value of σ = 3.456 kPa for the monodisperse 50:50 system and over four times the stress level of σ = 1.554 kPa determined for the 2:1 soft:hard size ratio system at p_g.

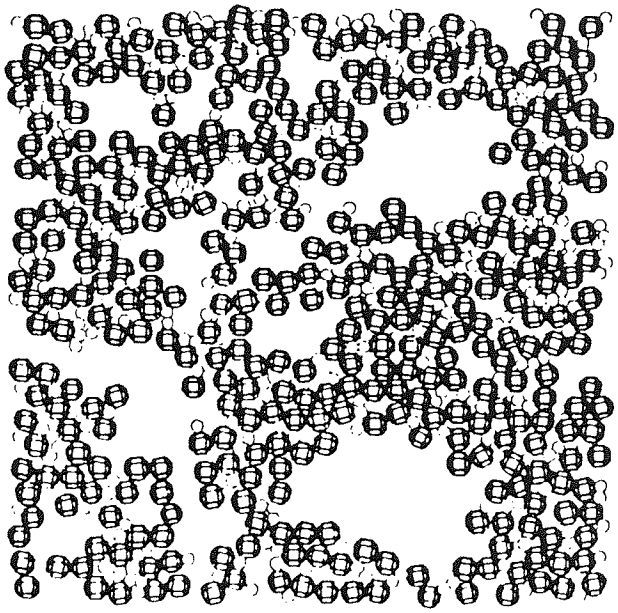

Figure 5.15 Percolating cluster for the 2/1 hard/soft size ratio, 50/50 assembly at the geometric percolation threshold.
[Hard particles ≡ Large circles; Soft particles ≡ small circles]

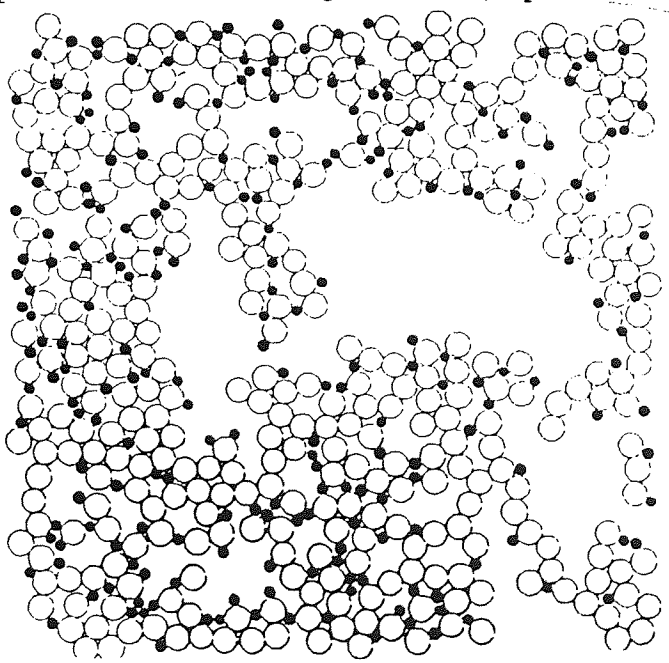

Figure 5.16 Percolating cluster for the 2/1 soft/hard size ratio, 50/50 assembly at the geometric percolation threshold.
[Hard particles ≡ small circles; Soft particles ≡ large circles]

The results presented in figures 5.15 and 5.16 show that soft and hard particles are equally involved in the development of percolating clusters and the presence of a particle size difference within an assembly appears to have a noticeable effect on the attainment of connectivity at p_g.

Once the position of p_g had been determined for the 2:1 size ratio assemblies, quasi-static isotropic compression was performed and stress-strain curves produced with p_g as the origin. The stress-strain curves were then used in the determination of the elastic percolation threshold p_e for the different size ratio assemblies, using the method described in section 5.2. The effect of a difference in particle sizes on the stress level at p_e, was interpreted in terms of a transition in behaviour or by empirical curve-fitting, and details of the procedures used are presented in section 5.2. It can be clearly seen from the curves of stress against the proportion of hard spheres in the assembly p visible in figure 5.17, that a *transition* in behaviour is apparently visible for both bimodal and monodisperse versions of the 50:50 assembly around $p = 0.5$. However, the linear stress scale used in this figure will also affect the subjective positioning of the transition point.

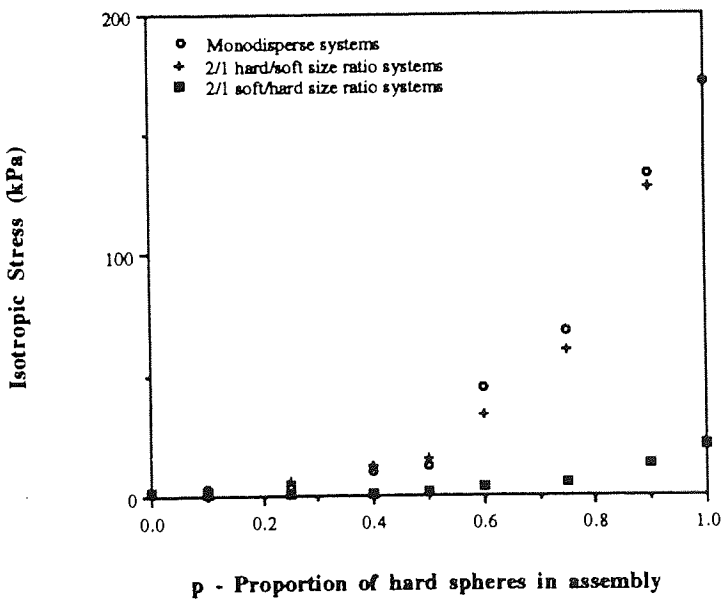

Figure 5.17 Comparison between isotropic stress values at the elastic percolation threshold for the monodisperse and the bimodal assemblies using the idea of a transition in behaviour.

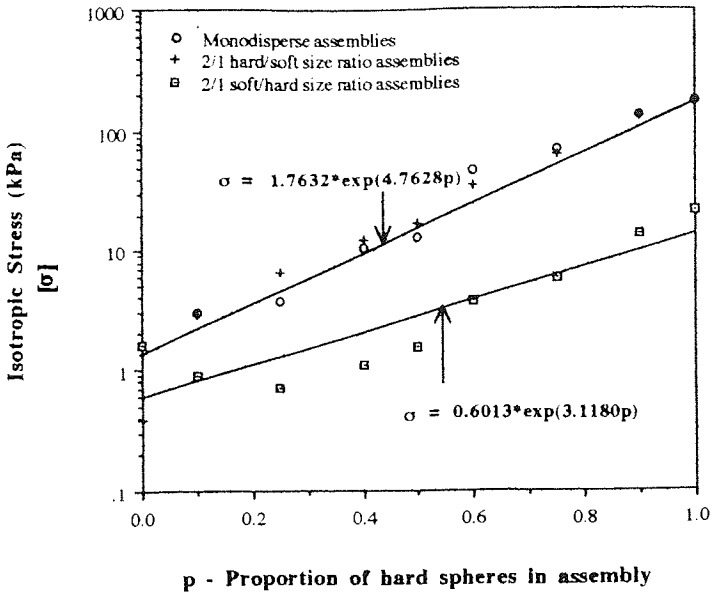

Figure 5.18 Comparison between isotropic stress values at the elastic percolation threshold for the monodisperse and the bimodal assemblies using exponential curve-fitting.

Therefore, it is useful to consider the semi-log figure 5.18, where the exponential best-fit curve for the data from the monodisperse assemblies also provides an acceptable fit to the data obtained from the 2:1 hard:soft size ratio assemblies. However, the simple exponential relationship (5.2) is unable to provide a good fit to the data obtained from the 2:1 soft:hard size ratio assemblies in figure 5.18. It is clear from the evidence presented in both figures 5.17 and 5.18 that the development of rigidity within the 2:1 soft:hard size ratio assemblies is different to that observed for the monodisperse or 2:1 hard:soft size ratio assemblies. The quantitative similarity between the results for the monodisperse and 2:1 hard:soft size ratio assemblies presented in figure 5.18 suggests that differences in particle size alone are not responsible for the behaviour of the 2:1 soft:hard size ratio assemblies. Therefore, the complex, combined effect of compositional and geometric differences between the particles in the 2:1 soft:hard size ratio assemblies must influence the particle-particle interactions and percolation structures within such assemblies and hence their macroscopic behaviour. This point of view will be examined in latter parts of this section, along with a study of the effects of different particle sizes within an assembly, on parameters such as the assembly solid fraction ϕ and the mechanical co-ordination number Z_m.

The relationships between ϕ and p for the bimodal and monodisperse assemblies subject to quasi-static compaction are presented in figure 5.19 and this data indicates that the behaviour of the three types of assembly is qualitatively-different.

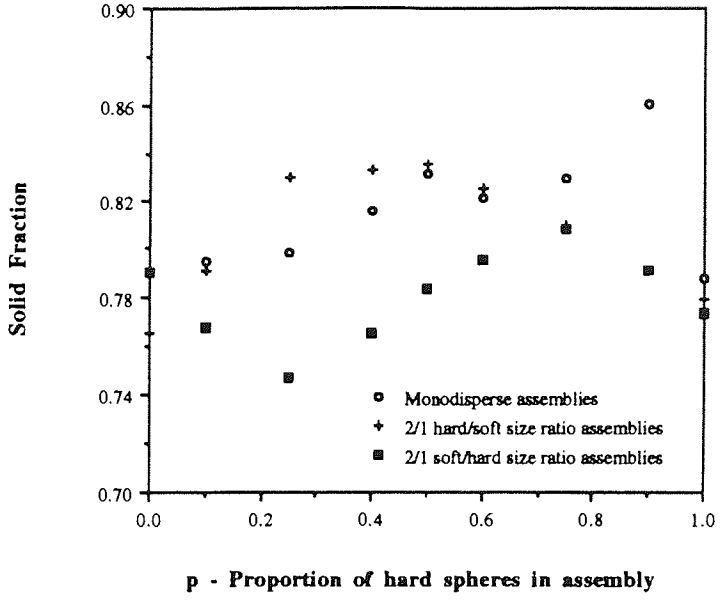

Figure 5.19 The effects of the particle size ratio on the relationship between assembly solid fraction and the proportion of hard spheres in the assembly at the elastic percolation threshold.,

The curve obtained from the 2:1 hard:soft size ratio assemblies shows a rapid increase in the value of ϕ up to $p = 0.25$, a gradual increase in ϕ values in the range between $p = 0.25$ and $p = 0.5$ and then a steady decline in the value of ϕ when $p > 0.5$. The curve for the 2:1 soft:hard size ratio assemblies however, shows a decline in the value of ϕ up to $p = 0.25$, a steady increase in the value of ϕ between $p = 0.25$ and $p = 0.75$ and a decline in the value of ϕ when $p > 0.75$. The results differ from those obtained from the monodisperse assemblies at p_e, which are discussed in more detail in section 5.2. The curves obtained from the bimodal assemblies are complex but generally indicate that denser packing structures are formed, as large particles are initially introduced into a 100% small particle assembly. However, as more large particles are added (i.e. the composition range $p = 0.25$ to $p = 0.75$), the assembly packing structure becomes more complex and less dense, and this produces the lower values of ϕ observed in figure 5.19.

Particle rigidity must play a role in packing structure behaviour, since the introduction of low quantities of small, hard particles to a 100% large, soft particle system has a more noticeable qualitative effect, than the introduction of low quantities of small, soft particles to a 100% large, hard particle assembly. Further work however, needs to be carried out in this area to clarify the situation. Figure 5.20 shows that the curves of Z_m against p for the three different types of assembly also differ qualitatively.

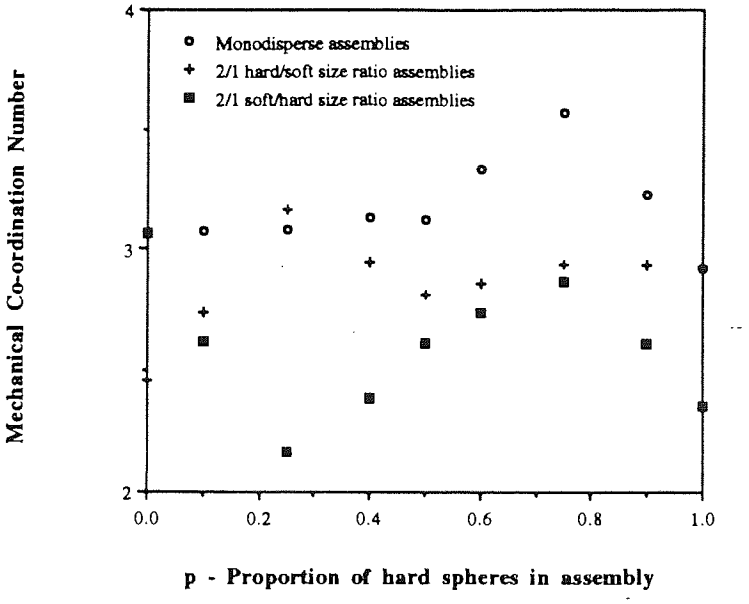

Figure 5.20 The effects of the particle size ratio on the relationship between mechanical co-ordination number and the proportion of hard spheres in the assembly at the elastic percolation threshold.

The curve for the 2:1 hard:soft size ratio assembly in figure 5.20, shows that there is an increase in the value of Z_m when $p < 0.25$, a decrease in the value of Z_m between $p = 0.25$ and $p = 0.5$ and then a gradual increase in the value of Z_m when $p > 0.5$. The curve for the 2:1 soft:hard size ratio assembly however, indicates that the value of Z_m decreases rapidly for $p < 0.25$, increases in value between $p = 0.25$ and $p = 0.75$ and decreases rapidly again, when $p > 0.75$. Therefore, this curve shows almost the reverse of the behaviour exhibited in the curve for the 2:1 hard:soft size ratio assemblies. The Z_m behaviour of the monodisperse assemblies is reviewed in more detail in section 5.2.

Particle rigidity has an important qualitatitive influence on the ϕ and Z_m behaviour of the bimodal assemblies, because the introduction of low quantities of small, hard particles to a 100% large, soft particle system in figures 5.19 and 5.20, has more noticeable qualitative effects, than the introduction of low quantities of small, soft particles to a 100% large, hard particle assembly. Further work however, needs to be carried out in this area, to clarify the situation.

The introduction of assembly compositions with a difference in particle size should also affect microstructural parameters, such as the assembly contact force distribution at p_e.. Figure 5.21 shows the effect of such changes on the contact force distribution for the 50:50 hard:soft mixture, which remains exponential for both of the 2:1 size ratio assemblies studied.

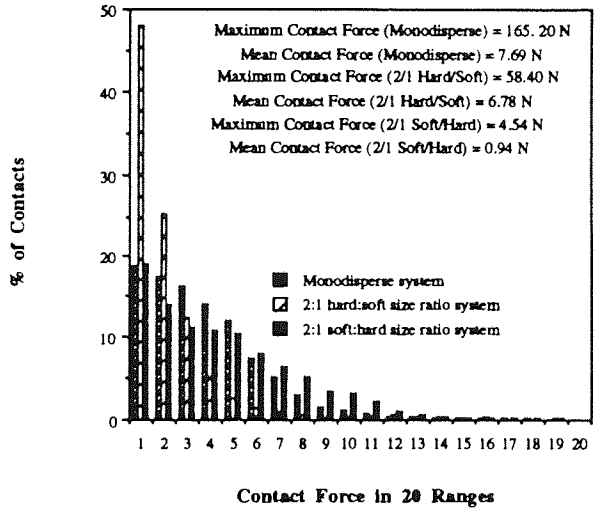

Figure 5.21 The effect of particle size ratio on the contact force distribution for the 50/50 hard/soft assembly at the elastic percolation threshold.

However, further inspection of figure 5.21 indicates that the mean force level for the 2:1 soft:hard size ratio system is much lower than for the other assemblies. Particle rigidity may account for some of this behaviour, but it is also reasonable to assume, that the nature of the force transmission pathways within the assembly at p_e is important. In a similar manner to the contact force behaviour, the presence of bimodal assemblies has little effect on the Gaussian appearance of the contact area and contact pressure distributions for the 50:50 hard:soft mix, which are presented in figures 5.22 and 5.23 respectively.

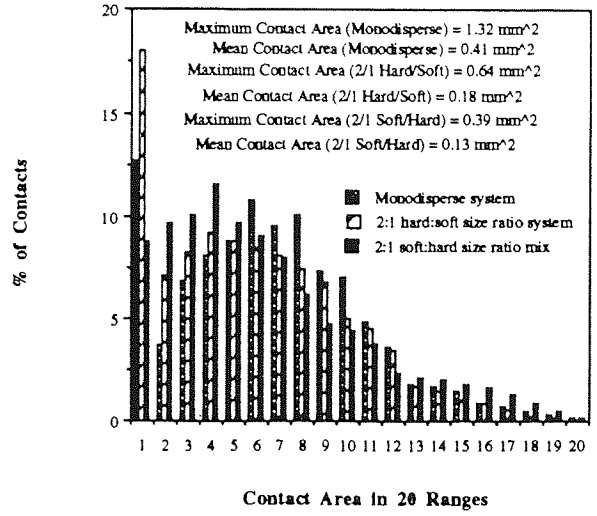

Figure 5.22 The effect of particle size ratio on the contact area distribution for the 50/50 hard/soft assembly at the elastic percolation threshold.'

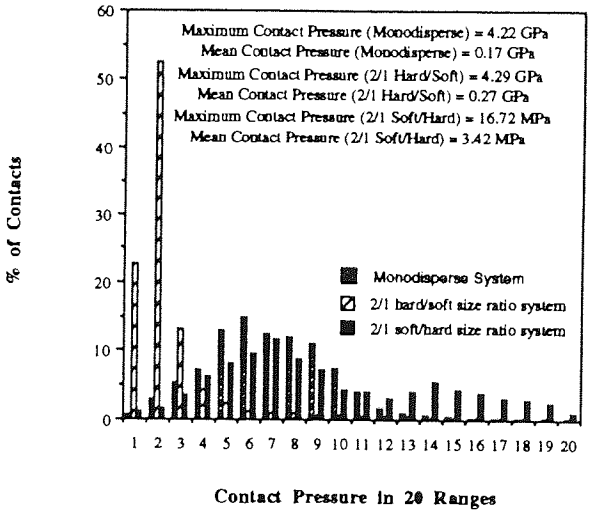

Figure 5.23 The effect of particle size ratio on the contact pressure distribution for the 50/50 hard/soft assembly at the elastic percolation threshold.

The data obtained from the various assemblies however, does differ quantitatively, which suggests that the force transmission pathways and particle contacts, which were first discussed in terms of the contact force distribution behaviour in figure 5.21, are important in this context.

The effects of a particle size ratio within an assembly, could also influence percolation parameters such as the fractal dimension d_f of the percolating cluster at the geometric percolation threshold p_g The value of d_f is calculated for the 2:1 hard:soft size ratio and 2:1 soft:hard size ratio assemblies using an average particle radius in (5.6) and is presented in figure 5.24. From the evidence of this figure, qualitative differences in behaviour between the bimodal and the monodisperse assemblies, which were first observed for microstructural characteristics, also seem to affect percolation-based parameters. The curve for the 2:1 hard:soft size ratio assemblies shows that, the value of d_f increases with p until $p = 0.75$ and this is followed by a rapid decline in the value of d_f, when $p > 0.75$. The behaviour is qualitatively similar to that observed for the monodisperse assemblies in the same figure and suggests that the development process for the percolating clusters in both systems may be similar.

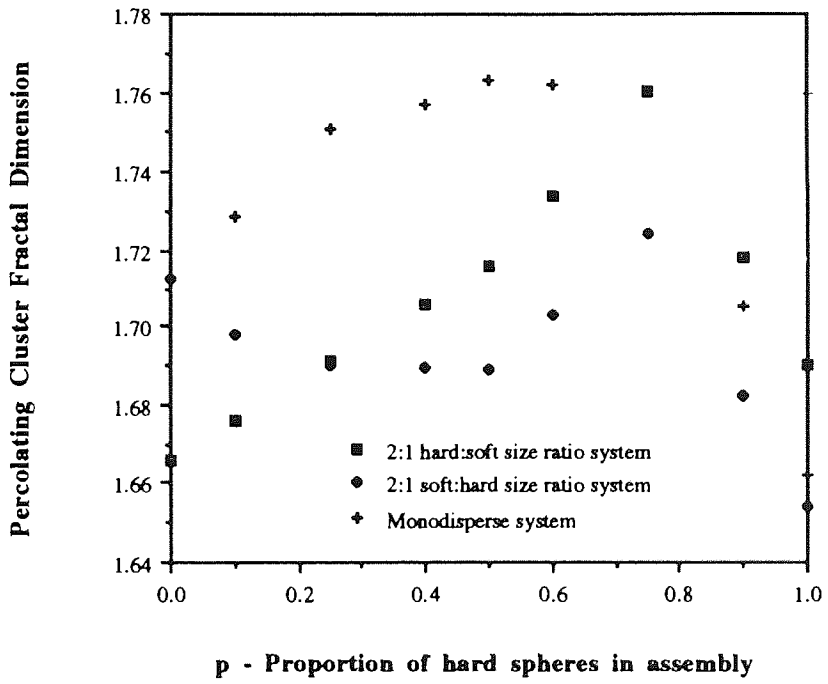

Figure 5.24 Effect of particle size ratio on the fractal dimension values for the percolating clusters at the geometric percolation threshold.

The qualitative behaviour of the 2:1 soft:hard size ratio assemblies is different to that observed for the other types of assembly and this therefore, suggests that the development of percolating clusters is also peculiar to these assemblies.

The differences in qualitative behaviour are illustrated by the curve for the assemblies in figure 5.24, which shows that the value of d_f is reduced for $p < 0.5$, followed by an increase in the value of d_f between $p = 0.5$ and $p = 0.75$ and a sharp reduction in the value of d_f for $p > 0.75$.

The cluster backbone at p_e for the size ratio assemblies was determined in a similar manner to that discussed in section 5.2 for the monodisperse assemblies. Figure 5.25 illustrates the values of the backbone fractal dimension D_B calculated for both the size ratio and monodisperse assemblies using (5.6). One important observation from the figure is that qualitatively-similar curves are obtained from both the monodisperse and 2:1 hard:soft size ratio systems.

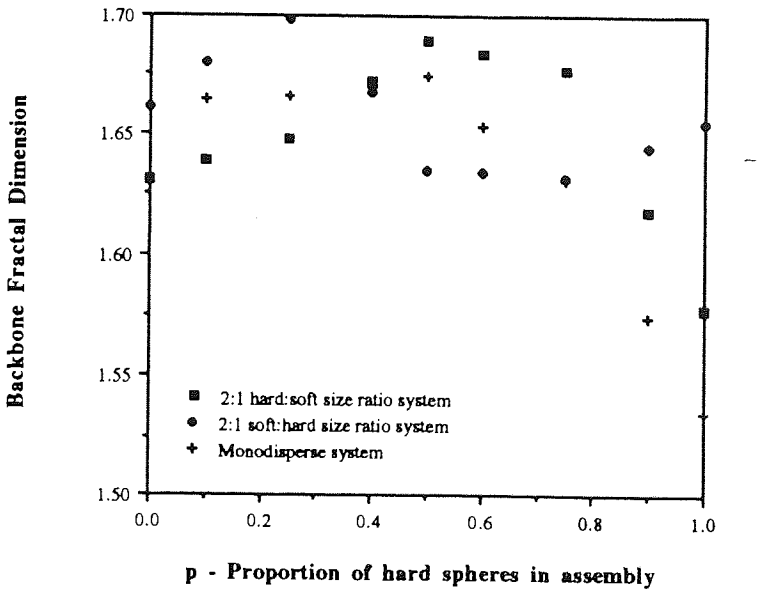

Figure 5.25 Effect of particle size ratio on the fractal dimension values for the assembly backbones at the elastic percolation threshold,

Therefore, both of these curves have a positive gradient for $p < 0.5$ and a negative gradient for $p > 0.5$. The presence of such a transition point around $p = 0.5$ may be responsible for the transition in stress-strain behaviour observed in figure 5.17. The differences in qualitative behaviour between the 2:1 soft:hard size ratio assemblies and the other assembly types observed in figure 5.25, may also account for the different curve fits required for the stress-strain data presented in figure 5.18.

Further evidence of the importance of assembly backbone characteristics on macroscopic behaviour is presented in figure 5.26, where the composition of the assembly backbone for both the bimodal and monodisperse assemblies is plotted against the composition of the assembly.

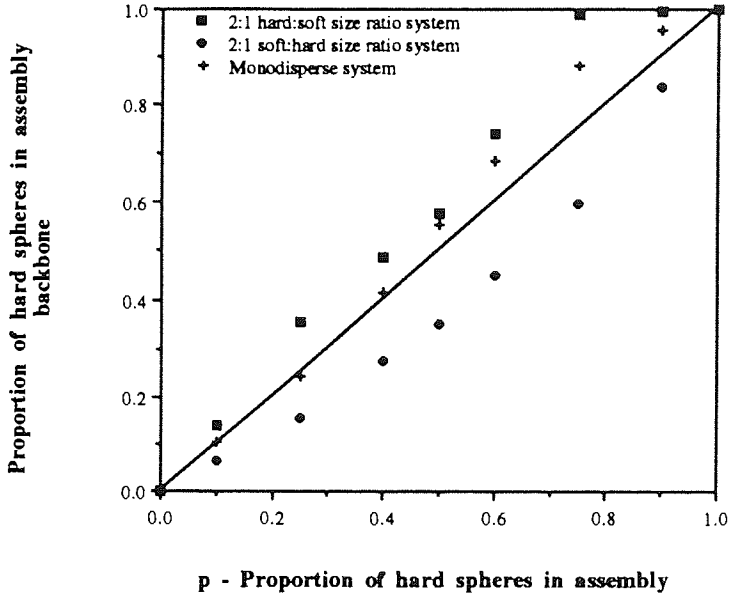

Figure 5.26 Effect of the particle size ratio on the relationship between the proportion of hard spheres in the assembly backbone and the proportion of hard spheres in the assembly at the elastic percolation threshold.

The curve for the 2:1 soft:hard size ratio assemblies presented in figure 5.26, shows that soft particles are quantitatively the most important particle type in the assembly backbones. These results are the opposite of those obtained from the 2:1 hard:soft size ratio assemblies in figure 5.26, where hard particles are quantitatively the most important components of the assembly backbones. Therefore, these results appear to indicate that the assembly backbone will try to avoid using the small particles in the assembly for force transmission. The differences in backbone composition between the two types of bimodal assembly with the same composition, will also affect macroscopic parameters such as the assembly stress tensor, because the rigidity of the particles in the backbone will also influence the magnitude of the forces being carried by the backbone.

5.4 Three-dimensional quasi-static compression

The use of three-dimensional assemblies in simulation work should provide a more accurate picture of the behaviour of real particle assemblies, which are always three-dimensional entities. The simulation work performed on three-dimensional assemblies is presented in more detail in chapter 8. The procedure for identifying the geometric percolation threshold p_g for such assemblies is more complicated than that used for two-dimensional assemblies (see section 5.2). Major difficulties arise in accurately determining p_g in three-dimensions, since connectivity of the percolating cluster at this point must be confirmed across all three co-ordinate dimensions of the solution cell i.e. the x-, y- and z- directions. In order to identify when geometric percolation occurs, cross-sections through the assembly were produced using the graphics routines of the TRUBAL code. The premise is that if the largest particle cluster observed using the **PLOt CLUster** command line (see Appendix A), at a particular point during compaction, is visible on all cross-sections, then it is assumed to be percolating. Figure 5.27 helps to illustrate the procedure adopted in specifying p_g (see section 4.6).The planes shown in figure 5.27 are only examples of those taken along the x-axis of the periodic cell (for clarity). The determination of p_g in three-dimensions also requires sections to be taken along the y- and z-axis of the periodic cell.

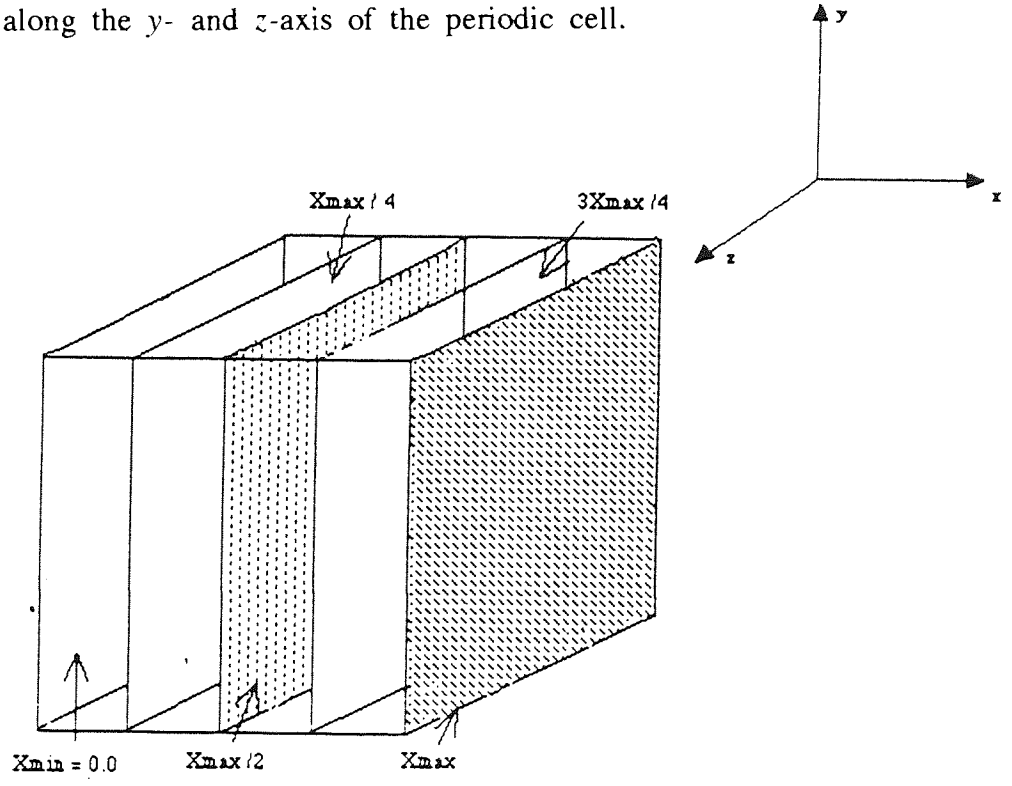

Figure 5.27 Cross-sections of the periodic cell used in the determination of the geometric percolation threshold for a three-dimensional assembly.

The *percolating* cluster detected using this method for the three-dimensional 50:50 mixture is illustrated in figure 5.28. A section from this cluster, taken at the x_{min} plane of the assembly periodic cell is presented in figure 5.29. The other sections used to determine that a percolating cluster was first detectable in the 50:50 mixture at this point, are presented in Appendix B.

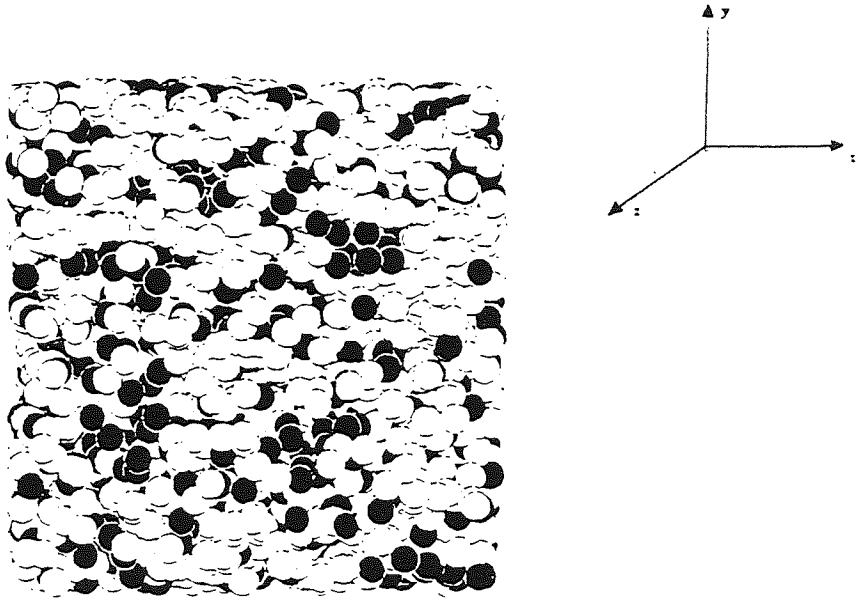

Figure 5.28 The three-dimensional 50/50 assembly at the geometric percolation threshold.

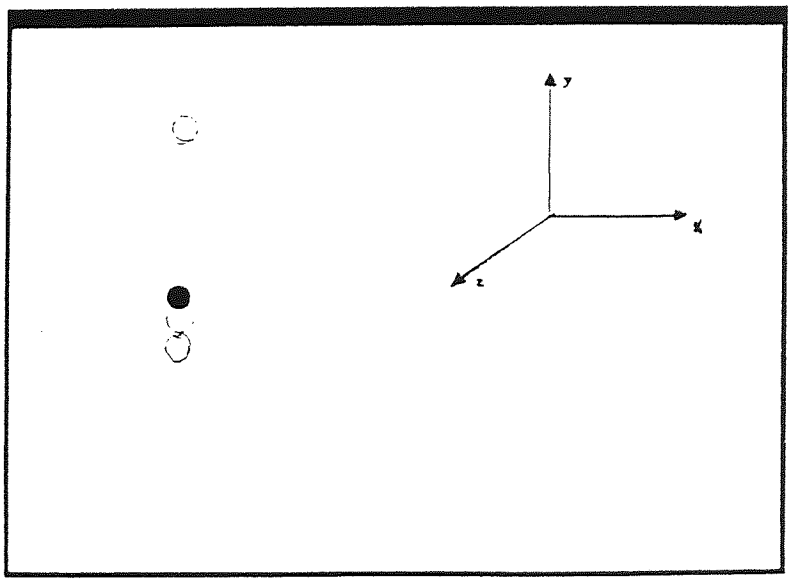

Figure 5.29 Cross-section taken at x_{min} for the three-dimensional 50/50 assembly at the geometric percolation threshold.

Having determined p_g, quasi-static isotropic compression was then applied to the assemblies and a stress strain curve produced with its origin at p_g. The value of p_e for the assemblies was determined from these graphs by detection of the point at which appreciable lattice rigidity was first developed i.e. when a rapid increase in the gradient of the stress-strain curve appeared (see figure 5.30). Further examples of the detection of p_e for various three-dimensional assemblies are presented in Appendix B, figures B27 - B30.

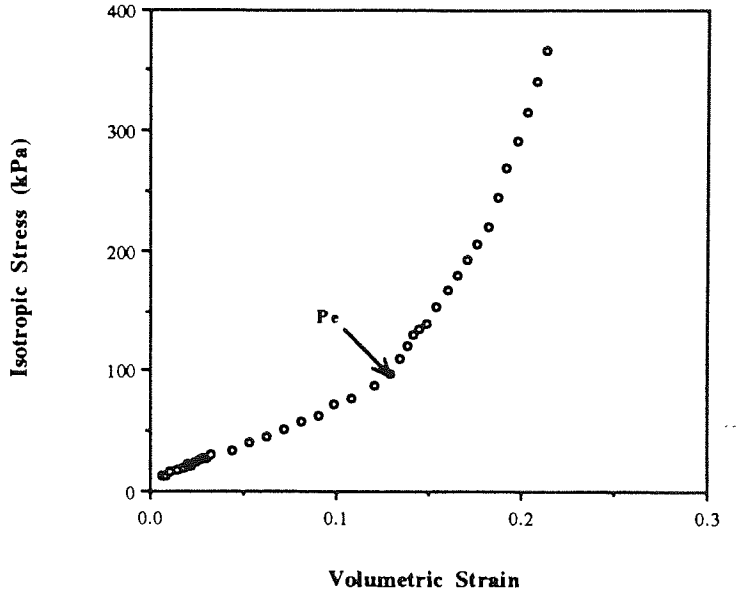

Figure 5.30 Identification of the elastic percolation threshold for the three-dimensional 50/50 assembly

The stress levels associated with the onset of p_e for the three-dimensional assemblies were determined using the **PRInt STResses** command line of the TRUBAL code (see Appendix A). The presence of a transition in behaviour or the use of empirical curve-fitting, which were first considered in the interpretation of the stress level behaviour of the two-dimensional assemblies in section 5.2, can also be used in the interpretation of the stress level behaviour of three-dimensional assemblies. The stress level results plotted against the proportion of hard spheres in the assembly p for the two- and three-dimensional assemblies are presented in figure 5.31. If the idea of a transition in behaviour is used in the interpretation of this figure, then two transition points are observed for the data obtained from the three-dimensional assemblies. The first transition point is around $p = 0.4$ and the second is around $p = 0.75$, and this behaviour contrasts with the solitary transition point observed for the two-dimensional assembly data at $p = 0.5$.

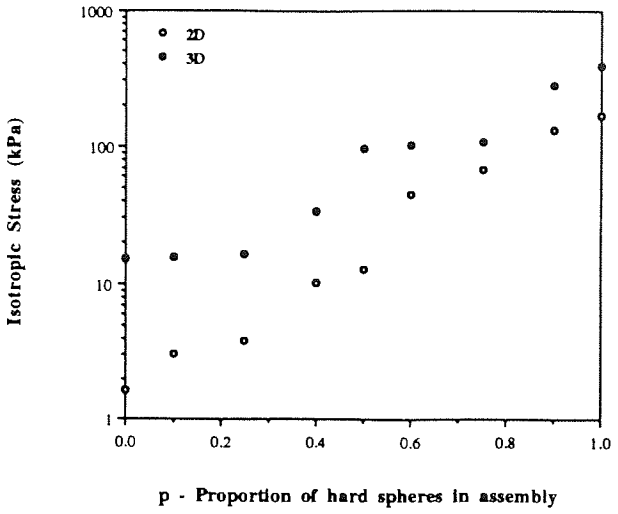

Figure 5.31 The effect of assembly dimensionality on the relationship between the stress level at the elastic percolation threshold and the proportion of hard spheres in the assembly, interpreted in terms of a transition in behaviour.

The limited amount of data presented in figure 5.31 however, indicates that further simulation work is required to accurately determine the position of such transition points. If the less subjective process of curve-fitting is used in the interpretation of the data presented in figure 5.30, then the semi-log plot of figure 5.32 can also be considered.

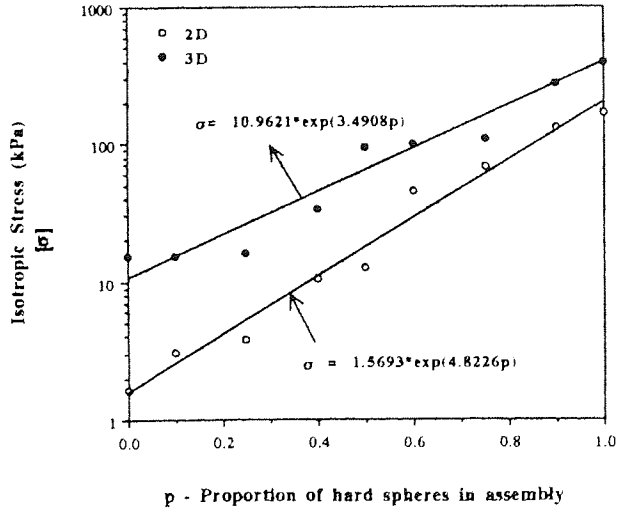

Figure 5.32 The effect of assembly dimensionality on the relationship between the stress level at the elastic percolation threshold and the proportion of hard spheres in the assembly, interpreted by exponential curve fitting.

Exponential curves were able to provide the best fits to the data obtained from the two- and three-dimensional assemblies in this figure. However, the curves for the two sets of data have different gradients, with the data from the three-dimensional assemblies requiring a curve with a shallower gradient. If (5.4) is used in the interpretation of these curves, then it is found that the shallower gradient for the three-dimensional data represents a smaller ratio between the stress levels at p_e for the 100% hard and 100% soft assemblies. The greater degrees of freedom associated with three-dimensional assemblies may help to explain why such differences in assembly composition, have less effect on the stress level required for assembly rigidity.

The idea of a transition in behaviour at p_e, as the value of p is changed, can also be used in the interpretation of the solid fraction ϕ and mechanical co-ordination number Z_m curves for the three-dimensional assemblies, which are presented in figure 5.33.

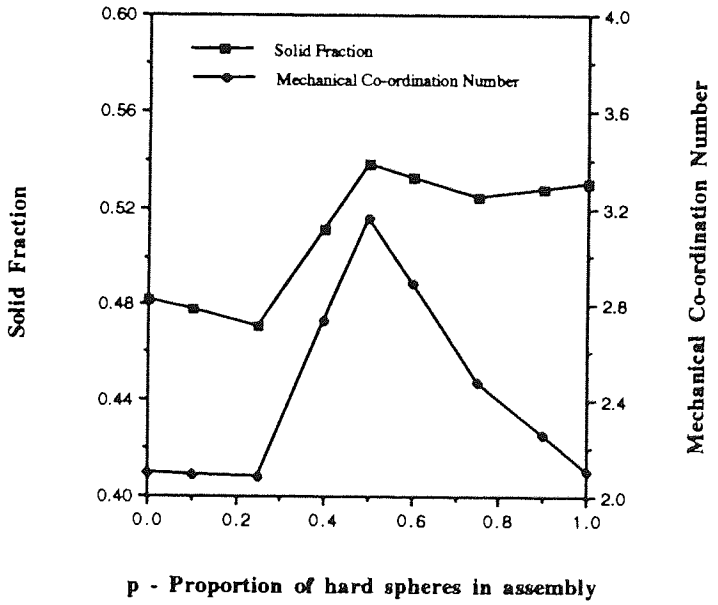

Figure 5.33 The solid fraction and mechanical co-ordination number behaviour of the three-dimensional assemblies at the elastic percolation threshold.

Both of the curves visible in figure 5.33 have the same qualitative behaviour, because there are two distinct transition points around $p = 0.25$ and $p = 0.5$. The transition point around $p = 0.5$ suggests that three-dimensional assemblies which have the densest, packing and particle force-carrying structures, will have an approximately equal composition of hard and soft spheres.

However, a limited amount of data is used in the determination of such transition points and the positions of the transition points for two-dimensional assemblies, which are presented in figures 5.6 and 5.7, are different. Therefore, more precise positioning of such transition points is required for clarification of the situation.

The microstructural behaviour of the three-dimensional assemblies at p_e, can be interpreted from the particle contact force, contact area and contact pressure distributions obtained from the same assemblies. A similar approach is used for the two-dimensional assemblies reviewed in section 5.2, which suggests that it is useful to compare the contact information distributions obtained from the two- and three-dimensional assemblies. Therefore in this section, the distributions obtained from the two- and three-dimensional versions of the 50:50 assembly will be used as the examples for this interpretative procedure. Figure 5.34 shows that the contact force distributions for the two- and three-dimensional assemblies at p_e are both exponential in form. Further investigation of this figure however, indicates that lower mean contact forces develop between the particles in the three-dimensional assembly.

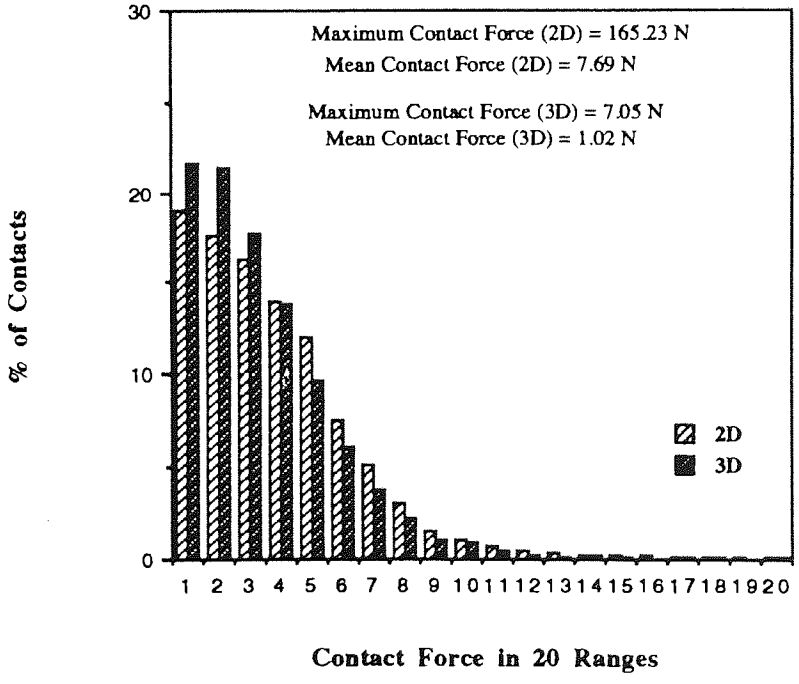

Figure 5.34 Contact force distributions at the elastic percolation threshold for the two- and three-dimensional versions of the 50/50 assembly.

The greater degrees of freedom available to the particles in the three-dimensional assembly (c.f. the particles in the two-dimensional assembly) would permit such low particle contact forces at p_e, because a large number of force transmission pathways would be available within this assembly to transfer the applied load. The contact area distributions for the two- and three-dimensional versions of the 50:50 assembly, which are presented in figure 5.35, are both Gaussian in form and Gaussian contact pressure distributions for the same assemblies, are also observed in figure 5.36.

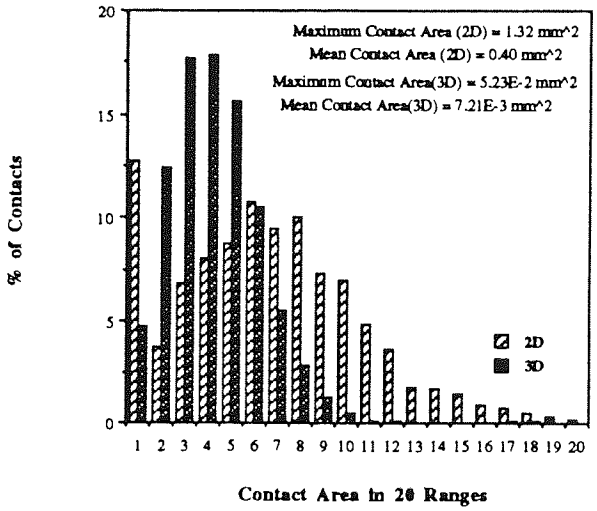

Figure 5.35 Contact area distributions at the elastic percolation threshold for the two- and three-dimensional versions of the 50/50 assembly .

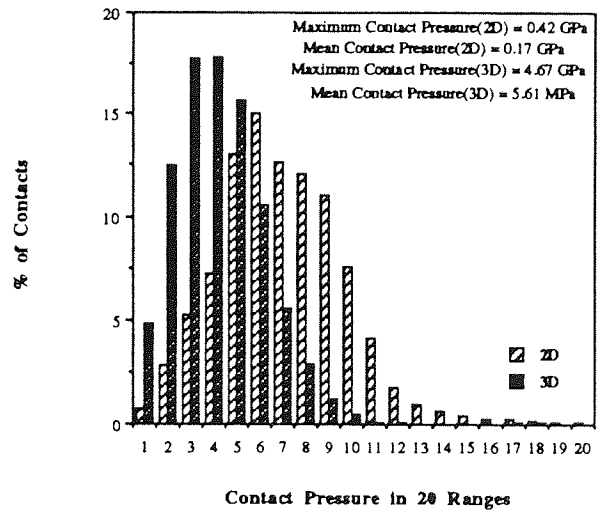

Figure 5.36 Contact pressure distributions at the elastic percolation threshold for the two- and three-dimensional versions of the 50/50 assembly .

The quantitative differences between the results obtained from the two- and three-dimensional versions of the 50:50 assembly in figures 5.35 and 5.36, are probably caused by the different internal force transmission networks within the two types of assembly, which was discussed earlier.

The fractal dimension d_f of the percolating cluster at p_g for a three-dimensional assembly, is determined by the use of three-dimensional parameters in (5.6). The maximum value for d_f in three-dimensions would therefore, be $d_f = 3.00$, since this would represent complete spatial occupation of the simulation periodic cell by a cluster. Figure 5.37 shows how the value of d_f for the two- and three-dimensional assemblies at p_g, varies with the assembly composition p. Sharp transition points in behaviour are observed at $p = 0.25$, $p = 0.5$ and $p = 0.75$ for the three-dimensional assemblies in this figure and these results contrast strongly with the relatively minor changes in behaviour observed for the two-dimensional assemblies with the same composition. The greater degrees of freedom associated with the particles in a three-dimensional simulation assembly, are responsible for these quantitative differences with the two-dimensional particle systems. The differences in the d_f value at p_e, between the assemblies with different values of p, would be more marked in the relatively open, three-dimensional systems.

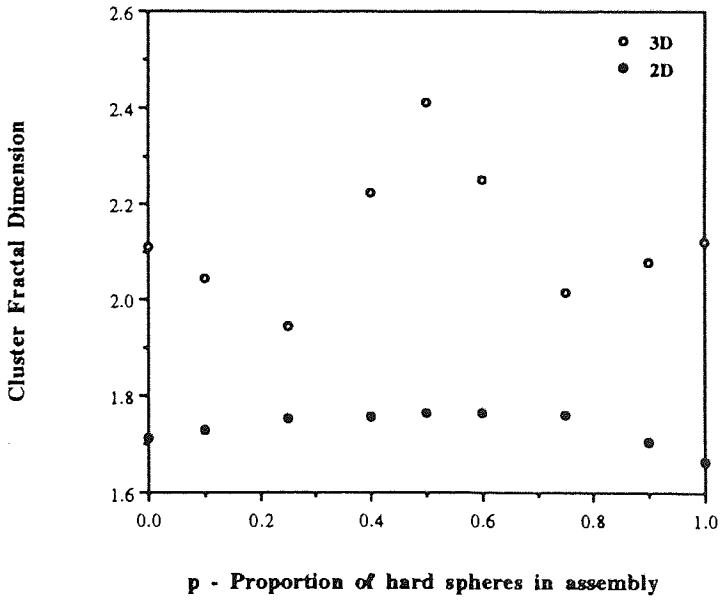

Figure 5.37 The effect of assembly dimensionality on the value of the fractal dimension of the percolating cluster for an assembly at the geometric percolation threshold.

The sectioning technique presented earlier in this section, can also be used as an aid in determining the fractal dimension of the cluster backbone D_B for the three-dimensional assemblies. The assembly backbone was determined using the burning technique (see section 5.1) and confirmed by viewing slices of the backbone across the three co-ordinate axis of the periodic cell containing the assembly. One view of the complete backbone for the three-dimensional 50:50 assembly is presented in figure 5.38.

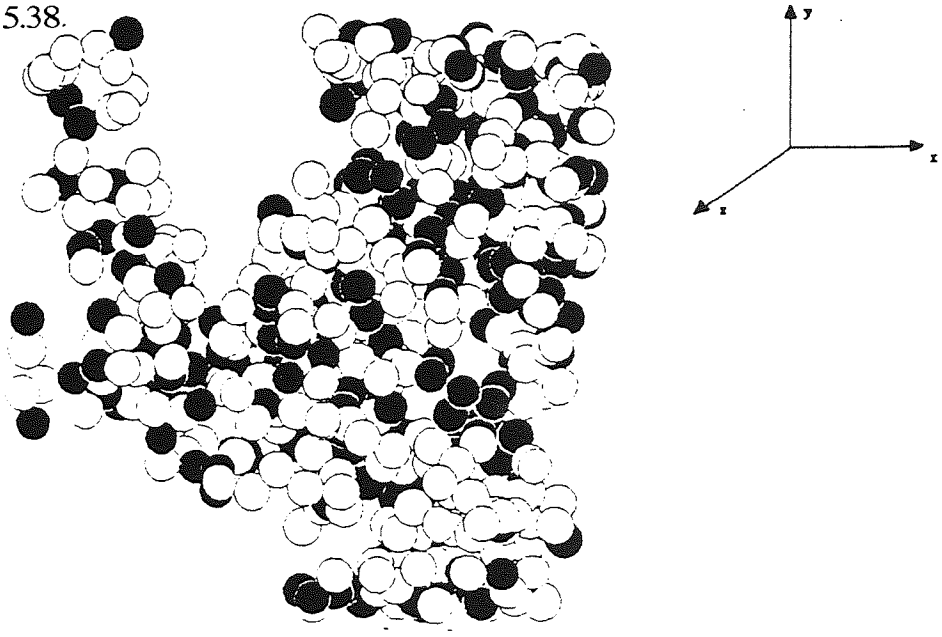

Figure 5.38 Assembly backbone at the elastic percolation threshold for the three-dimensional 50/50 assembly.

The effects of assembly composition on the values of D_B for the two- and three-dimensional assemblies at p_e, are presented in figure 5.39.

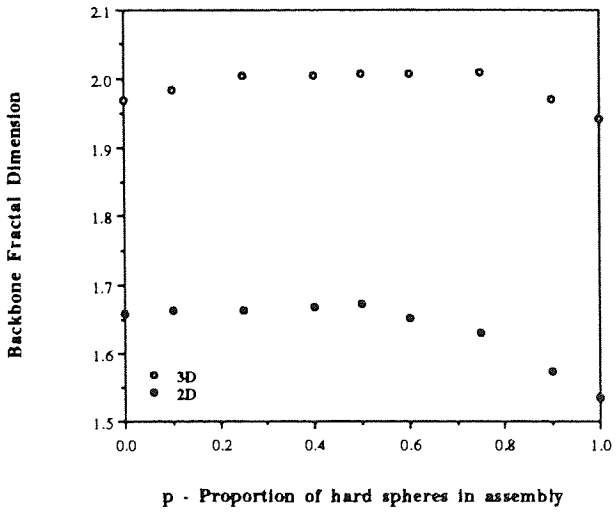

Figure 5.39 Effect of assembly dimensionality on the relationship between the backbone fractal dimension and the proportion of hard spheres in the assembly at the elastic percolation threshold

Qualitatively-similar behaviour, which can be generalised as a gradual increase in D_B values until $p = 0.5$, followed by a gradual decrease in D_B values when $p > 0.5$, is observed for both sets of data in figure 5.39. Therefore, from the evidence of figure 5.39, it appears to be a reasonable suggestion that, similar processes are responsible for the development of the assembly backbones at p_e in both two- and three-dimensions.

In figure 5.40, the backbone composition at p_e is compared with the assembly composition, for the two- and three-dimensional assemblies subject to quasi-static compaction. Only small quantitative differences are observed between these two compositions for the three-dimensional assemblies in the figure and the results suggest that in three-dimensional assemblies, backbone composition may be of lesser importance in determining macroscopic mechanical properties.

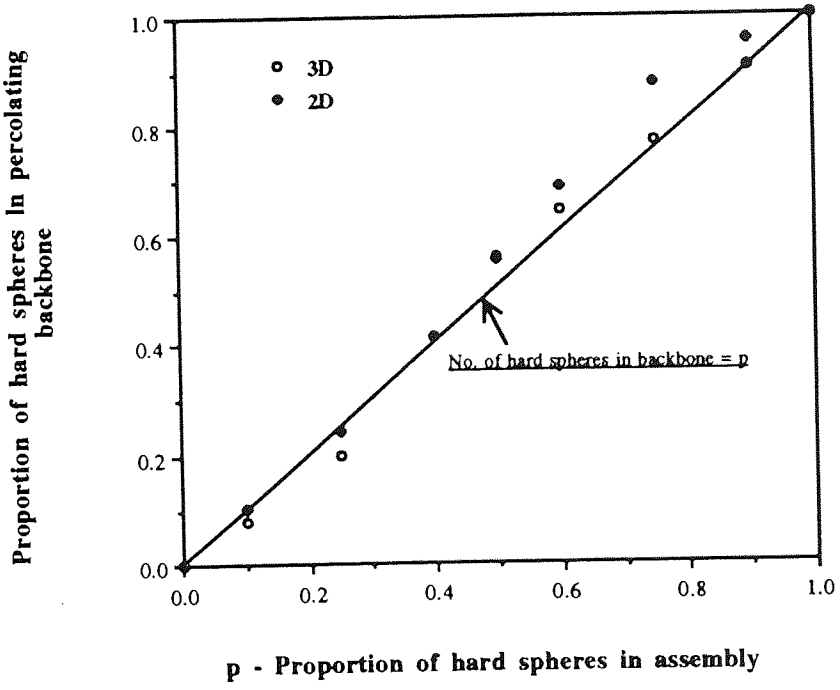

Figure 5.40 The relationship between assembly composition and backbone composition for the three-dimensional assemblies at the elastic percolation threshold.

5.5 Summary

In this chapter, the use of percolation 'thresholds' as ground states for mechanical measurement was considered. Therefore, the macroscopic, microstructural and percolation-based behaviour of both two- and three-dimensional assemblies at the elastic percolation threshold p_e was studied, to allow further consideration of such ground states.

The macroscopic stress-strain behaviour of the two- and three-dimensional assemblies at p_e was found to be adequately described by both the idea of a physical transition point and by a simple exponential relationship. It was also shown that the parameters of the exponential relationships were sensitive to the assembly composition. The behaviour of parameters which were general descriptors of the structure of an assembly, like solid fraction ϕ and mechanical co-ordination number Z_m was considered. The results of the simulation experiments indicated that the values of such parameters at p_e were also composition-sensitive.

The development of micromechanical characteristics such as particle contact force, area and pressure at p_e was studied. It was shown that the contact force distribution for all the assemblies examined was exponential, indicating that only a small number of particles in the assemblies carried large forces. The form of the contact area and contact pressure distributions for the same assemblies however, was more complex, because the contribution from the various types of particle contacts e.g. hard-soft particle contacts was significant.

The nature of important percolation-based parameters such as the cluster fractal dimension d_f at p_e, which describes the spatial occupation of the percolating cluster, was also examined. The behaviour of both d_f and the cluster *backbone*, which is closely related to the strongest forces network within an assembly, was found to be sensitive to both assembly and particle cluster composition.

It is important to remember that for statistical accuracy a large number of simulation experiments need to be performed. This was a more straightforward process for the majority of workers presented in chapter 3, because they only had to study relatively simple elastic lattice systems. Further simulation work is therefore, an important area of future work. The limited quantitative information presented in this chapter however, does not prevent a useful qualitative interpretation of particle assembly behaviour at p_e to be performed.

Chapter 6

Two-dimensional quasi-static compaction

6.1 Introduction

In this chapter, results of computer simulated, quasi-static isotropic compression of two-dimensional assemblies of binary mixtures are reported. The binary nature is due to the contrast in physical properties between the hard (steel) particles and soft (rubber) particles which composed the assemblies. The effect of mixture composition (expressed as the proportion of hard spheres) is examined in terms of both macroscopic and microscopic data. In this way, additional understanding of the mechanical behaviour of binary mixtures may be obtained.

The number of simulations carried out, one for each of the eleven generated particle assemblies, may appear to be limited; especially when compared with the number of experimental tests that are usually performed on photoelastic disc assemblies, Travers *et al* (1986,1987 and 1989), Oger *et al* (1991). However, unlike such physical testing, all microscopic quantities such as interparticle contact forces are easily accessed and many test reference states can be archived for future re-examination.

6.2 Particle specifications and simulation procedures

All the two-dimensional assemblies were composed of 1000 particles. The number of spheres within the test assembly is directly proportional to the execution time of the program and this influenced the decision to select 1000 particles as the optimum assembly size. Two dimensional simulations performed by Barnes (1985) indicated that an assembly of this size provides sufficient data for statistical analysis of the results.

Davis and Deresiewicz (1977) conducted physical disc tests from which they showed that, if only one particle size is used, large regular regions develop during compaction. In order to avoid the formation of regular packed domains, five different particle sizes were used in the simulated experiments (see figure 6.1). The mean particle radius of 2.0 mm was originally chosen to allow comparison of results with the photoelastic assemblies of Travers *et al* (1986, 1987 and 1989), Oger *et al* (1991) and Troadec *et al* (1991).

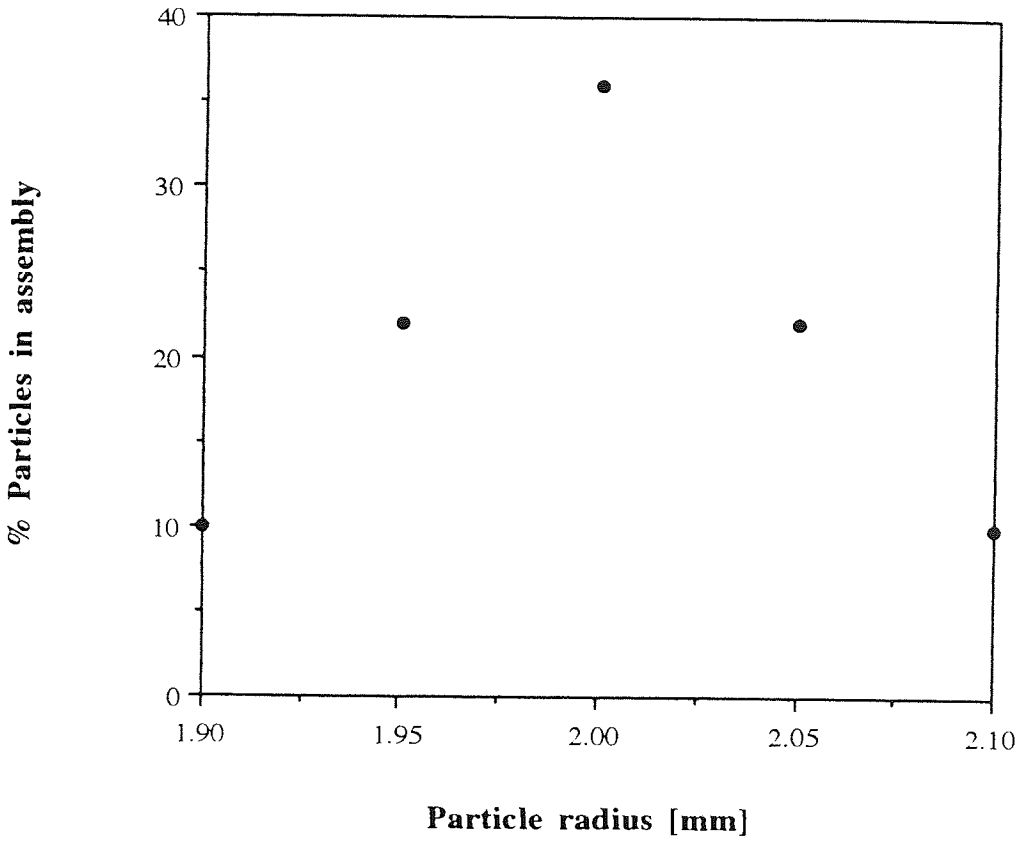

Figure 6.1 Particle size distribution for a two-dimensional simulation assembly.;

Other parameters required to specify the particle properties were obtained from standard engineering data (Anderson et al, 1985) and are listed in table 6.1.

Property	Hard (Steel)	Soft (Rubber)
Young's Modulus (E)	200 GPa	0.1 GPa
Density (ρ)	[7.8E3] / {7.8E21} kg/m^3	[8.5E2] / {8.5E20} kg/m^3
Coefficient of friction (μ)	0.3	0.3
Poisson's ratio (ν)	0.35	0.35

Table 6.1 Properties of assembly particles.;
[ ] - Specified values { } - Density-scaled values.

For all the tests reported in this chapter, the simulation procedures were as follows. One thousand particles were generated at random locations in a periodic cell (16 cm by 16 cm). Particles with the largest radius were generated first, for both hard and soft particle types, before the next largest particle radius set was considered. The solid fraction, at generation, was 0.476 for all the tests reported in this chapter. Figure 6.2 illustrates an example of a two-dimensional assembly at generation.

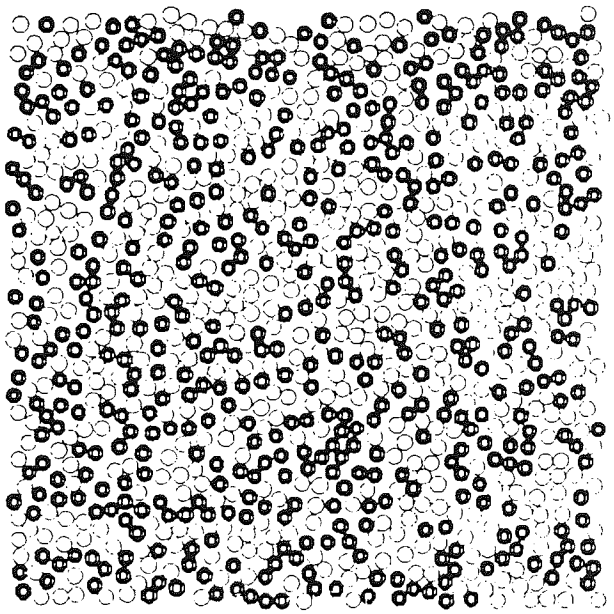

Figure 6.2 Two-dimensional 50/50 hard:soft particle assembly at generation.; [Dark circles = hard particles]

After generation, assemblies were subjected to isotropic compression using a strain rate of $\dot{\varepsilon} = 1.0E\text{-}7$ until the geometric percolation threshold p_g was identified by continuous monitoring of the assembly connection diagram (see chapter 5). Isotropic compression then continued at the same strain rate until the stress-strain curve indicated that the elastic percolation threshold had been reached. The numerical servocontrol was then activated (see section 4.8.2) to maintain the isotropic state of stress associated with the elastic percolation threshold and allow the assembly to relax to an approximate equilibrium condition.

Isotropic compression was continued by raising the stress level increments using the numerical servocontrol, up to a stress level of 1.0 MPa. At each stress level, at least 50,000 calculation cycles were specified to ensure a near equilibrium state prior to applying the next stress increment. The binary datafiles associated with each stress level were saved for later post-processing analysis (see chapter 4).

A number of physical control parameters had to be specified before the compaction of a generated assembly could proceed. A suitable damping constant (see section 4.7) was specified by the **DAMping** TRUBAL command line (see Appendix A).The damping constant specified for all the simulation experiments was 0.05. No global damping was employed (see section 4.7). The fraction of the critical timestep Δt_f that was required between calculation cycles (see section 4.6) was specified by the **FRAction** TRUBAL command line (see Appendix A). In order to carry out tests as quickly as possible by maximising the real-time rate of deformation, it was desirable to increase the calculation cycle timestep. Constraints however, have to be employed to obtain accurate and meaningful results. A value of $\Delta t_f = 0.05$ was therefore used in the simulation experiments, which ensured that the simulation assemblies did not become numerically unstable or deviate excessively from equilibrium (see section 4.6). The use of particle density-scaling (section 4.6) was also incorporated in these quasi-static simulation experiments to allow more rapid completion of simulation tests.

6.3 Macroscopic assembly behaviour

It was mentioned in chapter 2 that the stiffness, strength and volume change (volumetric strain) are the three basic features of granular media constitutive models. The results obtained from the quasi-static simulation experiments on the binary assemblies, and selected for display here, are designed to indicate how these macroscopic assembly features vary during the simulation of the isotropic compaction process up to 1.0 MPa. Therefore, the stress-strain behaviour and the evolution of the solid fraction, contact density and co-ordination numbers are considered.

6.3.1 Stress-strain behaviour

The stress-strain behaviour obtained from the quasi-static isotropic compression simulations is illustrated in figure 6.3 in the form of a double logarithmic plot of stress against strain. It can be seen that, for all mixture compositions, the curves tend to a constant gradient of 3/2 in the latter stages of compression. This value of 3/2 is also the value of the exponent m in the Hertzian force - displacement relationship of $F \sim \delta^{3/2}$ for two ideal elastic spheres in contact (see section 4.5.2), where F is the contact force at the contact point and δ is the displacement of the spheres.

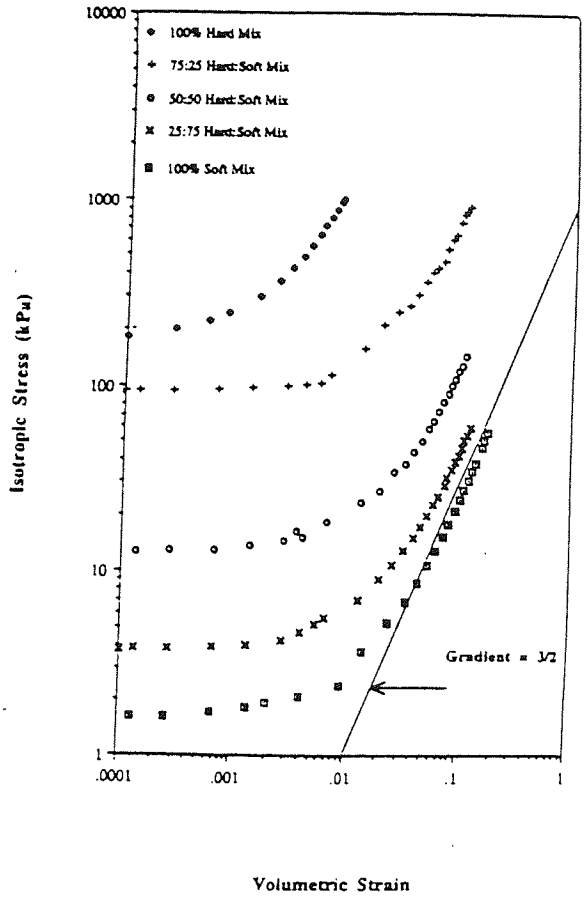

Figure 6.3 Stress-strain behaviour of two-dimensional, binary mixtures subject to quasi-static compression.;

This value of $\cong 3/2$ for m contrasts with the values obtained from two-dimensional quasi-static compaction experiments ($\dot{\varepsilon} = \bullet 4.5E\text{-}8$) involving random, photoelastic, *hard* cylinder assemblies by Travers *et al* (1987,89), where $m = 3.9 \pm 0.3$ (see section 2.3.1). This value for m does, however, agree with some of the results produced from two-dimensional, quasi-static ($\dot{\varepsilon} = \bullet 4.5E\text{-}8$) compaction studies of binary assemblies of rubber and Plexiglas cylinders by Travers *et al* (1986), Oger *et al* (1991) and Troadec *et al* (1991). These workers obtained a value of $m = 1.4 \pm 0.1$ for pure rubber assemblies, which is very close to the value of the Hertzian exponent. All this work is reviewed in more detail in section 2.3 of this thesis. The close correspondence with the Hertzian exponent (at higher stresses) for *all* the *binary* particle assemblies used in the quasi-static simulation experiments presented here has however, not been previously reported. Walton (1987), who performed a theoretical analysis of random packings of elastic spheres, argued that such Hertzian-type behaviour would only be visible in an assembly after a significant amount of compaction, because particle rearrangement would have already occurred. The stress-strain data obtained for p = 0.0, 0.5 and 1.0 are replotted in figures 6.4a, b and c using natural scales. Superimposed on each graph is the best-fit, second order polynomial.

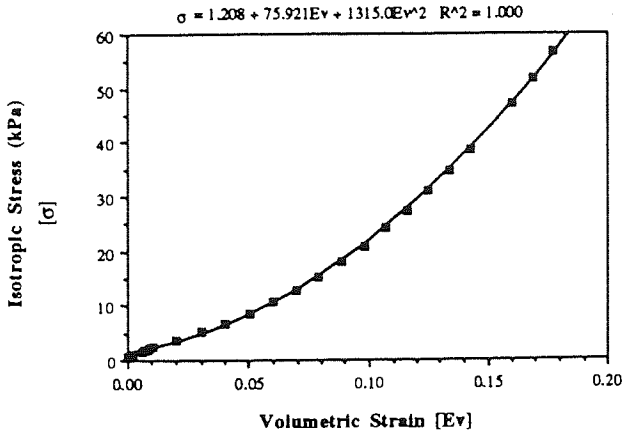

a)

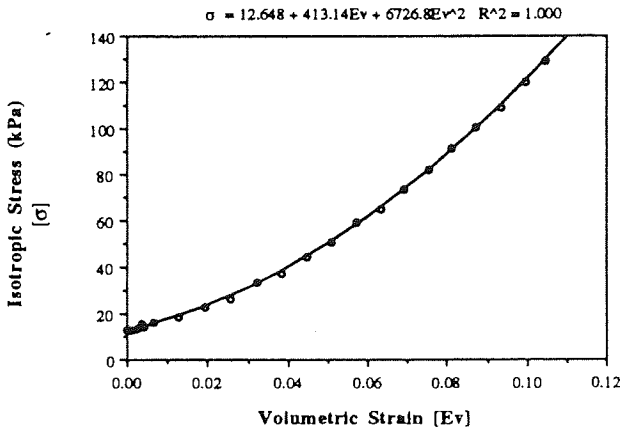

b)

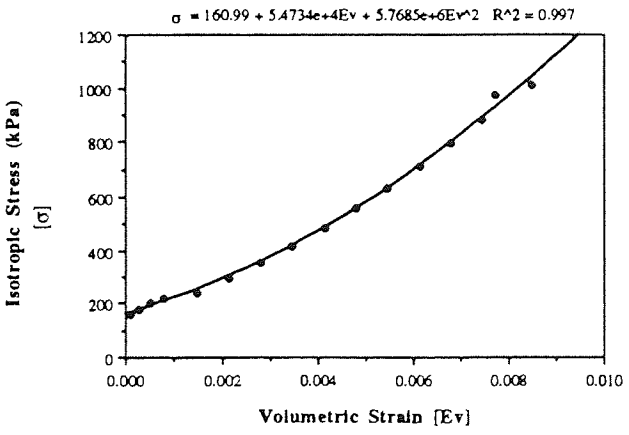

c)

Figure 6.4 Stress-strain curves for **a**) 100% soft assembly **b**) 50/50 hard:soft assembly **c**) 100% hard assembly subject to quasi-static compression.;

The agreement is excellent and, for all mixtures (as shown in Appendix C, figures C1 - C3), the stress-strain curves are accurately described by the equation:

$$\sigma = \mathbf{A} + \mathbf{B}\varepsilon_v + \mathbf{C}\varepsilon_v^2 \tag{6.1}$$

from which the Bulk modulus K is given as

$$\mathbf{K} = \frac{\mathbf{d}\sigma}{\mathbf{d}\varepsilon_v} = \mathbf{B} + 2\mathbf{C}\varepsilon_v \tag{6.2}$$

and the rate of change of modulus with strain is

$$\frac{\mathbf{dK}}{\mathbf{d}\varepsilon_v} = 2\mathbf{C} \tag{6.3}$$

Therefore, the general stress-strain relationship may be written as

$$\sigma = \sigma_o + \mathbf{K}_o\varepsilon_v + \frac{\mathbf{1}}{\mathbf{2}}\left(\frac{\mathbf{dK}}{\mathbf{d}\varepsilon_v}\right)\varepsilon_v^2 \tag{6.4}$$

where σ_o and K_o are the initial stress state and initial bulk modulus respectively, at the elastic percolation threshold.

The effect of mixture composition on the three coefficients of the second-order polynomial is shown in figure 6.5. It would appear that all the coefficients are reasonably approximated by exponential functions of the proportion of hard spheres in the assembly. On this basis, the initial stress σ_o may be expressed as

$$\sigma_o = \sigma_{o\,(p=0)}\exp(\mathbf{ap}) \tag{6.5}$$

where

$$\mathbf{a} = \mathbf{Ln}\left[\frac{\sigma_{o(p=1)}}{\sigma_{o(p=0)}}\right] \tag{6.6}$$

the initial bulk modulus K_o may be defined as

$$\mathbf{K}_o = \mathbf{K}_{o(p=0)}\exp(\mathbf{bp}^2) \tag{6.7}$$

where

$$\mathbf{b} = \mathbf{Ln}\left[\frac{\mathbf{K}_{o(p=1)}}{\mathbf{K}_{o(p=0)}}\right] \tag{6.8}$$

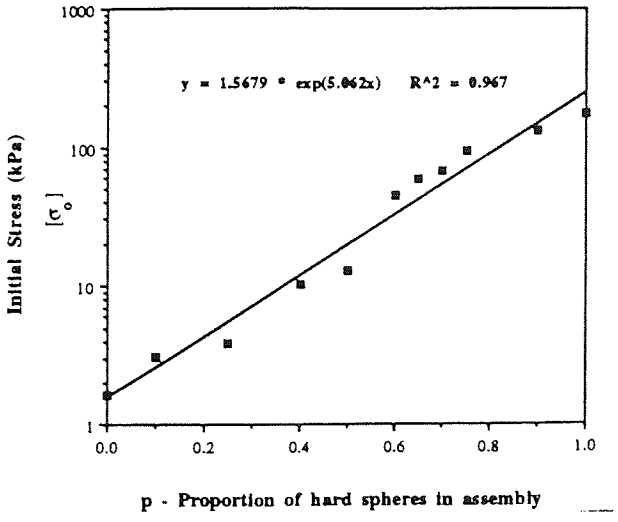

a)

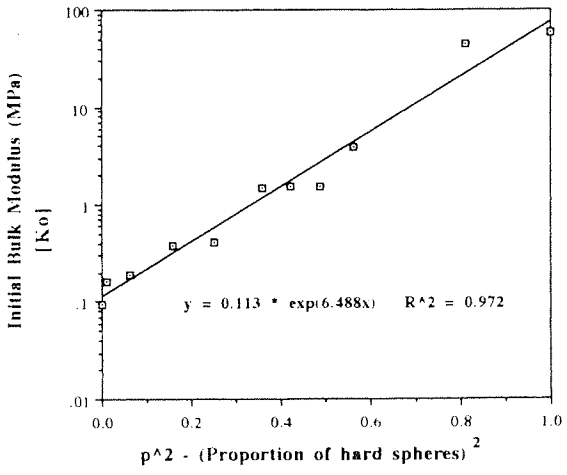

b)

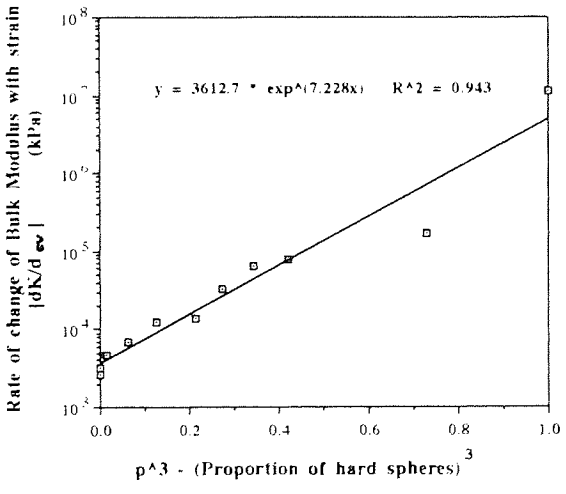

c)

Figure 6.5 Effect of mixture composition on initial stress state (**a**) initial bulk modulus (**b**) and rate of change of bulk modulus with strain (**c**) for the two-dimensional assemblies subject to quasi-static compression.;

The rate of change of modulus with strain can be approximated by

$$\frac{dK}{d\varepsilon_v} = \left(\frac{dK}{d\varepsilon_v}\right)_{(p=0)} \exp\left(c\,p^3\right) \tag{6.9}$$

where

$$c = \mathrm{Ln}\left[\frac{\left(dK/d\varepsilon_v\right)_{(p=1)}}{\left(dK/d\varepsilon_v\right)_{(p=0)}}\right] \tag{6.10}$$

In a die compaction experiment, the particle assembly may be at a stress level, solid fraction etc., above that associated with the elastic percolation threshold. Consequently, it is necessary to check whether the second-order polynomial representation will be satisfactory under these conditions. All the stress-strain results obtained from the simulations were replotted using new origins based on stress states higher than those at the elastic percolation threshold. The results of this exercise demonstrated that, in all cases, a second-order polynomial provided an accurate representation of the stress-strain curve. Typical examples of such polynomial curve fits are shown in figure 6.6. A comparison of figure 6.6 with figure 6.4 clearly shows that the coefficients of the second-order polynomial representation are very sensitive to the definition of the ground state which is used as the origin of the stress-strain curves.

By following the curve fitting procedures illustrated in figure 6.4 it is implied by (6.2) that the bulk modulus varies linearly with strain. Therefore, for each mixture composition, the simulation output data was re-examined to calculate the stress increment associated with each increment of strain. From this data the bulk modulus was calculated and plotted against the volumetric strain as shown in figure 6.7 for assemblies with composition $p = 0.0$, 0.5 and 1.0.

a)

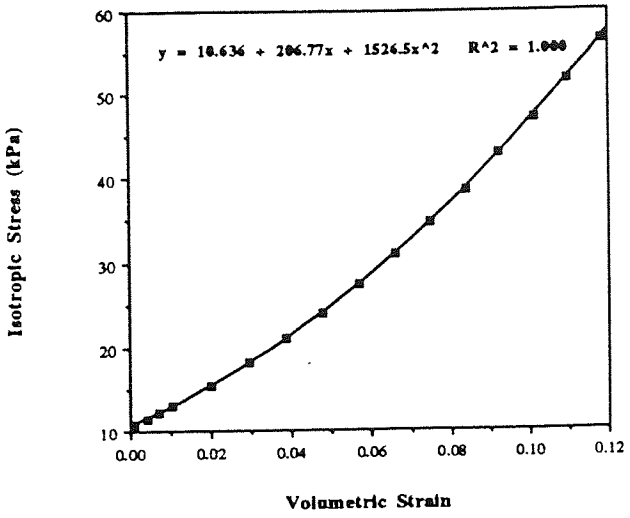

b)

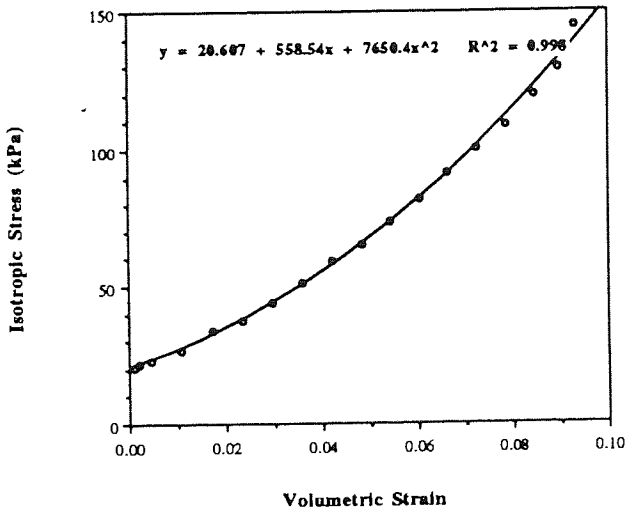

c)

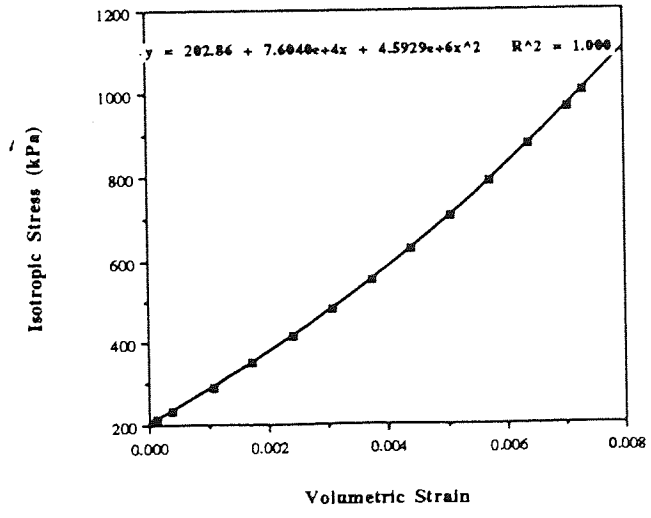

Figure 6.6 Stress-strain curves for the

a) 100% soft assembly [Normalised to $\sigma = 10$ kPa]

b) 50/50 hard:soft assembly [Normalised to $\sigma = 20$ kPa]

c) 100% hard assembly [Normalised to $\sigma = 200$ kPa].;

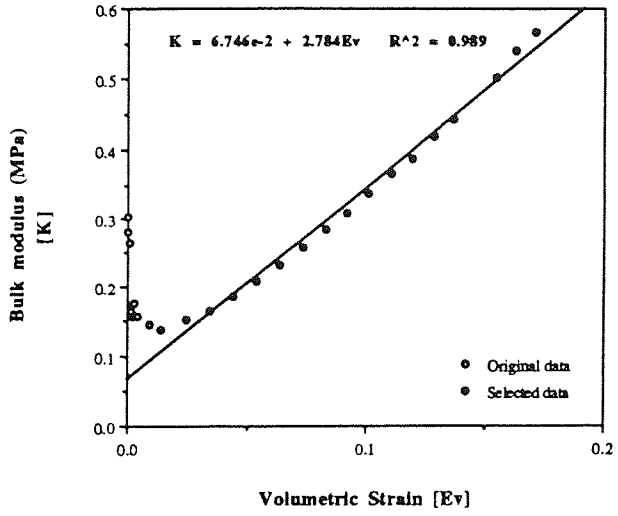

a)

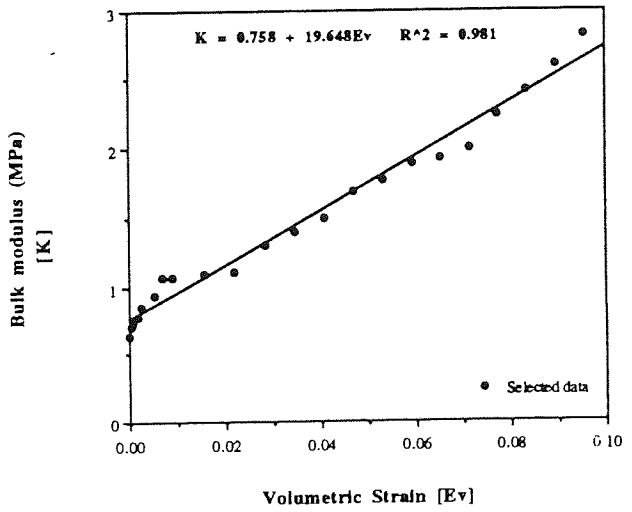

b)

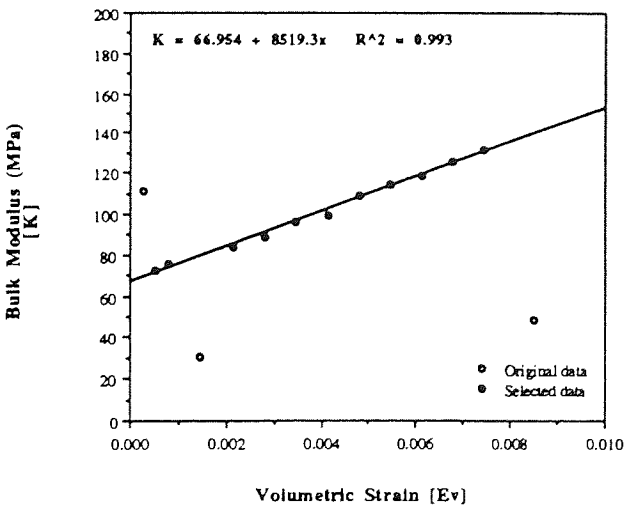

c)

Figure 6.7 Evolution of bulk modulus with strain for the (**a**) 100% soft assembly (**b**) 50/50 hard:soft assembly (**c**) 100% hard assembly.;

Two sets of data are shown for each mixture presented in figure 6.7. The data-set represented by clear circles, includes datapoints which differ significantly from the general range and these are ignored in the data-set represented by dark circles. Although there is significant scatter in the clear circle data shown in figure 6.7, it is clear that the rate of change of bulk modulus with strain is essentially linear for the majority of datapoints visible. The evolution of bulk modulus with strain, obtained from the simulations of the other particle mixtures, is shown in Appendix C, figures C4 - C6.

6.3.2 Evolution of structure

The simplest definition of the structure of particulate media is the void ratio, porosity or solid fraction ϕ. In soil mechanics, these parameters are normally plotted against the logarithm of stress. Figure 6.8 shows a plot of this type for the 50:50 mixture and the general form is typical of all the simulations reported in this chapter.

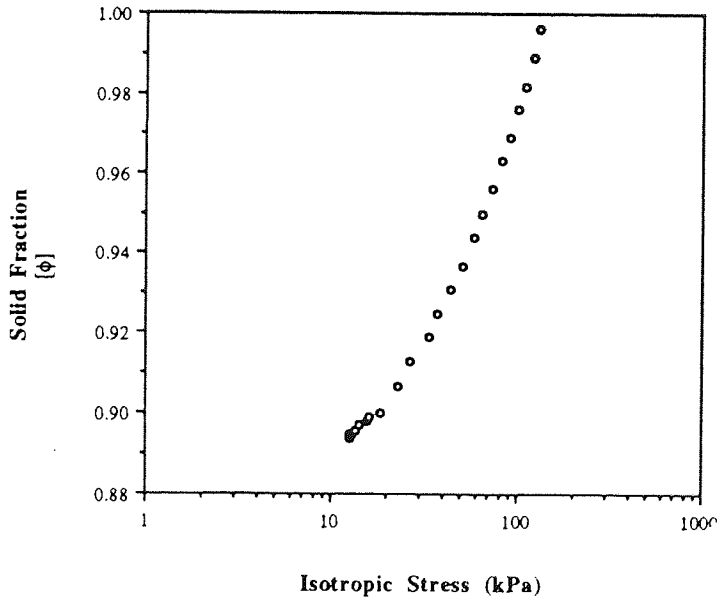

Figure 6.8 The relationship between solid fraction and isotropic stress for the 50/50 hard-soft assembly during quasi-static compaction.;

For sand, Hardin (1987) suggested a dependence on the square root of the stress. For $p = 0.0$, 0.5 and 1.0, figure 6.9 shows the relationship between solid fraction and $(\sigma/\sigma_o)^{1/2}$ where σ_o is the isotropic stress at the elastic percolation threshold. A linear relationship between the two parameters is observed for all the mixtures shown in this figure and little data scatter is visible.

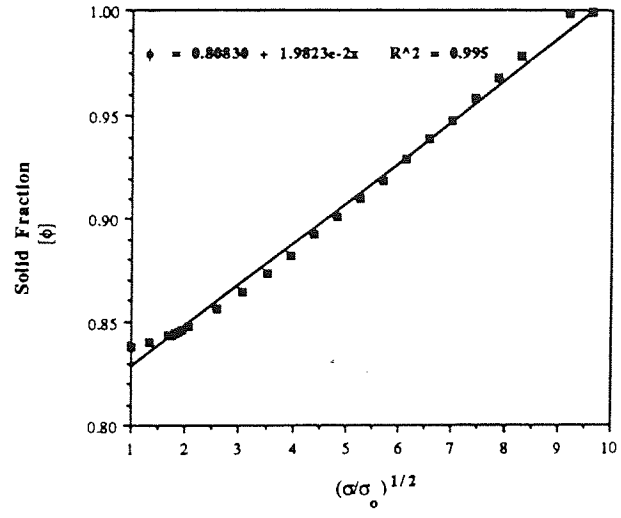

a)

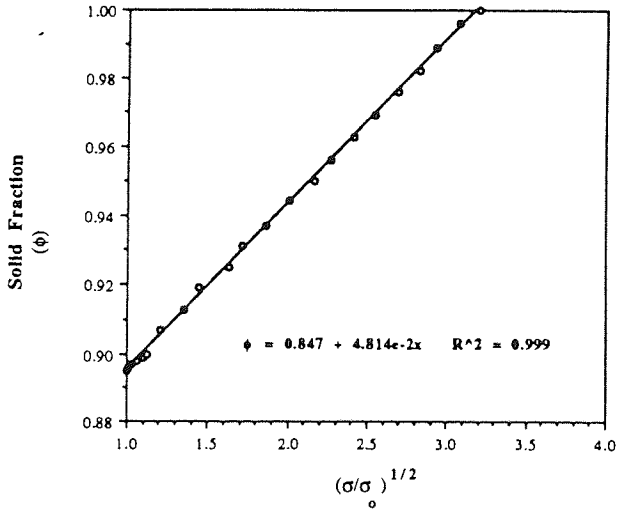

b)

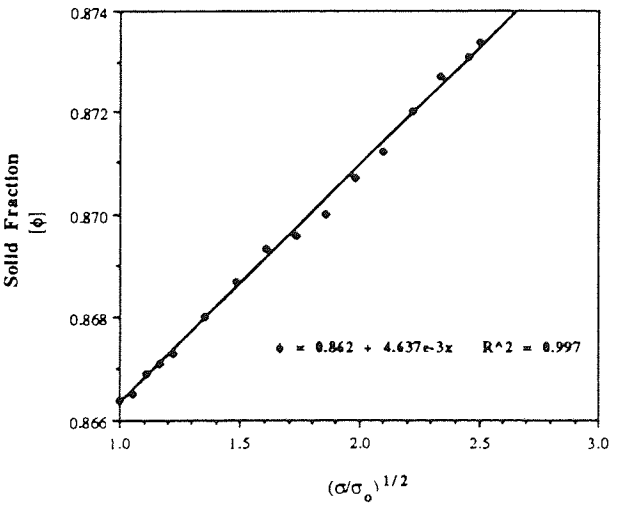

c)

Figure 6.9 The relationship between solid fraction ϕ and $(\sigma/\sigma_0)^{1/2}$ for the (**a**) 100% soft assembly (**b**) 50/50 hard:soft assembly (**c**) 100% hard assembly.;

In his paper, Hardin suggested that the linear relationship between ϕ and $(\sigma/\sigma_0)^{1/2}$ was only valid for granular materials below the stress level where particle crushing is a significant mechanism of deformation. The simulation assemblies are composed of purely elastic particles and are subject to low stress levels during isotropic compression. Therefore, it is not surprising that Hardin's relationship is also applicable to the data presented in figure 6.9. The relationship presented in figure 6.9 takes the form

$$\phi = \phi_o + \mathbf{c}\left(\frac{\sigma}{\sigma_0}\right)^{1/2} \tag{6.11}$$

where ϕ_o is the initial solid fraction. The variation of the coefficient c with mixture composition p is shown in figure 6.10. It is clear from this figure that the value of c is significantly affected by the mixture composition and hence assembly stiffness. Hardin (1987) proposed that the value of c was related linearly to the stiffness of a granular mixture during compression.

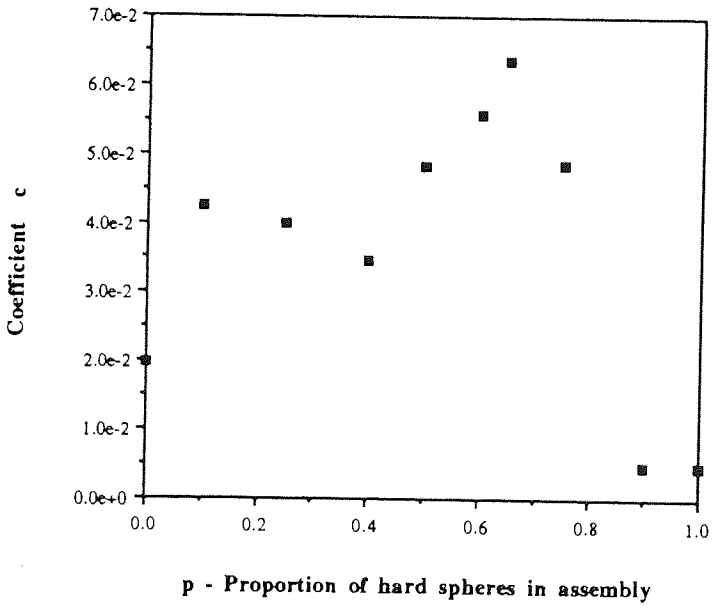

Figure 6.10 The variation of coefficient c with mixture composition p for the simulation assemblies subject to quasi-static compaction.;

However, the nature of the interparticle interactions within the assembly also appears to significantly affect c, since the relationship between p and c in figure 6.10 is more complex than that suggested by Hardin.

The assembly contact density C is another micromechanical parameter that is important descriptor of granular assembly behaviour and is defined in (4.72). The evolution of contact density with solid fraction for $p = 0.0$, 0.5 and 1.0 is shown in figures 6.11a, b and c respectively.

a)

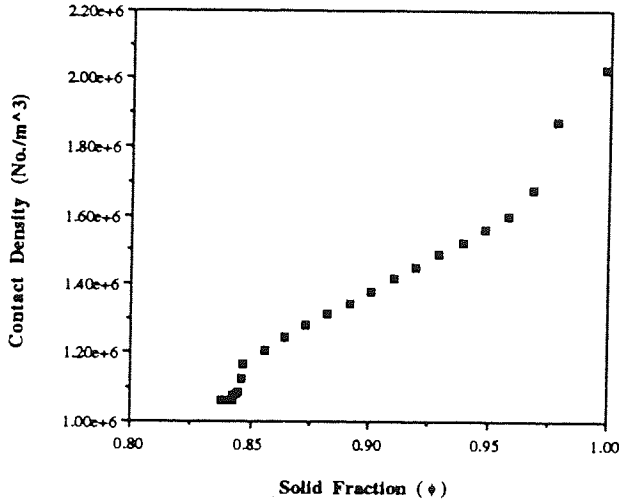

b)

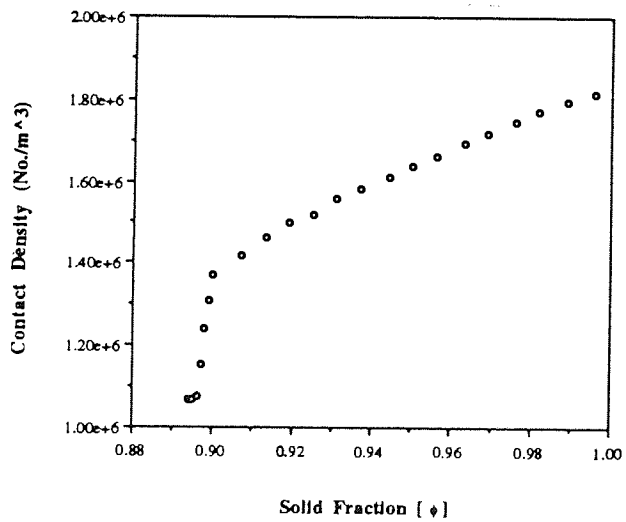

c)

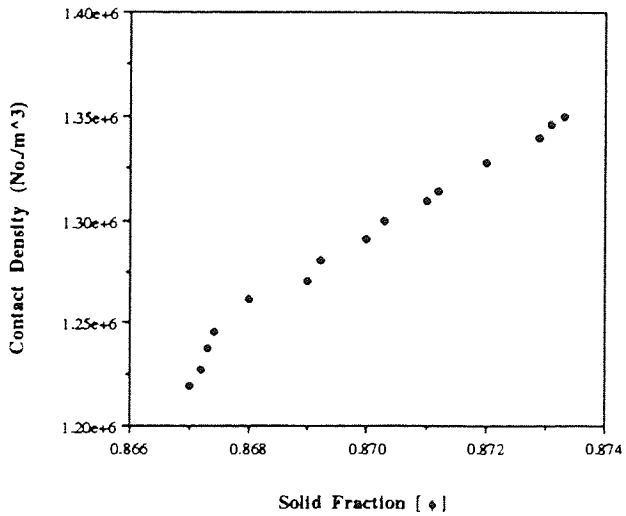

Figure 6.11 Evolution of contact density with solid fraction for the (**a**) 100% soft assembly (**b**) 50/50 hard:soft assembly (**c**) 100% hard assembly.;

For all the mixtures shown, the contact density increases rapidly during the initial stages of densification. A linear relationship between contact density and solid fraction is then observed for each mixture as densification proceeds. The behaviour presented in figure 6.11 is qualitatively similar to the stress-strain behaviour of the same mixtures during compression, since ordered stress-strain behaviour (Hertzian) is only visible in figure 6.3 after a significant amount of densification. The qualitative importance of the evolution of assembly structure on the macroscopic stress-strain behaviour of an assembly is suggested by such interpretation of the data.

The geometric co-ordination number Z_g represents the extent of particle connectivity within a particle assembly and is defined in (4.70). The mechanical co-ordination number Z_m, which is defined by (4.71), provides quantitative information about the development of load-carrying particle networks within a particle assembly (see section 4.9.1) and is another important descriptor of the structure of particulate material. It is useful to plot the evolution of Z_g and Z_m with solid fraction during isotropic compression. Figures 6.12a, b and c show such plots for mixtures where $p = 0.0$, 0.5 and 1.0 respectively and in all these figures, the values of both Z_g and Z_m increase rapidly during the initial stages of densification. The behaviour observed in figure 6.12 is also qualitatively similar to that seen in figure 6.11, because there is a initial steep gradient followed by a steady, shallower gradient as compaction proceeds.

Further densification of the mixtures leads to a relatively linear relationship between the co-ordination numbers and the assembly solid fraction, which is again qualitatively similar to the behaviour observed in figure 6.11. Densification for all the mixtures shown in figure 6.12, results in an increased number of load-carrying particles present within the assembly structures. For $p = 0.0$ and 0.5 in figure 6.12, Z_g and Z_m are equal in the linear portion of the curve. Similar behaviour is observed for other mixtures in Appendix C, figures C7 - C9.

However, for $p = 1.0$ in figure 6.12c, a relatively constant quantitative difference between the values of Z_g and Z_m is observed throughout the densification process. An explanation for such behaviour could be provided by examination of the structure of the assembly backbones for these mixtures.

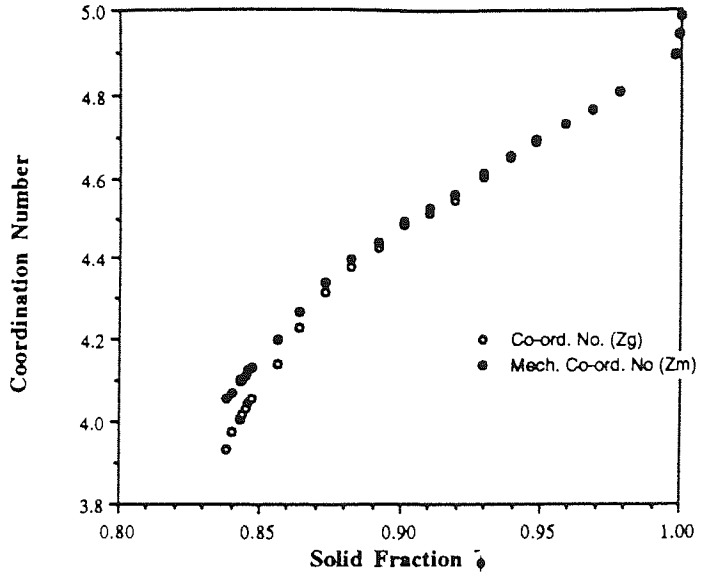

a)

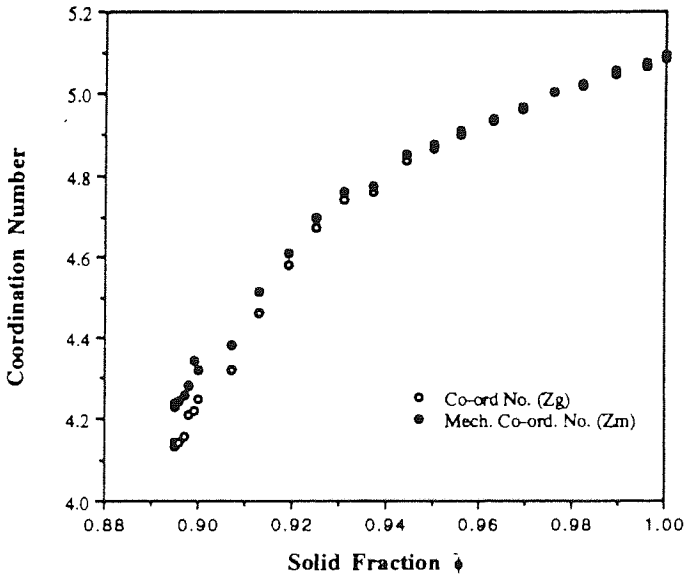

b)

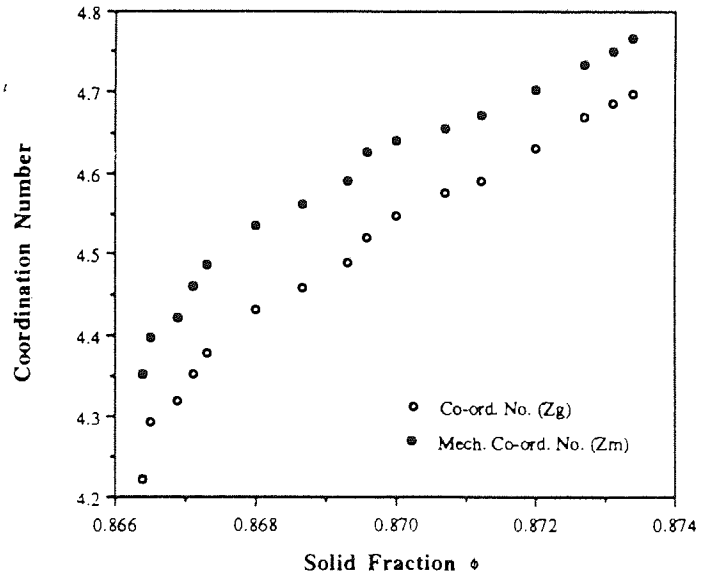

c)

Figure 6.12 Evolution of geometric co-ordination number Z_g and mechanical co-ordination number Z_m with solid fraction for the (**a**) 100% soft assembly (**b**) 50/50 hard:soft assembly (**c**) 100% hard assembly.

A relatively linear backbone structure, such as that shown by the p = 1.0 assembly at p_e in figure 5.1a , suggests that only a small number of the assembly particles are required for load transfer and hence Z_m may never equal Z_g during densification. However, for an assembly like p = 0.5, the backbone visible at both p_e (figure 5.1c) and at higher stresses (see later), indicates that a large number of particles are involved in a more co-operative process of load transfer across the assembly. Therefore, Z_g may eventually equal Z_m as densification proceeds.

6.4 Visual observations from the tests

In this section some of the plots produced by the TRUBAL program (see Appendix A), which are associated with various stages of the quasi-static compaction process will be displayed. In order to present a concise picture, the compaction behaviour of only one assembly will be examined here in great detail. The behaviour of other assemblies is presented in Appendix C. The representative assembly studied is the 50:50 hard:soft particle assembly. The positions on the stress-strain curve from which data is analysed are presented in figure 6.13.

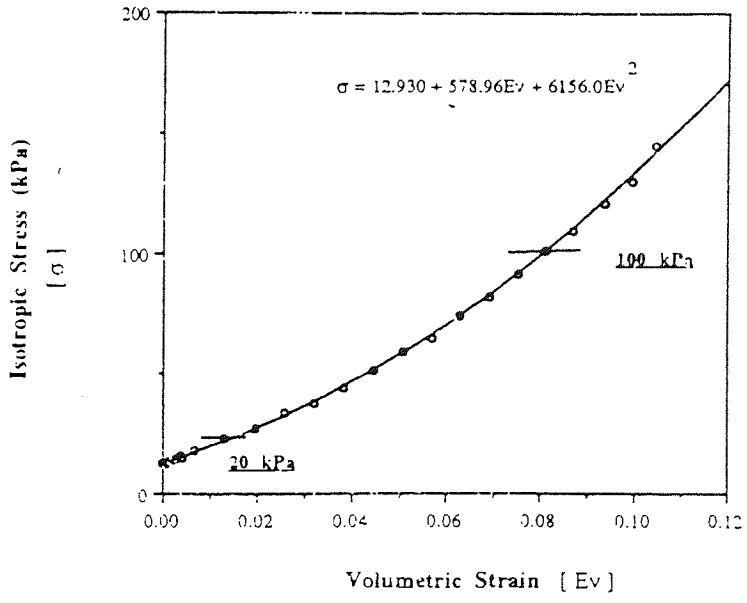

Figure 6.13 Analysis points on the 50/50 assembly compaction curve.

These stress states were chosen to help in interpretation of the general structural development of the assembly during the quasi-static compaction process. The 20 kPa point should represent assembly behaviour during the early stages of compaction and the 100 kPa point should represent the latter stages of compaction, when the stress/strain behaviour from figure 6.3 appears to be reasonably Hertzian in nature.

The assembly connection diagram produced using the TRUBAL **PRInt cnd** command line (see Appendix A) indicates the pattern and extent of particle connectivity within an assembly. The nature of such particle connectivity is useful as an aid in the analysis of microstructural characteristics such as the force-carrying particle network. Figure 6.14 presents the assembly connection diagrams for the 50:50 assembly at both 20 and 100 kPa.

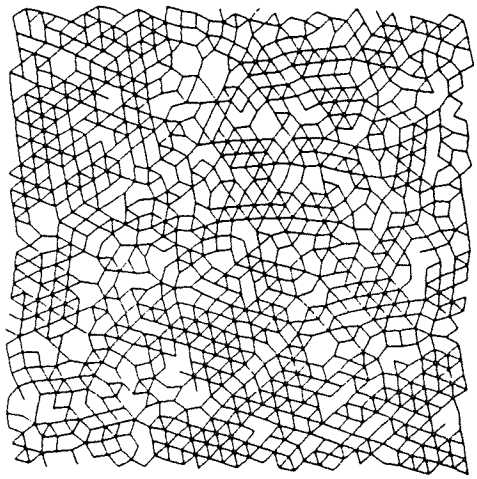

a)

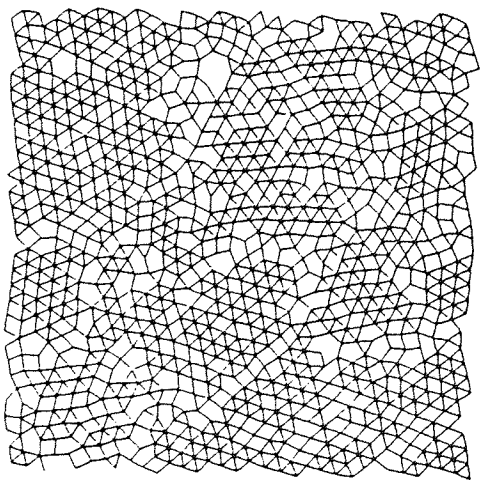

b)

Figure 6.14 Assembly connection diagrams for 50/50 assembly subject to quasi-static compaction.
a) σ = 20 kPa **b)** σ = 100 kPa;

It is evident from both of these figures that extensive and complex interparticle connections have developed within the assembly during the quasi-static compaction process. This visual evidence is confirmed by analysis of the values of Z_m at these points, which indicate a high degree of particle connectivity i.e. $Z_m = 4.416$ at $\sigma = 20$ kPa and $Z_m = 5.040$ at $\sigma = 100$ kPa. Bouvard and Lange (1991), who studied bimodal powder mixtures (see chapter 4), suggested that the number of triangular and tetrahedral supports between connected particles (visible in a connection diagram) will be very noticeable when $Z_m > 4$. This point of view is supported by the visual evidence of figure 6.14. It should also be noted that at all the compaction stages, for both the 50:50 (see figure 6.13) and other assemblies (see Appendix C), the number of contacts where slippage occurred was small. The same observation has been reported from physical shear tests of photoelastic discs by Oda and Konishi (1974).

The development of the assembly solid fraction ϕ during the quasi-static compaction process provides a quantitative indication of the effectiveness of the particle packing process within the assembly (see section 4.9.2). The value of ϕ increased from $\phi = 0.902$ at $\sigma = 20$ kPa to $\phi = 0.976$ at $\sigma = 100$ kPa. These solid fraction ϕ values are affected by the calculation method in two-dimensions (see section 1.2) and this statement is confirmed by the ϕ values presented in chapter 8 for the 50:50 three-dimensional assembly during quasi-static compaction, at the same stress levels, which are much lower. Figure 6.15 provides visual evidence of the qualitative nature of the assembly particle packing structure at both $\sigma = 20$ kPa and 100 kPa. All of the assembly particles are dark in this figure to improve visual interpretation of the pore structure. The use of the servo control mode within the TRUBAL program (see section 4.8.2) apparently allows a reasonably regular packing structure to be developed within the assembly, even when $\sigma = 20$ kPa. The low value of $\dot{\varepsilon}$ applied to the assembly can be reasonably expected to produce *shuffling* or small rearrangements of particles within the assembly. The small particle movements inherent in such shuffling, should permit more efficient occupation of the periodic space by the particles, resulting in the reasonably regular packings observed in figure 6.15. However, the packing structures observed in figure 6.15 are not entirely regular, since some *arching* of the particles (pores surrounded by immovable particles) is visible.

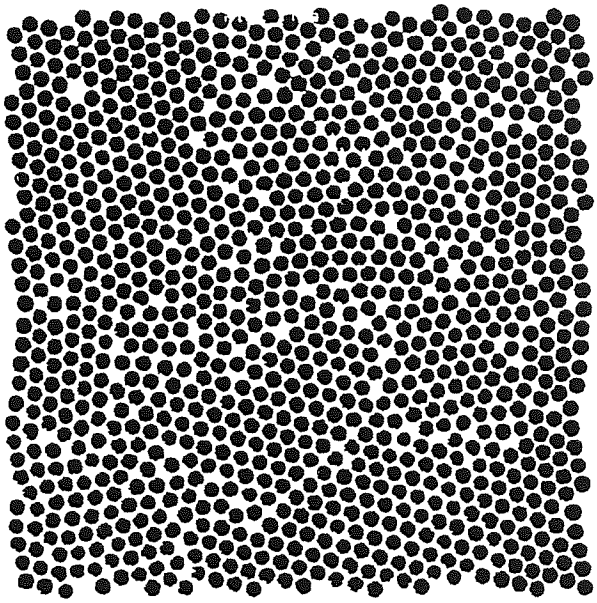

a)

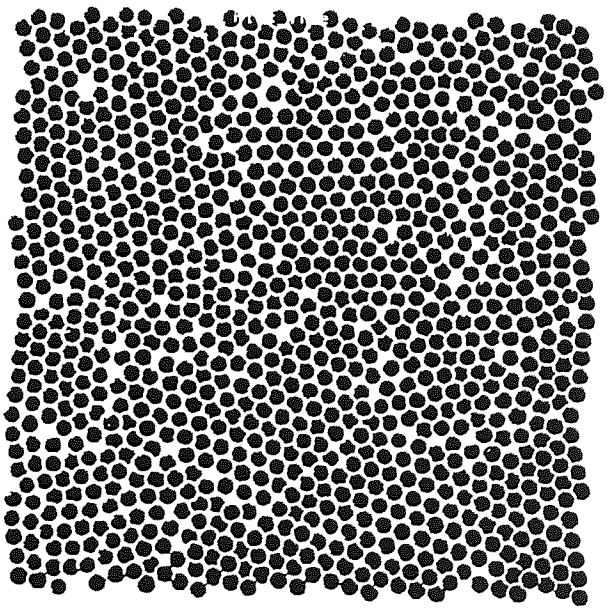

b)

Figure 6.15 Packing structure of the 50/50 assembly at different stress levels during quasi-static compaction **a**) σ = 20 kPa **b**) σ = 100 kPa.;

Visual analysis of the particle contact force development during compaction is provided by the TRUBAL program using the **PLOT FORces** command line (see Appendix A). Figures 6.16a and b present views of the stress network at $\sigma = 20$ and 100 kPa that support the idea of a discrete network of stressed particles proposed by Drescher and De Josselin de Jong (1972) in section 2.3.1. However, this discrete network may develop throughout the assembly as the applied compaction stress is increased, if the thick force line network expands in the same manner as that visible in figures 6.16a and b.

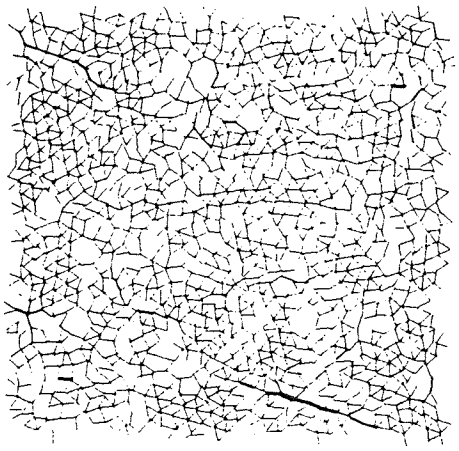

a)

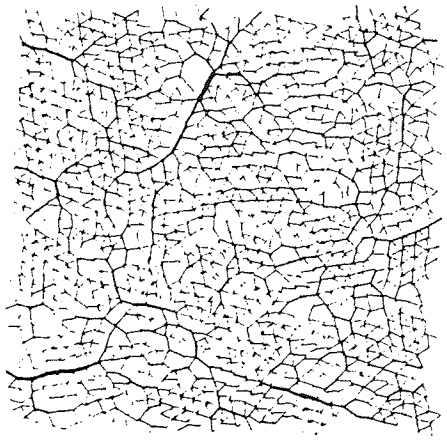

b)

Figure 6.16 Contact force network for the 50/50 assembly at different stress levels during quasi-static compaction
a) $\sigma = 20$ kPa **b)** $\sigma = 100$ kPa.;

6.5 Contact force, area and pressure distributions

Microstructural characteristics such as the particle contact force distribution within an assembly are important indicators of the assembly's internal development during the quasi-static compaction process. The development of such microstructural characteristics for the 50:50 assembly, at the stress levels used in section 6.4, will be reviewed in this section.

The particle contact force distribution within an assembly provides a general quantitative picture of the particle stress network developed at a particular stage of compaction. The macroscopic stress/strain behaviour of a particle assembly is also the sum of the behaviour at the individual particle-particle contacts within the assembly. Therefore, knowledge of the qualitative and quantitative nature of the particle contact force distribution is important for an accurate understanding of the macroscopic behaviour of an assembly. The particle contact force distributions considered in this work involve the contact normal forces, and are obtained during a simulation experiment by the use of the **PRINT CHIst** TRUBAL command line (see Appendix A).

Figure 6.17 shows the development of the particle contact force distribution during the compaction procedure described in section 6.2 and also indicates that, the contact force distribution within the assembly remains essentially exponential in form as the applied stress level is increased above the value at p_e (see section 5.1.2). The exponential force distribution shows that the largest contact forces are transmitted through the assembly by a limited number of particle-particle contacts. The particle contact force distribution has also been found to exhibit such an exponential form in other numerical simulation studies of powder compaction for *hard* particle systems by Bagi (1993) and Cundall *et al* (1989). Figure 6.17a shows the contact force distribution for the assembly at $\sigma = 20$ kPa in terms of the different particle-particle contact types such as hard-hard particles (see section 4.9.2). The overall contact force distribution had to be analysed in this manner for this compaction state, because the general form of the distribution used in figures 6.17b was too complex to interpret. The different particle contact-type distributions obtained with this approach were all found to be exponential in form (see Appendix C, figures C10 - C12).

Rothenburg (1980) suggests that the exponential nature of a granular assembly contact force distribution, is the result of competition between chains of force-carrying particles within the assembly for transmission of the applied stresses, particularly when there are no adhesive forces acting between the particles. Rothenburg also suggests that, the presence of such interparticle adhesive forces would result in more equal or co-operative load-sharing by the assembly particles and hence a (normal) form of contact force distribution. The contact force distribution for the 100% soft assembly at stress levels greater than the value for p_e, is also (normal) in form (see Appendix C). The co-operative nature of the load sharing by the assembly particles in this case, is probably assisted by the more conforming nature of the soft particles as the applied stress reaches larger values.

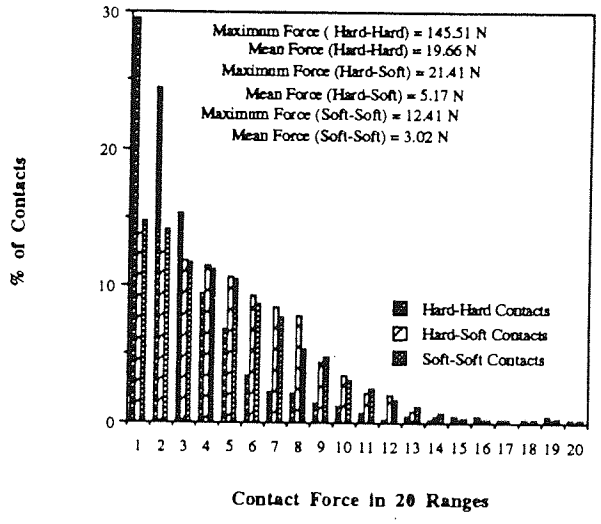

a)

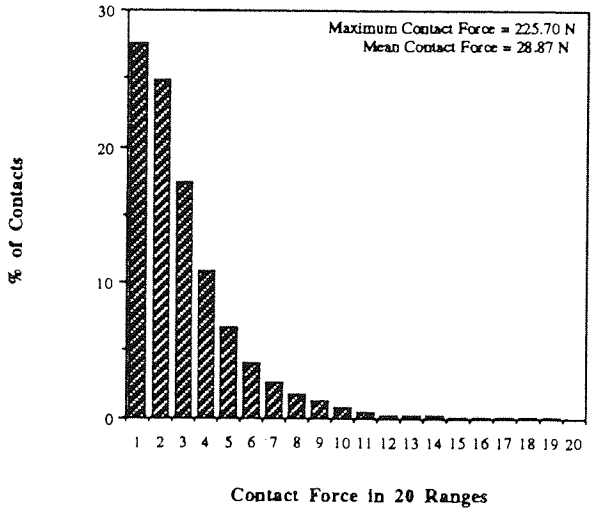

b)

Figure 6.17 Particle contact force distributions for 50/50 assembly at different stress levels during quasi-static compaction.; **a**) σ = 20 kPa **b**) σ = 100 kPa.;

Evidence of the importance of the particle stiffness specified in the **YMD** TRUBAL command line for a simulation assembly is provided by the results of a quasi-static compaction experiment, initially involving a 100% hard assembly (see Appendix C). In this simulation experiment the Young's modulus of the particles was decremented from 200 GPa to 0.2 GPa, allowing 50,000 calculation cycles at each step, with the isotropic stress level held constant at σ = 50.0 kPa. The assembly contact force distribution from this experiment was found to alter in shape as the particle modulus was decreased. The contact force distribution was exponential in form when E = 200 GPa and (normal) at E = 0.2 GPa, as illustrated in figure 6.18. These results indicate that the modulus specified for the particles is important in determining the form of the contact force distribution.

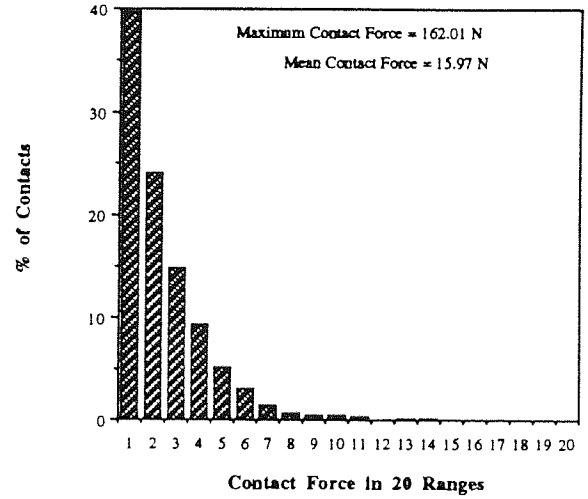

a)

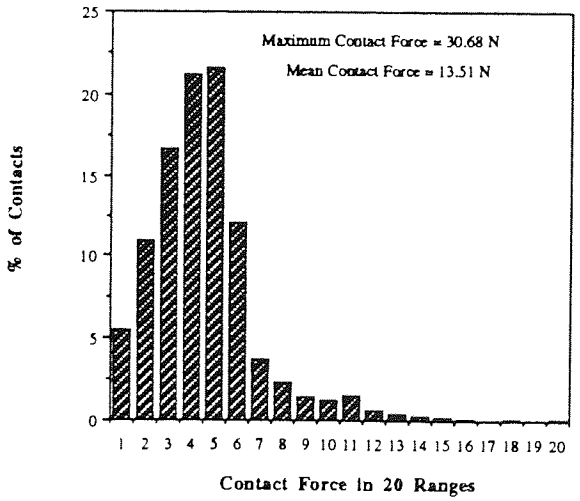

b)

Figure 6.18 Contact force distribution for assembly at a stress level of σ = 50 kPa **a**) E = 200 GPa **b**) E = 0.2 GPa.;

The qualitative and quantitative nature of particle contact areas influences not only the micromechanics of particle assembly behaviour (see section 4.5.2) but also the processing behaviour of granular systems e.g. during sintering. The particle contact area at a contact point is determined using the **PRINT CHIst** TRUBAL command line (see Appendix A).The development of inter-particle contact areas during the quasi-static compaction of the 50:50 assembly (see section 6.5) is presented in figure 6.19. The overall form of the particle contact area distributions at both σ = 20 kPa and 100 kPa is complex and therefore particle contact-type distributions have been analysed to provide a clearer picture (see section 4.9.2). Normal forms of contact area distribution are observed for all the different particle contact-types (see Appendix C, figures C13 - C18), indicating that within each of these contact sets the applied stress during compaction is shared amongst the particles. Figure 6.19, also shows that there is greater deformation of those contacts involving soft particles, which is due to the lower modulus specified for the particles.

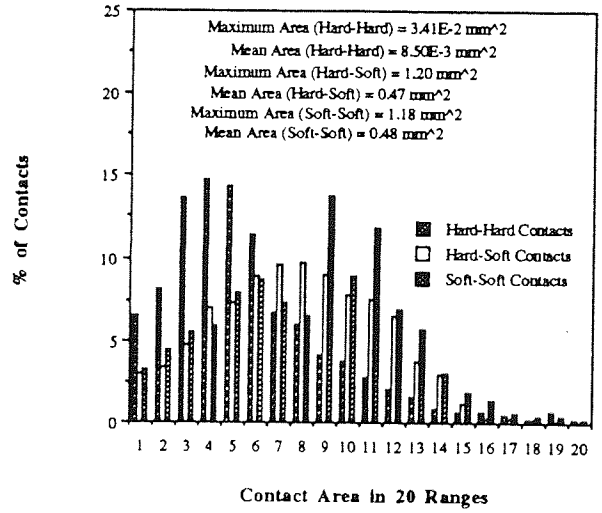

a)

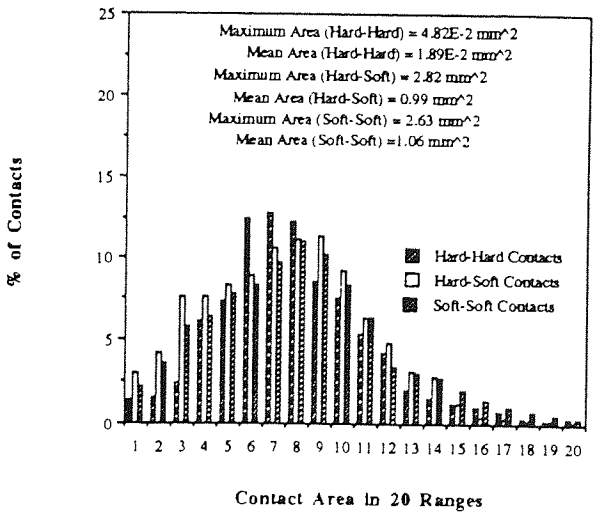

b)

Figure 6.19 Particle contact area distributions for the 50/50 assembly at different stress levels, during quasi-static compaction **a)** σ = 20 kPa **b)** σ = 100 kPa.;

The average normal pressure at a particle contact is determined by the TRUBAL program using the **PRInt CHIst** command line (see Appendix A). The shape of the particle contact pressure distribution is dependent upon the shape of both the contact force and contact area distributions. Figure 6.20 presents the particle contact pressure distributions for the 50:50 assembly at stress levels of 20 kPa and 100 kPa and shows the different distributions for the different particle-particle contact types, i.e. hard-hard, hard-soft and soft-soft. The contact pressure distributions for the particle contact-types presented in figure 6.20 are Gaussian in form (see Appendix C, figures C19 - C24), indicating that the pressures at the particle contact points are randomly distributed throughout the assembly. Figures 6.20a and b however, do show that, there is a very narrow contact pressure range for the soft-soft and hard-soft particle contacts at $\sigma = 20$ kPa and $\sigma = 100$ kPa and that this leads to the bimodal overall distribution visible in both of these figures.

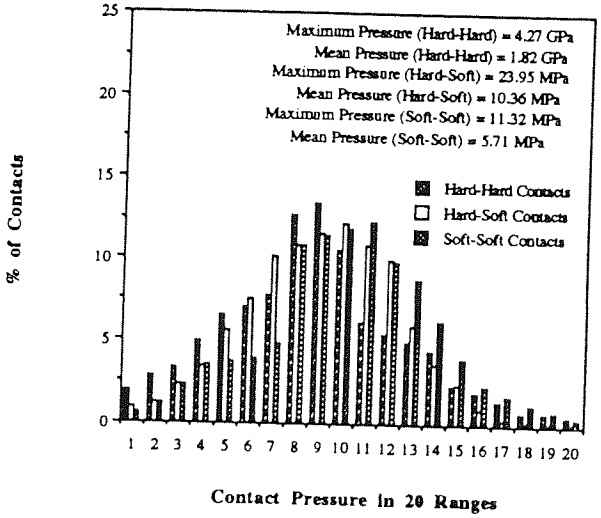

a)

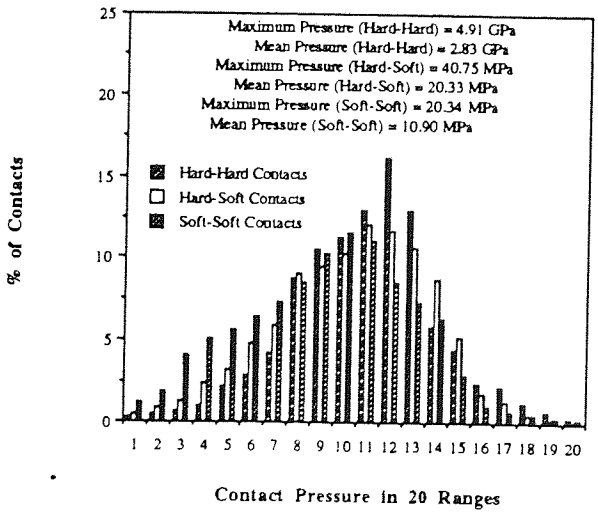

b)

Figure 6.20 Particle contact pressure distributions at different stress levels for the 50/50 assembly subject to quasi-static compaction.; **a)** $\sigma = 20$ kPa **b)** $\sigma = 100$ kPa;

6.6 Statistical analysis of contact distributions

It may be convenient to specify a contact force, area or pressure distribution as being exponential or Gaussian in form, as in the work of Cundall *et al* (1989) or Gherbi *et al* (1993), but it is not quantitatively correct to use such specifications without performing statistical analysis on the distributions. A number of theoretical frequency distributions have been developed for continuous populations of data such as this particle contact information (Hastings and Peacock, 1975). The goodness of fit of such a theoretical frequency curve type to experimental data can be determined using the chi-square (χ^2) distribution (Burr, 1974):-

$$\chi^2 = \sum_{i=1}^{k} \frac{(f_i - F_i)^2}{F_i} \qquad (6.12)$$

where F_i is the expected (theoretical) frequency in the ith class of data and f_i is the observed or experimental frequency in this ith class.

The χ^2 test provides reasonably wide applicability and ease of interpretation for a goodness of fit test (Burr ,1974). Good fits of simulation data to a theoretical population distribution can only be produced if low values of χ^2 are obtained from the analysis exercise. A specified theoretical distribution will only fit an experimental distribution if the value of χ^2 is less than that specified for 95% (obtained from statistical tables) of the theoretical distribution's population (Burr, 1974). Analysis of the contact force, area and pressure distributions for a number of the simulation assemblies displayed in this chapter (see Appendix C, figures C25 - C27), using this test, indicated that the Beta distribution (or Pearson type I) was a good general fit for the contact distributions:-

$$f(x) = \frac{x^{v-1}(1-x)^{w-1}}{B(v,w)} \qquad (6.13)$$

where f(x) is the probability density function and B (v, w) is the beta function with shape parameters v, w defined by:

$$B(v,w) = \int_0^1 u^{v-1}(1-u)^{w-1}\,du \qquad (6.14)$$

where u is an independent variable. A numerical approximation is used (see Hastings and Peacock (1975)) to allow a reasonably accurate value of the beta function to be determined i.e.

$$B(v,w) = \frac{(v-1)!(w-1)!}{(v+w-1)!} \tag{6.10}$$

Figure 6.21 presents examples of the ability of the Beta distribution to accurately describe some experimentally generated contact distributions.

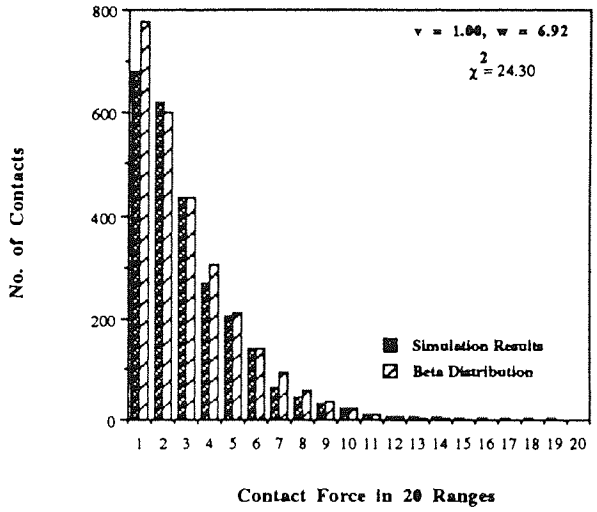

a)

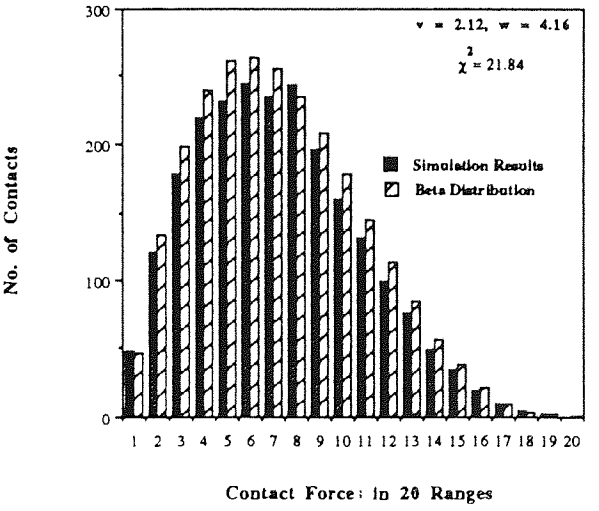

b)

Figure 6.21 The Beta distribution and experimental contact force distributions a) 50:50 assembly at 100 kPa b) 100% soft assembly at 20 kPa

The shape parameters v and w determine the form of the theoretical beta distribution that will fit an experimental contact data distribution. The value of *v* in particular increases as the form of the simulation distribution changes, from *exponential* to *normal* in figure 6.21. The relationship between the assembly composition p and the values of v and w is illustrated in figure 6.22. It clear from this figure, that the value of w rapidly increases when $p < 0.5$ and then becomes reasonably constant above $p = 0.5$. The value of v in figure 6.22 also remains relatively constant when $p > 0.5$ but increases rapidly as the value of p approaches $p = 0.0$. The evidence presented in figure 6.22 seems to support that shown in figure 6.18 and suggests that the form of the contact force distribution is composition sensitive.

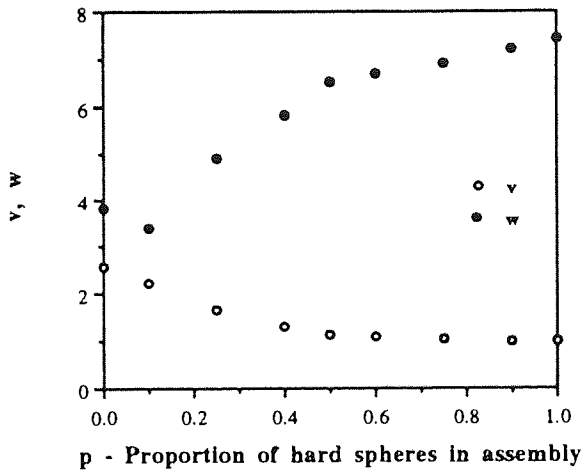

Figure 6.22 The relationship between assembly composition and the shape parameters for the Beta distribution fits.;

However, to complicate matters, figure 6.23 shows that the shape of the contact force distribution from a simulation is also stress-level dependent. It is clear from figure 6.23, that changes in the applied stress level produce significant changes in the shape of the contact force distribution i.e. a Gaussian distribution is observed for the 100% hard particle assembly at $\sigma = 500$ kPa in figure 6.23a. The complex relationship between assembly composition and compaction stress level and its effect on the overall form of a contact force distribution, is not well understood. Therefore, this area is worthy of further study.

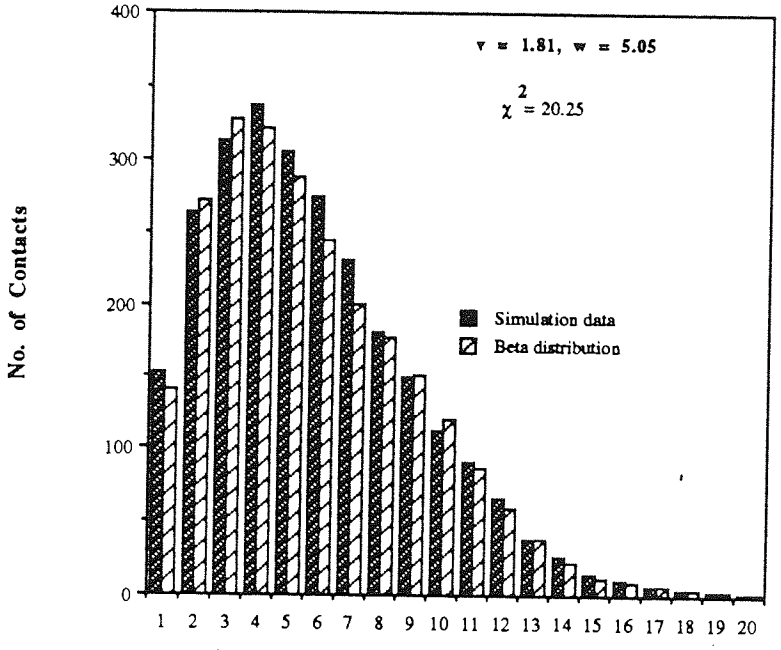

a)

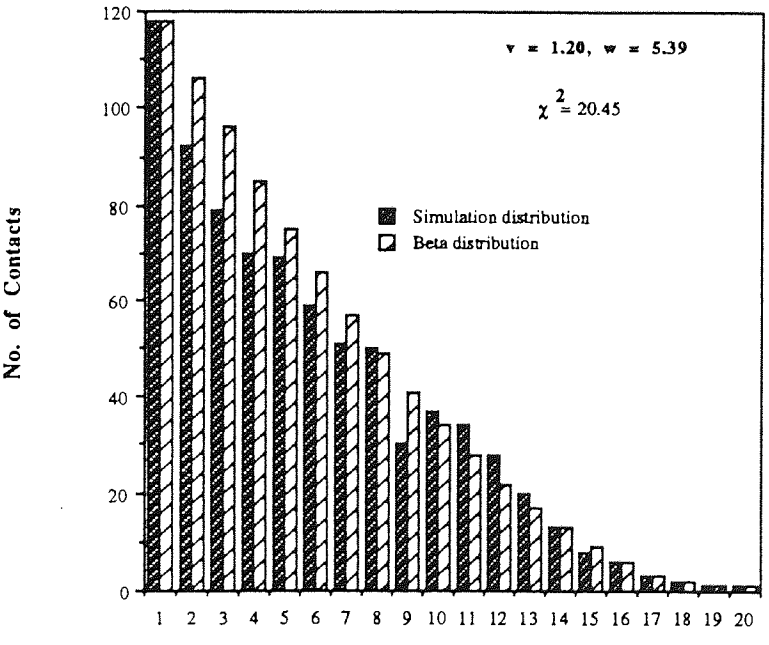

b)

Figure 6.23 The stress level dependence of the Beta distribution
a) Gaussian distribution for 100% hard assembly at $\sigma = 500$ kPa
b) Exponential distribution for 100% soft assembly at $\sigma = 2.5$ kPa

Gherbi *et al* (1993) who performed theoretical, numerical and experimental compaction studies (at 41 kPa) on a two-dimensional P.V.C cylinder assembly (see section 2.4) stated that possibly a Gamma or Weibull distribution (Hastings and Peacock, 1975) provided a good fit to their contact force data. The use of a goodness of fit test or other detailed statistical analysis of these distributions was not mentioned by these workers. However, Bagi (1993) did undertake more detailed statistical analysis of contact forces distributions for a 100% hard sphere simulation assembly isotropically compressed at 138 kPa and found that only an exponential form of distribution provided a good fit to the data. The ability of the Beta distribution to provide a good general fit to all the contact data distributions for both pure e.g. 100% soft and binary e.g. 50:50 assemblies has therefore, to the author's knowledge, not been presented previously.

6.7 Percolation-based parameters

Analysis of percolation-based parameters (see chapter 5), can also help in the qualitative description of assembly behaviour during quasi-static compaction above p_e. The nature of the assembly backbone (see section 4.9.2) at the stress levels used in section 6.5 can be determined and this provides an alternative view of the particle stress-network development within the 50:50 assembly. Figures 6.24a and b provide examples of the development of the 50:50 assembly backbone development during compaction. The pictures indicate that the physical appearance of the assembly backbone changes as the applied stress level is increased during the compaction process. The presence of both hard and soft particles in the assembly backbone contradicts the ideas of Travers *et al* (1986) and Troadec *et al* (1991), who claimed that the *backbone* is composed of purely hard components. However, these workers did use binary, photoelastic, cylinder assemblies (see section 2.3.2) and were thus unable to satisfactorily analyse the behaviour of the opaque soft cylinders. Analysis of the simulation data also indicated that, less severe quantitative changes to the composition of the simulation assembly backbone during compaction i.e. the composition changed from ~ 70% hard particles at σ = 20 kPa to ~ 80% hard particles at σ = 100 kPa, were observed compared with those produced by changes in assembly composition at p_e (see section 5.2.3). The value of the cluster fractal dimension for the assembly backbones could also be extracted using the TRUBAL program and this remained roughly constant during the compaction process, since it varied from d_f = 1.6410 at σ = 20 kPa to d_f = 1.6449 at σ = 100 kPa.

The small changes in composition and spatial occupation properties, i.e. d_f of the backbone, indicate that the general structure of the backbone appears to become established, as the assembly stress-strain behaviour becomes Hertzian-like (see figure 6.3). However, the changes in backbone physical appearance emphasised in the nine-periodic cell views of figure 6.25 (see section 4.9.2), appear to indicate that changes in the stress-transmission pathways through the particle assembly still occur even at higher compaction pressures. The assembly backbone can therefore be viewed as a dynamic system, with particles involved in the stress transmission pathways through the assembly, apparently being changed in a regular fashion, as the applied stress level is increased, even during this quasi-static compaction process.

The concept of multifractality was first mentioned in section 3.4, where the experimental work of de Arcangelis *et al* (1985) on random resistor networks was reviewed. De Arcangelis *et al* (1985) found that a multifractal system was characterised by the presence of a complete, continuous distribution of data such as contact resistance values. Roux (1991) argued that, the stress and strain distributions within two-dimensional cylinder assemblies subject to compaction, like those used in the work of Travers *et al* (1986,1987 and 1989), could be considered to be multifractal. If the simulation assemblies used here, are generally regarded to act as elastic lattice systems, then the multifractal concept could also be used in analysis of their behaviour. The microstructural behaviour of the simulation assemblies used in the quasi-static compaction experiments can be considered to be multifractal, because complete, continuous distributions of data were obtained from analysis of assembly contact information such as particle contact forces. Figure 6.26 illustrates multifractal-like distributions for the contact force, area and pressure for the example 50:50 assembly.

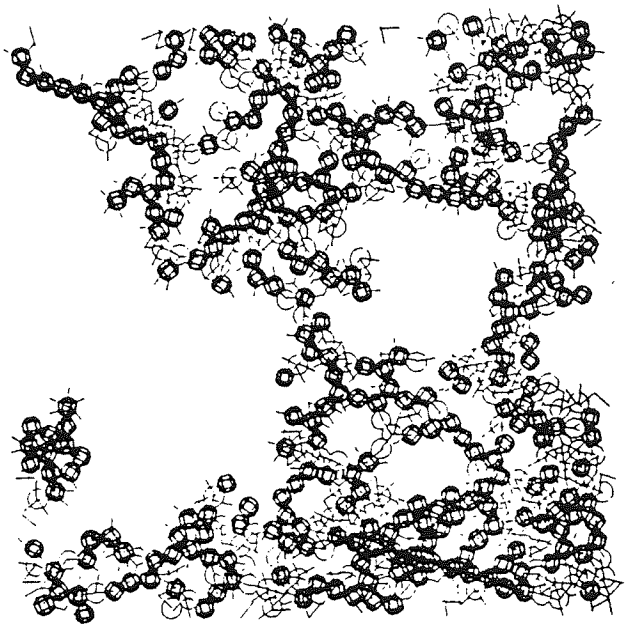

a)

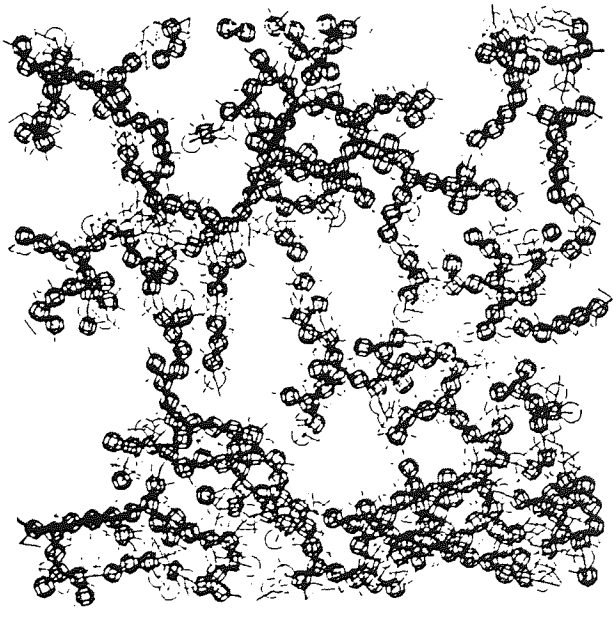

b)

Figure 6.24 Cluster backbones for the 50/50 assembly during quasi-static compaction

a) σ = 20 kPa **b**) σ = 100 kPa.; (Lines on diagram from cluster connection diagram).

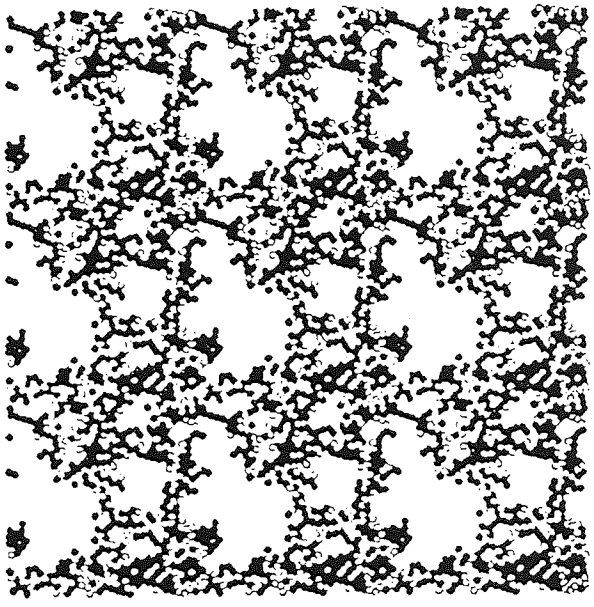

a)

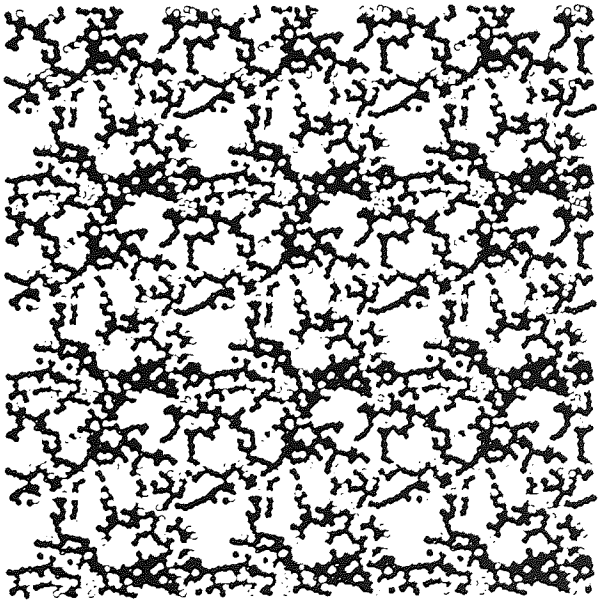

b)

Figure 6.25 Nine-periodic cell views of 50/50 assembly backbones during quasi-static compaction at **a)** $\sigma = 20$ kPa **b)** $\sigma = 100$ kPa.;

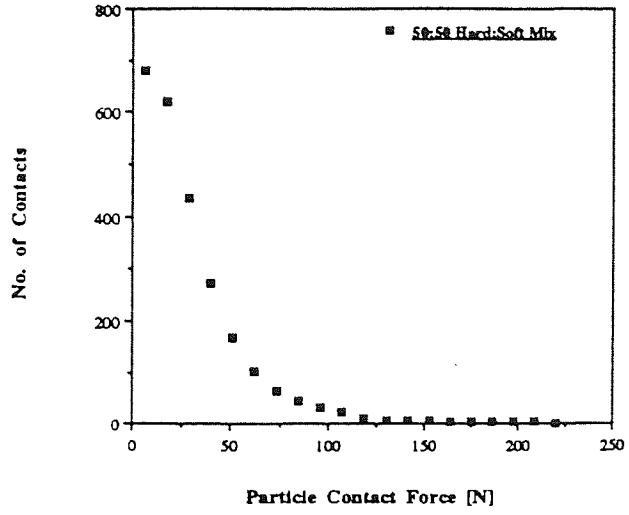

a)

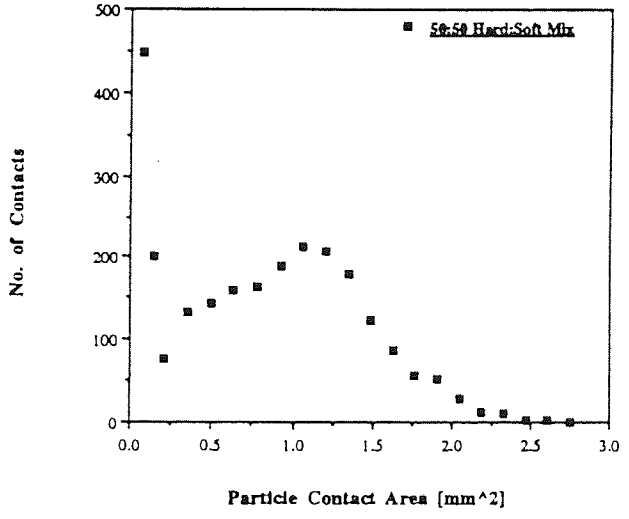

b)

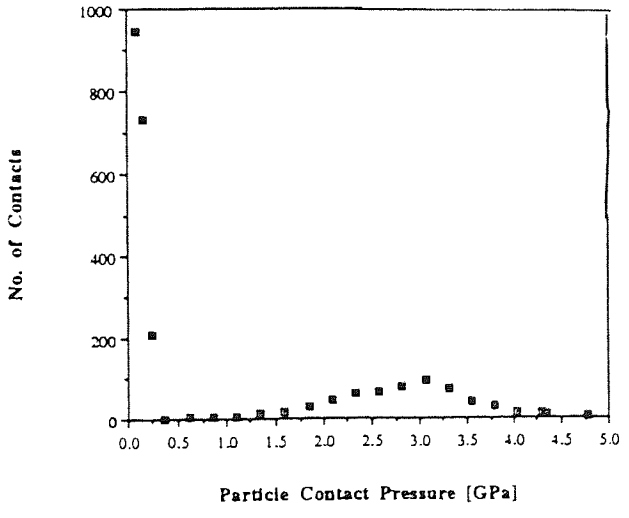

c)

Figure 6.26 Mutifractal contact information distributions for the 50/50 assembly subject to quasi-static compaction.

a) Contact force at $\sigma = 100$ kPa

b) Contact area at $\sigma = 100$ kPa **c**) Contact pressure at $\sigma = 100$kPa.;

6.8 Summary

The qualitative features of the macroscopic, microscopic and percolation-based behaviour of two-dimensional particle assemblies subjected to quasi-static compaction were presented in this chapter. In terms of the macroscopic analysis, the stress-strain behaviour of the assemblies was found to be adequately described by a second-order polynomial function and became Hertzian-like at higher compaction pressures. The co-efficients of the polynomial functions were related to fundamental assembly parameters at p_e and were also sensitive to assembly composition. The structural evolution of the assemblies during compaction showed that sensitivity to assembly composition was again important. The theoretical argument of Hardin (1987), from his studies on sand, that there is a linear relationship between the solid fraction ϕ and $(\sigma/\sigma_o)^{1/2}$ was exhibited by the simulation assemblies.

It was demonstrated in this chapter that the elastic properties of the component particles in a binary assembly had a noticeable effect on the appearance of the microstructural particle contact distributions. The qualitative nature of the contact distributions was however, apparently unaffected by changes in the applied compaction pressure. The results presented in this chapter also indicated that the theoretical Beta statistical distribution provided an adequate qualitative and quantitative description of the contact force distributions for the various assemblies.

Percolation-based analysis of assembly behaviour was shown to be related to both macroscopic and microscopic assembly parameters. The development of the *strongest stresses* network or *backbone* of a binary, simulation assembly was shown to involve both hard and soft particles, contradicting previous, limited photoelastic studies. The dynamic nature of the assembly backbone during compaction was also found to contradict Drescher and De Josselin de Jong's (1972) concept of *rigid* particle chains in this strongest stresses network. The satisfactory use of multifractality in a description of microstructural assembly behaviour was confirmed from the simulation work.

Chapter 7

The effects of particle size on quasi-static compaction

7.1 Introduction

In chapter 6, the quasi-static compaction behaviour of binary particle assemblies was reviewed, but the work only considered monodisperse systems. Any real particle system consists of a distribution of particle sizes (polydisperse) and it would, therefore, be useful to perform simulation experiments which considered the compaction behaviour of a polydisperse, binary assembly. However, such studies require a great deal of computing power and so the work presented here, is limited to systems with two different particle sizes (bimodal). A few workers have performed experimental and computer simulation studies of polydisperse particle systems. Bideau and Troadec (1984) studied random, two-dimensional packings of 1000 hard discs with a diameter ratio varying from 1.25:1 to 5:1. The proportion of the large particles in the assembly varied from 0.1 to 0.9. This work however, only considered the behaviour of the assembly when it was subject to *gravity*. Similar experimental work was also performed by Dodds (1975) and Powell (1980b, 1991). Suzuki and Oshima (1983, 1985) performed computer simulation experiments on randomly generated, two-dimensional (1983) and three-dimensional (1985) polydisperse particle compact beds. These compact beds were only subject to gravitational forces and not to any externally applied loads. Bouvard and Lange (1991) used both aspects of percolation theory (see chapter 3) and computer simulation techniques to study the three-dimensional deformation behaviour of binary, bimodal particle assemblies. The radius ratio between the hard inclusions and soft matrix particles within these assemblies varied from 0.33:1 to 3:1. Further details of their work is provided in section 2.4.

In the series of simulation experiments reported in this chapter, a particle radius ratio of 2:1 was adopted. Both systems composed of mixtures of large hard particles and small soft particles and systems consisting of large soft particles and small hard particles were studied.

7.2 Simulation experiment characteristics

The binary assemblies used in the experiments reported in this chapter, were generated using a similar approach to that described in section 6.2. All the two-dimensional, bimodal assemblies were composed of 1000 particles and the properties of both particle types in these systems, irrespective of size, were the same as those presented in table 6.1.

The particle radius was specified according to the type of particle and size ratio system required. For each type of size mixture the diameters of the large particles were in the range 2.0 mm ± 0.1 mm with the same particle size distribution (figure 6.1) as that used for the monosized mixtures reported in chapter 6. The sizes of the small particles were similarly distributed in the range 1.0 mm ± 0.1 mm. The particle generation sequence was designed to allow all the larger particles to be generated first, followed by the smaller particles.

The solid fraction ϕ at generation for the 2:1 hard:soft size ratio assemblies varied in value between $\phi = 0.476$ for the 100% hard particle assembly and $\phi = 0.421$ for the 50:50 hard:soft assembly. In the case of the 2:1 soft:hard size ratio assemblies, the value of ϕ varied from $\phi = 0.440$ for the 25:75 hard:soft assembly to $\phi = 0.517$ for the 50:50 hard:soft assembly. Figure 7.1 displays an example of a 2:1 hard:soft size ratio assembly at generation and figure 7.2 shows an example of a 2:1 soft:hard size ratio assembly at the same state.

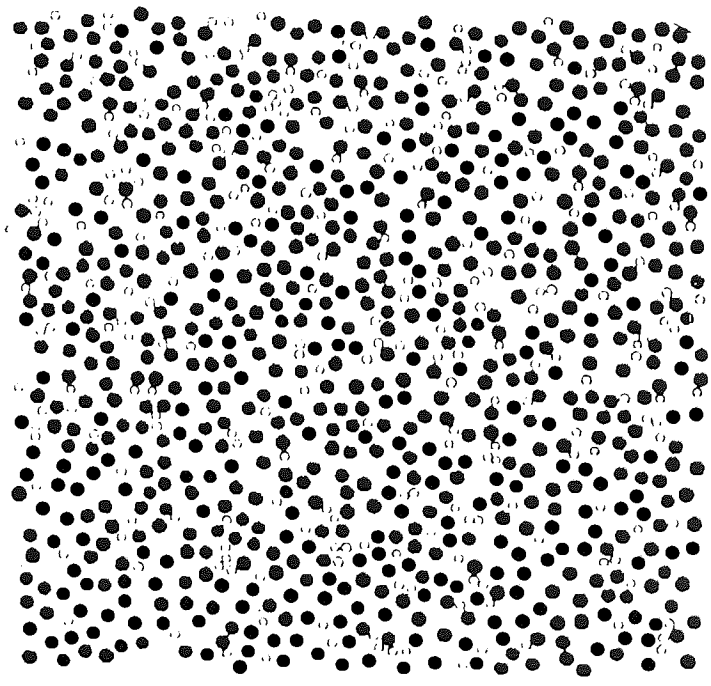

Figure 7.1 2/1 hard:soft size ratio, 75/25 hard:soft particle assembly at generation.;
[Dark circles = hard particles]

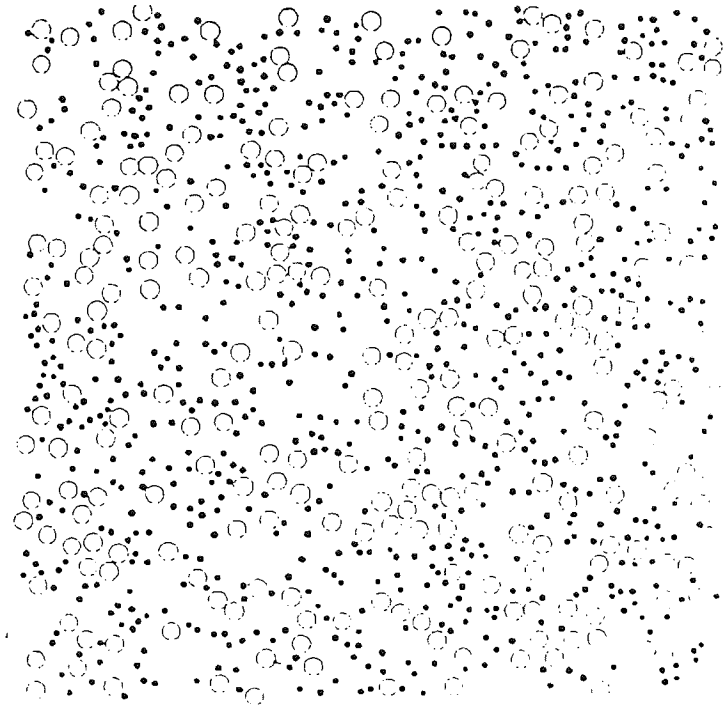

Figure 7.2 2/1 soft/hard size ratio, 75/25 hard:soft particle assembly at generation.;
[Dark circles = hard particles]

The particle size ratio assemblies were then subject to quasi-static isotropic compaction tests using the same procedures as adopted for the monodisperse assemblies reported in chapter 6 (see section 6.2).

7.3 Stress-strain behaviour

In a similar manner to the work presented in chapter 6, the ground state for all macroscopic assembly measurements presented in this chapter is the assembly equilibrium state at p_e. A selection of log-log stress-strain curves were produced for the bimodal assemblies using ground states at p_e and the compaction procedure described in more detail in section 6.2. The curves generated for the assemblies were qualitatively similar to the stress-strain curves of the monodisperse assemblies presented in figure 6.3, since reasonably linear, Hertzian-like behaviour was also observed at high compaction strains. Examples of log-log stress-strain curves for various bimodal assemblies are presented in Appendix D.

The stress-strain data for bimodal assemblies can be plotted using natural scales and curve fitting attempted. Second-order polynomials were generally able to provide good fits to the data generated from both the 2:1 hard:soft size ratio assemblies presented in figure 7.3 and the 2:1 soft:hard size ratio assemblies shown in figure 7.4, in a similar manner to that observed for the monodisperse assemblies in figure 6.4.

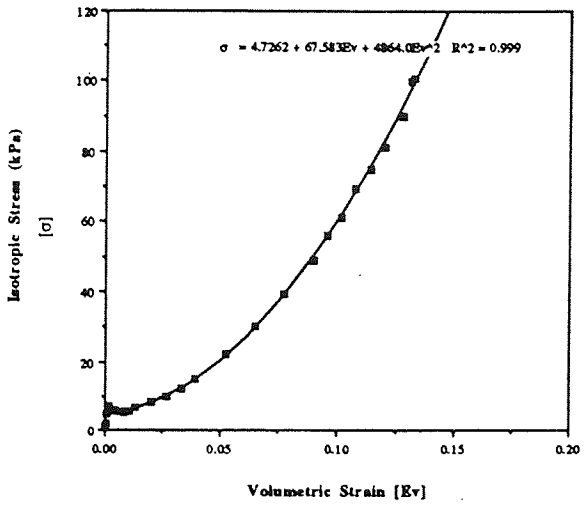

a)

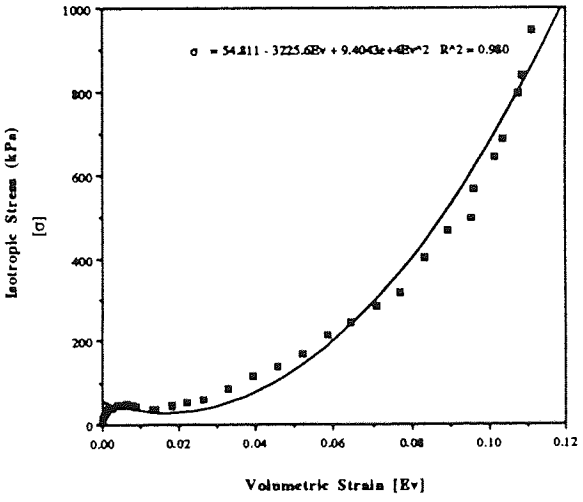

b)

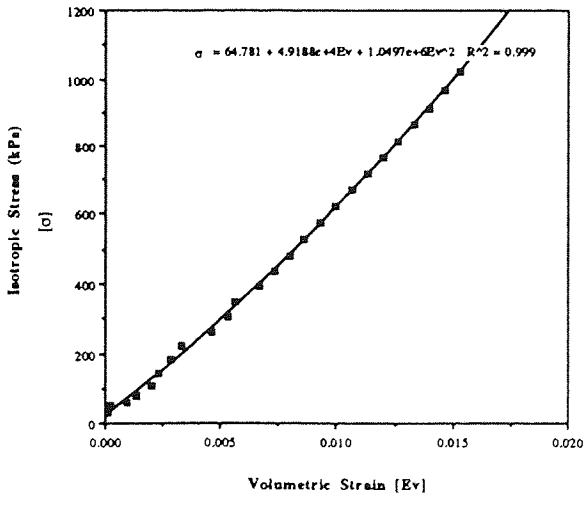

c)

Figure 7.3 Stress-strain curves for 2/1 hard/soft size ratio assemblies subject to quasi-static compression **a)** 25/75 hard:soft mix **b)** 50/50 hard/soft mix **c)** 75/25 hard/soft mix;

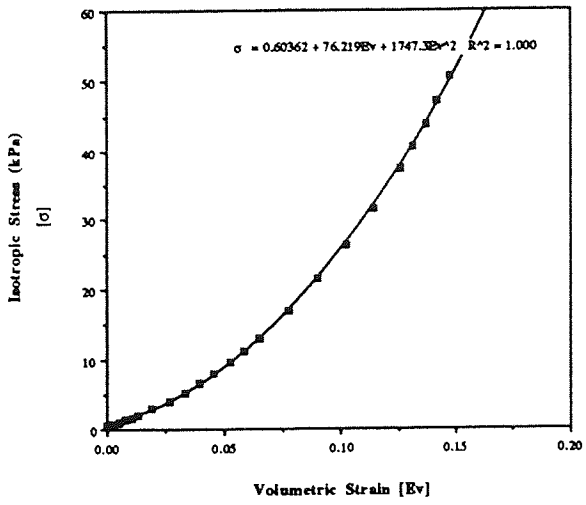

a)

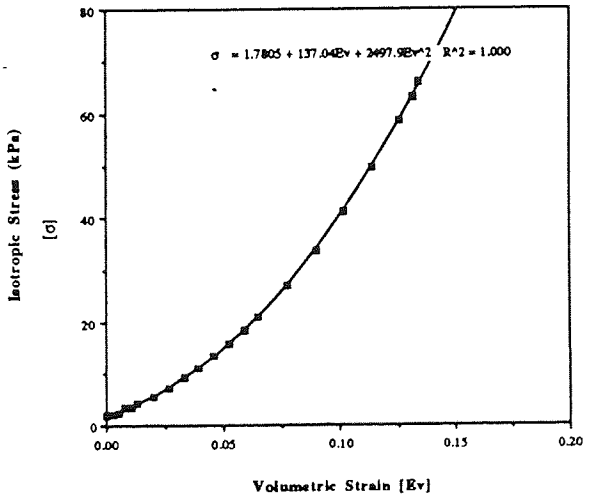

b)

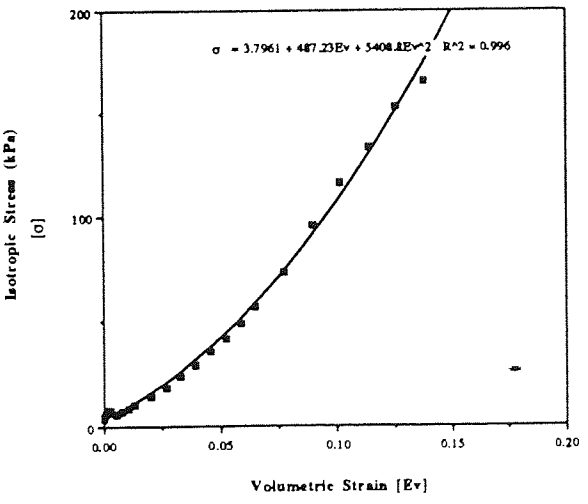

c)

Figure 7.4 Stress-strain curves for 2/1 soft/hard size ratio assemblies subject to quasi-static compression **a**) 25/75 hard/soft mix **b**) 50/50 hard/soft mix **c**) 75/25 hard/soft mix.;

The presence of equal quantities of large hard and small soft particles in the 50:50 assembly leads to more irregular stress-strain behaviour and this is observed in figure 7.3b, where the curve fitting process is not entirely satisfactory. The stress-stain behaviour of the 40:60 and 60:40 assemblies with large hard and small soft particles, which is presented in Appendix D is also relatively irregular, which suggests that the internal characteristics of such assemblies are worthy of some study.

The three coefficients of the second-order polynomials presented in figures 7.3 and 7.4 represent the same parameters as those shown in section 6.3. The effect of mixture composition on the polynomial coefficients for the two forms of bimodal assembly are visible in figure 7.5. It would appear from this figure, that only the coefficients for the large soft and small hard particle assemblies are reasonably approximated by exponential functions of the proportion of hard spheres in the assembly, in a similar manner to the monodisperse assembly behaviour presented in figure 6.5. The coefficients for the large hard and small soft particle assemblies show alternative behaviour in figure 7.5, because a rapid increase in the value of p^2 and p^3 around $p \cong 0.5$ followed by a relatively gradual gradient at higher p^2 and p^3 values is observed. The significance of an assembly composition around $p = 0.5$ is again emphasised by these results. Possible explanations for such macroscopic behaviour will be explored later in this chapter.

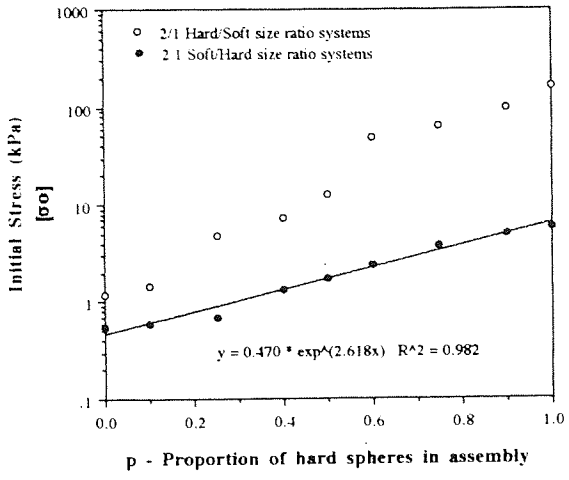

a)

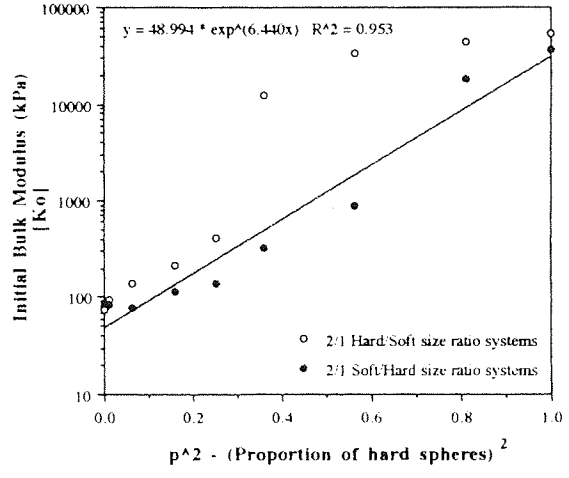

b)

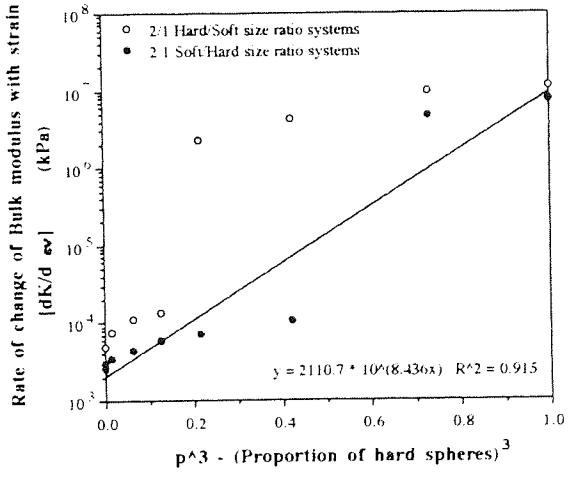

c)

Figure 7.5 Effect of mixture composition on **a**) initial stress state **b**) initial bulk modulus **c**) rate of change of bulk modulus with strain for bimodal assemblies subject to quasi-static compression.;

In order to check that the stress-strain behaviour of the bimodal assemblies was consistent at stress levels associated with die-compaction experiments, the approach described in section 6.3.1 was used. Therefore, the original stress-strain results for some of the bimodal assemblies were replotted using new origins based on stress states greater than those at p_e and these results are presented in figure 7.6. It is clear from this figure that second-order polynomial representation is reasonably accurate for the data shown and the behaviour exhibited by the bimodal assemblies is qualitatively similar to that shown by the monodisperse assemblies in figure 6.6. Further examples of second-order polynomial curve fitting to stress-strain data at die-compaction stress levels for other assemblies, are presented in Appendix D.

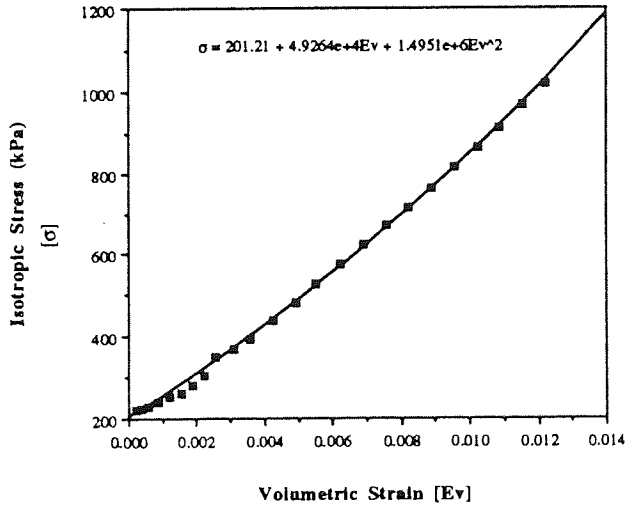

a)

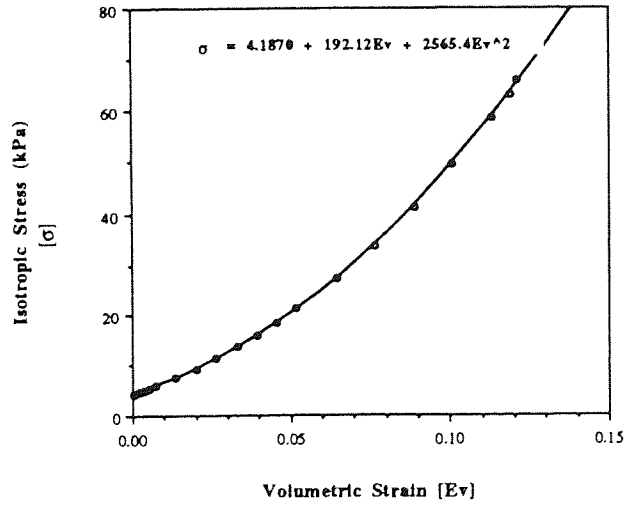

b)

Figure 7.6 Stress-strain curves from bimodal assemblies at specified stress level ground states: **a**) 75/25 hard:soft mix, 2:1 hard/soft size ratio assembly **b**) 50/50 hard/soft mix, 2/1 soft/hard size ratio assembly.;

It was shown in (6.2) in chapter 6, that the bulk modulus of a particle assembly varied linearly with strain. Using the procedure adopted in section 6.3.1, the bulk modulus for bimodal assemblies where p = 0.25, 0.5 and 0.75 was calculated and plotted against the volumetric strain in figures 7.7a, b and c respectively.

a)

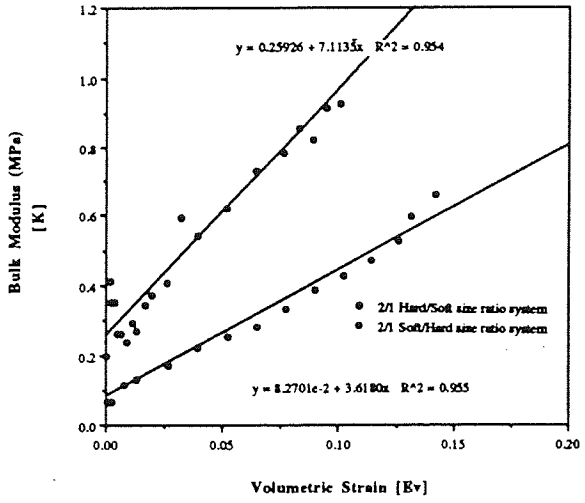

b)

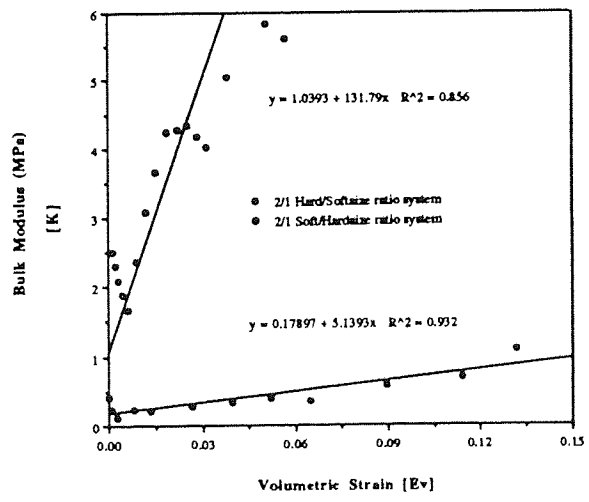

c)

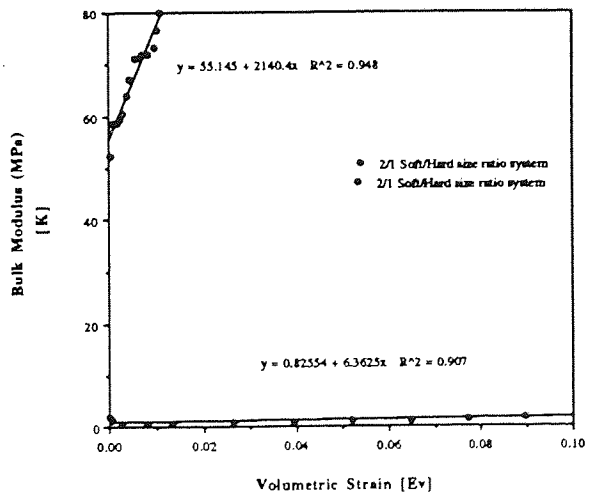

Figure 7.7 Evolution of the bulk modulus with strain for bimodal assemblies **a)** 25:75 hard:soft mix **b)** 50:50 hard:soft mix **c)** 75:25 hard:soft mix;

It can clearly be seen from the data presented in figure 7.7, that the rate of change of bulk modulus with strain is essentially linear for the majority of the bimodal assembly examples. The linearity in bulk modulus-strain behaviour is similar to that observed for the monodisperse assemblies presented in figure 6.7. Closer investigation of the linear relationships presented in figure 7.7, indicates that the coefficients of the relationships are composition-sensitive. Further scrutiny of the bulk modulus-strain data also reveals that, the data obtained from the large hard and small soft particle assemblies is less linear than that observed for the large soft:small hard particle assemblies and the 50:50 hard:soft mix in particular, shows fairly non-linear behaviour. The irregularity of the macroscopic behaviour of the 50:50 large hard:small soft particle assembly has already been observed earlier in this section, and analysis of the internal characteristics of this assembly during compaction should provide a better understanding of such behaviour.

7.3.2 Evolution of structure

The importance of the assembly solid fraction ϕ as a structural parameter for particulate assemblies was explained in section 6.3.2. In figure 7.8 the standard plot from soil mechanics, of ϕ plotted against the logarithm of stress, is shown for an example composition. It is clear from this figure, that the gradients of the curves plotted increase rapidly as the compaction stress is increased and that qualitatively similar behaviour is observed for both the monodisperse and bimodal assemblies during compaction. The general form of the curves presented in figure 7.8 are typical of all the simulations presented in this chapter.

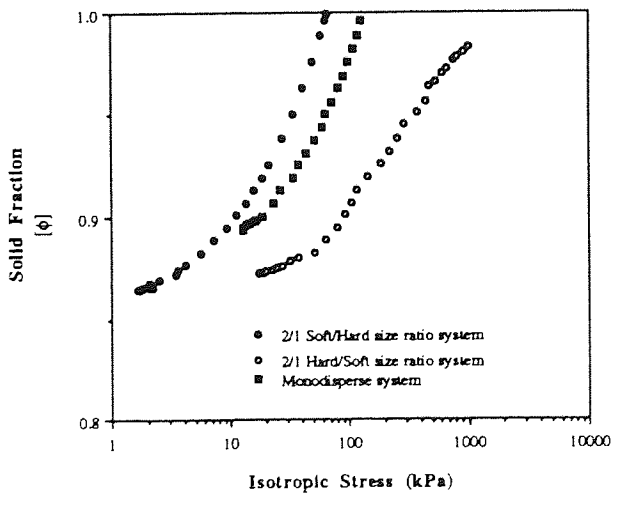

Figure 7.8 The relationship between solid fraction and isotropic stress for the bimodal and monodisperse assemblies with 50/50 hard/soft particles during quasi-static compaction.;

The results presented in section 6.3.2 showed that the linear relationship between ϕ and $(\sigma/\sigma_o)^{1/2}$ proposed by Hardin (1967), where σ_o was the isotropic stress at the elastic percolation threshold, was observed for monodisperse assemblies. The evidence provided in figures 7.9 and 7.10 indicates that linearity between ϕ and $(\sigma/\sigma_o)^{1/2}$ is also generally observed for bimodal assemblies subject to quasi-static compaction.

a)

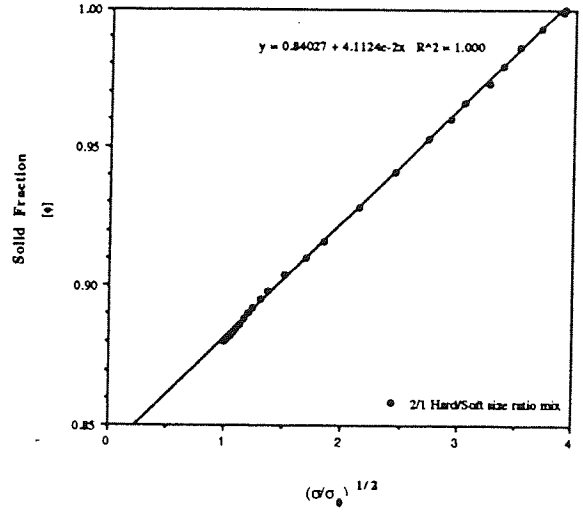

b)

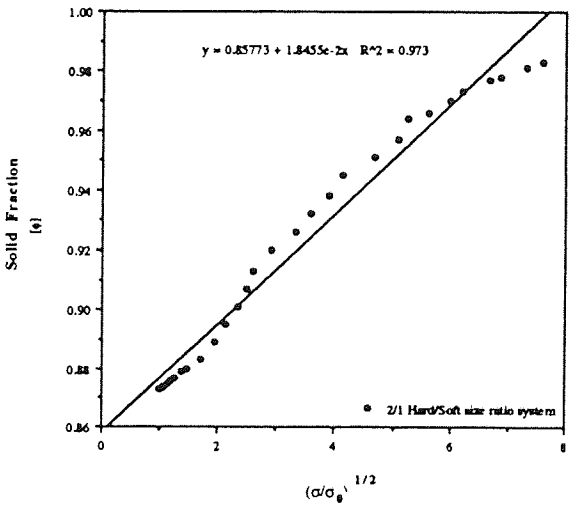

c)

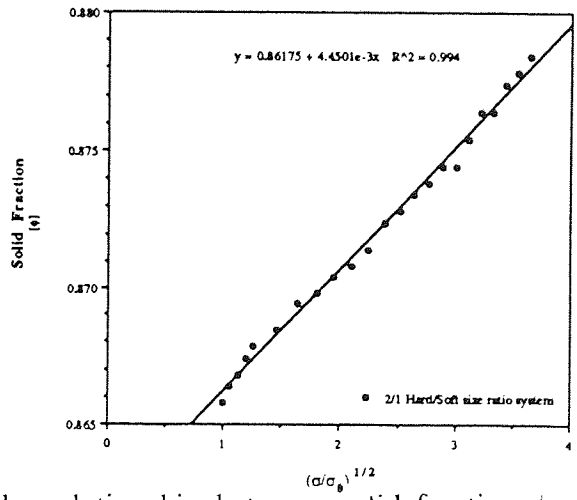

Figure 7.9 The relationship between solid fraction ϕ and $(\sigma/\sigma_o)^{1/2}$ for some 2/1 hard/soft size ratio assemblies **a**) 25/75 hard:soft mix **b**) 50/50 hard/soft mix **c**) 75/25 hard/soft mix;

a)

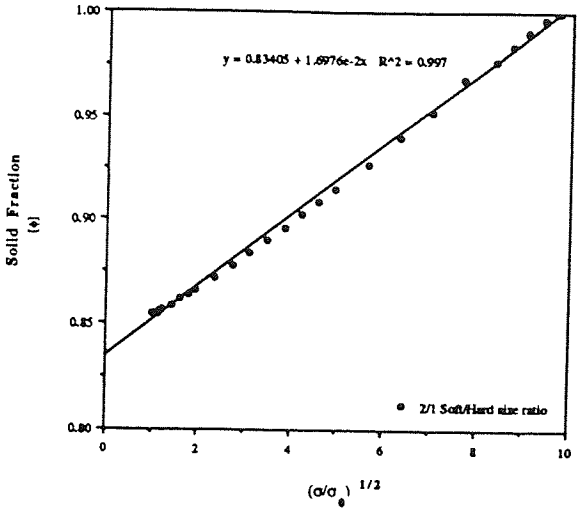

b)

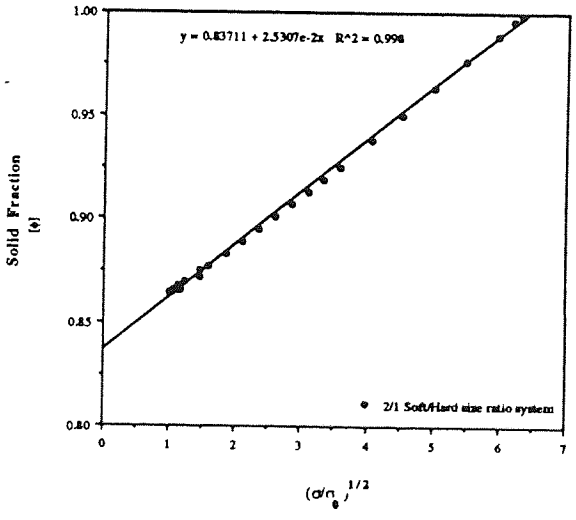

c)

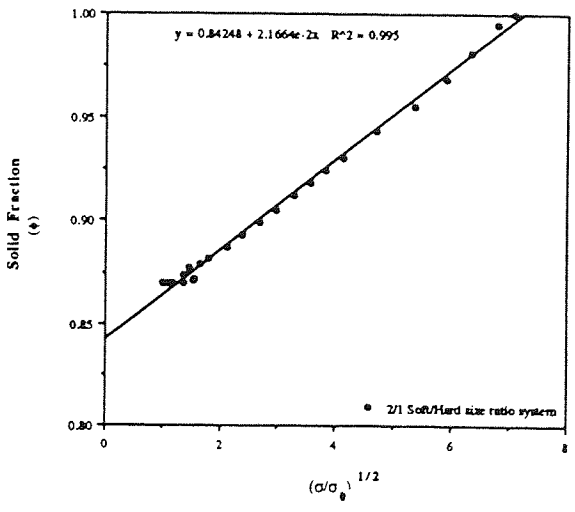

Figure 7.10 The relationship between solid fraction ϕ and $(\sigma/\sigma_o)^{1/2}$ for some 2/1 soft/hard size ratio assemblies **a**) 25/75 hard:soft mix **b**) 50/50 hard/soft mix **c**) 75/25 hard/soft mix;

However, the data from the 50:50 assembly mix with large hard and small soft particles is more random and therefore, a linear relationship provides only an average fit to this data-series. A more detailed interpretation of the relatively random behaviour of this assembly will be provided later in this chapter.

Using (6.11), it is possible to determine the variation of coefficient c with the mixture composition p for the bimodal assemblies and the results of this exercise are plotted in figure 7.11. The curves for both forms of bimodal assembly in figure 7.11 are complex and definitely do not follow the linear relationship between c and p proposed by Hardin (1967). The curve for the assemblies with large hard and small soft particles shows a rapid increase in the value of c up to $p = 0.25$, followed by a rapid decline in the c value between $p = 0.25$ and $p = 0.75$ and no significant change in the gradient when $p > 0.75$. The curve for the assemblies with large soft and small hard particles is qualitatively different and shows a gradual decline in value up to $p = 0.25$, followed by a rapid increase in the gradient between $p = 0.25$ and $p = 0.5$, a very gradual reduction in the gradient between $p = 0.5$ and $p = 0.75$ and finally a sharp drop in the value of c when $p > 0.75$. The qualitative differences between the two curves show that there is a complex relationship between the compositional and geometrical features of a particle assembly, since particle size or composition alone are not responsible for such behaviour.

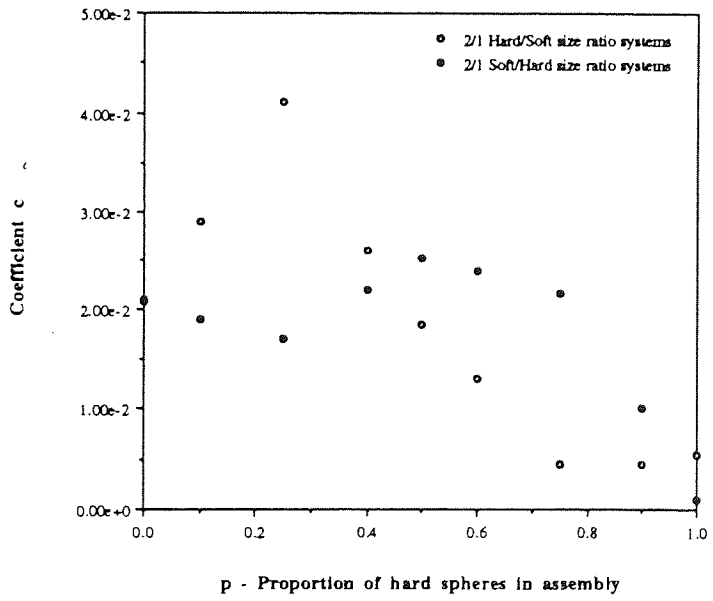

Figure 7.11 The variation of coefficient c with mixture composition p for the bimodal assemblies subject to quasi-static compaction.;

The relationship between contact density C, which is another important micromechanical assembly parameter, and solid fraction ϕ for some example bimodal assemblies is presented in figure 7.12.

a)

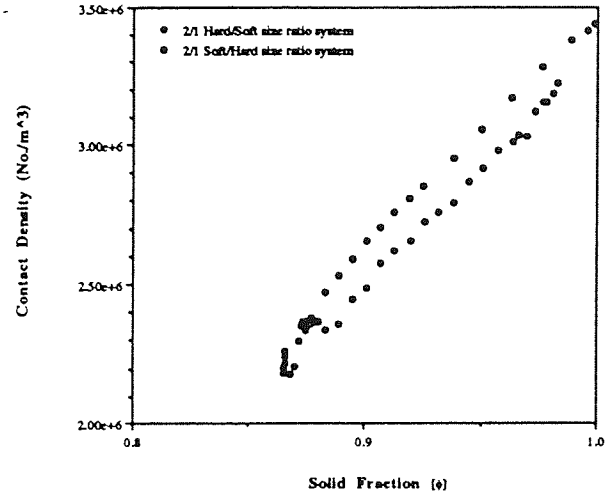

b)

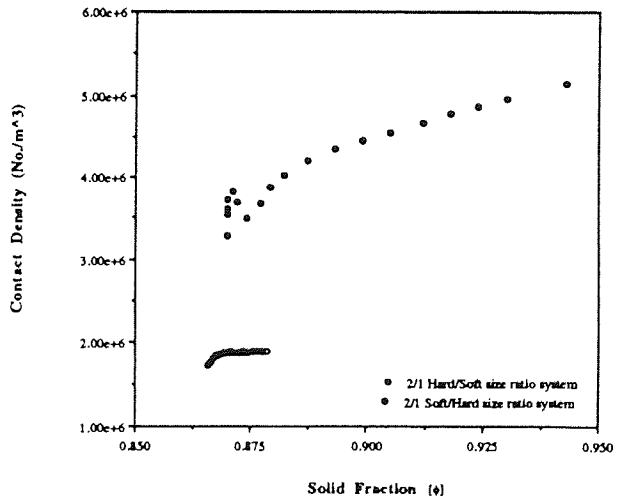

c)

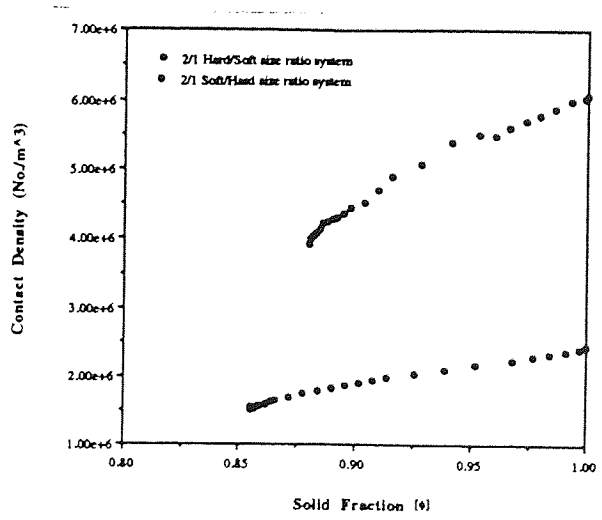

Figure 7.12 Evolution of contact density with solid fraction for some bimodal assemblies **a**) 50/50 hard/soft mix **b**) 25/75 hard/soft mix **c**) 75/25 hard/soft mix.;

In general for each assembly composition shown in figure 7.12, similar qualitative behaviour is observed for the two forms of bimodal assembly. For the 50:50 hard:soft particle mix in figure 7.12a, only slight quantitative differences between the large hard:small soft and large soft:small hard particle assemblies are observed. However, as the percentage of large particles with either a hard or soft composition in an assembly goes above 50%, a rapid increase in the value of C is observed in figures 7.12b and c. High values of C are not obtained in the assemblies with the same value of p, but composed predominantly of small particles and therefore, marked quantitative differences between the curves from these two types of assembly are observed in figures 7.12b and c. It is useful to suggest here that such behaviour is probably caused by the internal geometric arrangement of the assemblies, and evidence presented later in this chapter will support such an idea.

The importance of the geometric Z_g and mechanical Z_m co-ordination numbers to assembly behaviour were highlighted in section 6.3.2, where plots of the evolution of Z_g and Z_m with solid fraction for bimodal assemblies were presented. A similar procedure can be adopted for the bimodal assemblies studied in this chapter and figure 7.13 is the result. For assemblies with low percentages of large particles, such as those shown in figures 7.13a and b, the development of Z_g and Z_m during compaction is qualitatively and quantitatively similar. However, from data presented in figure 7.13c and Appendix D, figures D11 - D12, for assemblies with 75% large particles, the quantitative evolution of Z_g and Z_m with ϕ appears to be dependent upon the stiffness of the large particles. Therefore in figure 7.13c, where 75% of the particles are large and hard the Z_g and Z_m curves are quantitatively different, but in figure D12 presented in Appendix D for an assembly with 75% large soft particles, the curves are quantitatively similar. The results indicate that the development of particle connectivity within an assembly during compaction is sensitive to the elastic behaviour of the components of the particle network. The validity of this point of view will be shown later in this chapter.

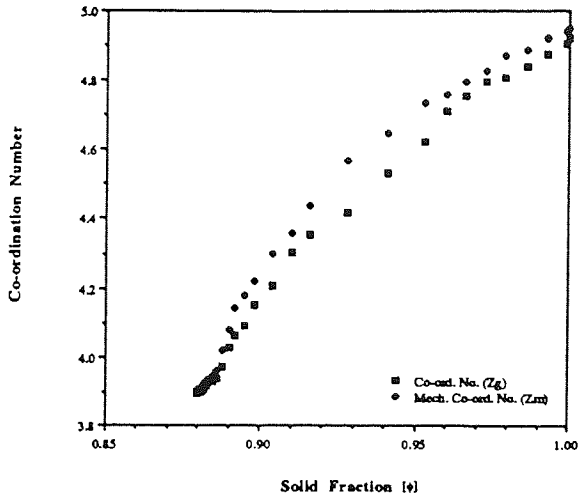

a)

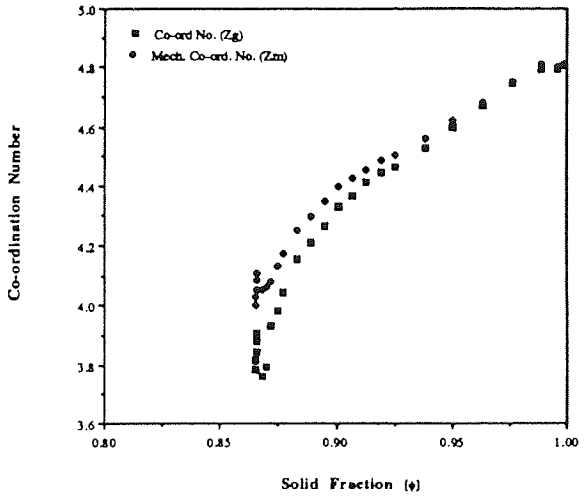

b)

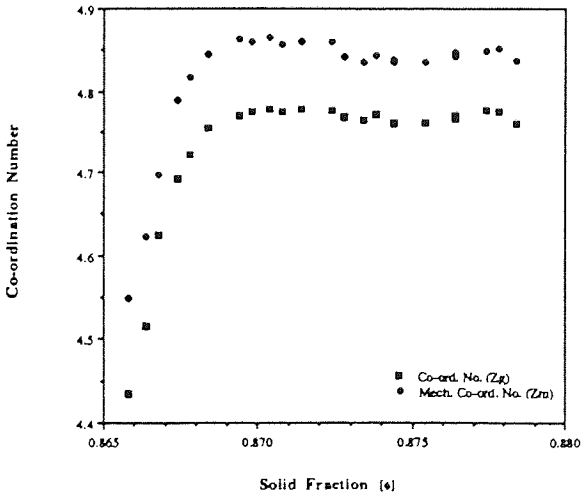

c)

Figure 7.13 Evolution of geometric co-ordination number Z_g and mechanical co-ordination number Z_m with solid fraction for **a**) p = 0.25, 2/1 hard/soft size ratio assembly **b**) p = 0.5, 2/1 soft/hard size ratio assembly **c**) p = 0.75, 2/1 hard/soft size ratio assembly.

7.4 Visual observations

All the figures presented in this section were generated for the example bimodal assemblies at the stress levels shown in figure 7.14. The stress levels were selected to represent typical compaction behaviour for the particle mixes.

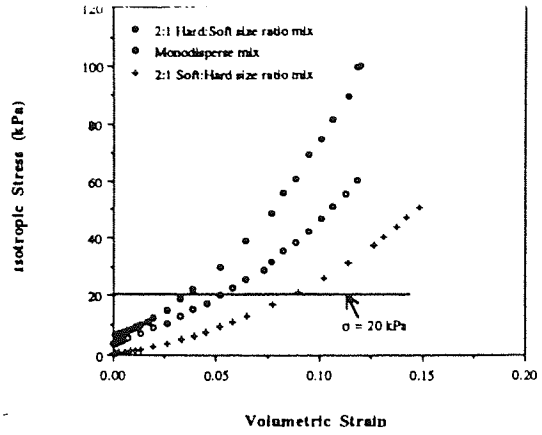

a)

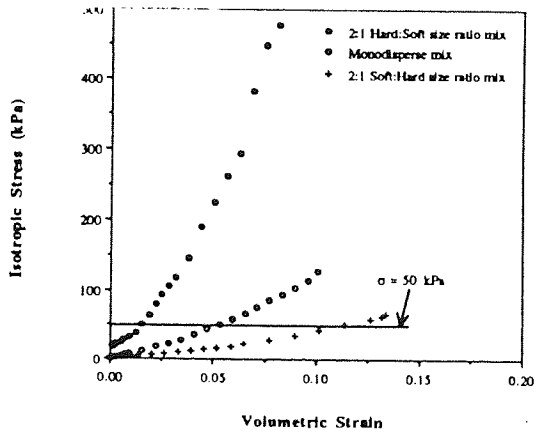

b)

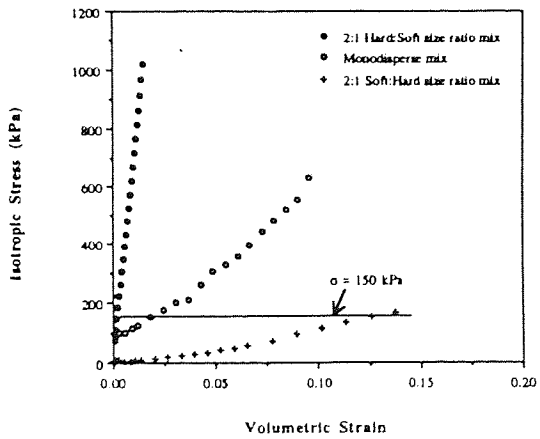

c)

Figure 7.14 Selected stress levels for visual observation of bimodal assemblies **a**) 25/75 hard/soft mix (σ = 20 kPa)
b) 50/50 hard/soft mix (σ = 50 kPa)
c) 75/25 hard/soft mix (σ = 150 kPa).

The assembly connection diagram provides details of assembly connectivity and figure 7.15 shows the assembly connection diagrams for the monosized and bimodal systems for the 25:75 hard:soft mix at a stress level of σ = 20 kPa. Dodds (1975) found that for a random, two-dimensional assembly if the ratio of the largest and smallest discs in a bimodal system was less than 6.46, then a small disc would not fit inside the cavity within a triangle formed by three large discs in contact, which was an indicator of perfect packing. This finding indicates that efficient packing of particles within the bimodal assemblies is not expected because the ratio between the large and small spheres is only 2.0. Dodd's ideas are confirmed by the evidence presented in figure 7.15. In figure 7.15a, the connection diagram for the monosized system shows that the connection regions are not exactly, equally sized but a lot of dense, almost regularly packed regions. If the size of the soft particles are reduced, then figure 7.15b indicates that fewer 'dense packed' zones are visible in the connection diagram but the connectivity is still evenly distributed across the assembly. However, if the size of the hard particles in the assembly is reduced, then figure 7.15c shows that there are now no 'dense packed' zones of any significant size and a significant number of large, irregular shaped voids are present. The behaviour observed in figure 7.15 is supported by the images of the particle packing structures for the same assemblies, which are shown in figure 7.16. The dark particles used for both types of particles in the assemblies shown in this figure, help to highlight the pore structures visible at σ = 20 kPa. The calculation of important microstructural parameters such as the solid fraction ϕ and mechanical co-ordination number Z_m during a simulation experiment was also undertaken to provide further support to the ideas generated by the visual evidence.

a)

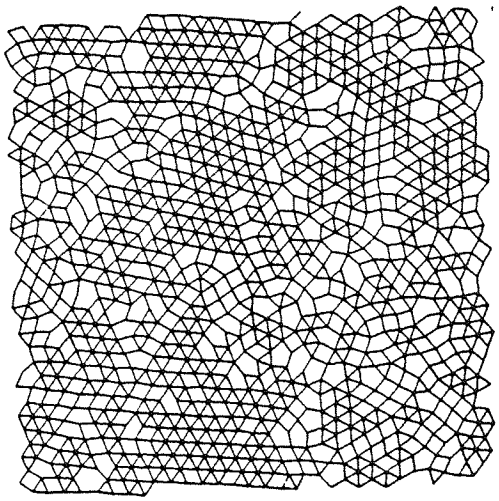

Z_m = 4.858
ϕ = 0.932

b)

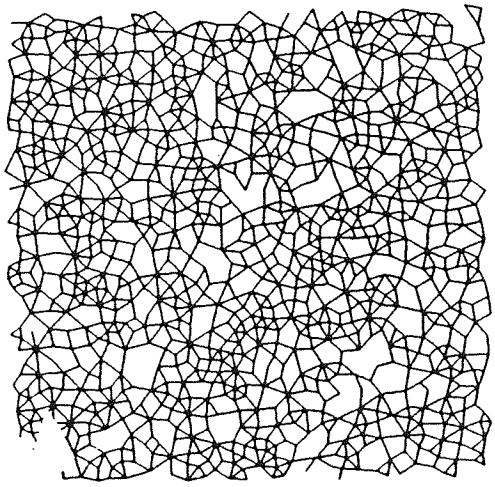

Z_m = 4.392
ϕ = 0.916

c)

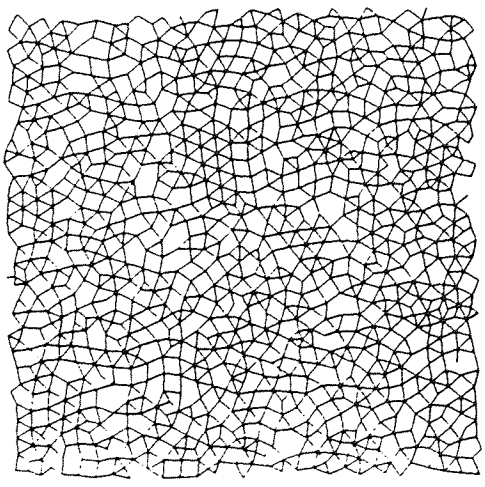

Z_m = 4.786
ϕ = 0.922

Figure 7.15 Connection diagram for the 25/75 hard/soft mix subject to quasi-static compaction (σ = 20 kPa).
a) Monosized assembly **b**) 2/1 hard/soft size ratio assembly
c) 2/1 soft/hard size ratio assembly.;

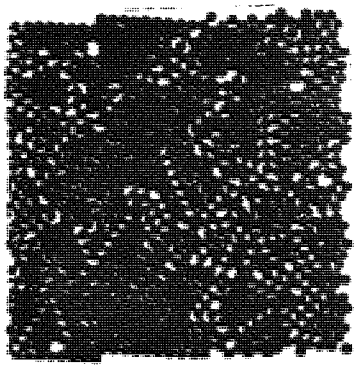

a)

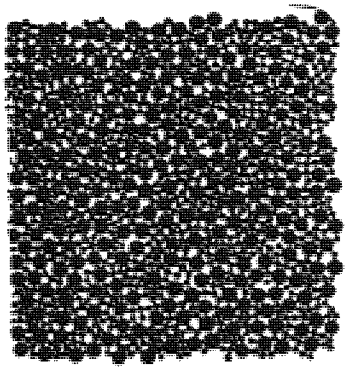

b)

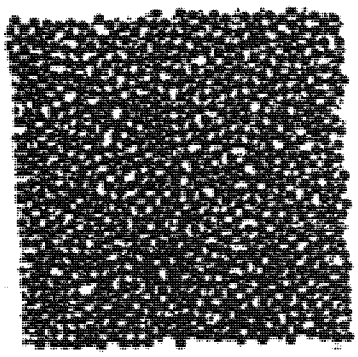

c)

Figure 7.16 Particle packing structures for the 25/75 hard/soft mix subject to quasi-static compaction (σ = 20 kPa).
a) Monosized assembly **b**) 2/1 hard/soft size ratio assembly
c) 2/1 soft/hard size ratio assembly.;

Figures 7.17 and 7.18 provide respectively, a comparison between the connection diagrams for the 50:50 hard:soft mixtures at a stress level of 50 kPa and supporting particle packing structure evidence.

a)

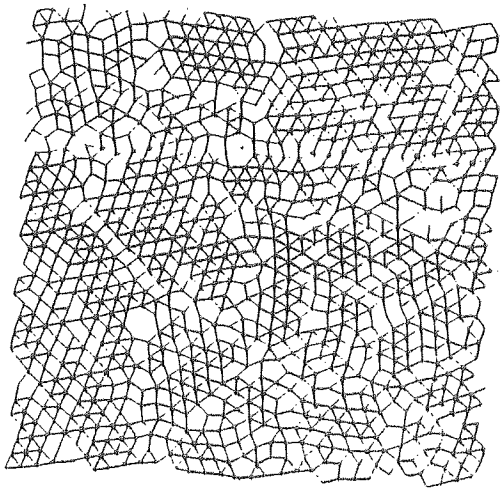

Z_m = 4.851
ϕ = 0.937

b)

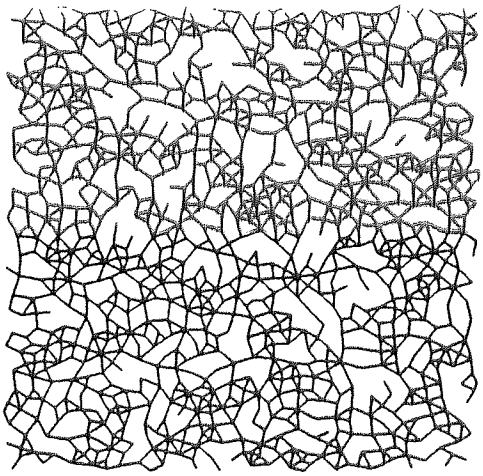

Z_m = 4.119
ϕ = 0.883

c)

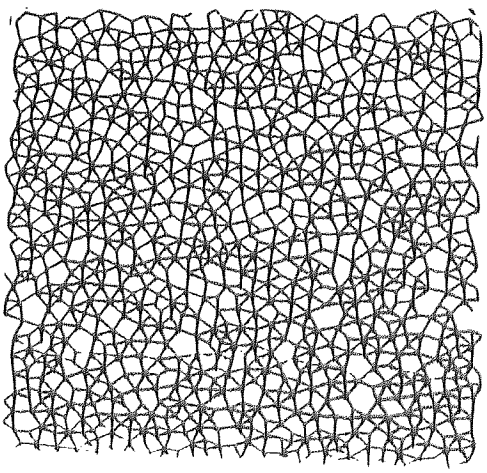

Z_m = 4.752
ϕ = 0.976

Figure 7.17 Connection diagram for the 50:50 hard:soft mix subject to quasi-static compaction (σ = 50 kPa).
a) Monosized assembly b) 2:1 hard:soft size ratio assembly
c) 2:1 soft:hard size ratio assembly.;

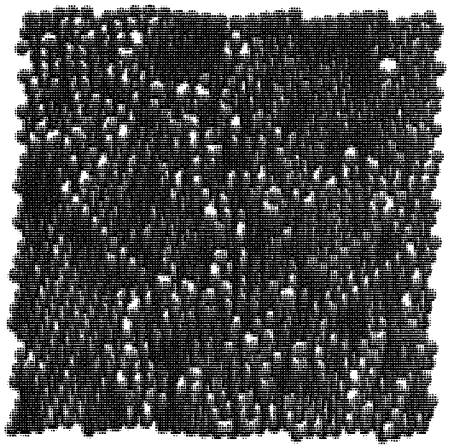

a)

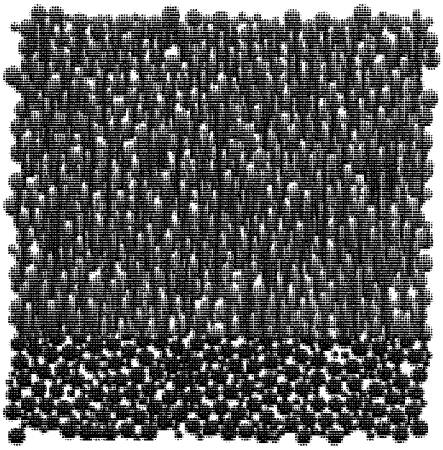

b)

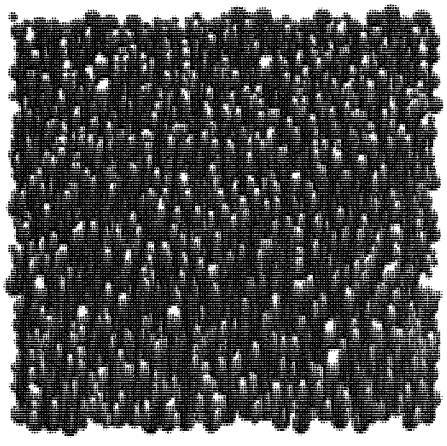

c)

Figure 7.18 Particle packing structures for the 50:50 hard:soft mix subject to quasi-static compaction (σ = 50 kPa).
a) Monosized assembly b) 2:1 hard:soft size ratio assembly
c) 2:1 soft:hard size ratio assembly.;

For the monosized assembly presented in figure 7.17a, a large proportion of the assembly connection diagram consists of regular 'dense-packed' regions and this is confirmed by the particle packing structure visible in figure 7.18a. If the size of the soft spheres in the assembly is reduced, then figure 7.17b shows that the connection diagram consists of relatively few, small dense packed zones, which are composed of randomly distributed, large irregular shaped voids. It is also important to note that a large number of dead end connections are visible in the same diagram. Figure 7.18b shows that a more irregular particle packing structure is observed for this assembly. The irregularity visible in figures 7.17b and 7.18b must cause the irregular macroscopic behaviour observed for this assembly in section 7.3, because large-scale assembly characteristics are dependent upon the internal assembly structure. If the size of the hard spheres in the assembly is reduced, figure 7.17c indicates that connectivity is evenly distributed in the assembly and many small 'dense packed' zones are visible. The visual evidence from the particle packing structure presented in figure 7.18c supports this argument.

The structures visible in the connection diagrams for the assemblies with 75% hard particles are presented in figure 7.19 and the corresponding particle packing structure diagrams are shown in figure 7.20. In figure 7.19a, the connection diagram for the monosized assembly indicates that although the assembly is at a higher strain level, there are fewer and smaller 'dense packed' zones due to the large number of hard particles present. If the size of the soft particles is reduced, figure 7.19b shows that connectivity within the assembly is relatively evenly distributed. However, this distribution is not quite as well distributed as that for the small hard sphere system presented in figure 7.19c, because more irregularly shaped voids are present in figure 7.19b. The particle packing structures presented in figure 7.20 and parameters such as ϕ and Z_m tend to support such observations.

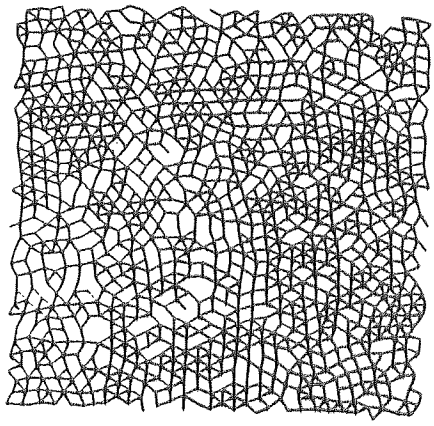

Z_m = 4.824
ϕ = 0.919

a)

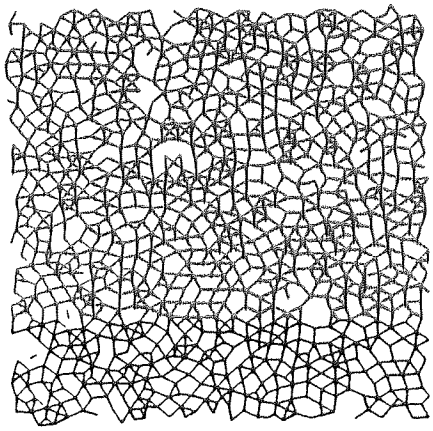

Z_m = 4.847
ϕ = 0.868

b)

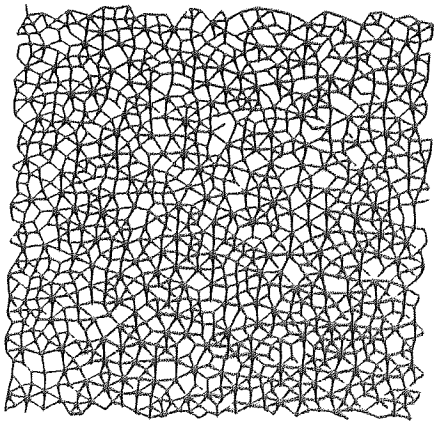

Z_m = 4.70
ϕ = 0.989

c)

Figure 7.19 Connection diagram for the 75:25 hard:soft mix subject to quasi-static compaction (σ = 150 kPa).
a) Monosized assembly b) 2:1 hard:soft size ratio assembly
c) 2:1 soft:hard size ratio assembly.;

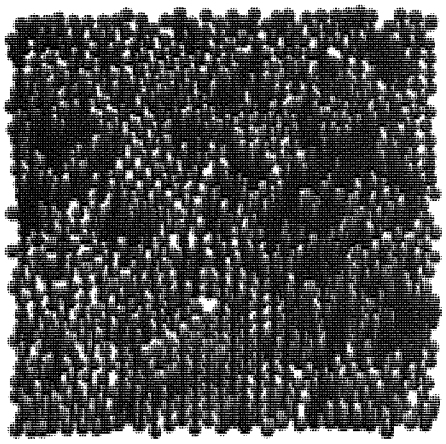

a)

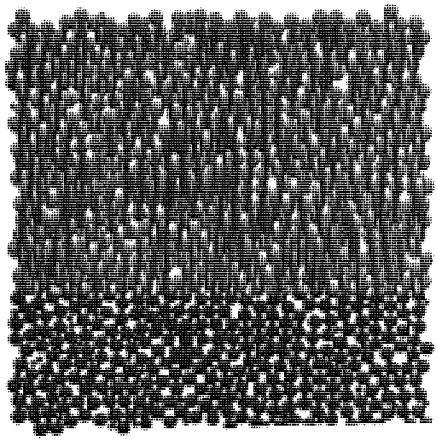

b)

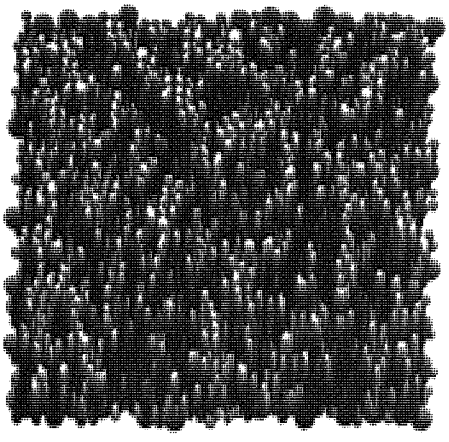

c)

Figure 7.20 Particle packing structures for the 75:25 hard:soft mix subject to quasi-static compaction (σ = 150 kPa).
a) Monosized assembly b) 2:1 hard:soft size ratio assembly
c) 2:1 soft:hard size ratio assembly.;

The particle contact force network for the bimodal size mixtures subjected to quasi-static compaction is shown for different mixture compositions in figures 7.21, 7.22 and 7.23. In the figures, the thickness of the lines indicate the magnitude of the force scaled to the current maximum. Figure 7.21, shows the contact force networks for 25:75 hard:soft particle mixes.

a)

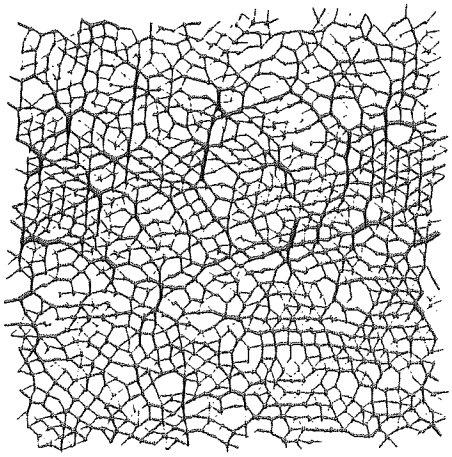

b)

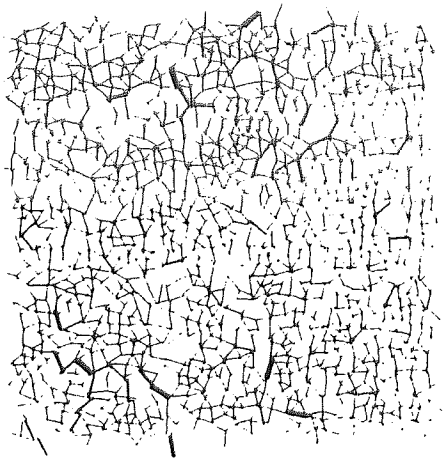

c)

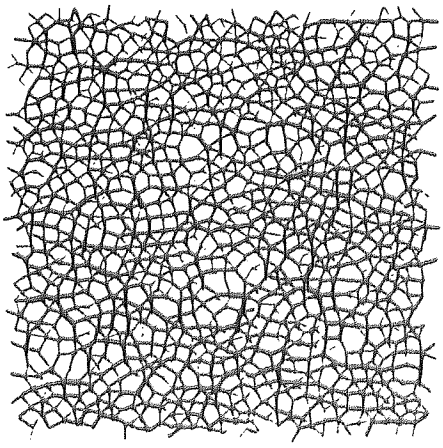

Figure 7.21 Contact force networks for 25/75 hard/soft mixes subject to quasi-static compaction (σ = 20 kPa).
a) Monosized assembly b) 2/1 hard:soft size ratio assembly
c) 2/1 soft:hard size ratio assembly.;

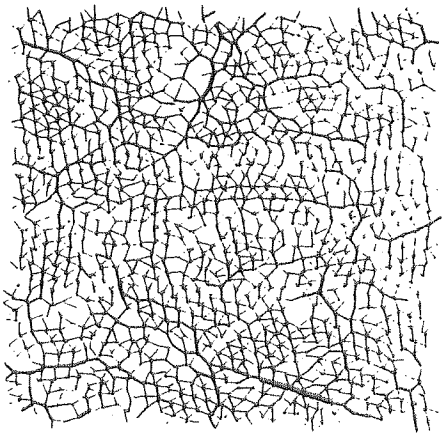

a)

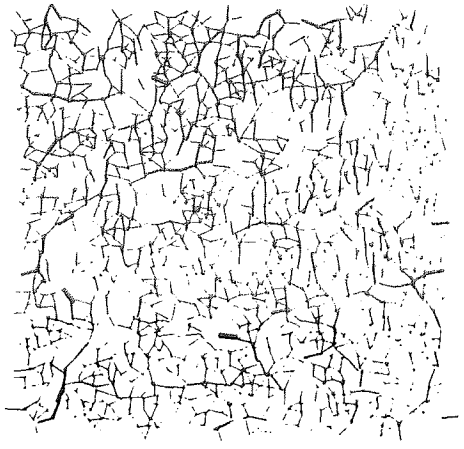

b)

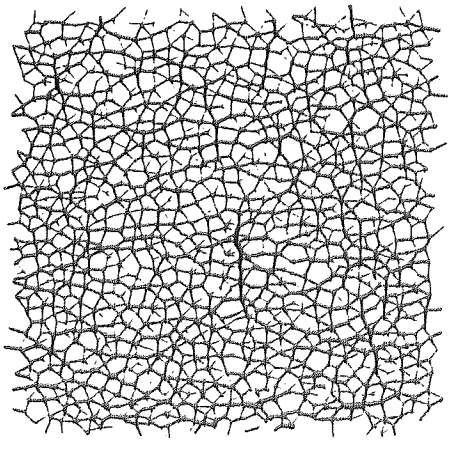

c)

Figure 7.22 Contact force networks for 50:50 hard:soft mixes subject to quasi-static compaction (σ = 50 kPa).
a) Monosized assembly **b**) 2:1 hard:soft size ratio assembly
c) 2:1 soft:hard size ratio assembly.;

For the monosized assembly presented in figure 7.21a, a relatively uniform distribution of contact forces is visible. However, a few significantly higher forces are visible, which must occur at contacts between two hard spheres from the assembly contact force information presented in section 7.5. The size of soft spheres in the assembly is decreased in figure 7.21b. The line thickness is scaled to the current maximum and it would therefore appear that, there are a few very large contact forces (presumably between two hard particles) which distort the scaling and this makes it difficult to interpret the figure. Figure 7.21c shows the contact force network when the size of the hard particles in the assembly is reduced and indicates that there is a much more uniform overall distribution of contact force magnitudes.

Figure 7.22 shows the contact force networks for 50:50 hard:soft particle mixes at a stress level of $\sigma = 50$ kPa. The force network presented in figure 7.22a for the monosized assembly has a fairly uniform distribution of contact forces, except for a small number of strong force chains. If the size of the soft particles in the assembly is reduced then figure 7.22b indicates that, there are more large forces present than those observed in figure 7.21b. These large forces again tend to make it difficult to comment on the distribution of the forces within the assembly and hence its influence on the unusual macroscopic assembly behaviour reported in section 7.3. In contrast, figure 7.22c shows that is fairly easy to observe a relatively uniform distribution of contact forces for the large soft:small hard particle assembly.

Different contact force networks are observed for the 75:25 hard:soft mixes in figure 7.23, where the majority of particles in the assemblies are hard.

a)

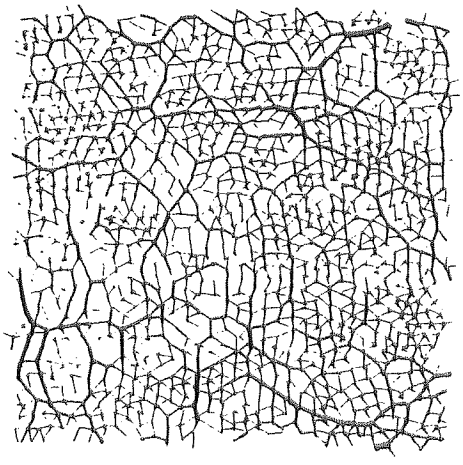

b)

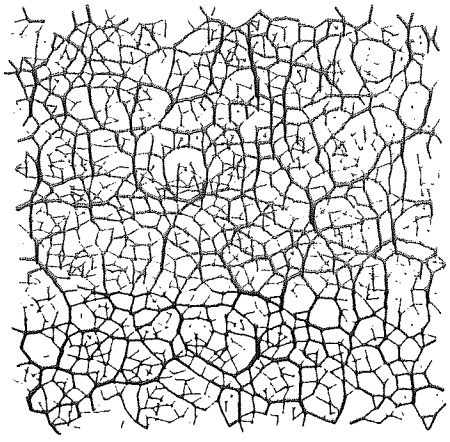

c)

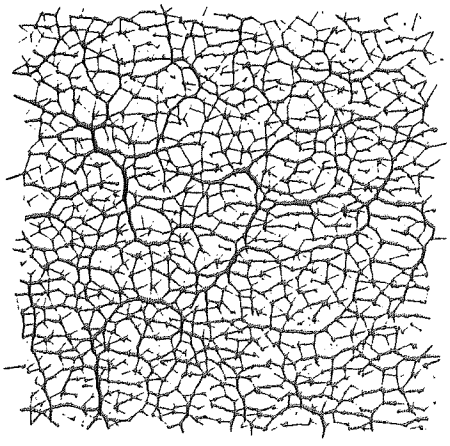

Figure 7.23 Contact force networks for 75:25 hard:soft mixes subject to quasi-static compaction (σ = 150 kPa).
a) Monosized assembly b) 2:1 hard:soft size ratio assembly
c) 2:1 soft:hard size ratio assembly.;

For the monosized assembly in figure 7.23a, a few strong force chains are seen and there is a relatively uniform distribution of the force chains. When the minority of particles in the assembly are small soft spheres, these allow the large hard spheres to dominate. Therefore, a uniform force distribution is observed in figure 7.23b. Figure 7.23c indicates that, with a majority of small hard particles in the assembly the contact force distribution is no longer as uniform as those observed for assemblies with lower percentages of hard particles.

7.5 Microstructural parameters

No previous work on the effects of particle size on the development of particle assembly microstructural characteristics such as the contact force distribution, has been encountered by the author. In this section, data obtained for the 25:75, 50:50 and 75:25 hard/soft particle systems will be presented to illustrate the effect of mixture sizes on the distribution of contact force, contact area and mean contact pressure. The corresponding contact data distributions for other mixtures are presented in Appendix D, figures D14 - D19.

The contact force distributions were determined at the stress levels indicated in figure 7.9. Figures 7.24, 7.25 and 7.26 show the contact force distributions for the monodisperse and two bimodal size mixtures, for the selected hard/soft mixtures.

As demonstrated in Chapter 6, for monodisperse systems, hard particles tend to produce exponential distributions of the contact forces whereas soft particles produce more Gaussian-like distributions. If the proportion of hard particles is increased the contact force distribution becomes more exponential, if the proportion of soft particles is increased the contact force distribution becomes more Gaussian. It can be seen by comparing figures 7.24, 7.25 and 7.26 that this is true for bimodal mixtures. What can also be seen is that, for all mix proportions, the contact force distribution becomes more exponential if the size of the soft particles is reduced and more Gaussian if the hard particles are reduced in size.

The qualitative relationships between contact force distributions and contact force networks for monosized assemblies were discussed in chapter 6, and it is clear from examining the force network figures 7.21, 7.22 and 7.23 and the respective force distribution figures 7.24, 7.25 and 7.26, that similar relationships exist for bimodal assemblies.

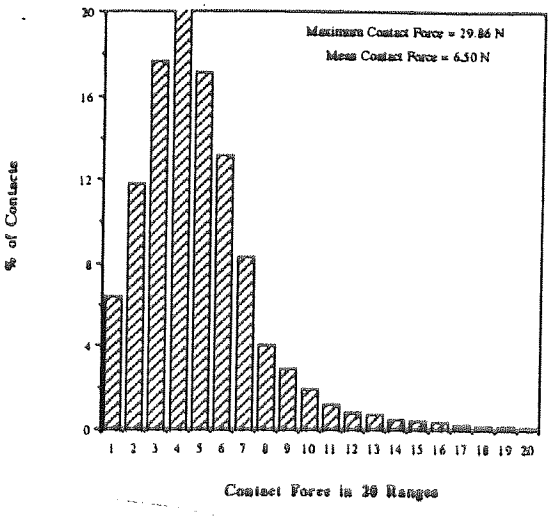

a)

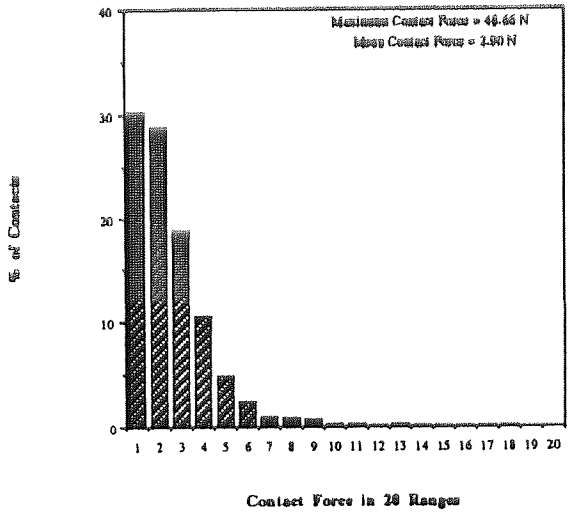

b)

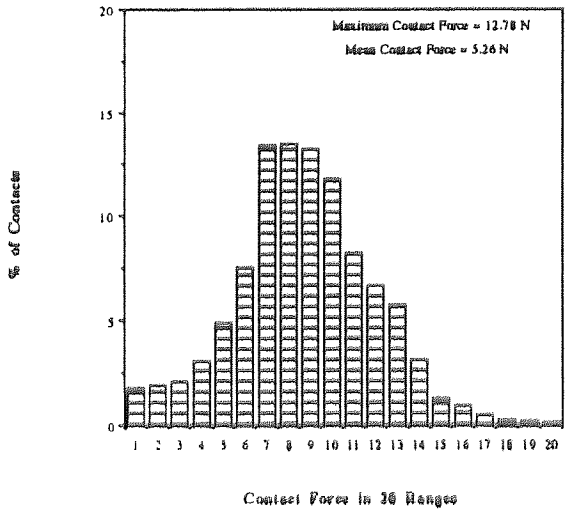

c)

Figure 7.24 Contact force distributions for 25/75 hard/soft mixtures at $\sigma = 20$ kPa **a)** Monodisperse assembly **b)** 2/1 hard/soft size ratio assembly **c)** 2/1 soft/hard size ratio assembly.:

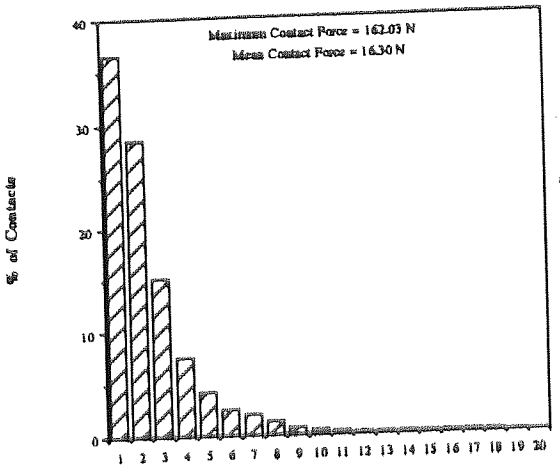

a)

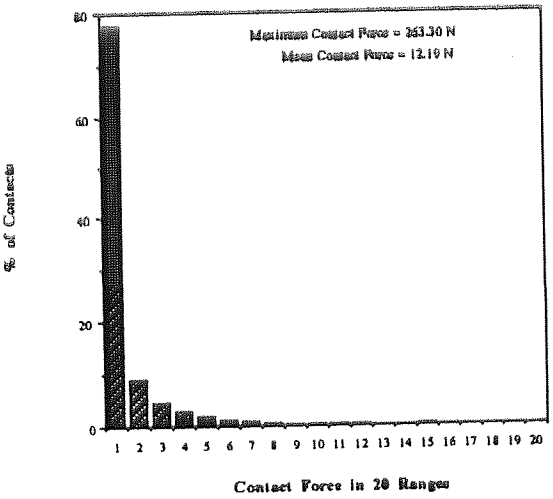

b)

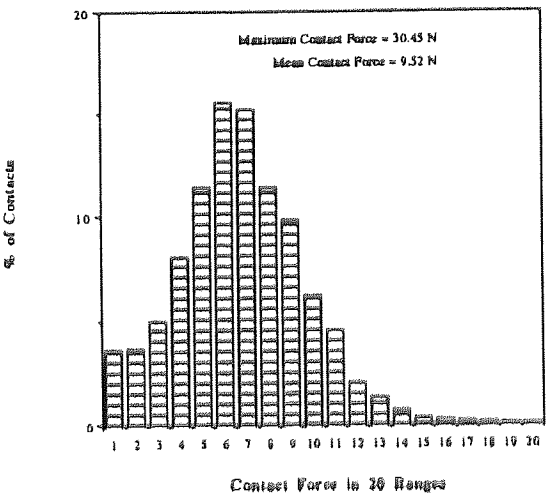

c)

Figure 7.25 Contact force distributions for 50/50 hard/soft mixtures at $\sigma = 50$ kPa **a)** Monodisperse assembly **b)** 2/1 hard/soft size ratio assembly **c)** 2/1 soft/hard size ratio assembly.;

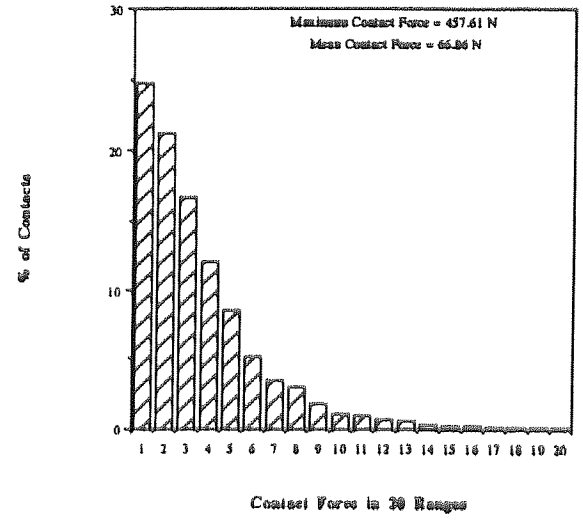

a)

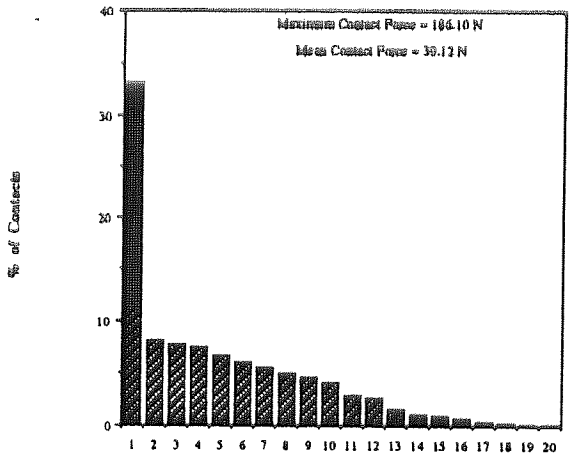

b)

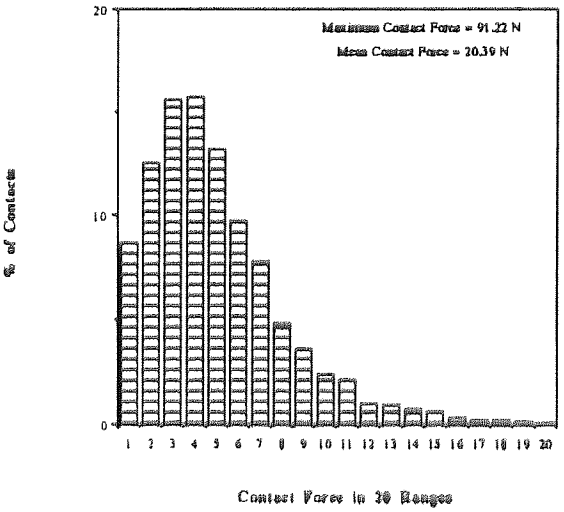

c)

Figure 7.26 Contact force distributions for 75/25 hard/soft mixtures at $\sigma = 150$ kPa **a)** Monodisperse assembly **b)** 2/1 hard/soft size ratio assembly **c)** 2/1 soft/hard size ratio assembly.;

The contact area distributions for bimodal and monodisperse assemblies with composition p = 0.25, 0.5 and 0.75 are presented in figures 7.27, 7.28 and 7.29 respectively. In figures 7.27a, 7.28a and 7.29a, bimodal distributions are observed for the monodisperse mixtures because the hard/hard contacts have a narrow range of very small contact areas, whilst the hard/soft and soft/soft contacts have a much broader range of contact areas. The contact area distributions for the large hard/small soft particle assemblies in figures 7.27b, 7.28b and 7.29b show the effects of increasing the number of large hard particles in a system on the contact behaviour. In figure 7.27b, the majority of particles in the assembly are soft and an essentially Gaussian distribution is observed. If the proportion of hard spheres is increased to p = 0.5, then a Gaussian distribution is still observed. However, figure 7.29b indicates that when the large hard particles are the major component in the system, the hard/hard contacts with their small contact areas form a contact distribution that is skewed towards low contact areas but the other contact types still exhibit Gaussian distributions. The influence of assembly composition on contact area behaviour is also examined for the large soft/small hard assemblies in figures 7.27c, 7.28 c and 7.29c. When the majority of the particles in this bimodal system are soft, figure 7.27c shows that an essentially Gaussian distribution is observed. If the numbers of small hard particles in the system are increased, then figures 7.28c and 7.29c show that the hard/hard particle contacts exhibit contact area distributions that become increasingly skewed towards low contact areas. The contacts involving soft particles still exhibit Gaussian distributions in figures 7.28c and 7.29c, but the size of the distributions becomes reduced as the number of hard particles in the assembly is increased. The evidence presented in figures 7.27, 7.28 and 7.29 therefore suggests that, geometric factors within a particle assembly i.e. particle size, have only a minor influence on the development of the assembly contact area distribution

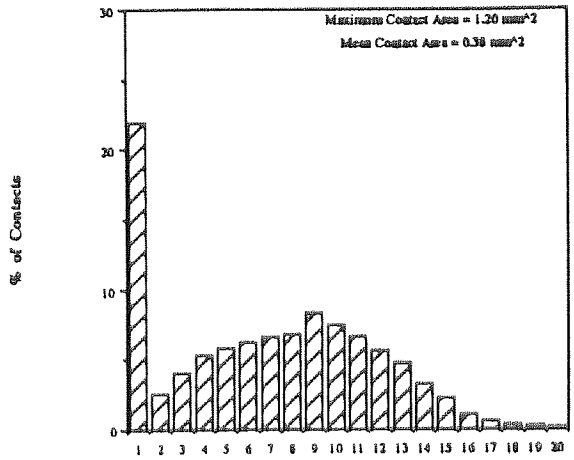

a)

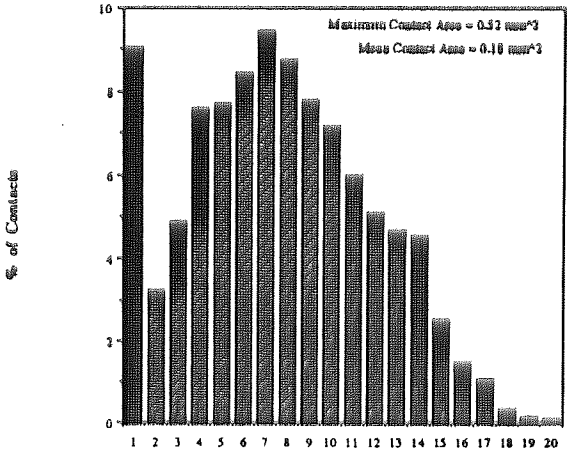

b)

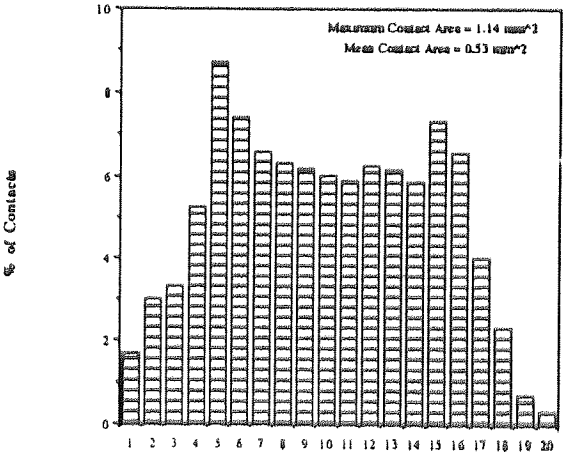

c)

Figure 7.27 Contact area distributions for 25/75 hard/soft mixtures at $\sigma = 20$ kPa **a)** Monodisperse assembly **b)** 2/1 hard/soft size ratio assembly **c)** 2/1 soft/hard size ratio assembly.;

a)

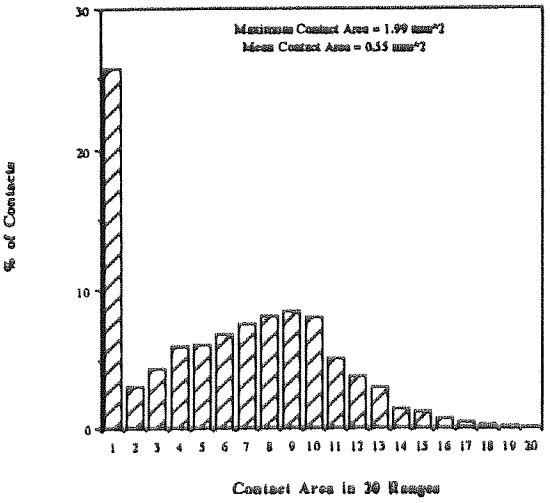

b)

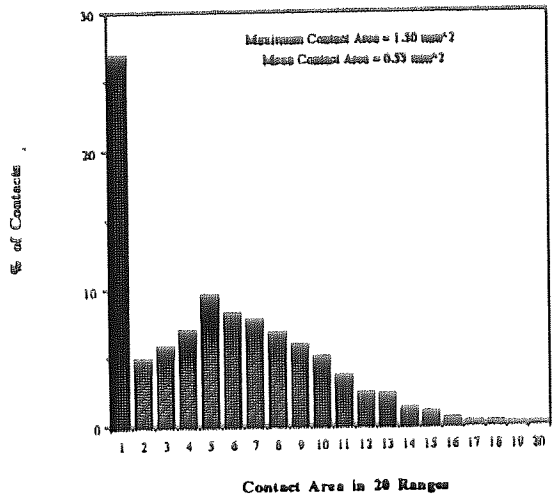

c)

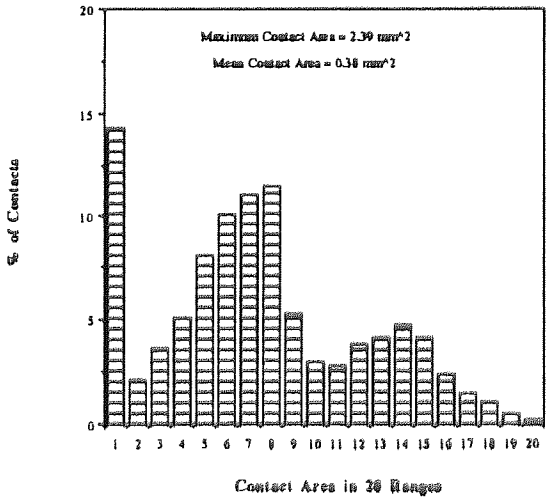

Figure 7.28 Contact area distributions for 50/50 hard/soft mixtures at $\sigma = 50$ kPa a) Monodisperse assembly b) 2/1 hard/soft size ratio assembly c) 2/1 soft/hard size ratio assembly.;

a)

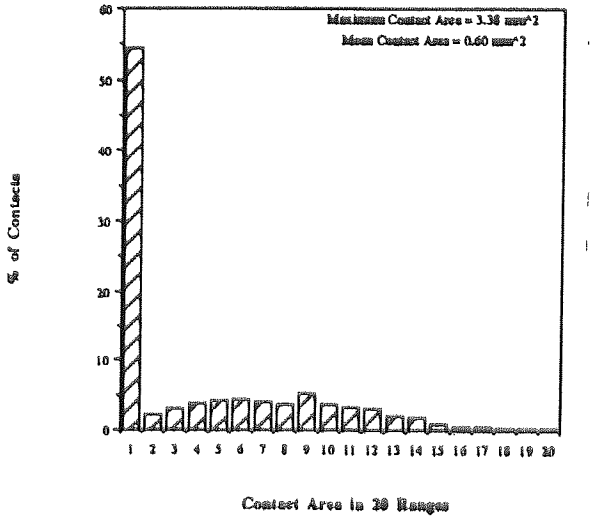

b)

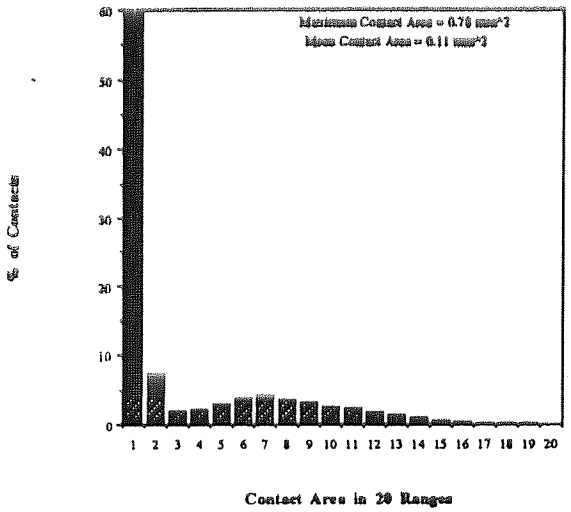

c)

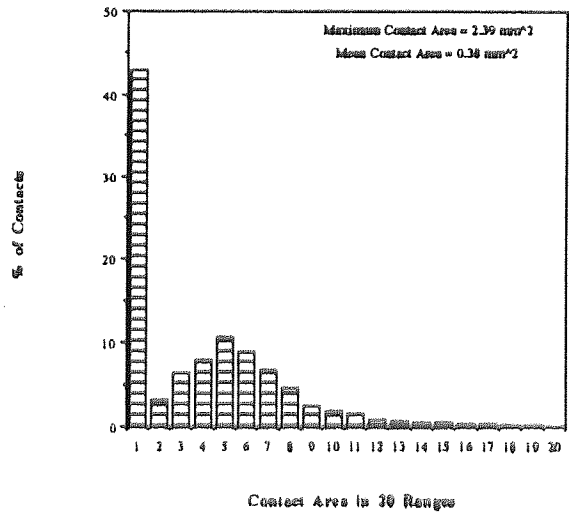

Figure 7.29 Contact area distributions for 75/25 hard/soft mixtures at $\sigma = 150$ kPa **a)** Monodisperse assembly **b)** 2/1 hard/soft size ratio assembly **c)** 2/1 soft/hard size ratio assembly.;

The size of the particles within an assembly also affects the form of the observed contact pressure distributions for both monodisperse and bimodal assemblies shown in figures 7.30, 7.31 and 7.32. The pressure distributions for monodisperse assemblies with composition $p = 0.25, 0.5$ and 0.75 are presented in figures 7.30a, 7.31a and 7.32a respectively. The figures indicate that there are a large percentage of contacts with very small contact pressures in the first data ranges of the assemblies. If the number of hard particles in the assembly is increased, figures 7.30a to 7.32a show that the numbers of contacts with pressures in the first data range is reduced and the number of contacts with higher contact pressures in a Gaussian-like distribution is increased. The contact pressure behaviour of bimodal assemblies with large hard and large soft particles and composition $p = 0.25$ is shown in figures 7.30b and 7.30c respectively. The data in figure 7.30c indicates that the presence of large soft particles in the assembly eliminates the small number of high contact pressure contacts. If the proportion of hard spheres in a large hard particle assembly is increased to $p = 0.5$, then figure 7.31b shows that more high contact pressure contacts are present in the assembly. The reduction in the size of the first data range suggests that the influence of soft particles on the microstructural behaviour of the assembly is reduced, since contacts involving these particles generate low contact pressures. The reduction of the soft particle influence on the microstructural behaviour of the large hard assembly, as the number of soft particles decreases, is also shown in figure 7.32b. When the proportion of hard spheres in an assembly with large soft particles is greater than $p = 0.25$, then the contact pressure distributions in figures 7.31c and 7.32c show that increasing numbers of high contact pressure contacts are present in the assemblies. However, the large soft particles appear to still play a significant role in the microstructural behaviour of these assemblies, because a high percentage of contacts have low contact-pressure values, even for $p = 0.75$ in figure 7.32c. The influence of large soft particles on the contact pressure distributions for bimodal assemblies is therefore worthy of further study.

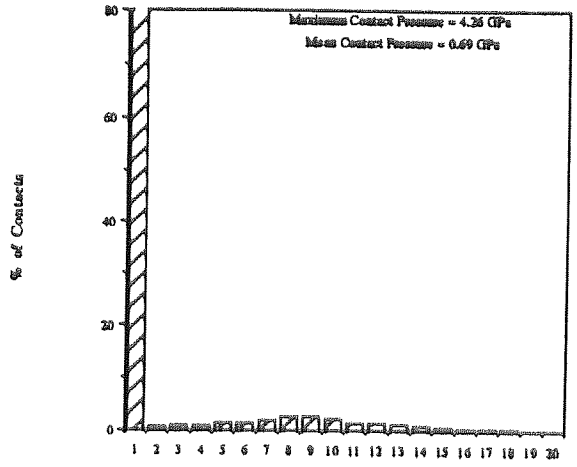

a)

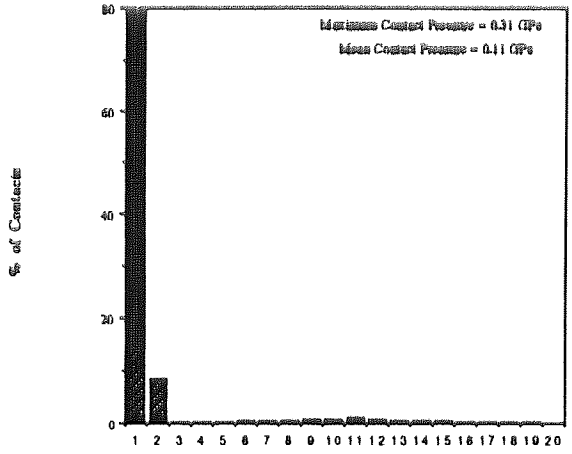

b)

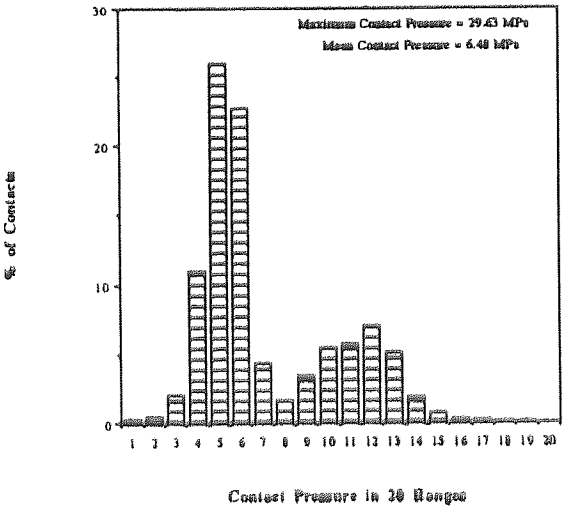

c)

Figure 7.30 Contact pressure distributions for 25/75 hard/soft mixtures at $\sigma = 20$ kPa **a**) Monodisperse assembly **b**) 2/1 hard/soft size ratio assembly **c**) 2/1 soft/hard size ratio assembly.;

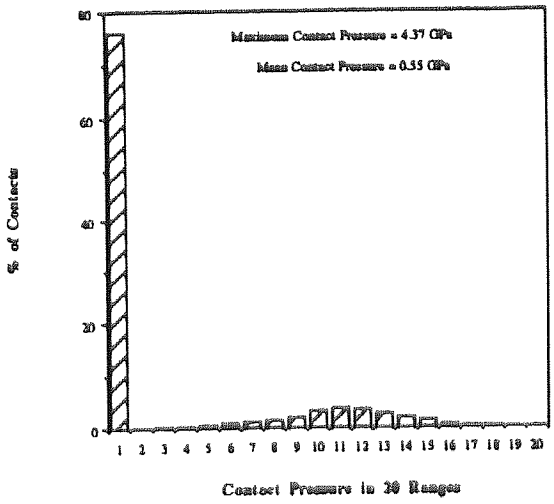

a)

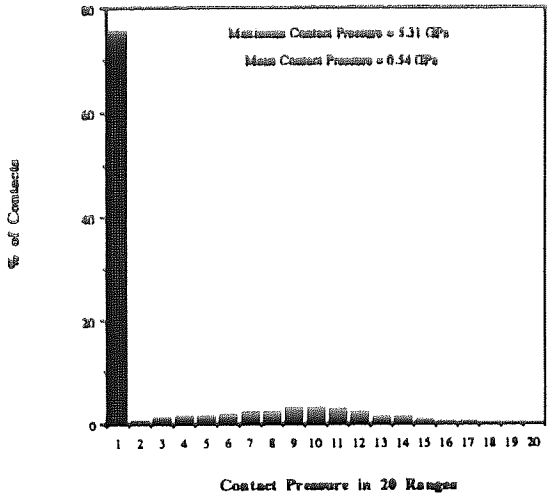

b)

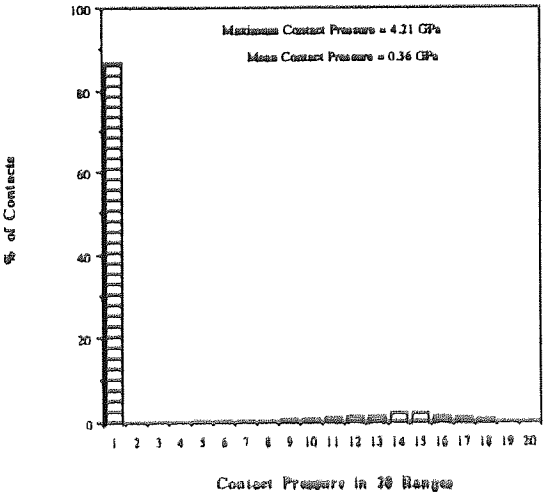

c)

Figure 7.31 Contact pressure distributions for 50/50 hard/soft mixtures at $\sigma = 50$ kPa **a)** Monodisperse assembly **b)** 2/1 hard/soft size ratio assembly **c)** 2/1 soft/hard size ratio assembly.;

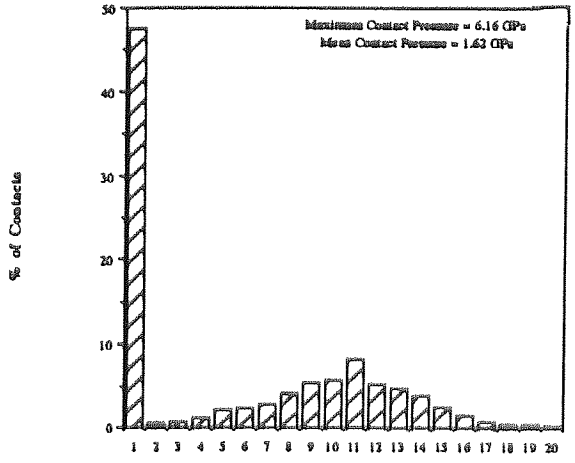

a)

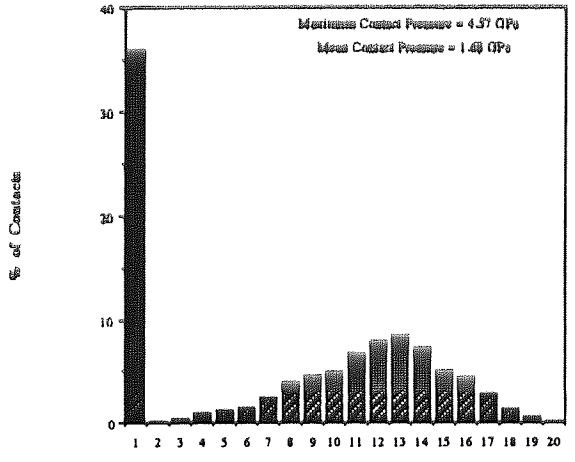

b)

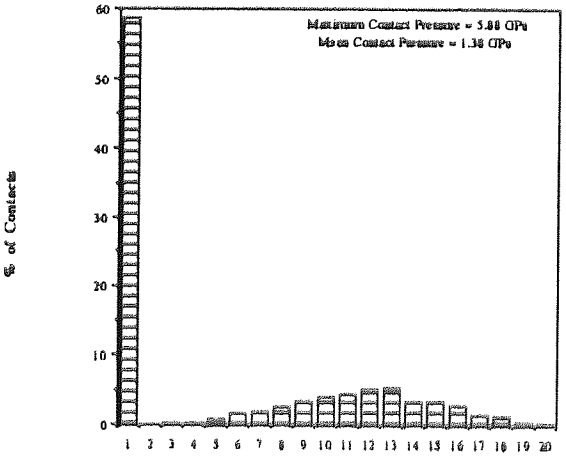

c)

Figure 7.32 Contact pressure distributions for 75/25 hard/soft mixtures at $\sigma = 150$ kPa a) Monodisperse assembly b) 2/1 hard/soft size ratio assembly c) 2/1 soft/hard size ratio assembly.;

7.6 Percolation-based parameters

The presence of different-sized, elastic particles in the simple elastic lattice system studies reviewed in section 3.5.2 was not considered. Therefore, the effects of such particles on the general percolation behaviour of a random, elastic, particle assembly is a new area of study. In this section, percolation concepts such as the assembly *backbone* (see section 4.9.2) and *multifractality* (see section 3.4), will be considered.

In all the cluster backbone figures that are presented here, shaded circles represent hard particles. Generally it was found that, the random selection processes involved in developing the cluster backbone ensured that different backbone structures for the bimodal and monosized assemblies were observed at the same stress level. Figure 7.33 illustrates the backbones for the monosized and bimodal mixtures of 25:75 hard:soft particle systems at a stress level of $\sigma = 20$ kPa. The backbones for the assemblies presented in this figure, use both hard and soft particles in force transmission. For the monosized assembly shown in figure 7.33a, a higher proportion (37%) of hard spheres are present in the backbone than in the overall assembly (25%). If the size of the soft spheres in the assembly is reduced, then figure 7.33b shows that the proportion of hard spheres in the backbone increases to ~ 50%. The backbone in this figure consists of fewer particles (355 in comparison with the 494 for the monodisperse case). Consequently the fractal dimension of the backbone is smaller ($D_B = 1.675$). If the size of the hard particles in the assembly is reduced, then figure 7.33c illustrates that the backbone consists of 534 particles including only about 19% of hard particles. The change in backbone composition is also accompanied by a reduction in physical size, since the value of D_B decreases to $D_B = 1.690$.

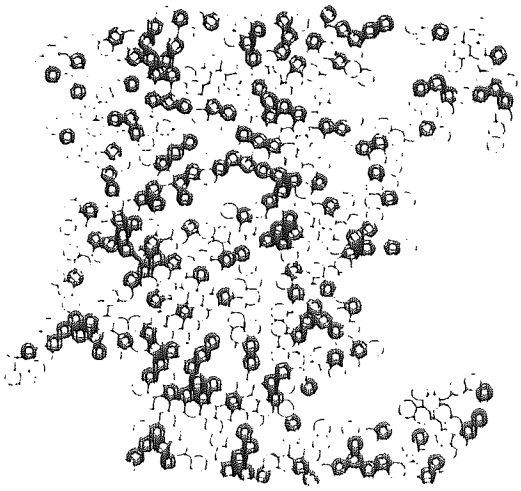

$D_B = 1.722$

a)

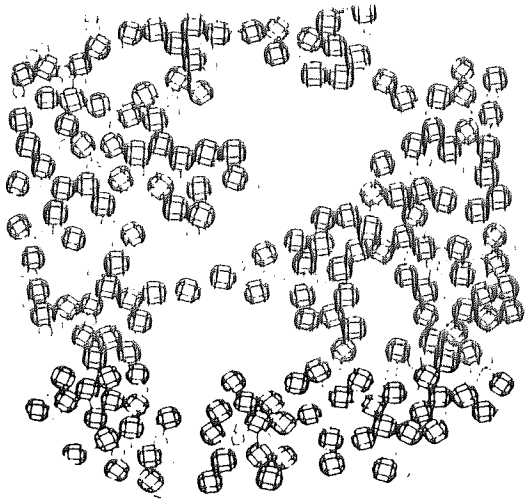

$D_B = 1.675$

b)

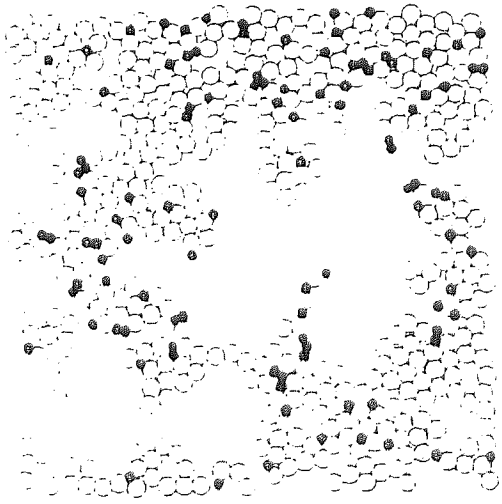

$D_B = 1.690$

c)

Figure 7.33 Cluster backbones for assemblies composed of 25/75 hard/soft particles, subject to quasi-static compaction (σ = 20 kPa).
a) Monodisperse assembly b) 2/1 hard/soft size ratio assembly
c) 2/1 soft/hard size ratio assembly.;

The backbones for the monosized and bimodal systems of the 50:50 hard:soft particle mix are presented in figure 7.34.

a)

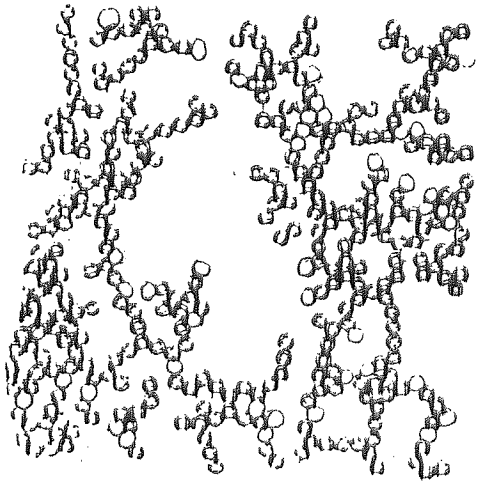

$D_B = 1.623$

b)

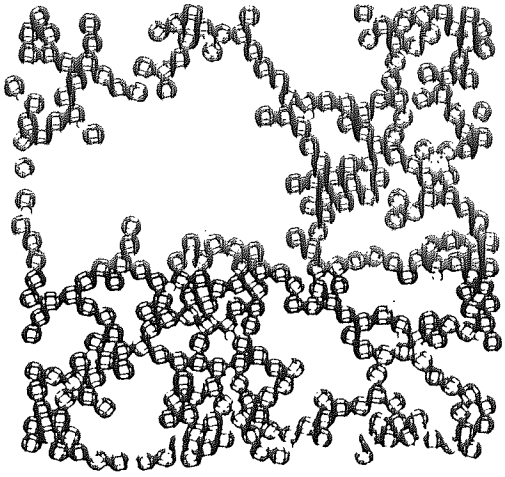

$D_B = 1.618$

c)

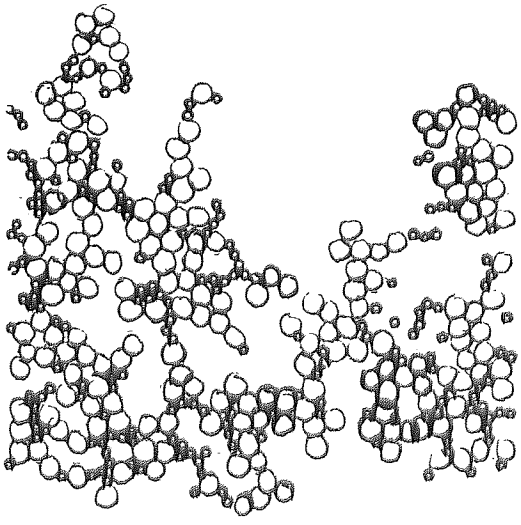

$D_B = 1.638$

Figure 7.34 Cluster backbones for assemblies composed of 50:50 hard:soft particles, subject to quasi-static compaction (σ = 50 kPa).
a) Monodisperse assembly b) 2/1 hard/soft size ratio assembly.
c) 2/1 soft/hard size ratio assembly.;

For the monodisperse assembly shown in figure 7.34a, the proportion of hard spheres in the backbone (~ 80 %) is much greater than the proportion of hard spheres in the assembly (50 %). If the size of the soft spheres in the assembly is reduced, then figure 7.34b shows that the proportion of hard spheres in the backbone increases to ~ 90 %. However, if the size of the hard particles in the assembly is reduced, then figure 7.34c indicates that the backbone is dominated by soft particles (~ 80%) and, consequently, the fractal dimension of the backbone is increased (D_B = 1.638)

The small quantitative difference between the hard particle composition of the 2:1 hard:soft and monosized assemblies does not readily explain the different macroscopic behaviour of the two assemblies observed in section 7.3. Therefore, it is unclear whether the rigidity of backbone particles on its own, has an important influence on force transmission and hence the macroscopic behaviour of an assembly. Clarification of the situation is also unfortunately not provided by the backbone structures obtained from monodisperse and bimodal assemblies composed of 75:25 hard:soft particles at a stress level of σ = 150 kPa.

The backbone structures for the monosized and bimodal systems with this composition are presented in figure 7.35. The backbones of the 2:1 hard:soft size ratio and monodisperse assemblies are both composed of ~ 100% hard particles, but this does not prevent quantitative differences in the stress-strain behaviour of the two assemblies in figure 7.14c. It is therefore, also important to consider additional factors relating to the mechanical performance of the backbone. One reason may be the fact that the backbone of the 2:1 hard:soft size ratio assembly in figure 7.35a is physically larger (D_B = 1.625) than the backbone of the monodisperse assembly (D_B = 1.572) in figure 7.35b. A larger backbone suggests that a greater number of pathways for the transmission of the largest forces are available and this may explain the quantitatively-different macroscopic behaviour observed. A similar argument could be used in the interpretation of the stress-strain behaviour of the 2:1 soft:hard size ratio assembly in figure 7.14c, but the presence of ~ 20% of large, soft particles in the backbone structure may be more significant.

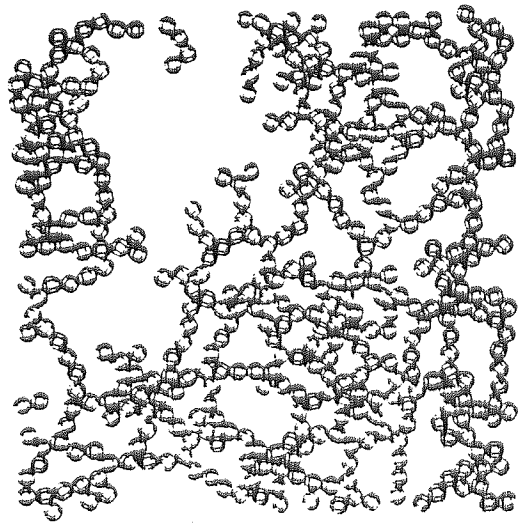

$D_B = 1.625$

a)

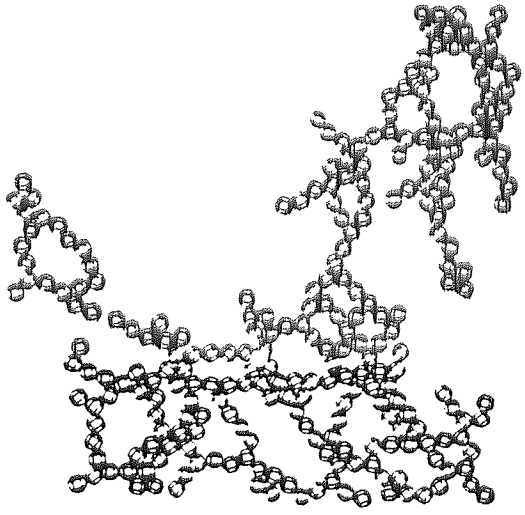

$D_B = 1.572$

b)

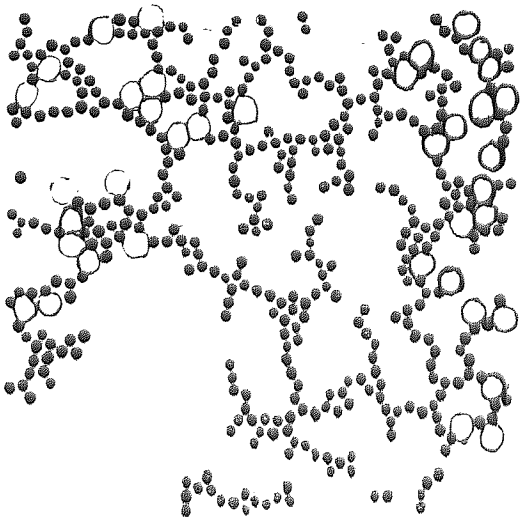

$D_B = 1.634$

c)

Figure 7.35 Cluster backbones for assemblies composed of 75/25 hard/soft particles, subject to quasi-static compaction (σ = 150 kPa).
a) 2/1 hard/soft size ratio assembly b) Monodisperse assembly
c) 2/1 soft/hard size ratio assembly.

The idea expressed in chapter 6 that multifractality is a fundamental characteristic of elastic particle assemblies is supported by the evidence of figure 7.36, which shows a complete, continuous distribution of assembly contact areas for the 2:1 hard:soft size ratio, 50:50 hard:soft particle assembly. The ability to obtain this type of distribution for the contact behaviour of a bimodal assembly, suggests that multifractality could also be used to improve the understanding of the microstructural aspects of bimodal assembly behaviour. However, the practicalities of using multifractality in such a interpretative process requires further work.

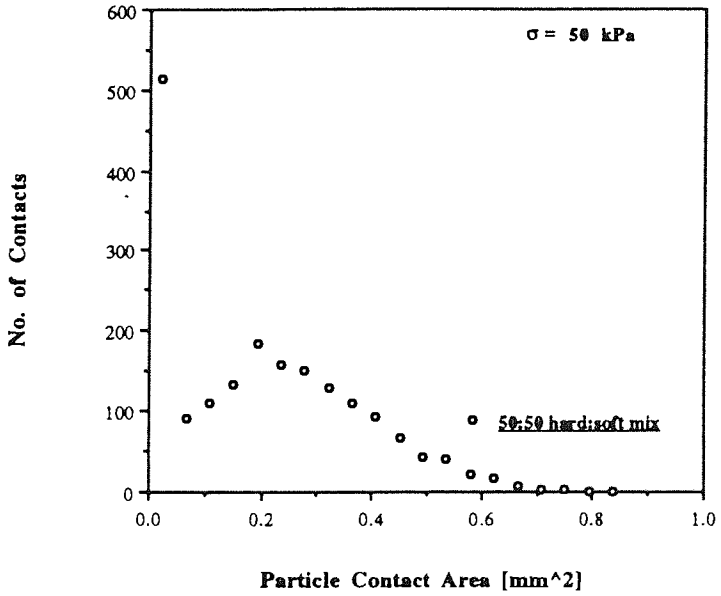

Figure 7.36 Multifractal contact area distribution for 2/1 hard/soft size ratio , 50/50 hard/soft mixture subject to quasi-static compaction.;

7.7 Summary

The effects of dissimilar particle sizes on the macroscopic, microstructural and percolation theory-based properties of two-dimensional assemblies subject to quasi-static compaction were considered in this chapter. The macroscopic stress-strain behaviour for such bimodal assemblies was generally found to be adequately described by a second-order polynomial function. The stress-strain behaviour was also found to become Hertzian-like at higher compaction pressures.

The relationships between the coefficients of the polynomial function and the composition of the assemblies were found to be linear for the large soft:small hard assemblies. Similar observations were made for the monosized assemblies in chapter 6. However, the relationship between the polynomial function coefficients and the assembly composition for the large hard:small soft particle systems was more complex and therefore could not be adequately described by such simple expressions.

The bimodal systems showed similar structural evolution during quasi-static compaction to that of the monosized assemblies presented in chapter 6, and followed the relationship of Hardin (1967). The development of both mechanical Z_m and geometric Z_g co-ordination numbers with solid fraction was also, in general terms, qualitatively similar to that of the monosized assemblies examined in chapter 6.

The presence of different-sized particles in the bimodal assemblies was found to have some qualitative and quantitative effects on microstructural parameters such as contact force, area and pressure distributions. Results from work on the structure of the cluster backbones for the bimodal particle assemblies also indicated that observation of such structures may help in a better understanding of the macroscopic behaviour. However, further work is required in the area of interpreting macroscopic assembly behaviour from backbone structures.

Chapter 8

Three-dimensional quasi-static compaction

8.1 Introduction

Simulation experiments using two-dimensional, binary particle assemblies, such as those presented in chapters 6 and 7 are useful, but do not allow accurate interpretation of the compaction behaviour of *real* particle systems, which are always three-dimensional. Therefore to obtain more practically useful data, a series of simulation experiments on 3620 particle, three-dimensional assemblies subject to quasi-static compaction were performed and the results from these experiments are reviewed in this chapter. Although the quasi-static state is virtually unattainable in a practical sense, its study is important because its allows a theoretical framework for three-dimensional, elastic assembly compaction behaviour to be developed. The development of even this relatively idealised, theoretical framework for three-dimensional compaction is a useful advance on the empirical work of Kawakita (1956) and Heckel (1961a, b), which was reviewed in chapter 2. In this chapter, the results from the three-dimensional, simulation experiments will be interpreted in terms of macroscopic, microscopic and percolation theory-based assembly characteristics, which is the approach used for the results from the two-dimensional simulation experiments considered in earlier chapters. The macroscopic assembly stress-strain characteristics obtained from the three-dimensional, simulation experiments will be interpreted in terms of both, theoretical models of elastic assembly behaviour such as Thornton (1991) and models developed from the empirical work of Kawakita (1956) and Heckel (1961a).

8.2 Simulation experiment characteristics

All the three-dimensional, simulation assemblies were composed of 3620 particles, since Sun and Thornton (1993) found that this was the optimum particle size for a three-dimensional simulation assembly subject to external loading in the Aston version of TRUBAL.

The particle size distribution for the three-dimensional assemblies used in the simulation experiments was similar to that of the two-dimensional assemblies studied in chapters 6 and 7 (see section 6.3). The solid fraction ϕ at generation for all assemblies was 0.355 c.f. a value of $\phi = 0.496$ for the 3620 particle assembly of Sun and Thornton (1993), where the average particle radius was 0.13 mm.

An example of a generated three-dimensional assembly is provided in figure 8.1. The generated three-dimensional assemblies contained different quantities of hard and soft particles according to their specified composition, which ranged from 100% soft to 100% hard particles. The physical parameters which were specified for both the hard and soft particles were the same as those used for the particles in the two-dimensional assemblies studied in chapters 6 and 7 (see table 6.1).

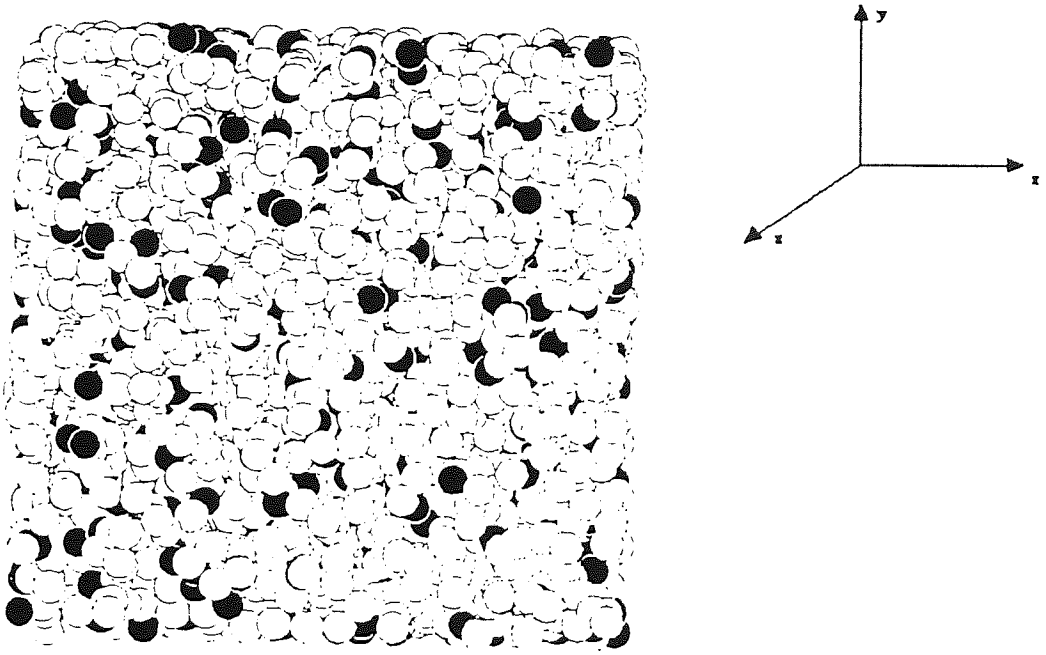

Figure 8.1 Three-dimensional 25/75 hard:soft particle assembly at generation.; [Dark spheres ≡ hard particles]

The general test procedure for the three-dimensional assemblies was similar to that adopted for two-dimensional assemblies in section 6.2. However, it should be noted that the position of p_g was determined using the slicing technique reviewed in section 5.4, and isotropic compaction of the particle assemblies occurred along all three periodic-cell co-ordinate axis, instead of just along the x- and y- axis in the two-dimensional case (see Appendix A). The isotropic compaction process in three-dimensions was also studied up to a stress level of $\sigma_0 = 5$ MPa, which is larger than the value of $\sigma_{mean} = 1$ MPa considered for the two-dimensional tests in chapters 6 and 7. A higher stress level for the three-dimensional work was required, because it allowed the collection of sufficient data points from the ground state at p_e to help in the interpretation of the macroscopic assembly behaviour. The control parameters for a three-dimensional compaction test were those specified in section 6.2. Particle density-scaling (reviewed in section 4.6) was also used to allow reasonable completion times for the experiments. The values of the particle densities used in the scaling process for the three-dimensional experiments were the same as those specified in the two-dimensional tests in table 6.1.

8.3 Assembly compaction relationships

In this section, an analysis will be made of the stress-strain behaviour obtained from the three-dimensional assemblies used in the simulation experiments. Interpretation of the simulation experiment results in terms of the work of Heckel (1961a), Kawakita (1956) will also be considered.

8.3.1 Stress-strain behaviour

The ground state for all the macroscopic, three-dimensional assembly measurements presented in this chapter was p_e, which was determined using the method described in section 5.4. Figure 8.2, shows a selection of three-dimensional assembly stress-strain curves, which describe assembly behaviour up to a stress level of $\sigma = 5$ MPa. All the assemblies shown in figure 8.2 exhibit stress-strain behaviour which is essentially Hertzian-like at high stress levels, since the gradient of the curve is $\cong 3/2$. A similar observation was made about the stress-strain curves for the two-dimensional assemblies in section 6.3.1. However, in the three-dimensional case, the stress-strain curves are slightly *noisy* at low stress levels and this was not observed in figure 6.3.

The relatively dynamic nature of particle interactions in a three-dimensional assembly during the early stages of compaction must limit its ability to exhibit idealised, elastic assembly behaviour. Therefore, the suggestion of Walton (1987), that such idealised behaviour would only be observed for a random, elastic particle assembly when the assembly is very compact, seems to be appropriate in describing three-dimensional assembly behaviour.

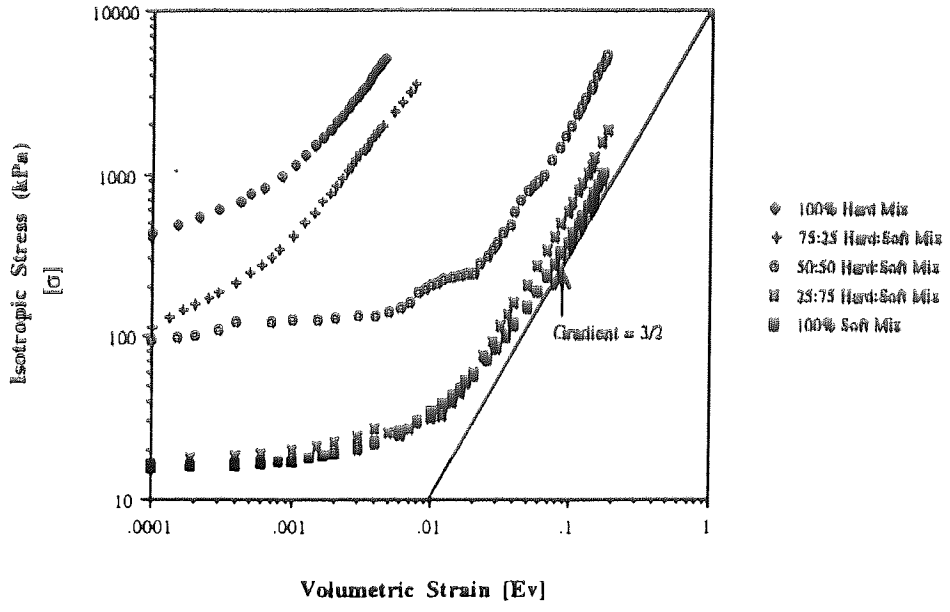

Figure 8.2 Stress-strain behaviour for some three-dimensional, binary; assemblies subject to quasi-static compression.;

If the stress-strain data for the assemblies is plotted to natural scales, then figure 8.3 indicates that second-order polynomial fits are again able to offer excellent agreement with the data shown (see chapters 6 and 7). Second-order polynomial expansions also provide good fits to the stress-strain curves from three-dimensional assemblies presented in Appendix E, figures E1 and E2. The stress levels indicated on the graphs in figure 8.3 will be used as the states from which microstructural and percolation theory-based information is interpreted in later sections of this chapter.

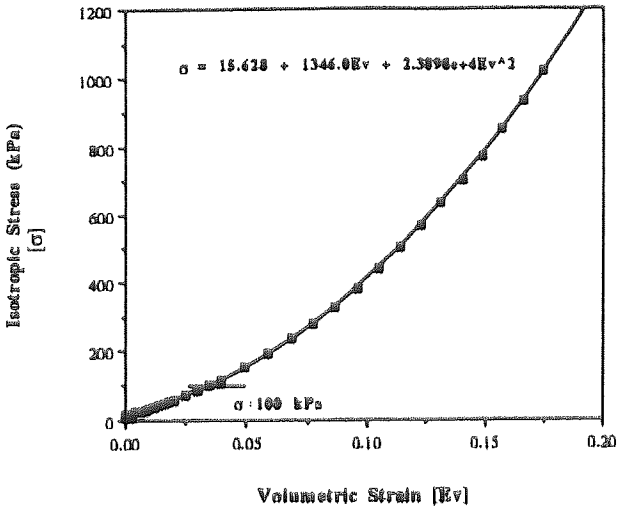

a)

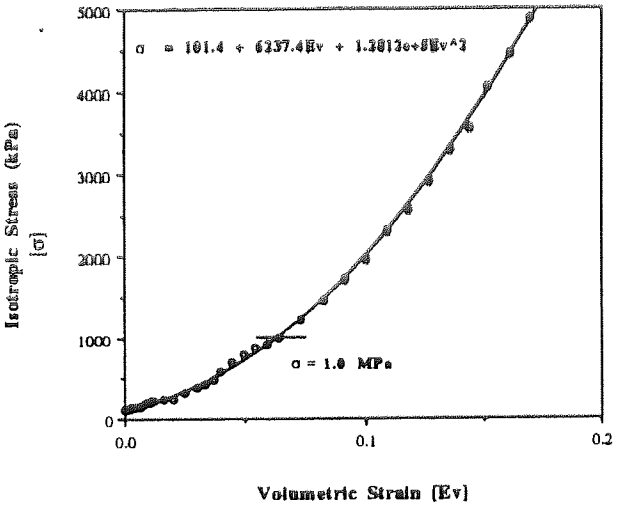

b)

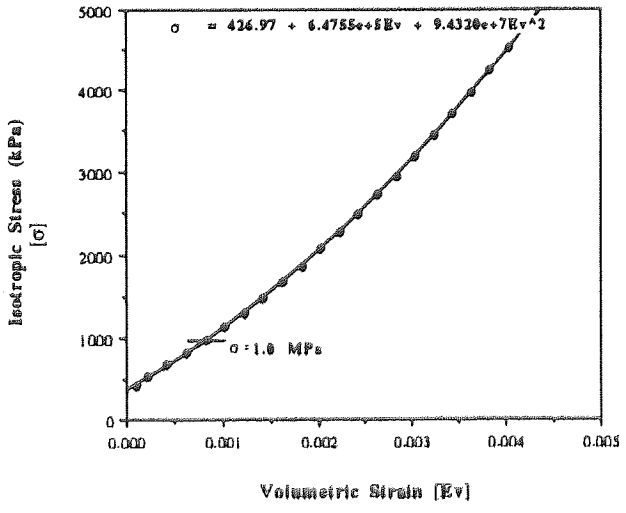

c)

Figure 8.3 Stress-strain curves and second-order polynomial expansions for some three-dimensional assemblies subject to quasi-static; compression. **a**) 100% soft assembly **b**) 50:50 hard:soft assembly **c**) 100% hard assembly;

The coefficients of the second order expansions represent the same physical parameters as those indicated in section 6.3.1 and figure 8.4 shows the relationship between these coefficients and the assembly composition p.

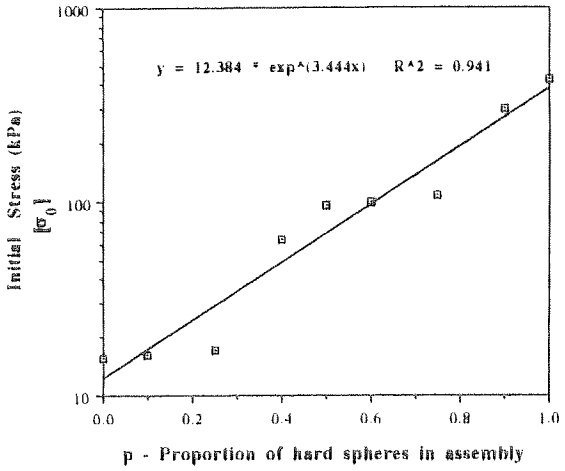

a)

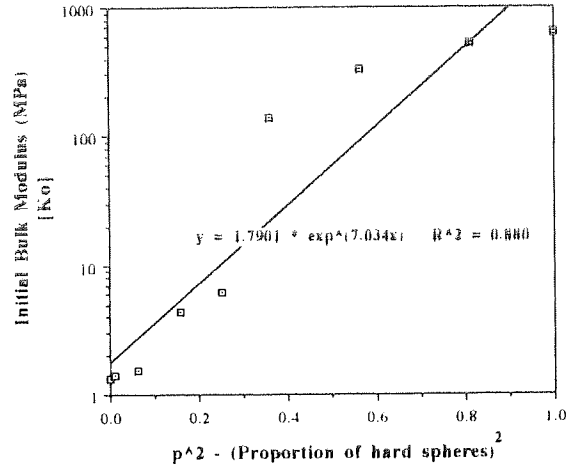

b)

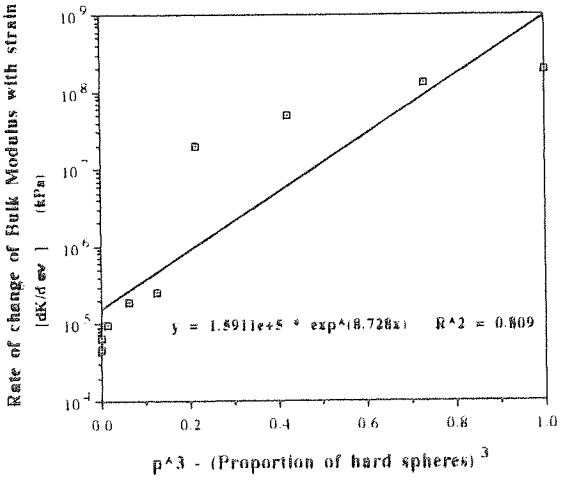

c)

Figure 8.4 Effect of mixture composition on initial stress state (**a**) initial bulk modulus (**b**) and rate of change of bulk modulus with strain (**c**) for the three-dimensional assemblies subject to quasi-static compression.;

In figure 8.4a, the exponential function provided by (6.5) provides a reasonable approximation of the relationship between the initial stress σ_0 at the percolation threshold and p. However, the relationship between the initial assembly bulk modulus K_0 and p^2 presented in figure 8.4b cannot be represented by the exponential function provided by (6.7), because assembly compositions with approximately large numbers of hard particles deviate from linearity. A poor fit of the exponential function provided by (6.9) to the data is also observed in figure 8.4c, where the rate of change of bulk modulus with strain is plotted against p^3. Therefore, the complexity of the interparticle interactions for three-dimensional assemblies with roughly equal numbers of hard and soft spheres appears to limit the validity of using a simple curve-fitting exercise to describe the development of the first and second order terms of the polynomial functions for such assemblies.

The second-order polynomial expansions imply that there is a linear relationship between the bulk modulus and the volumetric strain. Figure 6.7 showed that such a relationship was observed for two-dimensional assemblies subject to quasi-static compression and to check the validity of a linear modulus-strain relationship for three-dimensional assemblies, plots of the evolution of assembly bulk modulus with strain for $p = 0.0, 0.5$ and 1.0 are shown in figure 8.5. The data presented in figure 8.5 indicates that, generally, a linear relationship between bulk modulus and strain is also a reasonable approximation for the 3D assemblies. However, for $p = 0.0$, figure 8.5a, linearity is not observed at high or low strains and for $p = 1.0$, figure 8.5c, the data indicates a bilinear relationship. The data presented in figure 8.2, indicated that idealised elastic behaviour for three-dimensional assemblies was only apparent when the assemblies were sufficiently compact. Therefore, the non-linearity visible in the early stages of compaction for some of the assemblies presented in figure 8.5 can be explained by the absence of a dense assembly structure. If compaction were to continue beyond the range of elastic deformation then the non-linearity visible in the high strain range in figure 8.5a could be explained by the onset of plastic deformation of the 100% soft assembly. Figures E3 and E4 presented in Appendix E show that the linear modulus-strain relationship visible in figure 8.5 is also observed for other three-dimensional assemblies.

8.3.2 Empirical relationships and the simulation experiment results.

It is useful to interpret the compaction results from the three-dimensional simulation experiments in terms of the practically important, empirical compaction relationships of Heckel (1961a) and Kawakita (1956). A detailed review of the work of Heckel is provided in section 2.1.1 and that of Kawakita in section 2.1.2. The data from the three-dimensional simulation experiments is plotted in figure 8.6 as a graph of $\ln(1/(1-D))$ against compaction pressure P, where $1-D$ is the pore fraction, and this is more commonly known as a Heckel plot. Heckel (1961a) claimed a linear relationship between $\ln(1/(1-D))$ and P was obtained in his work, especially above $\sigma = 50$ MPa. Linearity can also be observed for significant portions of the curves in figure 8.6. It was shown in section 2.1.1, that Heckel was uncertain about the nature of $\ln(1/(1-D))$ against P curves at stress levels lower than $\sigma = 50$ MPa, because of poor qualitative interpretation of his compaction results. The results presented in figure 8.6 however, suggest that Heckel's relationship may be quantitatively correct at relatively low stress levels.

The data from the three-dimensional, simulation experiments can also be plotted in terms of Kawakita graphs of P/C against P, where C is the degree of compaction or volumetric strain. Figure 8.7 shows Kawakita plots for a selection of the three-dimensional assemblies and indicates that linearity is only achieved after sufficient compaction to limit particle rearrangement has occurred. The linearity observed after for the 50:50, 100% soft and 100% hard assemblies in figure 8.7 also seems to be consistent with the development of Hertzian stress-strain behaviour in figure 6.3. Plastic deformation of the 100% soft assembly above a stress level of $\sigma = 1.0$ MPa, which was suggested earlier in this chapter, is the probable cause of the non-linearity visible in figure 8.6c.

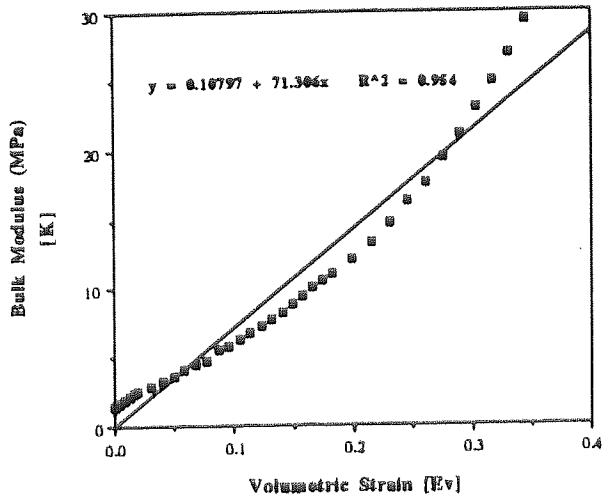

a)

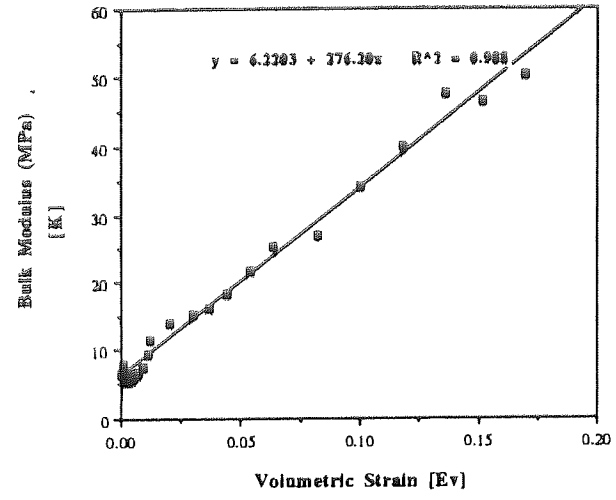

b)

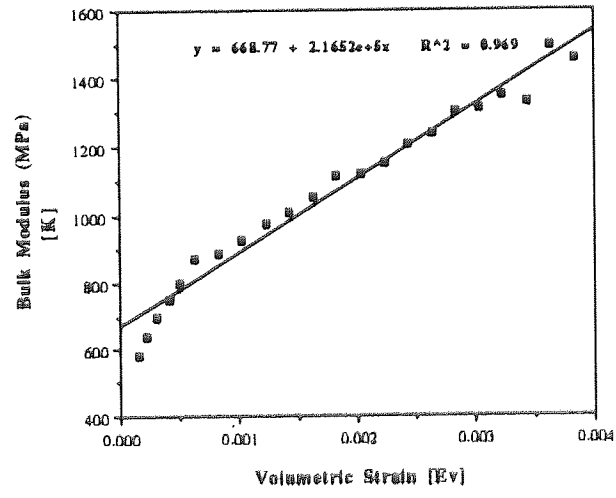

c)

Figure 8.5 The relationship between bulk modulus and volumetric strain for some three-dimensional assemblies subject to quasi-static compression.
a) 100% soft assembly b) 50:50 hard:soft assembly
c) 100% hard assembly.;

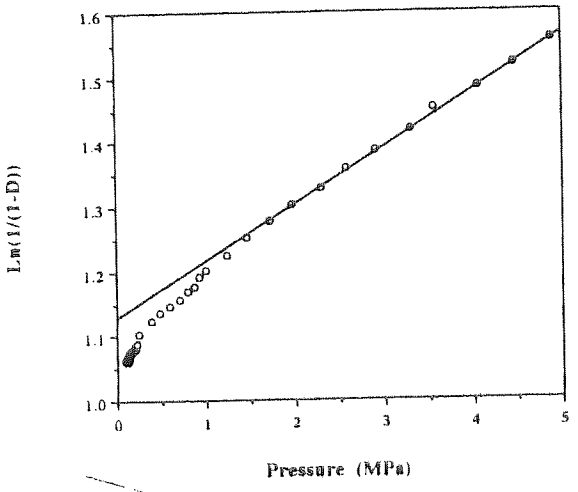

a)

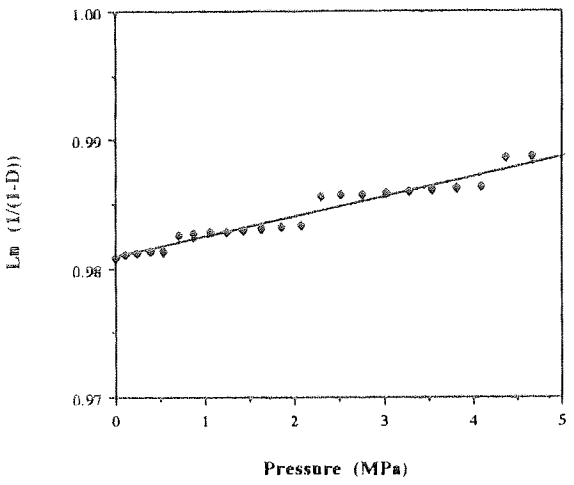

b)

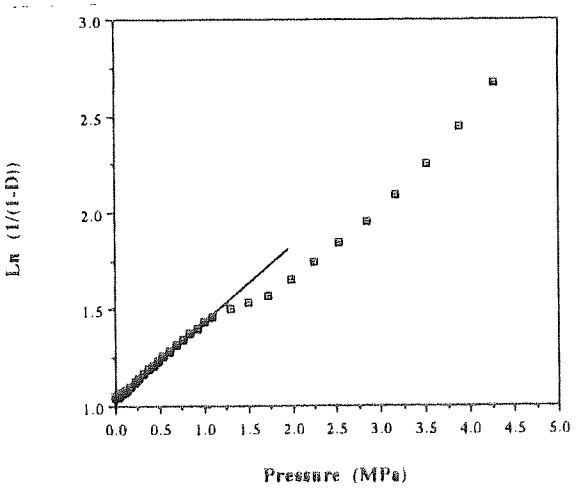

c)

Figure 8.6 Heckel plots for some three-dimensional, simulation assemblies subject to quasi-static compaction.
a) 50:50 hard:soft particle assembly **b)** 100% hard particle assembly
c) 100% soft particle assembly.;

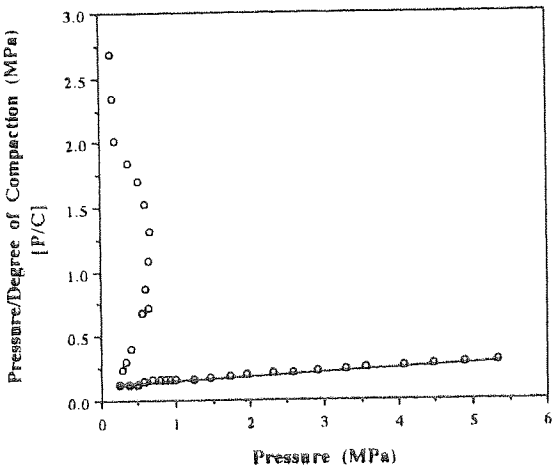

a)

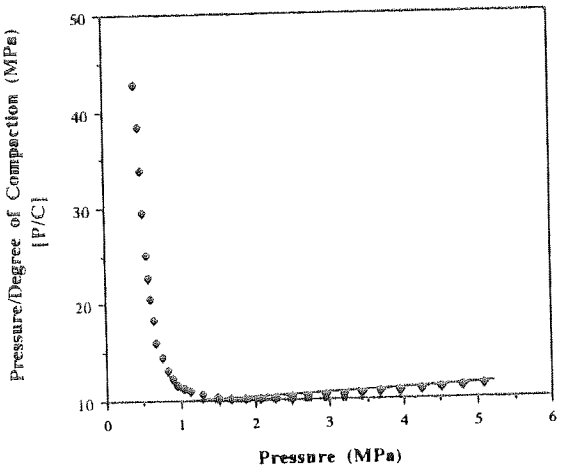

b)

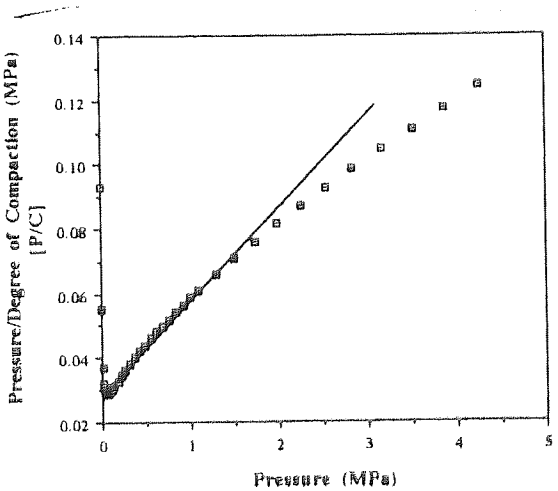

c)

Figure 8.7 Kawakita plots for some three-dimensional, simulation assemblies subject to quasi-static compaction.
a) 50:50 hard:soft particle assembly b) 100% hard particle assembly
c) 100% soft particle assembly.

The qualitative evidence for linearity provided by Kawakita and Ludde (1970) and reviewed in section 2.1.2, was not conclusive, because the *linear* behaviour observed by these workers was only visible at particle assembly stress levels at which plastic deformation was believed to be the dominant compaction process. Therefore, using Kawakita's relationship in any qualitative explanation of the compaction behaviour of the elastic simulation assemblies studied in this chapter is not sensible. Kawakita and Heckel plots for some of other three-dimensional, simulation assemblies are presented in Appendix E, figures E5 - E8.

8.4 Evolution of assembly structure

The work presented in section 6.3.2, indicated that the solid fraction ϕ was the simplest definition of the structure of particulate media and was normally plotted against the logarithm of stress in soil mechanics. Figure 8.8 shows a plot of this type for the three-dimensional 50:50 hard:soft mixture and the general form is typical of all the simulations reported in this chapter. It is also interesting to note that the curves for both the two- and three-dimensional versions of the assembly in this figure are qualitatively similar, which shows that the structural development of the assembly is not affected by dimensionality.

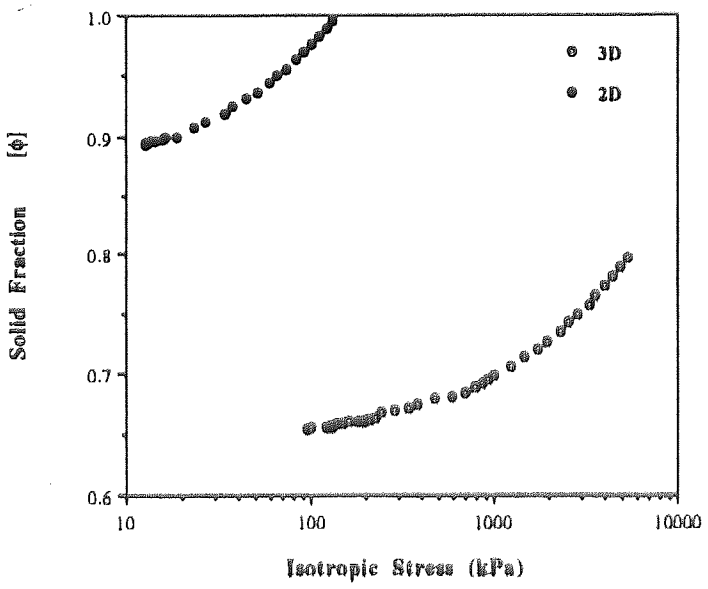

Figure 8.8 The relationship between solid fraction ϕ and isotropic stress for the three-dimensional 50:50 assembly subject to quasi-static compaction.;

The work of Hardin (1987) on sand, was examined in terms of two-dimensional assembly behaviour in section 6.3.2. Adopting Hardin's approach for three-dimensional assemblies, figure 8.9 shows the relationship between solid fraction ϕ and $(\sigma/\sigma_o)^{1/2}$ for $p = 0.0$, 0.5 and 1.0, where σ_o is the isotropic stress at the elastic percolation threshold.

a)

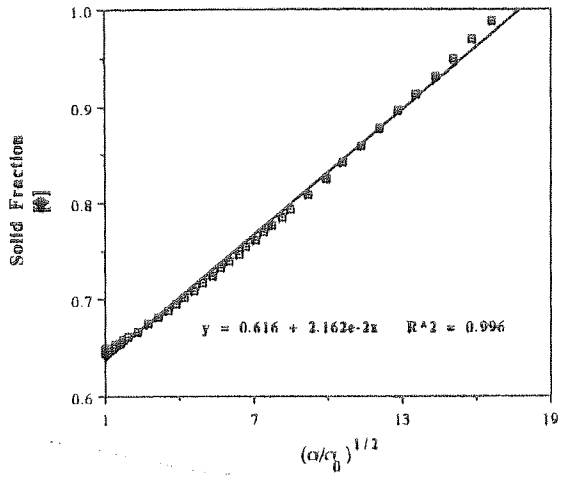

b)

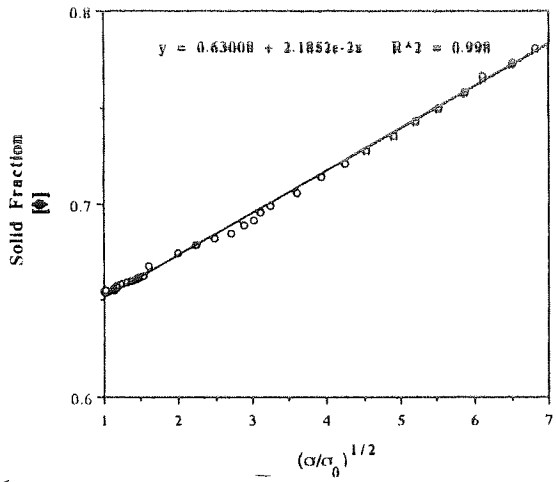

c)

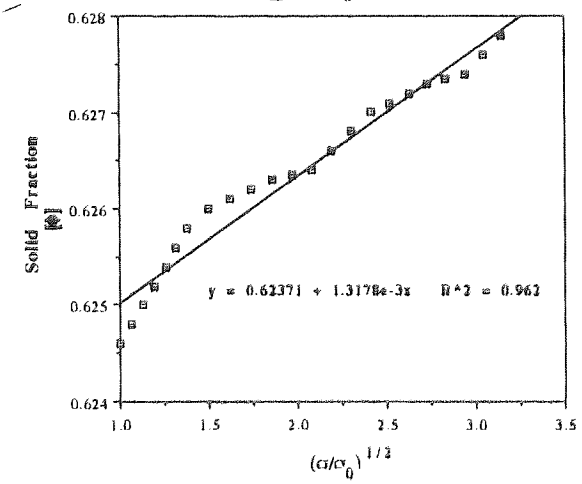

Figure 8.9 The relationship between solid fraction ϕ and $(\sigma/\sigma_o)^{1/2}$ for some three-dimensional assemblies subject to quasi-static compression. a) 100% soft assembly b) 50:50 hard:soft assembly c) 100% hard assembly.;

A linear relationship between the two parameters is observed for the majority of the data presented in figure 8.9. The relationship is less linear for the 100% hard assembly in figure 8.9c because some initial particle rearrangement must still occur at a stress level of $\sigma = 5$ MPa.

The relationship between the coefficient c from (6.11), used in the curve-fitting process and the assembly composition p was first examined in figure 6.10 for two-dimensional assemblies and figure 8.10 shows the non-linear relationship between p and c for three-dimensional assemblies. A gradual decrease in the value of c with p is observed in this figure up to a value of $p = 0.25$, followed by a rapid increase in the value of c between $p = 0.25$ and $p = 0.5$ and then a steady decline in c values between $p = 0.5$ and $p = 1.0$. Hardin (1987) believed that c was related to the stiffness of the assembly and thus the results of figure 8.10 suggest that, significant changes in assembly stiffness occur around assembly compositions of $p = 0.25$ and $p = 0.5$. Further examination of the microstructural behaviour of assemblies in this composition range is therefore required.

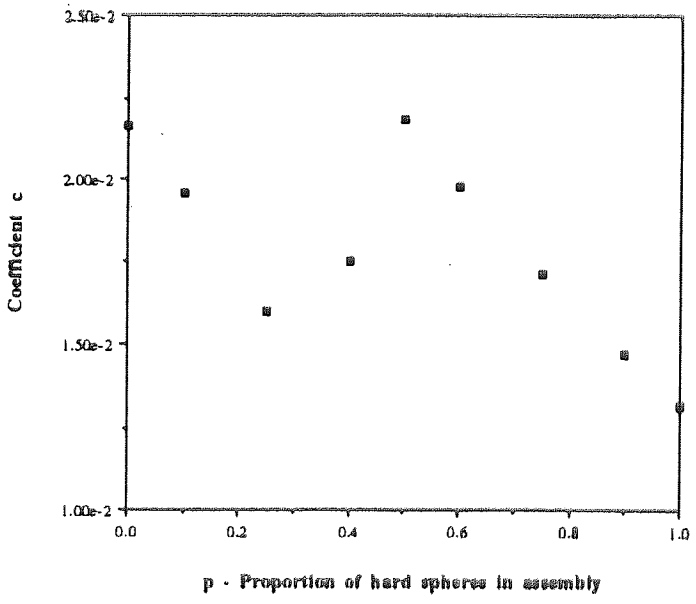

Figure 8.10 The relationship between coefficient c from the Hardin equation and assembly composition for three-dimensional assemblies subject to quasi-static compaction.;

The assembly contact density C is another important descriptor of granular assembly behaviour, which is determined by (4.72). For three-dimensional assemblies the periodic cell volume used in (4.72) is that defined in section 1.2.

The evolution of contact density with solid fraction for the 50:50 hard:soft assembly is presented in figure 8.11 and is typical of the behaviour shown by the other assemblies studied, since a fairly linear relationship between the two parameters is observed. Further examples of such curves are provided in Appendix E, figures E9 - E11.

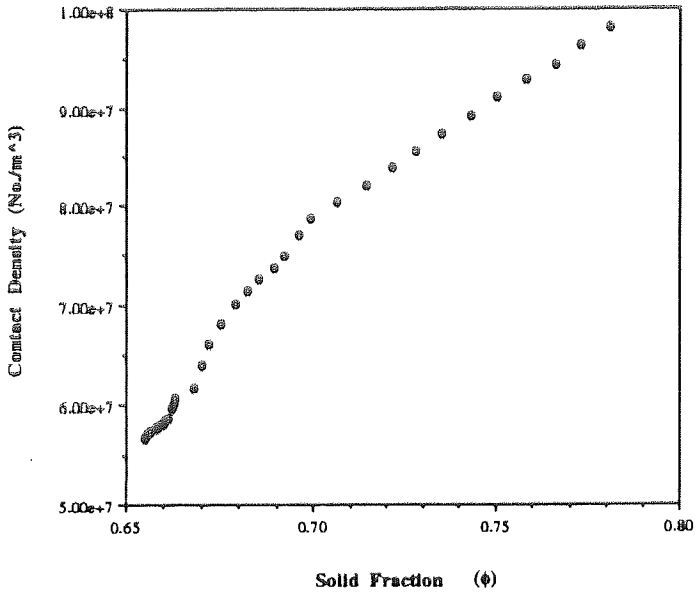

Figure 8.11 The relationship between contact density and solid fraction for the three-dimensional 50:50 hard:soft assembly subject to quasi-static compaction.;

The importance of the geometric co-ordination number Z_g and mechanical co-ordination number Z_m to understanding assembly behaviour was explained in section 6.3.2. Figure 8.12 shows the evolution of these two parameters with solid fraction for three-dimensional assemblies, where p = 0.0, 0.5 and 1.0. The results presented in figure 8.12 indicate that the development of both Z_g and Z_m during compaction is qualitatively similar for all the assemblies shown and only differs quantitatively for the 100% hard assembly (p = 1.0) in figure 8.12c. The quantitative difference between the values of Z_g and Z_m for this assembly suggests that the structure of the load-bearing particle network within the assembly is less dependent upon the degree of compaction. Therefore, further investigation of the nature of such networks would be useful.

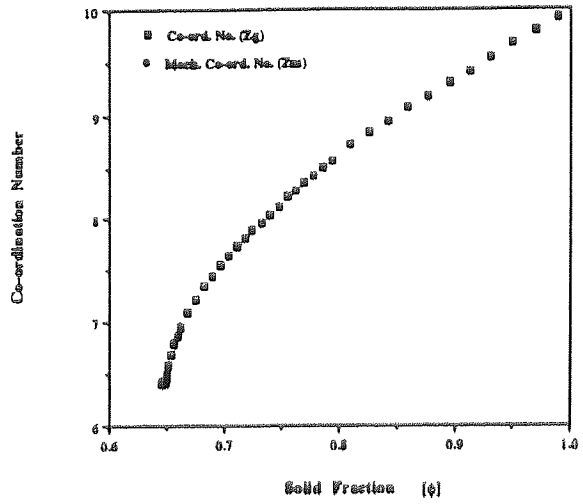

a)

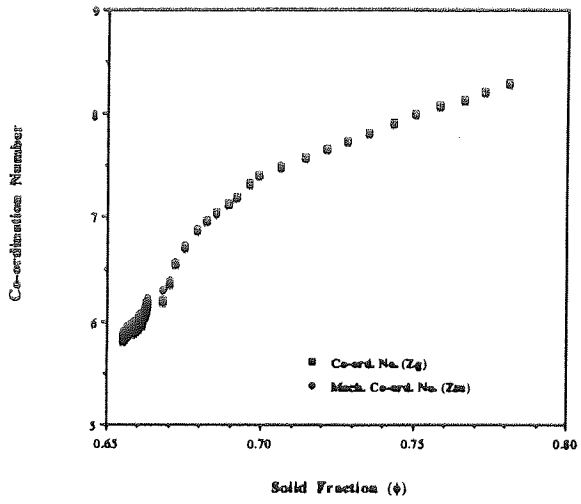

b)

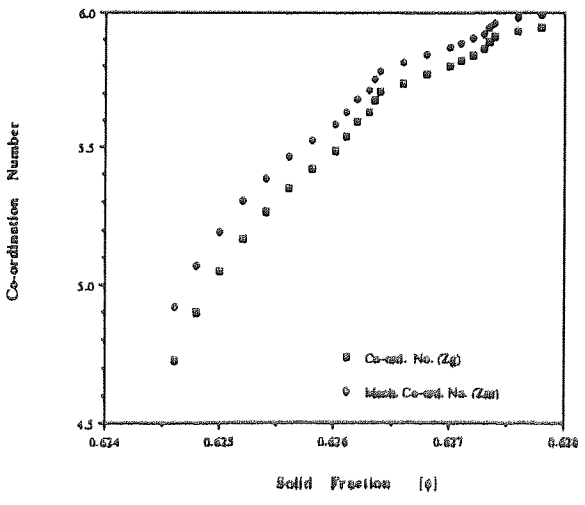

c)

Figure 8.12 The evolution of geometric co-ordination number Z_g and mechanical co-ordination number Z_m with solid fraction for some three-dimensional assemblies subject to quasi-static compression
a) 100% soft assembly b) 50:50 hard:soft assembly
c) 100% hard assembly.;

8.5 Microstructural parameters

8.5.1 General contact behaviour of assemblies

In three-dimensional simulation studies, direct visual interpretation of the microstructural characteristics of a particle assembly is difficult and it is therefore, often more useful to consider microstructural information such as the particle contact force distribution. The contact force behaviour of assemblies with a composition around $p = 0.5$ will be explored in the next section. The contact force distributions for some three-dimensional assemblies with other compositions are presented in figure 8.13. An exponential contact force distribution for the 100% hard particle assembly is presented in figure 8.13a and a Gaussian contact force distribution for the 100% soft particle assembly is presented in figure 8.13c. Similar contact force distributions are also observed for the two-dimensional versions of these particle systems. Figure 8.13b, which shows the distribution from the 25:75 assembly, indicates that a gradual transition in distribution shape from exponential to Gaussian is observed as the value of p is increased. However, the situation become more complex if the contact force distributions for the assemblies presented in figure 8.13 are examined at higher stress levels. Figure 8.14 shows some distributions at such stress levels and suggests that the shape of the contact force distribution for an assembly is sensitive to the applied stress level as well as to the composition of the assembly. Figure 8.14 also appears to show that a Gaussian distribution of contact forces will eventually develop during further compaction of an assembly. Such an idea is partially supported by the evidence of chapter 5, where exponential contact distributions were visible across the assembly compositional range at p_e in both two- and three-dimensions and also by the presence of Gaussian contact force distributions beyond p_e, for some of the two-dimensional assemblies subject to quasi-static compaction in Appendix B. The results of this work indicate that the composition of the assembly plays an important role in the stress level at which a Gaussian contact force distribution is first observed.

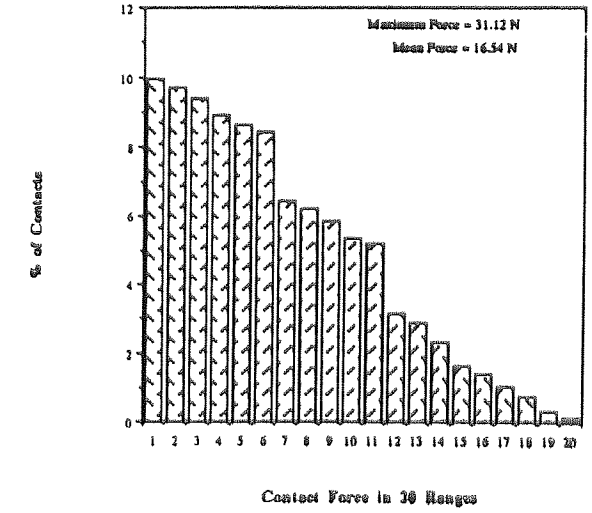

a)

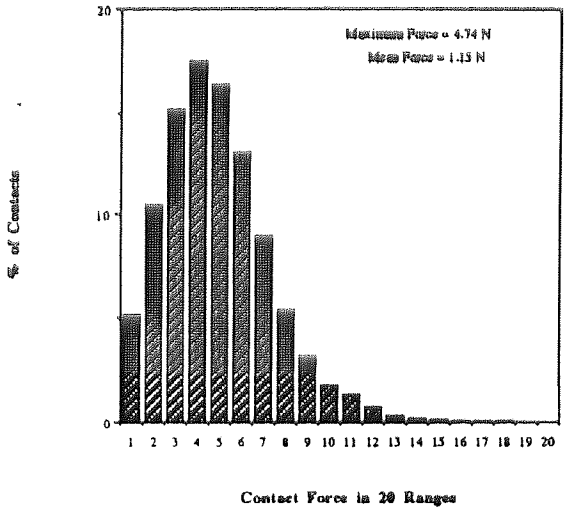

b)

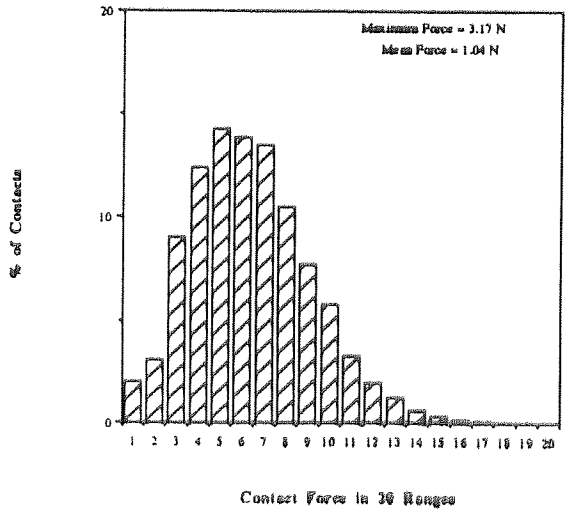

c)

Figure 8.13 Contact force distributions for three-dimensional assemblies subject to quasi-static compaction

a) 100% hard particle assembly (σ = 1 MPa)

b) 25:75 hard:soft particle assembly (σ = 100 kPa)

c) 100% soft particle assembly (σ = 100 kPa);

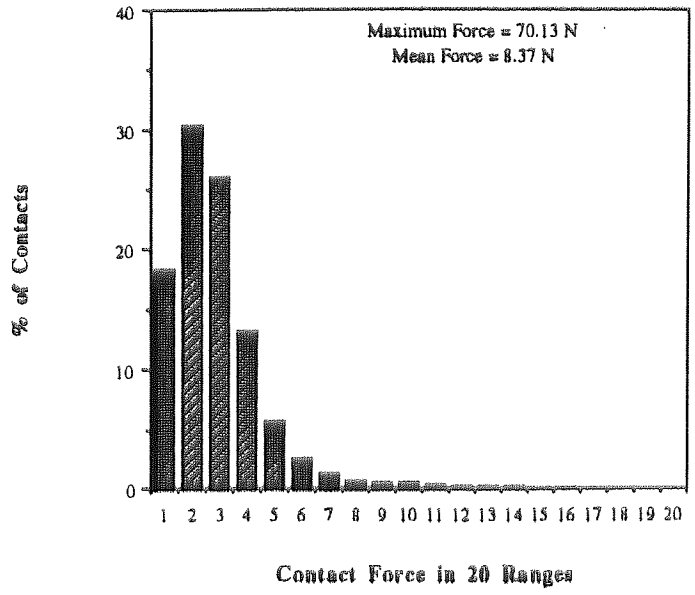

a)

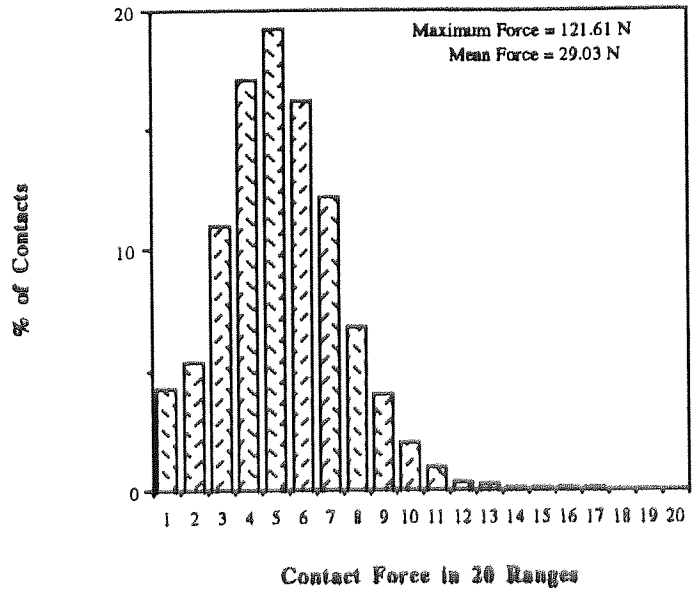

b)

Figure 8.14 Gaussian contact force distributions for three-dimensional assemblies subject to quasi-static compaction.
a) 100% hard particle assembly (σ = 2 MPa)
b) 25:75 hard:soft particle assembly (σ = 1 MPa);

Assemblies with a high proportion of soft spheres, such as the 100% soft assembly, can exhibit Gaussian contact force distributions at stress levels as low as $\sigma = 100$ kPa in three-dimensions (see figure 8.13c). However, assemblies which contain a high proportion of hard spheres, such as the 100% hard assembly, require larger stress levels to produce a Gaussian distribution such as $\sigma \sim 2.0$ MPa for the three-dimensional assembly in figure 8.13a. It should also be noted that, the exponential distributions which were observed for the two-dimensional 50:50 assembly at stress levels up to $\sigma = 100$ kPa in figures 6.17a change form when the applied stress level is greater than $\sigma = 1$ MPa, see Appendix B. If the ideas of Rothenburg (1980) are applied to this evidence, it is possible to suggest that soft particles quickly adopt a co-operative, load-sharing mode of operation during compaction, whilst particle force networks containing hard particles still seem to compete for stress transmission until appreciable compaction of the assembly has occurred. The importance of such internal processes on the observed contact force distribution for an assembly is obviously dependent on the assembly's composition and this would therefore, also influence the applied stress level at which a Gaussian distribution is observed.

The general forms of the contact area and contact pressure distributions for the three-dimensional assemblies are also of some practical interest. Figure 8.15, illustrates the contact area distributions for the 100% soft assembly at $\sigma = 100$ kPa and the 100% hard assembly at $\sigma = 1$ MPa. A more uniform distribution is observed for the 100% soft assembly in figure 8.15a and this form of distribution was also observed for particle contact-type specific, contact area distributions in Appendix E, figures E14 - E15. The contact area distribution for the 100% hard assembly in figure 8.15b, is skewed towards the low contact area values. Therefore, the degree of deformation for hard-hard particle contacts in the 100% hard particle assembly is not uniformly distributed amongst the contacts. The exponential nature of the contact force distribution for the same assembly in figure 8.13a is further evidence to support this suggestion.

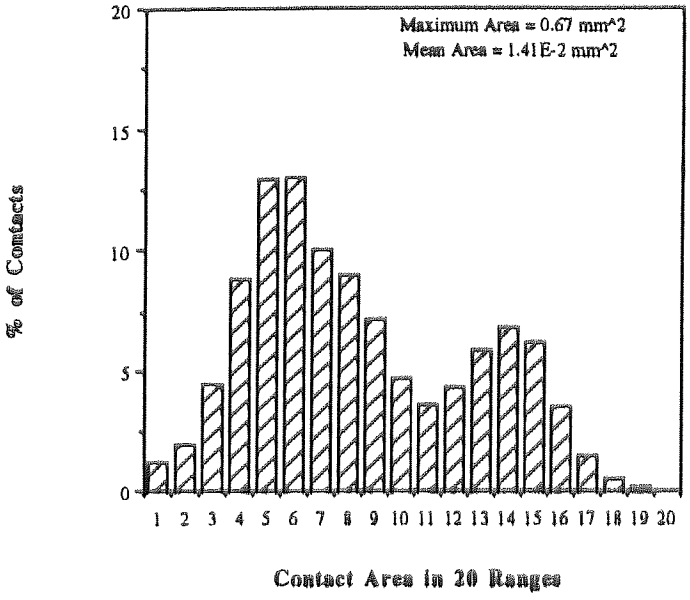

a)

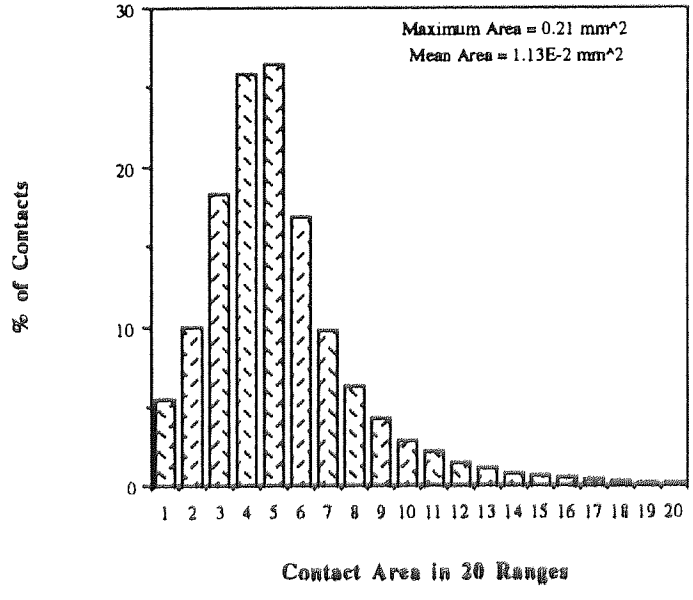

b)

Figure 8.15 Contact area distributions for three-dimensional assemblies subject to quasi-static compaction.
a) 100% soft particle assembly (σ = 100 kPa)
b) 100% hard particle assembly (σ = 1 MPa);

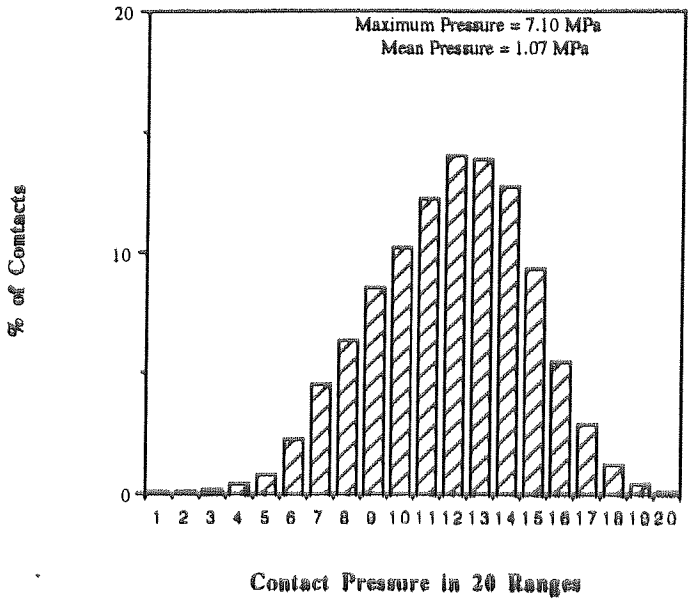

a)

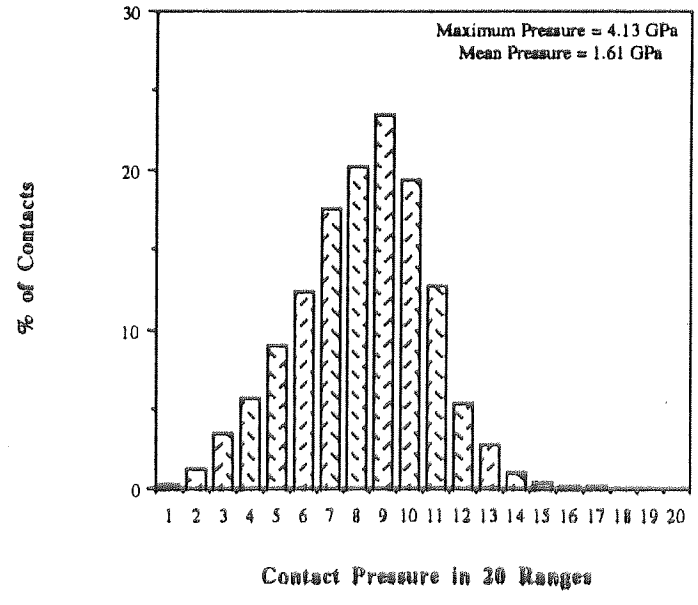

b)

Figure 8.16 Contact pressure distributions for three-dimensional assemblies subject to quasi-static compaction.

a) 100% soft particle assembly (σ = 100 kPa)

b) 100% hard particle assembly (σ = 1 MPa);

The contact pressure distributions presented in figure 8.16 are both Gaussian, even though the assemblies are at extremes of the composition range and at different stress levels. The contact pressure at a particle contact is determined by the relationship pressure = force/area and is therefore, affected by the nature of both the contact force and the contact area at the contact. A random distribution of pressure values represented by a Gaussian distribution would be expected, because of the contact force and contact area results presented earlier in this section.

8.5.2 Contact behaviour of assemblies around $p = 0.5$

In figure 8.2, which was presented earlier in this chapter, a large quantitative transition in stress-strain behaviour was observed for the three-dimensional assemblies with compositions between $p = 0.5$ and $p = 0.75$. Therefore, in this section, the contact force behaviour of the 50:50 and 75:25 assemblies will be examined in an attempt to provide clues to this observed macroscopic behaviour. The nature of the contact area and contact pressure distributions for these assemblies, although useful information, is considered to have less affect on such external, stress-strain behaviour and is therefore presented in Appendix E, figures E14 - E17. The contact force distributions shown in this section are at the common stress level of $\sigma = 1.0$ MPa, to limit stress level effects on the observed contact behaviour. The complexity of the assembly contact behaviour around $p = 0.5$ was first observed in section 6.5. The contact force distribution behaviour of the 50:50 and 75:25 three-dimensional assemblies is also complex and so to aid interpretation, all the contact information distributions presented here are a composite of the individual, contact-type specific distributions. Figure 8.17 illustrates such composite, contact force distributions for the selected assemblies. All the contact force, contact-type specific distributions for the 50:50 assembly, presented in figure 8.17a are exponential in form. However, the contact force distributions obtained from the 75:25 assembly and presented in figure 8.17b, show more complex behaviour and indicate that, the contact force distribution obtained from the hard-hard particle contacts is Gaussian in form, whilst the distributions from the hard-soft and soft-soft, particle contacts are heavily, concentrated in the lowest contact force ranges.

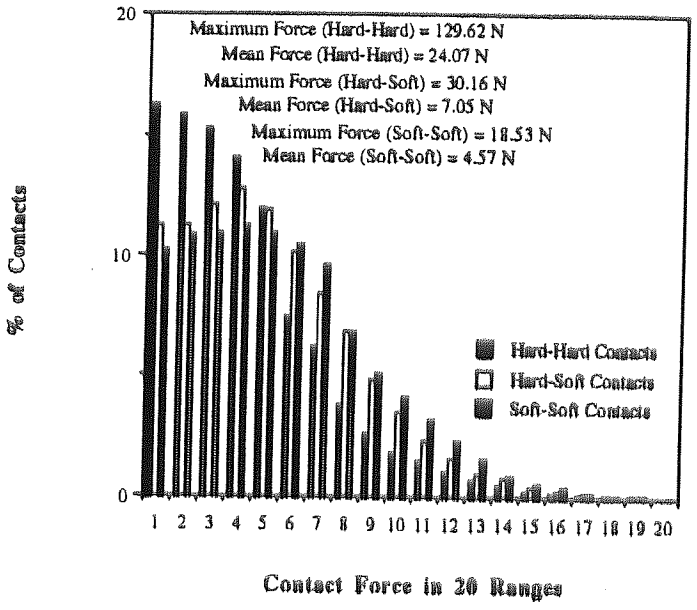

a)

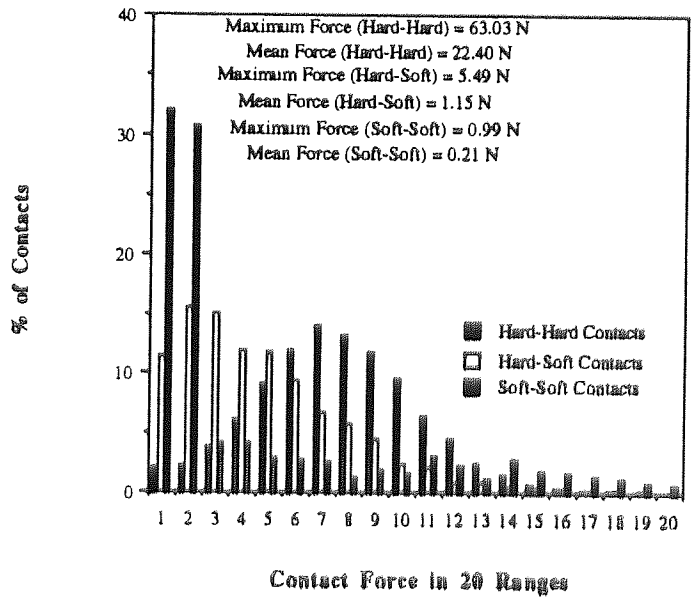

b)

Figure 8.17 Composite contact force distributions at a stress level of $\sigma = 1.0$ MPa for the **a)** 50:50 hard:soft, three-dimensional assembly **b)** 75:25 hard:soft, three-dimensional assembly.;

The information from figure 8.17 is difficult to interpret in terms of macroscopic assembly behaviour and therefore, a more detailed investigation of the particle contact-type, contact force distributions is required. Figure 8.18 is the result of such an investigation and presents the comparative results of the individual contact-type, force distributions obtained from the 50:50 and 75:25 particle assemblies. Figure 8.18a shows that, the contact force distribution for the hard-hard particle contacts in the 50:50 assembly is exponential in form, whilst a Gaussian distribution is obtained from the 75:25 assembly, as mentioned earlier. If the ideas of Rothenburg (1980) are used, then the Gaussian distribution visible in figure 8.18a suggests that co-operative load sharing between the hard-hard particle contacts will occur as sufficient numbers of such contacts become available in the assembly. Figures 8.18b and c show the contact force distributions for the hard-soft and soft-soft particle contacts respectively and in both of these figures, an increase in the number of hard particles in the assembly composition results in a narrower, more exponential distribution.

The results presented in figure 8.18 seem to indicate that all the different particle contact-types in the 50:50 hard:soft assembly compete for transmission of the applied forces across the assembly. However, in the case of the 75:25 assembly, load transmission appears to be a communal process for the hard-hard particle contacts and it is only the other contact types that compete for the privilege of being a large force-carrier. The differences in macroscopic, stress-strain behaviour between assemblies with compositions above and below $p \approx 0.5$, which were reviewed earlier in this chapter, therefore seem to be related to the nature of such individual contact-type, contact force distributions. Further studies are however, needed to confirm the validity of this statement.

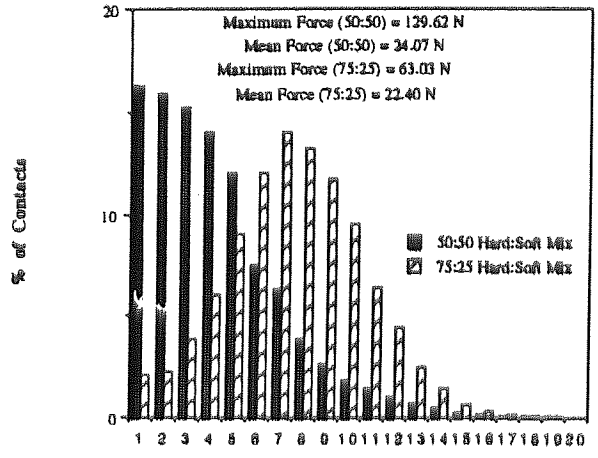

a)

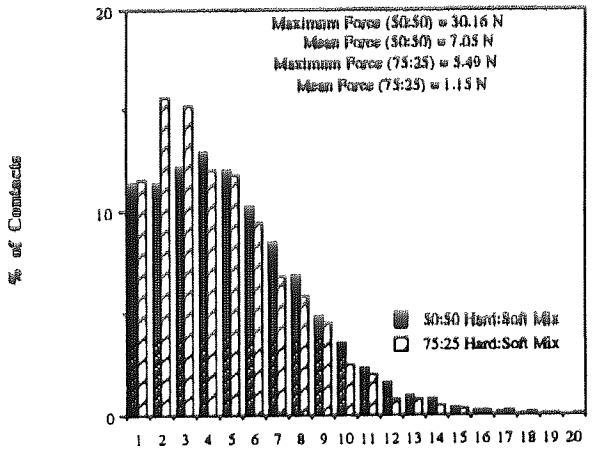

b)

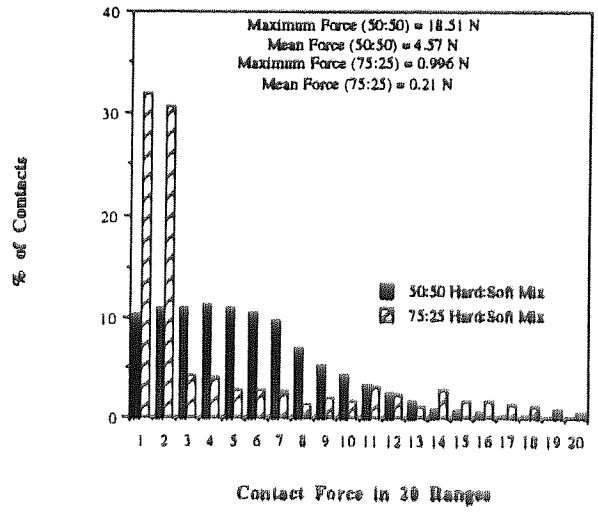

c)

Figure 8.18 Comparison between specific contact-type, contact force distributions for the 50:50 and 75:25 hard:soft, three-dimensional assemblies at a stress level of $\sigma = 1.0$ MPa. a) Hard-hard particle contacts b) Hard-soft particle contacts c) Soft-soft particle contacts;

8.6 Percolation theory-based parameters

The relevance of percolation theory to the interpretation of particle assembly behaviour was first considered in section 3.6, where this theoretical approach was found to be of some merit. The importance of percolation theory to the compaction behaviour of three-dimensional, particle systems was highlighted by the simulation work of Bouvard and Lange (1991) and the experimental studies of uniaxial compaction of binary, metal powders performed by Lange *et al* (1991). This work is reviewed in more detail in sections 2.4 and 2.2.1 respectively. The cluster backbones for the three-dimensional assemblies used in the simulation experiments were determined using the method described in section 5.4. The work presented in this section is significant, because it is an attempt to interpret the macroscopic behaviour of a three-dimensional assembly in terms of the internal structure of its cluster backbone and this has not been previously attempted.

Alterations to the assembly composition were responsible for significant quantitative changes in the macroscopic stress-strain behaviour presented in section 8.3.1 and an investigation of the structure of the cluster backbones for assemblies with different compositions at the same stress level of σ = 1.0 MPa was performed in this section, to help in interpretation of such macroscopic changes. In section 3.3.2 it was shown that, the value of the backbone fractal dimension D_B acted as a descriptor of the spatial occupation properties of assembly backbones. Therefore, the values of D_B presented in table 8.1 give an indication of the physical size of the backbones for the assemblies, which were compacted up to a stress level of σ = 1.0 MPa and show that by increasing the number of hard particles in the assembly composition, the size of the backbone is reduced. The physical size of the backbone can give an indication of the nature of the stress transmission pathways that compose the *strongest stressed* network. A smaller value of D_B for the 100% hard assembly (p = 1.0) in table 8.1, suggests that force transmission will occur in a more direct manner, than would be the case in the 100% soft assembly (p = 0.0), with its larger value of D_B.

The interpretation of D_B values could help to explain the quantitative increase in the gradient of the stress-strain curves presented in figure 8.2, because the stiffer assembly behaviour visible in this figure as p was increased could be caused by more direct transmission of forces through the assembly as D_B correspondingly decreased in value.

p - Proportion of hard spheres in assembly	D_B
0.0	2.093
0.25	2.072
0.4	2.051
0.5	2.031
0.6	1.959
0.75	1.958
1.0	1.953

Table 8.1 Values of the backbone fractal dimension for the backbones of the three-dimensional assemblies at a stress level of $\sigma = 1.0$ MPa.;

It is important to examine the composition of the backbones in the three-dimensional assemblies and use such analysis as an interpretative aid for the observed macroscopic, stress-strain behaviour reviewed in section 8.3.1. Table 8.2 shows the composition of the assembly backbones and the quantitative significance of the hard particles in the backbone structure at $\sigma = 1.0$ MPa. The quantitative importance of hard particles in the composition of the backbones at p_e was indicated in section 5.5 and isotropic compression of the backbone causes the backbone to be composed entirely of hard particles for $p \geq 0.5$ in table 8.2. The results presented in table 8.2 indicate that interpretation of the hard-hard particle contact behaviour is important in any explanation of the observed stress-strain behaviour for such assemblies and confirms the views expressed in section 8.5.2, where changes in assembly stress-strain behaviour around $p = 0.5$ were interpreted in terms of microstructural characteristics.

p - Proportion of hard spheres in assembly	% Soft spheres in backbone	% Hard spheres in backbone
0.0	100.0	0.0
0.25	25.3	74.7
0.4	3.0	97.0
0.5	0.0	100.0
0.6	0.0	100.0
0.75	0.0	100.0
1.0	0.0	100.0

Table 8.2 Backbone compositions for three-dimensional assemblies at a stress level of $\sigma = 1.0$ MPa.;

The 50:50 and 75:25 hard:soft assemblies at a stress level of $\sigma = 1$ MPa were studied and views of the backbones for these assemblies are presented in figures 8.19 and 8.20 respectively. The figures show unexpectedly that the composition of the backbone for both assemblies consists entirely of hard particles, as indicated in table 8.2. It should however, be noted that a transition in backbone composition was observed around $p = 0.25$, which confuses the situation.

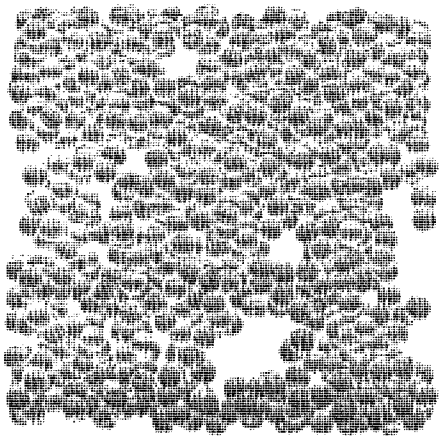

Figure 8.19 Cluster backbone for the three-dimensional, 50/50 hard:soft assembly subject to quasi-static compression at a stress level of $\sigma = 1.0$ MPa.;

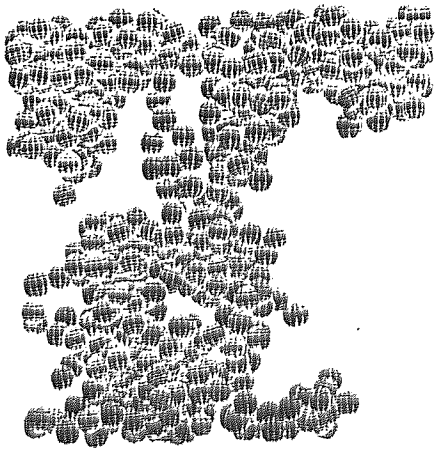

Figure 8.20 Cluster backbone for the three-dimensional, 75/25 hard/soft assembly subject to quasi-static compression, at a stress level of $\sigma = 1.0$ MPa.

Figure 8.21 presents the backbone for the 25:75 hard:soft assembly and clearly shows that soft particles are present in the assembly structure. Examination of the composition of this backbone in table 8.2 indicates that it is composed of ~25% hard particles, even after compaction up to a stress level of $\sigma = 1.0$ MPa. However, a rapid increase in the hard particle content of the backbones for the assemblies was observed in the data presented in this table, for compositions above $p = 0.25$.

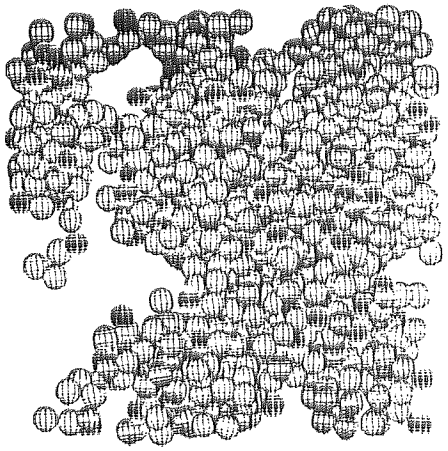

Figure 8.21 Cluster backbone for the three-dimensional, 25:75 hard:soft assembly subject to quasi-static compression, at a stress level of $\sigma = 1.0$ MPa.

The backbone for the 40:60 hard:soft particle assembly is presented in figure 8.22 and clearly shows that only a few soft particles are visible.

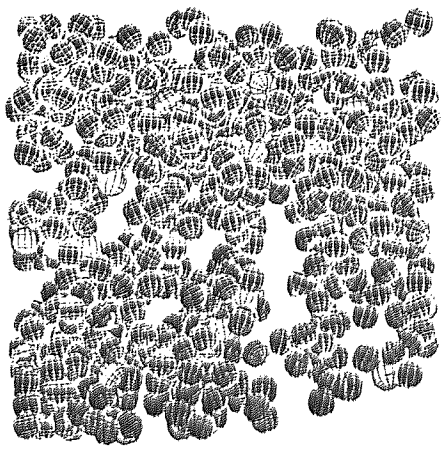

Figure 8.22 Cluster backbone for the three-dimensional, 40:60 hard:soft assembly subject to quasi-static compression, at a stress level of $\sigma = 1.0$ MPa.

The uniform nature of the backbone composition for both the 50:50 and 75:25 assemblies indicates that other microstructural factors such as the physical nature of the stress transmission pathways in these assemblies are more likely to be causes of the changes in macroscopic behaviour seen in section 8.3.1. Therefore, the area requires further investigation to clarify the situation.

The use of multifractality as a potentially convenient tool for the description of microstructural assembly behaviour for two-dimensional, particle assemblies was confirmed by the work presented in section 6.7. A more detailed review of multifractality is available in section 3.4 and work will be presented here to show that multifractal distributions are also able to describe the contact information from three-dimensional assemblies. Figure 8.23 shows the multifractal contact force distribution for the 25:75 hard:soft assembly compacted up to a stress level of $\sigma = 1.0$ MPa. The multifractal distribution is to be expected, if the three-dimensional, particle assemblies act in a similar manner to the elastic lattices studied by de Arcangelis *et al* (1985) in the original work on multifractality and this idea is apparently correct from the evidence obtained from the simulation experiments. Further examples of multifractal contact information distributions for three-dimensional assemblies are provided in Appendix E, figures E18 and E19.

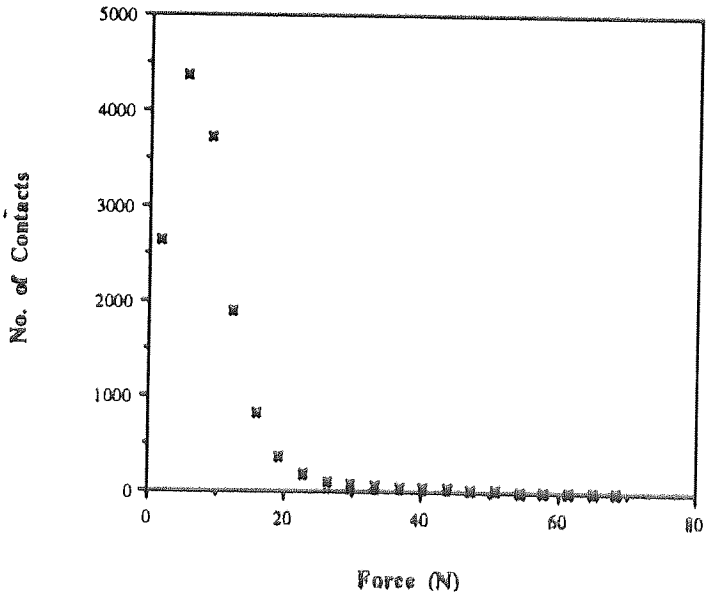

Figure 8.23 Multifractal contact force distribution for the three-dimensional, 25:75 hard:soft assembly at a stress level of $\sigma = 1.0$ MPa.;

8.7 Summary

The quasi-static compaction behaviour of three-dimensional particle assemblies was studied in this chapter. The macroscopic, stress-strain behaviour of the assemblies was found to be adequately described by second order polynomial expansions and became Hertzian-like at higher compaction stresses. Similar results were observed for the two-dimensional assemblies studied in chapter 6. The coefficients of the polynomial expansions presented in this chapter were found to be sensitive to the composition of the assembly. The work presented here also indicated that empirical relationships such as those developed by Kawakita (1956) and Heckel (1961a) for real powder systems, could also be used as adequate quantitative tools for analysis of the stress-strain behaviour exhibited by the simulation assemblies. The evolution of structural parameters of the simulation assemblies was also studied and the work of Hardin (1987) was found to be applicable to three-dimensional systems.

It was demonstrated in this chapter, that the observed forms of the microstructural contact force distributions for the simulation assemblies were dependent upon both the assembly composition and the degree of compaction. Therefore, softer or highly compacted assemblies exhibited Gaussian distributions and the distributions for harder or less compact assemblies were exponential. The shape of the contact force distribution for the hard-hard particle contacts also played a possible role in the changes in assembly, stress-strain behaviour around $p = 0.5$.

Examination of the cluster backbones for some of the three-dimensional assemblies compacted up to $\sigma = 1.0$ MPa, indicated that the backbones were entirely composed of hard particles when $p > 0.25$. Therefore, relating backbone composition and structure to macroscopic parameters was difficult. However, a transition in the values of the fractal dimension D_B for such backbones, which corresponds to a transition in their physical size was observed at the significant composition of $p \cong 0.5$.

The possible use of multifractality as a theoretical descriptor of the compaction behaviour of three-dimensional systems was also indicated by interpretation of the results from the three-dimensional simulation experiments.

Chapter 9

Concluding Remarks

An investigation of the isotropic compression behaviour of particle assemblies composed of hard and soft spheres, by means of computer simulation experiments using the TRUBAL program, has been reported in this thesis. The results from the simulation experiments have been assessed in terms of both macroscopic and microstructural parameters and theoretical considerations from the field of percolation theory. Throughout the text comments and conclusions have been provided where appropriate and it is, therefore, only necessary to add a few closing remarks and suggestions for future work in this final chapter.

The use of percolation theory in the mechanical analysis of particle assemblies has been a contentious issue between statistical physicists and other workers in the field of powder technology. Therefore, the study of assembly behaviour at percolation 'threshold' ground states in chapter 5 is important because it provides some simulation evidence that theoretical percolation concepts are useful in the qualitative interpretation of macroscopic parameters like stress-strain behaviour. Other work presented in chapter 5 showed that investigation of the percolating cluster 'backbone' for an assembly provided useful insights into internal assembly behaviour and that multifractality could be used in a theoretical description of the compaction behaviour of two- and three-dimensional particle systems. Limited work has been carried out by other workers on the extension of these theoretical concepts to relatively realistic particle assemblies and, therefore, the results presented in this text are a useful contribution to the area of study.

It is important to remember that, for statistical accuracy in determining percolation parameters, a large number of simulation experiments need to be performed. Reproduction of experiments was a more straightforward process for the majority of studies reviewed in chapter 3 because they only dealt with relatively simple elastic lattice systems. Further simulation work based on analysis of percolation-based parameters is, therefore, an important area of future work. The limited quantitative information presented in chapter 5, however, still permits a useful qualitative interpretation of particle assembly behaviour at p_e to be performed.

The bulk of the research described in this thesis has been concerned with an investigation of the isotropic compression behaviour of random assemblies composed of both hard and soft spheres. The behaviour of monodisperse two-dimensional assemblies subject to quasi-static compaction was studied in chapter 6.

The macroscopic stress-strain behaviour of such assemblies could be adequately described by a second-order polynomial function and became Hertzian-like at higher compaction pressures. The quasi-static state is a relatively idealised condition and this may explain the excellent agreement between the polynomial functions and the simulation data. The fundamental nature of the percolation threshold for an assembly, suggested by the results presented in chapter 5, also helps in acceptance of the relationships between the polynomial coefficients and assembly parameters at p_e. The structural evolution of the simulation assemblies presented in chapter 6 was similar to that of real powder systems because relationships such Hardin's (1987) were observed. However, such behaviour is less surprising once the theoretical background of the TRUBAL program (see chapter 4) and the idealised conditions of the quasi-static state are considered.

The influence of both assembly composition and particle stiffness on the shape of the contact force distribution for an assembly was illustrated in chapter 6. The results obtained from such work are new and indicate that a better understanding of the behaviour at particle contacts is required to improve analysis of microstructural behaviour at the particle assembly level. The importance of assembly and particle composition on the development on percolation-based structures such as assembly backbones was also presented for the first time in chapter 6. However, as mentioned earlier in this section, further experiments are required to verify the statistical accuracy of these results.

The quasi-static compaction behaviour of two-dimensional, bimodal assemblies composed of 2:1 hard:soft and 2:1 soft:hard size ratio particles was examined in chapter 7. Second-order polynomial functions were also able to provide an adequate description of the stress-strain behaviour for the majority of these assemblies, for the same reasons that were indicated for the monodisperse assemblies in the previous paragraph. The development of other macroscopic parameters such as assembly solid fraction ϕ during compaction was similar to that observed for the monodisperse assemblies, because the simulation experiments were still performed under fairly idealised quasi-static conditions. Geometrical factors within the assemblies e.g. particle size, were clearly responsible for some of the macroscopic results presented in chapter 7 which could not be adequately described by idealised models of assembly behaviour.

However, the influence of particle size on percolation structures like assembly backbones and on microstructural parameters such as contact force distributions was less clear, because analysis of these characteristics was made difficult by variations in both particle size and composition at the particle contacts. Therefore, further simulation work on bimodal systems is required to enable more detailed studies of the combined action of particle composition and size on microstructural parameters to be undertaken and to provide statistical accuracy for percolation-based studies.

The quasi-static compaction behaviour of three-dimensional, binary particle assemblies, which are more realistic models of granular media, was studied in chapter 8. The macroscopic, stress-strain behaviour of these assemblies was again adequately described by second order polynomial expansions and became Hertzian-like at higher compaction pressures. Such results suggest that second-order polynomial functions and the percolation parameters that they represent (see section 6.3), form a valid base for the future development of more realistic powder compaction theories. However, further simulation and experimental work is required to help in the development of such a theory, because the studies presented in this thesis only examined elastic particle systems.

The work presented in chapter 8 also indicated that the observed contact force distribution for an assembly was dependent upon both the assembly composition and the degree of compaction to which the assembly had been subjected. Therefore, analysis of the microstructural characteristics of three-dimensional particle assemblies is more difficult because another parameter has to be considered.

Only a limited number of tests have been carried out within this thesis and therefore, many more simulation experiments are required before a full understanding of the compaction behaviour of even relatively idealised elastic assemblies is obtained. These future tests could consider varying the physical properties of the particles, different particle gradings and different loading histories. Once the elastic range of assembly particle deformation has been explored, further simulation studies should then concentrate on examining elasto-plastic deformation of the particles because most experimental powder systems become compact via this mode of deformation.

The results presented in chapter 7 indicated that particle size was important. Therefore, simulation studies performed in the future should also consider the effects of particle shape on both elastic and elasto-plastic particle systems.

The isotropic compression simulation experiments that were carried out in this study were limited to low stress levels and the elastic region of assembly deformation. It is therefore important that modifications are made to the TRUBAL code to also allow consideration of the elasto-plastic region of deformation. However, the effects of such changes to the particle interaction laws on the observed macroscopic and microstructural assembly behaviour is unclear at the present time.

The second-order, stress-strain expansion showed that there was a link between idealised, mathematical models of elastic, particle assembly behaviour and the results obtained from simulation experiments. However, further theoretical and simulation work is required to expand and validate such models for more realistic particle assemblies and processing situations, such as die-compaction of a elasto-plastic particle system.

The use of percolation theory concepts in the interpretation of the macroscopic and microstructural behaviour of the elastic particle assemblies considered in the simulation experiments has not previously been attempted. Such concepts were found to be qualitatively useful, but as is the case with all pioneering studies, this work opens up further avenues of study. The use of percolation theory in a description of agglomerate behaviour during compaction is one potential area of study and the development of this theoretical concept to account for elasto-plastic particles within an assembly is another.

REFERENCES

1) Abdel-Ghani M., Petrie J.G., Selville J.P.K., Clift R. and Adams M.J. 1991. Mechanical properties of cohesive particulate solids. *Powder Technology*. **65** : 113-123.

2) Adams M.J. and McKeown R. 1995. Micromechanical analyses of the pressure-volume relationships for powcers under confined uniaxial compression. *Powder Technology*, in press.

3) Aharony A. 1987. Multifractality on percolation clusters. In R. Pynn and T. Riste, editors, *Time-Dependent Effects in Disordered Materials*, pages 163-171.

4) Allain C., Charmet J.C., Clement M. and Limat L. 1985. Comparison of the elastic moduli and the conductivity observed in a two-dimensional percolating system. *Phys. Rev. B.* **32** (11) : 7552-7554.

5) Allersma H.G.B. 1982. Photo-elastic stress analysis and strains in simple shear. In *IUTAM Conf. on Deformation & Failure of Granular Materials*, pages 345-354, Delft, Netherlands.

6) Ammi M., Travers T., Bideau D., Gervois A., Messager J.C. and Troadec J.P. 1988. Uniaxial compression of 2d and 3d packings: electrical conductivity measurements. *J. Physique*. **49** : 221-226.

7) Anderson J.C., Leaver K.D., Rawlings R.W. and Alexander J.M. 1985 *Materials Science*. 3rd edition, Van Nostrand Reinhold, Wokingham.

8) Annic C., Bideau D., Lemaitre J., Troadec J.P. and Gervois A. 1993 Geometrical properties of 2d packings of particles. In C. Thornton, editor, *Powders & Grains '93*, pages 11-16.

9) Arbabi S. and Sahimi M. 1993. Mechanics of disordered solids I : Percolation on elastic networks with central forces. *Phys. Rev. B.* **47**(2) : 695-702.

10) Arzt E. 1982. The influence of an increasing particle co-ordination on the densification of spherical powders. *Acta Metallurgica*. **30** : 1883-1890.

11) Athy L.F. 1930. Density, porosity and compaction of sedimentary rocks. *Bulletin American Association of Petroleum Geologists*. **14** (1) : 1-24.

12) Auvinet G. 1972. Generation of granular media by computer. In *Proc. 5th Panam. Conf. on Soil Mechanics & Foundation Engineering*, pages 205-216, Buenos Aires.

13) Bagi K. 1993. On the definition of stress and strain in granular assemblies through the relation between micro and macro-level characteristics. In C. Thornton, editor, *Powders & Grains '93*, pages 117-122.

14) Bak P., Tang C. and Wiesenfeld K. 1987. Self-organised criticality: an explanation for 1/f noise. *Physical Review Letters*. **59** (4) : 381-384.

15) Bak P., Tang C. and Wiesenfeld K. 1989. Comment on 'Relaxation on the angle of respose'. *Physical Review Letters*. **62** (1) : 110.

16) Balberg I. and Binenbaum N. 1987. Scher & Zallen criterion : applicability to composite systems. *Phys. Rev. B.* **26** (11) : 6254-6275.

17) Balshin M.Y. 1938. Contribution to theory of metallo-ceramic processes. Report IV contribution to theory of pressing process. *Vestnik Metalloprom.* **18** (2) : 124-137.

18) Barnes D.J. 1985. *A study of the Micro-mechanics of Granular Media.* PhD. Thesis, Aston University.

19) Benguigui L. 1984. Experimental study of the elastic properties of a percolating system. *Physical Review Letters.* **53** (21) : 2028-2030

20) Bergman D.J. 1985. Elastic moduli near percolation : universal ratio & critical exponent. *Phys. Rev. B.* **31** (3) : 1696-1698.

21) Bergman D.J. and Kantor Y. 1984. Critical properties of an elastic fractal. *Physical Review Letters.* **53** (6) : 511-514.

22) Beynon T.D., Hawkesworth M.R., McNeil P.A., Parker D.J., Bridgewater J., Broadbent C.J. and Fowles P. 1993. Positron based studies of powder mixing. In C. Thornton, editor, *Powders & Grains '93*, pages 377-382.

23) Bideau D. and Troadec J.P. 1984. Compacity & mean co-ordination number of dense packings of hard discs. *J. Phys. C : Solid State Phys.* **17** : L731-L735.

24) Bideau D., Troadec J.P and Dodds J.A. 1991. Compression of two dimensional packings of cylinders made of rubber. *Powder Technology.* **65** : 147-151.

25) Bockstiegel G. 1966a. The porosity-pressure curve and its relation to the pore-size distribution in iron powder compacts. In E. Hausner, editor, *Modern Developments in Powder Metallurgy*, pages 155-187.

26) Bockstiegel G. 1966b. Relations between pore structure and densification mechanism in the compactng of iron powders. *International Journal of Powder Metallurgy.* **2** : 13-26.

27) Bordia R.K. and Raj R. 1988. Hot isostatic pressing of ceramic/ceramic composites at pressures < 10 MPa. *Advanced Ceramic Materials.* **3** (2) : 122-126.

28) Born M. and Huang K. 1954. *Dynamical Theory of Crystal Lattices*, (Chapter 5). Oxford University Press, New York.

29) Bouvard D. and Lange F.F. 1991. Relation between percolation and particle co-ordination in binary powder mixtures. *Acta Metall. Mater.* **39**(12) : 3083-3090.

30) Briscoe B.J. 1981. *Phil. Mag.* **A43** : 511

31) Briscoe B.J. and Evans P.D. 1991. Wall friction in the compaction of agglomerated ceramic powders. *Powder Technology.* 65 : 7 - 20.

32) Briscoe B.J., Özkan N. and Ayoin I. 1994. A compaction study of alumina powders. In *1st International Particle Technology Forum.*, Volume 1, pages 208-213, Denver, U.S.A.

33) Broadbent S.R. and Hammersley J.M. 1957. *Proc. Cambridge Phil. Soc.* **53** : 629 - 633

34) Broese van Groenou A. 1980. Compaction of ceramic powders. *Powder Metallurgy International.* **12** : 221-228.

35) Bunde A., Coniglio A., Hong D.C. and Stanley H.E. 1985. Transport in a two-component randomly composite material : scaling theory and computer simulations of termite diffusion near the superconducting limit. *J. Phys. A : Math. Gen.* **18** : L137-144.

36) Bunde A. and Havlin S. (Eds.) 1991. *Fractals and Disordered Systems.* Springer-Verlag, Berlin.

37) Burr I.W. 1974. *Applied Statistical Methods.* Academic Press, New York.

38) Coniglio A. 1981. Thermal phase transition of the dilute s-state Potts and n-vector models at the percolation threshold. *Physical Review Letters.* **46** (4) : 250-253.

39) Cooper A.R. and Eaton L.E. 1962. Compaction behaviour of several ceramic powders. *J. Am. Ceram. Soc.* **45** (3) : 97-101.

40) Cundall P.A. 1971. A computer model for simulating progressive, large-scale movements in blocky rock systems. In *International Symposium on Rock Mechanics*, pages 11.8.1-11.8.12, Nancy, France.

41) Cundall P.A. 1988. Computer simulation of dense sphere assemblies. In M. Satake & J.T. Jenkins, editors, *Micromechanics of Granular Materials*, pages 113-123.

42) Cundall P.A. 1989. Numerical experiments on localization in frictional materials. *Ingenieur-Archiv.* **59** : 148-159.

43) Cundall P.A., Drescher A. and Strack O.D.L. 1982. Numerical experiments on granular assemblies; measurements and observations. In *IUTAM Conf. on Deformation & Failure of Granular Materials*, pages 355-370, Delft, Netherlands.

44) Cundall P.A., Jenkins J.T. and Ishibashi I. 1989. Evolution of elastic moduli in a deforming granular assembly. In J. Biarez and R. Gourves, editors, *Powders & Grains*, pages 319-322.

45) Cundall P.A. and Strack O.D.L. 1979a. *The distinct element method as a tool for research in granular material. Part II: Report to the NSF.* Department of Civil and Mineral Engineering, University of Minnesota.

46) Cundall P.A. and Strack O.D.L. 1979b. A discrete numerical model for granular assemblies. *Geotechnique.* **29** (1) : 47-65.

47) Cundall P.A. and Strack O.D.L. 1983. Modeling of microscopic mechanisms in granular material. In J.T. Jenkins and M. Satake, editors, *Mechanics of granular materials : New models and constitutive relations*, pages 137-149.

48) Dantu P. 1957. A contribution to the mechanical & geometrical study of non-cohesive masses. In *Proc. 4th Int. Conf. on Soil Mechanics & Foundation Engineering*, London, pages 144-148.

49) Davis R.A. and Deresiewicz H. 1977. A discrete probablistic model for the mechanical response of a granular medium. *Acta. Mechanica.* **27** : 69-89.

50) Day A.R., Tremblay R.R. and Tremblay A.M.S. 1986. Rigid backbone: a new geometry for percolation. *Physical Review Letters*. **56** (23) : 2501-2504.

51) De Arcangelis L., Redner S. and Coniglio A. 1985. Anomalous voltage distribution of random resistor networks and a new model for the backbone at the percolation threshold. *Phys. Rev. B*. **31** (7) : 4725-4727.

52) De Gennes P.G. 1976. On a relation between percolation theory and the elasticity of gels. *Journal de Physique Lettres*. **37** (4) : L1-L2.

53) Deptuck D., Harrison J.P. and Zawadzki P. 1985. Measurement of elasticity and conductivity of a three-dimensional percolation system. *Physical Review Letters*. **54** (9) : 913-916.

54) Deutscher G., Zallen R. and Adler J. (Eds.) 1983. *Percolation structures and Processes*. Adam Hilger, Bristol.

55) Donachie M.J. and Burr M.F. 1963. Effects of pressing on metal powders. *Journal of Metals*. **18** : 849-854.

56) Dodds J.A. 1975. Simplest statistical geometric model of the simplest version of the multicomponent packing problem. *Nature*. **256** : 187-189.

57) Dodds J.A. 1991. The structure of random packings formed by spheres with a mixture of sizes. In D. Bideau and J.A. Dodds, editors, *Physics of Granular Media*, pages 57-72.

58) Drescher A. 1976. An experimental investigation of flow rules for granular materials using optically sensitive glass particles. *Geotechnique*. **26** (4) : 591-601.

59) Drescher A. and de Josselin de Jong G. 1972. Photoelastic verification of a mechanical model for the flow of a granular material. *J. Mech. Phys. Solids*. **20** : 337-351.

60) Elam W.T., Kerstein A.R. and Rehr J.J. 1984. Critical properties of the void percolation problem for spheres. *Physical Review Letters*. **52** (17) : 1516-1519.

61) Esezebo S. and Pilpel N. 1976. Moisture and gelatin effects on the interparticle attractive forces and the compression behaviour of oxytetracycline formulations. *J. Pharm. Pharmac*. **29** : 75-81.

62) Feder J. 1988. *Fractals*. Plenum Press, New York.

63) Fedorchenko I.M., Kovynev R.A., Makovetskii V.A. and Sitnikov L.L. 1968. A photoelastic technique for examining contact stresses in powder compaction. *Soviet Powder Metallurgy & Metal Ceramics*. **11** (71) : 850-854.

64) Feng S. 1985. Percolation properties of granular elastic networks in two dimensions. *Phys. Rev. B*. **32** (1) : 510-513.

65) Feng S. and Sen P.N. 1984. Percolation on elastic networks : new exponent and threshold. *Physical Review Letters*. **52**(3) : 210-219.

66) Feng S., Sen P.N., Halperin B.I. and Lobb C.J. 1984. Percolation on two-dimensional elastic networks with rotationally invariant bond-bending forces. *Phys. Rev. B*. **30** (9) : 5386-5389.

67) Fischmeister H.F., Arzt E. and Olson L.R. 1978. Particle deformation and sliding during compaction of spherical powders : A study by quantitative metallography. *Powder Metallurgy.* **4** : 179-187.

68) Funkebusch P.D. and Li E.K.H. 1991. HIP of bi-modal powder mixtures - modelling and experiment. In *Proc. 3rd Int. Conf. HIP*, Osaka, pages 17-21.

69) Gherbi M., Gourves R. and Oudjehane F. 1993. Distribution of contact forces inside a granular media. In C. Thornton, editor, *Powders & Grains '93*, pages 167-172.

70) Guyon E. 1991. Mechanical percolation. In D. Bideau and J.A. Dodds, editors,*Physics of Granular Media*, pages 103-112.

71) Guyon E., Roux S., Hansen A., Bideau D., Troadec J.P. and Crapo H. 1990. Non-local and non-linear problems in the mechanics of disordered systems : Application to granular media and rigidity problems. *Reports of Progress in Physics.* **53** : 373-419.

72) Halperin B.I., Feng S. and Sen P.N. 1985. Differences between lattice and continuum percolation transport exponents. *Physical Review Letters.* **54** (22) : 2391-2394.

73) Hansen A. and Roux S. 1988. Multifractality in elastic percolation. *J. Stats. Phys.* **53** : 759-771.

74) Hardin B.O. 1987. 1-D strain in normally consolidated cohesionless soils. *Journal of Geotechnical Engineering.* **113** (12) : 1449-1467.

75) Hastings N.A.J. and Peacock J.B. 1975. *Statistical Distributions.* Butterworths, London.

76) Heckel R.W. 1961a. Density - Pressure relationships in powder compaction. *Trans. Metall. Soc. AIME.* **221** : 671-675.

77) Heckel R.W. 1961b. Analysis of powder compaction phenomena. *Trans. Metall. Soc. AIME.* **221** : 1001-1008.

78) Herrmann H.J., Hong D.C. and Stanley H.E. 1984. Backbone and elastic backbone of percolation clusters obtained by the new method of burning. *J. Phys. A : Math. Gen.* **17** : L261-L266.

79) Herrmann H.J. and Stanley H.E. 1984. Building blocks of percolation clusters : volatile fractals. *Physical Review Letters.* **53** (12) : 1121-1124.

80) Herrmann H.J., Stauffer D. and Roux S. 1987. Violation of linear elasticity due to randomness. *Europhys. Lett.* **3** (3) : 265-267.

81) Isherwood D.P. 1987. Die wall friction effects in the compaction of polymer granules. In Briscoe B.J. and Adams M.J., editors, *Tribology in Particulate Technology*, pages 234-248.

82) Jagota A. 1993. Effective viscosities and sintering rates of composite random packings. In C. Thornton, editor, *Powders & Grains '93*, pages 201-206.

83) Jagota A. and Scherer G.W. 1993. Viscosities and sintering rates of a two-dimensional granular composite. *J. Am. Ceram. Soc.* **76** (12) : 3123-3135.

84) James P.J. 1972. Fundamental aspects of the consolidation of powders. *Powder Metallurgy International.* **4** (4) : 193-198.

85) Jenkins J.T., Cundall P.A. and Ishibashi I. 1989. Micromechanical modelling of granular materials with the assistance of experiments and numerical simulations. In J. Biarez and R. Gourves, editors, *Powders & Grains*, pages 257-264.

86) Jetzer W., Leuenberger H. and Sucker H. 1983. The compressibility and compactability of pharmaceutical powders. *Pharmaceut. Tech.* **22** : 33-39.

87) Johnson K.L. 1985.*Contact Mechanics.* Cambridge University Press, Cambridge.

88) de Josselin de Jong G. 1959. *Statics and kinematics in the failable zone of a granular material.* Waltmann, Delft.

89) de Josselin de Jong G. and Verrujit A. 1969. Étude photo-élastique d'un empilement de disques. *Cahiers du Groupe Francais de Rhelogie.* **2** (1) : 73-86.

90) Kafui K.D. and Thornton C. 1993. Computer simulated impact of agglomerates. In C. Thornton, editor, *Powders & Grains '93*, pages 401-406.

91) Kamm R., Steinberg M. and Wulff J. 1947. *J. Trans. Amer. Inst. min. (metall.) Engrs.* **171** : 439-447.

92) Kantor Y. and Itzhak W. 1984. Elastic properties of random percolating systems. *Physical Review Letters.* **52** (21) : 1891-1894.

93) Kawakita K. 1956. A study of powder compression. *Science Japan.* **26** : 149-150.

94) Kawakita K. 1963. Compression of powders (I) The compression equation and the anomaly of infrared spectra of pellet method. *J. Japan Society of Powder and Powder Metallurgy.* **10** : 236-244.

95) Kawakita K. and Ludde K.H. 1970. Some considerations on powder compression equations. *Powder Technology.* **4** : 61-68.

96) Kawakita K. and Tsutsumi Y. 1966. A comparison of equations for powder compression. *Bulletin Chem. Soc. Japan.* **39** : 1364-1368.

97) Kunin N.F. and Yurchenko B.D. 1968. Net compaction pressure of metal powders.*Soviet Powder Metallurgy & Metal Ceramics.* **8** (68) : 604-609.

98) Kurup T.T. and Pilpel N. 1978. Compression characteristics of pharmaceutical powder mixtures. *Powder Technology.* **19** : 147-155.

99) Lafer M., Bouvard D., Stutz P., Pierronnet M. and Raisson G. 1991. Densification behaviour of particle reinforced superalloy powder during hot isostatic pressing. In *Proc. 3rd Int. Conf. HIP*, Osaka, pages 209-214.

100) Laidlaw D., Mackay G. and Jan N. 1987. Some fractal properties of the percolating backbone in 2D. *J. Stats. Phys.* **46** (3) : 507-515.

101) Lange F.F., Atteraas L. and Zok F. 1991. Deformation consolidation of metal powders containing steel inclusions. *Acta. Metall. Mater.* **39** (2) : 209-219.

102) Last B.J. and Thouless D.J. 1971. Percolation theory and electrical conductivity. *Physical Review Letters.* **27** (25) : 1719-1721.

103) Lemieux M.A., Breton P. and Tremblay A.M.S. 1985. Unified approach to numerical transfer matrix methods for disordered systems : applications to mixed crystals and to elastic percolation. *J. Physique Lett.* **46** (1) : L1-L7.

104) Leuenberger H. 1982. The compressibility & compactability of powder systems. *Int. Journ. Pharmaceutics.* **12** : 41-55.

105) Leuenberger L. and Jetzer W. 1984. The compactability of powder systems - a novel approach. *Powder Technology.* **37** : 209-218.

106) Lian G., Kafui D. and Thornton C. 1993. *TRUBAL - A 3D computer program for simulating particle assemblies.* Department of Civil Engineering, Aston University.

107) MacLeod H.M. and Marshall K. 1977. The determination of density distributions in ceramic compacts using autoradiography. *Powder Technology.* **16** : 107-122.

108) Mandlebrot B.B. 1974. Intermittent turbulence in self-similar cascades: divergence of high moments and dimension of the carrier. *J. Fluid Mechanics.* **62** (2) : 331-358.

109) Mandlebrot B.B. 1982. *The Fractal Geometry of Nature.* W.H. Freeman and Company, New York.

110) Mandelbrot B.B. 1986. Self-affine fractal sets. In L. Pietronero and E. Tosatti, editors, *Fractals in Physics*, pages 3-28.

111) Mandlebrot B.B. 1987. Fractals. *Encyclopedia of Physical Science and Technology.* **5** : 579-593.

112) Mindlin R.D. 1949. Compliance of elastic bodies in contact. *Journal of Applied Mechanics.* **16** : 259-268.

113) Mindlin R.D. and Deresiewicz H. 1953. Elastic spheres in contact under varying oblique forces. *Journal of Applied Mechanics.* **20** : 327-344.

114) Ng T.T., Dobry R. 1992. A non-linear numerical model for soil mechanics.*Int. J. Num. Anal. Meth. Geomechanics.* **16** : 247-263.

115) Nienhuis B. 1982. Analytical calculation of two leading exponents of the dilute Potts model. *J. Phys. A : Math. Gen.* **15** : 199-213.

116) Ning Z. and Thornton C. 1993. Elastic-plastic impact of fine particles with a surface. In C. Thornton, editor, *Powders & Grains '93*, pages 33-38.

117) Nystrom C. and Karehill P.G. 1986. Studies on direct compression of tablets XVI. The use of surface area measurements for the evaluation of bonding surface area in compressed powders. *Powder Technology.* **47** : 201-209.

118) Oda M. 1972a. Mechanism of fabric changes during compression. *Soils and Foundations.* **12** (2) : 1-18.

119) Oda M. 1972b. Deformation mechanism of sand in triaxial compression. *Soils and Foundations.* **12** (4) : 45-63.

120) Oda M. and Konishi J. 1974. Microscopic deformation mechanism of granular material in simple shear. *Soils and Foundations*. **14** (4) : 25-38.

121) Oda M., Konishi J. and Nemat-Nasser S. 1980. Some experimentally based fundamental results on the mechanical behaviour of granular materials. *Geotechnique*. **30** (4) : 479-495.

122) Oger L., Bideau D., Troadec J.P. and Poirier C. 1991. Effects of disorder in the behaviour of the Schneebeli models. In *Proc. US - Japan Seminar on Micromechanics of Granular Materials*, pages 151-155, Potsdam, New York.

123) Oger L., Troadec J.P., Bideau D., Dodds J.A. and Powell M.J. 1986. Properties of disordered sphere packings. II Electrical properties of mixtures of comducting and insulating spheres of different sizes. *Powder Technology*. **46** : 133-140.

124) Onoda G.Y. and Hench L.L 1978. *Physical Characterisation Terminology, Ceramic Processing before Firing*. Wiley-Interscience, New York.

125) Palmer H.K. and Rowe R.C. 1974. A study of the compaction behaviour & pore structure of polymer compacts using mecury porosimetry. *Powder Technology*. **10** : 225-230.

126) Petersen J., Roman H.E., Bunde A. and Dieterich W. 1989. Nonuniversality of transport exponents in continuum percolation systems: Effects of finite jump distance. *Phys. Rev. B*. **39** (1) : 893-896.

127) Pflueger J.C. 1988. *The Behavior of Particle Beds in Simulation*. MSc thesis, MIT, Cambridge, Mass.

128) Pike R. and Stanley H.E. 1981. Order propagation near the percolation threshold. *J. Phys. A : Math. Gen.* **14** : L169-L177.

129) Powell M.J. 1980a. Site percolation in random networks. *Phys. Rev. B*. **21** : 3725-3728.

130) Powell M.J. 1980b. Computer simulated random packing of spheres. *Powder Technology*. **25** : 45-52.

131) Roberts R.J. and Rowe R.C. 1986. The compaction of pharmaceutical and other model materials - a pragmatic approach. *Chemical Engineering Science*. **42** (4) : 903-911.

132) Rothenburg L. 1980. *Micromechanics of idealized granular systems*. Phd thesis, Carleton University, Ottawa, Ontario.

133) Roux S. 1991. Effect of disorder on the elastic behaviour of pilings. In D. Bideau and J.A. Dodds, editors,*Physics of Granular Media*, pages 157-169.

134) Sahimi M. and Arbabi S. 1993. Mechanics of disordered solids. II Percolation on elastic networks with bond-bending forces. *Phys. Rev. B*. **47** (2) : 703-711.

135) Saleur H. and Duplantier B. 1987. Exact determination of the percolation hull exponent in two dimensions. *Physical Review Letters*. **58** (22) : 2325-2328.

136) Savkoor A.R. and Briggs G.A.D. 1977. The effect of tangential force on the contact of elastic solids in adhesion. *Proc. R. Soc. Lond. A* **356** : 103-114.

137) Scher H. and Zallen R. 1970. Critical density in percolation processes. *J. Chem. Phys.* **53** : 3759-3761.

138) Schneebeli G. 1956. Mecanique des sols - une analogie mecanique pour les terres sans cohesion. *C.R. Acad. Sciences Paris.* **243** : 125-126.

139) Schwartz L.M., Johnson D.L. and Feng S. 1984. Vibrational modes in granular materials. *Physical Review Letters.* **52** (10) : 831-834.

140) Shapiro I. and Koltoff I.M. 1947. The compressibility of silver bromide powders. *J. Phys. & Colloid Chemistry.* **51** : 483-493.

141) Shaxby J.H. and Evans J.C. 1923. The variation of pressure with depth in columns of powders. *Trans. Faraday Soc.* **12** : 60-72.

142) Stanley H.E. 1977. Cluster shapes at the percolation threshold: an effective cluster dimensionallity and its connection with critical-point exponents. *J. Phys. A : Math. Gen.* **10** (11) : L211-L220.

143) Stanley-Wood N. and Johansson M. 1980. A porosity compaction relationship from the compaction of fine powders. *Acta. Pharmaceutica Technologica.* **26** (4) : 215-219.

144) Stauffer D. 1987. Simulation of disordered systems of cylinders. II Mechanical behaviour. *J. Physique.* **48** : 347-351.

145) Stauffer D. 1992. *An introduction to Percolation Theory.* 2nd Edition, Taylor & Francis, London.

146) Strenski P.N., Bradley R.M., Debierre J.M. 1991. *Physical Review Letters.* **66** : 133-138.

147) Sundstrom B.O. and Fischmeister H.F. 1973. A continuum mechanical model for hot and cold compaction. *Powder Metallurgy International.* **5** (4) : 171-174.

148) Suzuki M. and Oshima T. 1983. Estimation of the co-ordination no. in a multi-component mixture of spheres. *Powder Technology.* **35** : 159-166.

149) Suzuki M. and Oshima T. 1985. Co-ordination no. of a multi-component randomly packed bed of spheres with size distribution. *Powder Technology.* **44** : 213-218.

150) Sykes M.F. and Essam J.W. 1964. Exact critical percolation probabilities for site and bond percolation in two dimensions. *J. Math. Phys.* **5** : 1117-1127.

151) Szalwinski C.M. 1985. Flexibility of a contact area of an isotropic elastic body. *Trans. ASME: J. Appl. Mech.* **52**: 62-66.

152) Thornton C. 1987. Computer-simulated experiments on particulate materials. In Briscoe B.J. and Adams M.J., editors, *Tribology in Particulate Technology*, pages 292-302.

153) Thornton C. and Barnes D.J. 1986. Computer simulated deformation of compact granular assemblies. *Acta. Mechanica.* **64** : 45-61.

154) Thornton C. and Randall W. 1988. Applications of theoretical contact mechanics to solid particle system simulation. In M. Satake & J.T. Jenkins, editors, *Micromechanics of Granular Materials* , pages 133-142.

155) Thornton C. and Sun G. 1993. Axisymmetric compression of 3D polydisperse systems of spheres. In C. Thornton, editor, *Powders & Grains '93*, pages 129-134.

156) Thornton C. and Yin K.K. 1991. Impact of elastic spheres with and without adhesion. *Powder Technology*, **65** : 153-166.

157) Train D. 1956. An investigation into the compaction of powders. *Journal of Pharmacy and Pharmacology*. **8** : 745-761.

158) Train D. 1957. Transmission of forces through a powder mass during the process of pelleting. *Trans. Instn. Chem. Engrs*. **35** : 258-266.

159) Travers T., Ammi M., Bideau D., Gervois A., Messager J.C. and Powell M.J. 1987. Uniaxial compression of 2D packings of cylinders. Effects of weak disorder. *EuroPhys. Lett.* **4** (3) : 329-332.

160) Travers T., Bideau D., Gervois A., Troadec J.P. and Messager J.C. 1986. Uniaxial compression effects on 2D mixtures of 'hard' and soft cylinders. *J. Phys. A: Math. Gen.* **19** : L1033-1038.

161) Trent B.C. 1988. Microstructural effects in static and dynamic numerical experiments. In *Proc. 29th U.S. Symp. Rock Mechanics*, pages 395-402, Minneapolis.

162) Troadec J.P., Bideau D. and Dodds J.A. 1991. Compression of two-dimensional packings of cylinders made of rubber and plexiglass. *Powder Technology*. **65** : 147-151.

163) Unckel H. 1945. *Arch. Eisenhüttenw.* **18** : 125 and 161.

164) Van der Zwan J. and Siskens C.A.M. 1982. The compaction and mechanical properties of agglomerated materials. *Powder Technology*. **33** : 43-54.

165) Walker E.E. 1923. The compressibility of powders. *Trans. Faraday Soc.* **12** : 73-82.

166) Walton K. 1987. The effective elastic moduli of a random packing of spheres. *J. Mech. Phys. Solids*. **35** (2) : 213-226.

167) Wakabayashi T. 1957. Photoelastic method for determination of stress in powdered mass.*Proc. 7th Japan Nat. Congress Appl. Mech.*, pages 153-158, Tokyo.

168) Wakabayashi T. 1959. Photoelastic method for determination of stress in powder mass. In *Proc. 9th Japan Nat. Congress Appl. Mech.*, pages 133-140, Tokyo.

169) Zallen R. 1983. *The Physics of Amorphous Solids*. John Wiley & Sons, New York.

170) Zhang Y. and Cundall P.A. 1986. Numerical simulation of slow deformation. In *Proc. 10th U.S. National Congress on Applied Mechanics*, pages 347-349, Austin, Texas.

Appendix A

Command List for TRUBAL

A 1 Introduction

The command summary here applies to the versions of TRUBAL resident on the workstations RS1 (for three-dimensional work) and RS2 (for two-dimensional work) as at 1st April 1996. The commands listed here may be given in any order that is physically meaningful except for the **STArt** and **REStart** commands which must be given as the first command in any command file. Parameters and commands that start with an upper-case letter are typed literally -- either in upper- or lower-case. These commands and keywords may be typed in full, or truncated to just those letters in upper-case. For example, the command **PRInt CONtacts** may be given as p c, Pr cO or any other variation. Parameters may be separated by any number of spaces, commas, brackets ( ) or slashes. For clarity it is helpful to give a minimum of three letters.

When starting *TRUBAL*, a file called *TRUBAL.DIR* should exist in the current working directory. If this file contains the word BATCH, the program will operate in batch mode and take its input from the file *TRUBAL.DAT* and place its output in *TRUBAL.OUT*. If *TRUBAL.DIR* contains the word TERM, the program will expect input from the keyboard and send its output to the display. Input and output redirection may however be used in this case to take input from and send output to specified files. Examples of *TRUBAL.DAT* files representing all the commands and keywords used in the simulation work presented in chapters 5 to 8 will be illustrated in this appendix.

A 2 Two-Dimensional Isotropic Compression

A 2.1 Assembly Generation

The following example shows how a random two-dimensional 50:50 hard:soft assembly of 1000 particles is automatically generated by TRUBAL:

example file1

```
STArt 0.157 0.157 0.157 1000 1200 2 Log
* 50:50 Mix
2-D
RAD 0.00210 1
RAD 0.00205 2
RAD 0.00200 3
RAD 0.00195 4
RAD 0.00190 5
YMD 2.0E11 1
YMD 1.0E8 2
PRA 0.3 1
PRA 0.3 2
FRIc 0.35 1
FRIc 0.35 2
DENs 7.8E3 1
DENs 8.5E2 2
RGEn 50 1 1 1
RGEn 50 1 2 1
```

```
RGEn 110 2 1 1
RGEn 110 2 2 1
RGEn 180 3 1 1
RGEn 180 3 2 1
RGEn 110 4 1 1
RGEn 110 4 2 1
RGEn 50 5 1 1
RGEn 50 5 2 1
SAVe mix.50%
STOp
```

The second command line (prefixed by *) is a comment line and is not executed by the TRUBAL program.

A 2.1.1 Command Lines

STArt x_{max} y_{max} z_{max} **nbox nball nwall [Log]**

This command (or the **Restart** command) must be the first one given to **TRUBAL**. The parameters x_{max}, y_{max} and z_{max} are the maximum dimensions of the box volume (or periodic volume) in the x, y and z directions, respectively. The size of the periodic cell in *example file1* is 15.7 cm by 15.7 cm (z_{max} is ignored in 2D work).

nbox is the number of boxes requested i.e. 1000, and **nball** is the maximum number of spheres that may be needed i.e. 1200. There is no problem if fewer spheres are subsequently generated, since the purpose of the **STArt** command is to allocate enough memory to hold all the required boxes and particles. The parameter **nwall** indicates the maximum number of walls that may be needed i.e. 2. The optional keyword **LOG** turns the "log" facility on immediately i.e. output is echoed to the output file *TRUBAL.OUT* unless redirected.

2-D

This command causes TRUBAL to operate in two-dimensional mode. The particles are still regarded as spheres, but they are constrained to move in the x-y plane only. Although the equations of motion are truncated to two dimensions, the force-displacement calculation (subroutine HFORD) still operates in three dimensions. This could be modified to improve running speed. In 2D mode, the generation routine sets the z coordinate of all particles to the same value, corresponding to the centre of the box volume in the z direction. Only one box should be specified in the z direction, although TRUBAL will not complain if more are requested.

RADius r isize

r is taken as the radius of particles of size type **isize.** In *example file1* five sizes of particle are specified, all ~2 mm in radius.

YMD ymod mtyp

Specifies a Young's modulus value of **ymod** for all particles of material-type **mtyp**. In *example file1* **mtyp** = 1 for hard spheres and **mtyp** = 2 for soft spheres.

PRA v mtyp

Specifies the Poisson ratio value **v** for material-type **mtyp**.

FRIction amu mtyp

The friction coefficient is set to **amu** for particles or walls of material type **mtyp**. For the two different material types in contact in *example file1* , the smaller of the two coefficients is used in the program.

DENsity d mtyp

d is taken as the mass density of all particles of material type **mtyp**. The values of **d** used in *example file1* are real steel and rubber density values for **mtyp** = 1 and **mytp** = 2 particles respectively.

RGEnerate n isize mtyp nagg

n particles of size type **isize** and material type **mtyp** are randomly generated in a region previously specified in the **STArt** command. In *example file1* **n** = 1000, **isize** = 1-5 and **mytp** = 1, 2 and a distribution, in terms of particle sizes, is used. No effort is made to fit particles into gaps between other particles. If a candidate particle overlaps an existing particle, it is rejected and another is tried. Before issuing this command, a radius must already have been defined for the size type **isize.** If several sizes of particles are to be combined in an assembly, the larger ones should be generated first (see *example file1*) since it is easier to fit small particles into gaps. **nagg** indicates the agglomerate number for which the particles are generated. In *example file1* **nagg** = 1.

SAVe [filename]

The current problem state is saved on the file **filename**. If a file name is not given, a default file name **save.new** is assumed. If a file name is specified that already exists, the existing data is over-written. The saved state records all positions, velocities, forces, options and so on, at a given stage in a run; it corresponds to a "snapshot" at a single point in time. The **SAVe** command does not record a sequence of commands.

A 2.2 Servo-Controlled Compression

The following example shows how Mode 1 servo control (see section 4.8) is used to maintain a constant stress level, during preparation of a 50:50 mix assembly.

example file2

```
REStart mix50.eper
* Servo control
2-D
FRAc 0.05
MODe 1
DENs 7.8E21 1
DENs 8.5E20 2
```

GAIn 0.2 -1.0E-7
DAMping 0.05 0.5 1 0 1
CYCle 100000 **S1MS2** -1.277E4
SAVe mix50.servo
STOp

The values of **DENsity** specified for the two material types are the scaled values required to permit quasi-static experimentation within acceptable time-scales (see section 4.6).

A 2.2.1 Command List

REStart [filename]

A previously-saved problem is restored from the file **filename.** If a file name is not given, a default file name of **save.old** is assumed. The command **Restart** may only be given as the first command of a run.

FRAction f

The fraction of the critical time-step is set as **f.** The critical time step Δt_{crit} is based on the Rayleigh wave speed (see section 4.6). The time it takes for the wave to traverse each particle is computed and the minimum of these times is used as Δt_{crit}.The default value of **f** is 1.0 and if numerical instability is suspected, the value of **f** should be reduced.

The value of **f** = 0.05 used in *example file2* was found to be sufficient to ensure numerical stability in the simulation work undertaken.

MODe n

This selects the type of servo control. **MODe 1,** used in *example file2* selects "velocity control", whereby the grid velocity is set directly by the servo. In the present version of TRUBAL, **MODe 1** works for control of the mean stress in 3D σ_0 and the 'two-dimensional mean stress' in 2D $(\sigma_{11} + \sigma_{22})/2$.**MODe 0,** which is the default, selects "velocity increment control", in which the increment in grid velocity is proportional to the error (difference between measured value and desired value). In **MODe 0,** the increments are added to the velocities prescribed by the user. Mode 0 is normally used when doing a test in which the strain rate is expected to approach a steady state. **MODe 1,** however, ignores any strain-rate that may have been given and so it is useful for getting an equilibrium condition of zero velocity. In such a case, the **MODe 0** servo would be unsatisfactory because it would continue to "hunt," without coming to final equilibrium.

GAIn g edmax

The servo gain **g,** and the maximum allowed strain-rate **edmax,** are set as 0.2 and -1.0E-7 respectively in *example file2.* In this mode 1 form of operation (see **MODE** command) the parameter **g** is $\Delta\dot{e} / \sigma_{error}$. The optimum value of **g** is, to some extent, a matter of trial and error. If it is too high, the servo will "hunt" or will be unstable; if **g** is too low, the servo will be sluggish and the error may be too large. The value of 0.2 was found to be acceptable after some trial simulation

experiments. In **MODe 0** (see **MODe** command), the parameter **g** represents $\Delta\dot{e}$ / σ_{error}, where $\Delta\dot{e}$ is the change in grid strain-rate that occurs for an error in the controlled stress σ_{error}. The "controlled stress" is the one given on the **CYCle** command, and the "error" is the difference between the given value and the measured value for the assembly of particles.

DAMping frac freq imass istiff iswitch

Damping is specified in terms of the Rayleigh damping parameters, where **frac** is the fraction of critical damping at the modal frequency **freq**. In *example file2* **frac** = 0.05 and **freq** = 0.5, since these values were found to produce acceptable results. Rayleigh damping involves mass-proportional (global) damping and stiffness-proportional (contact) damping. The former is switched off in *example file2* by giving **imass** as 1. The latter can be switched off by giving **istiff** as 1. Otherwise these parameters should be set to zero for full Rayleigh damping. Contact damping may require a reduction in time step for numerical stability so **istiff** would then be given the value 1. The damping parameters are specified for ball-to-ball contact in *example file2* since **iswitch** = 1. If **iswitch** = 0 the damping parameters would be specified for ball-to-wall contact.

CYCle n [S1MS2 v]
[S0 v]

The program executes **n** calculation cycles, and returns control to the user when they are complete e.g. **n** = 1000 in *example file2*. The optional keywords denote that the servo-control will attempt to hold the specified variable constant at the value **v**. The optional keyword **S1MS2** specified in *example file2* corresponds to the "two-dimensional mean stress" i.e. $(\sigma_{11}+\sigma_{22})/2$. Optional keyword **S0** corresponds to the mean stress in three-dimesional work σ_0 where $\sigma_0 = (\sigma_{11}+\sigma_{22}+s_{33})/3$. Combinations of control keywords may be used when this is physically reasonable. See related commands **GAIn** and **MODe**.

A 2.3 Isotropic Compression Stage

The datafile presented below is an example of the isotropic compaction process following assembly preparation. The 50:50 particle mix (used in both *example files 1* and 2) in this example is subjected to quasi-static compression.

example file3

REStart mix50.servo
*Strain
2-D
FRAc 0.05
DENs 7.8E21 1
DENs 8.5E20 2
GRId -0.0000001 -0.0000001 -0.0 .0 .0 .0
DAMping 0.05 0.5 1 0 1
CYCle 1000
SAVe mix50.1k
PRInt balls grid info stress chist chd cluster contacts gap map entries energy

PLOt balls circle cnd cluster 100 200 force
STOp

Density-scaling is again used to allow quasi-static compression to be performed within an acceptable timescale.

A 2.3.1 Command List

GRID ed11 ed22 ed33 ed12 ed23 ed31

The strain-rates $\dot{\varepsilon}_{11}$, $\dot{\varepsilon}_{22}$, $\dot{\varepsilon}_{33}$, $\dot{\varepsilon}_{12}$, $\dot{\varepsilon}_{23}$, $\dot{\varepsilon}_{31}$, of periodic space are set. Note that the strain rates $\dot{\varepsilon}_{12}$, $\dot{\varepsilon}_{23}$ and $\dot{\varepsilon}_{31}$ are not used, although they should be entered on the **GRId** command line as zero. The components $\dot{\varepsilon}_{11}$, $\dot{\varepsilon}_{22}$ and $\dot{\varepsilon}_{33}$ cause the periodic volume to change shape. In *example file3*, which illustrates two dimensional compression, $\dot{\varepsilon}_{11}$ and $\dot{\varepsilon}_{22}$ are set to the value of 1.0E-7 and $\dot{\varepsilon}_{33}$ is set to zero. The zero value of $\dot{\varepsilon}_{33}$ indicates that compression does not place in the z direction in 2D.

PRInt **BALls**
CHD [**HAR**]
[**SOF**]
[**MIX**]
CHIst
CLUster
CONtacts [**ALL**]
[**HAR**]
[**SOF**]
[**MIX**]
[**GAP**]
ENErgy
ENTries
GRId
INFo
MAP
STRess

A printout is made of various quantities. The above parameters correspond, respectively, to: *balls, contact data histogram, contact histogram, cluster information, contacts, energy t erms, box entries, grid size, general information, memory map and stress tensor.* The optional keywords **HAR**, **SOF** and **MIX** (after the **CHD** parameter) request that contact force, contact area and contact pressure histograms are only printed for hard-hard, soft-soft and hard-soft particle contacts respectively. The optional keyword **ALL** (after the **CONtacts** parameter) requests that all contacts are printed, rather than just those taking load, which is the default. The optional keywords **HAR**, **SOF** and **MIX** request that only hard-hard particle contacts, soft-soft particle contacts and hard-soft particle contacts respectively are printed. The optional keyword **GAP** (used in *example file3*) causes contact overlaps, normal forces, contact areas and contact pressures for the contact type to be printed. Several keywords may be given on the same line, as shown in example file3.

PLOt **BALl**
CIRcle
CLUster [n1 n2]
[BAK]
CND [NEW] [DEL] [EXI] [SLI]
FORces

The **PLOt** command produces either 2D (*x* - *y*) or 3D (*x* - *y* - *z*) graphics using Personal graPHIGS routines on the IBM RS/6000. The parameter **BALl** shows the particles as spheres (3D) or shaded circles (2D). **CIRcle** represents the particles by wireframe spheres (3D) or unshaded circles (2D). **CLUster** plots different particle clusters in different colours to help in the analysis of percolating clusters. The optional parameters **n1, n2** are given in *example file3* i.e. **n1** = 100 and **n2** = 500. Particle clusters containing numbers of balls between **n1** and **n2** are plotted. Note that the assignment of colours to different clusters is not automatic: the cluster sizes present have to be identified by using the **PRInt CLUster** command, after which the eight colours red, blue, green, cyan, magenta, yellow, white and black can be assigned to different clusters. The cluster colour assignment is accomplished by modifying the subroutine BPLOT in the graphics suite TRB_GP.F and recompiling the source code.

By specifying **n1** = **n2**, a fragment of a specific size can be displayed. The optional keyword **BAK** (after the parameter **CLUster**) specifies that only particles in the cluster which carry the largest contact forces (relative to a force level scaled to the current maximum force) are displayed. **CND** shows the connection diagram. This is a diagram that results from comparing two states of the sample and identifying contacts which are present in both states as existing contacts (**EXI**), contacts which are present in the new state but not in the old as new contacts (**NEW**) and contacts in the old state which are not in the new state as deleted contacts (**DEL**). Sliding contacts are also identified if the **SLI** option is specified. The centres of particles with these contacts are joined with lines of different colours to yield the connection diagram. The keyword **FORce** shows contact forces as lines oriented in the direction of the force. Compressive and tensile forces are identified with different colours and the thickness of each line is proportional to the magnitude of the contact force (scaled to the current maximum force).

A 3 Three-Dimensional Isotropic Compression

A 3.1 Assembly Generation

The following example shows how a random three-dimensional 50:50 hard:soft assembly of 3620 particles is automatically generated by TRUBAL:

example file4

```
STArt 0.07 0.07 0.07 512 4000 2 Log
* 3D 50:50 Mix
RAD 0.00210 1
RAD 0.00205 2
RAD 0.00200 3
RAD 0.00195 4
RAD 0.00190 5
YMD 2.0E11 1
YMD 1.0E8 2
```

```
PRA 0.3 1
PRA 0.3 2
FRIc 0.35 1
FRIc 0.35 2
DENs 7.8E3 1
DENs 8.5E2 2
RGEn 181 1 1 1
RGEn 181 1 2 1
RGEn 398 2 1 1
RGEn 398 2 2 1
RGEn 652 3 1 1
RGEn 652 3 2 1
RGEn 398 4 1 1
RGEn 398 4 2 1
RGEn 181 5 1 1
RGEn 181 5 2 1
SAVe 3Dmix.50%
STOp
```

The dimensions of the box volume are 7 cm in both x, y and z directions. The material parameters used for the two types of particle are the same as for the two-dimensional case (see *example file1*)

A 3.2 Isotropic Compression Stage

The datafile presented below is an example of the three-dimensional isotropic compression process following assembly preparation. The 50:50 particle mix used in this example (generated in *example file 4*) is subjected to quasi-static compression.

example file5

```
REStart 3Dmix50.servo
*Strain
FRAc 0.05
DENs 7.8E21 1
DENs 8.5E20 2
GRId -0.0000001 -0.0000001 -0.0000001 .0 .0 .0
DAMping 0.05 0.5 1 0 1
CYCle 1000
SAVe 3Dmix50.1k
PRInt balls grid info stress chist chd cluster contacts gap map entries energy
PLOt balls circle cnd cluster 100 200 force
STOp
```

Density-scaled values are also used for the three-dimensional simulation studies.

In three-dimensional work the $\dot{\varepsilon}_{33}$ strain rate value in the **GRId** command line is now non-zero, since compression of the periodic volume occurs along all three co-ordinate axis.

Appendix B

Further test results at p_e

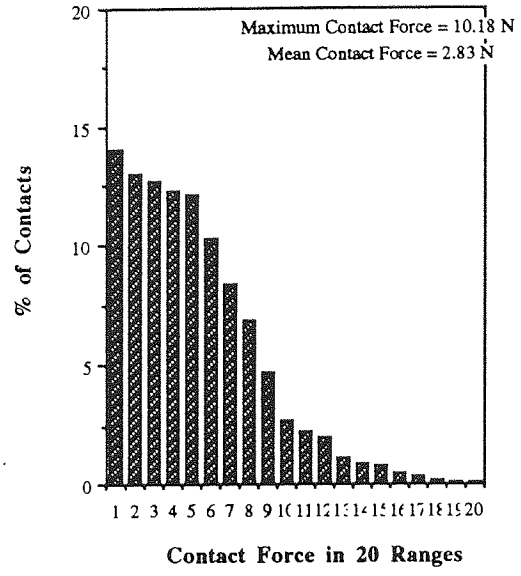

Figure B.1 Contact force distribution at p_e for 0% hard assembly subject to quasi-static compression.;

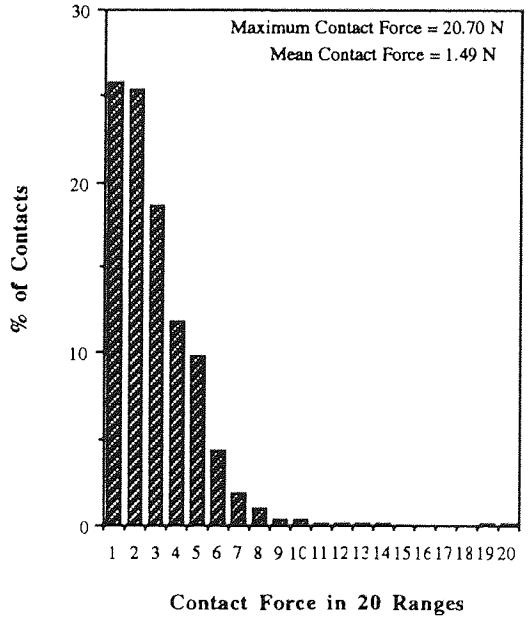

Figure B.2 Contact force distribution at p_e for 25% hard assembly subject to quasi-static compression.;

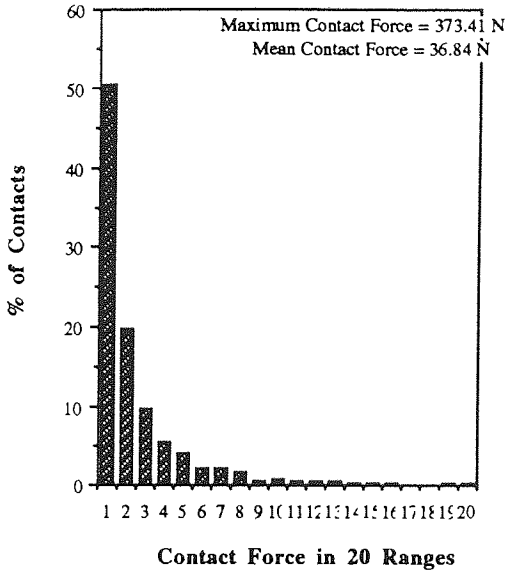

Figure B.3 Contact force distribution at p_e for 75% hard assembly subject to quasi-static compression.;

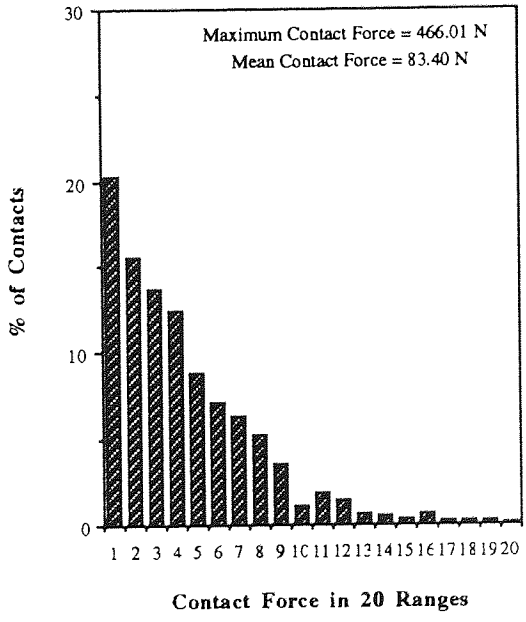

Figure B.4 Contact force distribution at p_e for 100% hard assembly subject to quasi-static compression.;

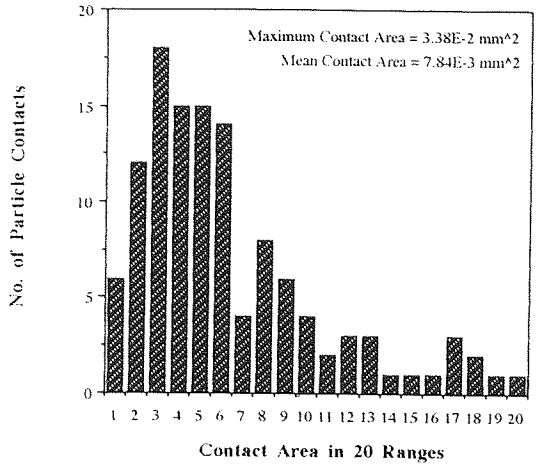

Figure B.5 Contact area distribution at p_e for 50% assembly hard-hard particle contacts.;

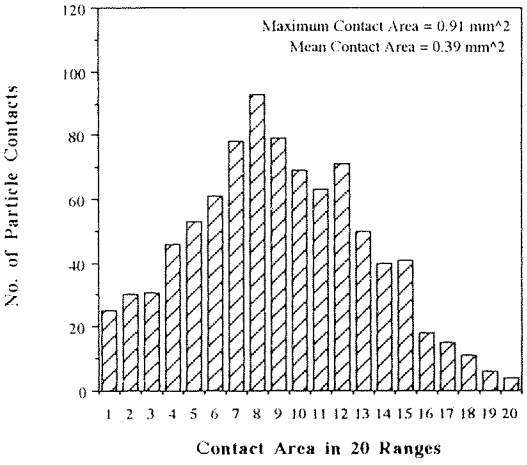

Figure B.6 Contact area distribution at p_e for 50% assembly hard-soft particle contacts.;

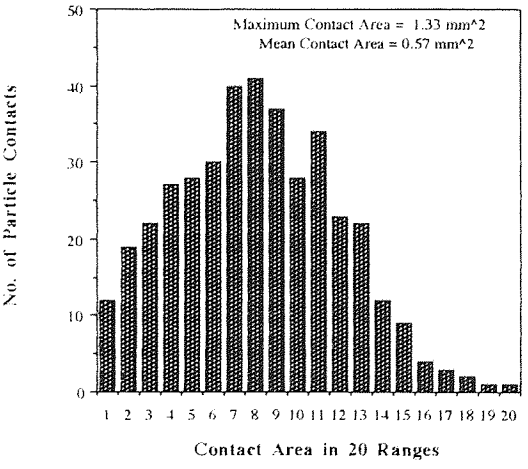

Figure B.7 Contact area distribution at p_e for 50% assembly soft-soft particle contacts.;

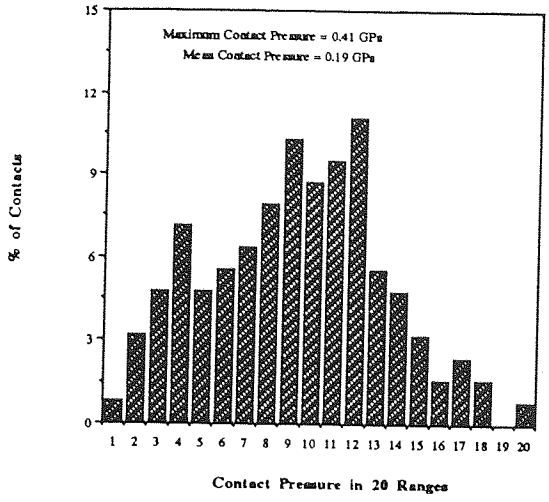

Figure B.8 Contact pressure distribution at p_e for 50% assembly hard-hard particle contacts.;

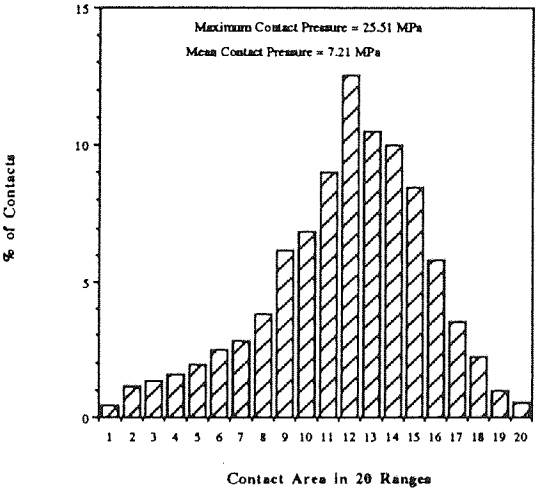

Figure B.9 Contact pressure distribution at p_e for 50% assembly hard-soft particle contacts.;

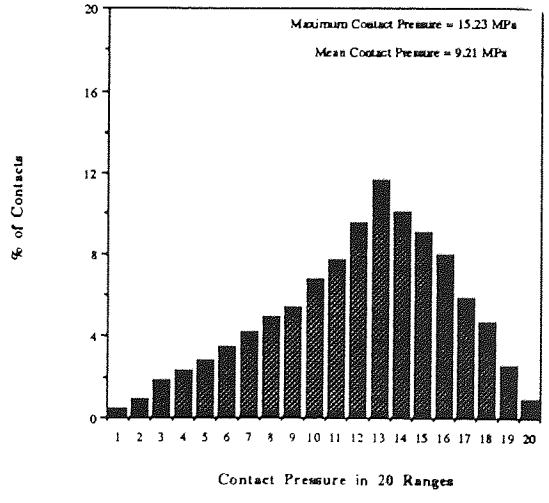

Figure B.10 Contact pressure distribution at p_e for 50% assembly soft-soft particle contacts.;

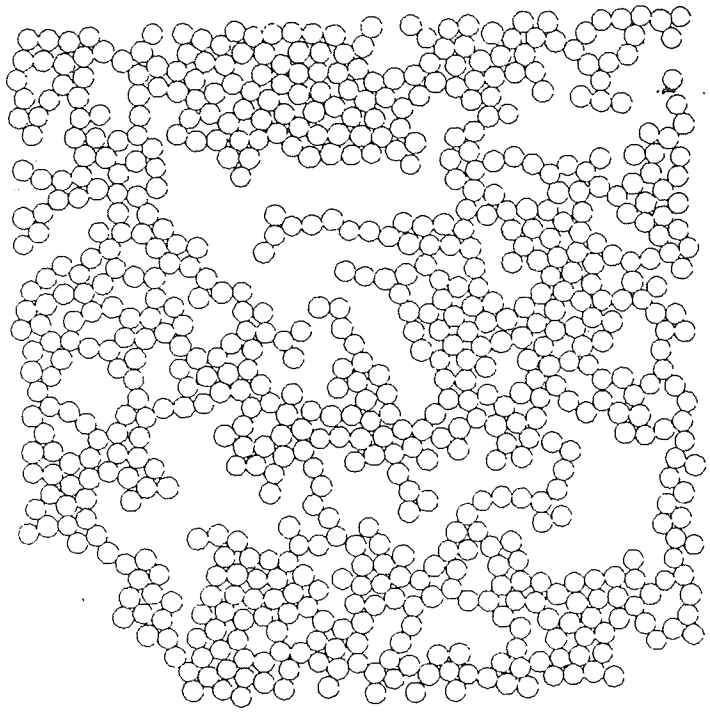

Figure B.11 Percolating cluster at p_g for 0% hard assembly.;

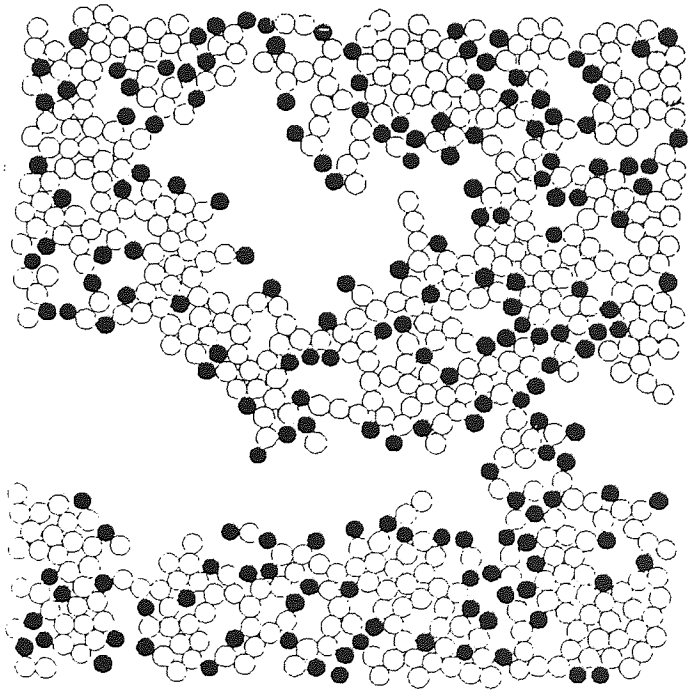

Figure B.12 Percolating cluster at p_g for 25% hard assembly.;

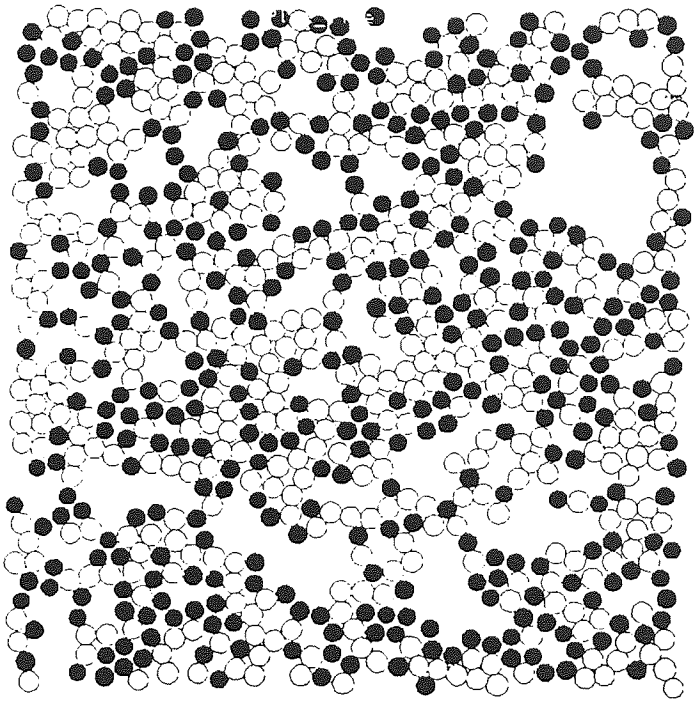

Figure B.13 Percolating cluster at p_g for 75% hard assembly.;

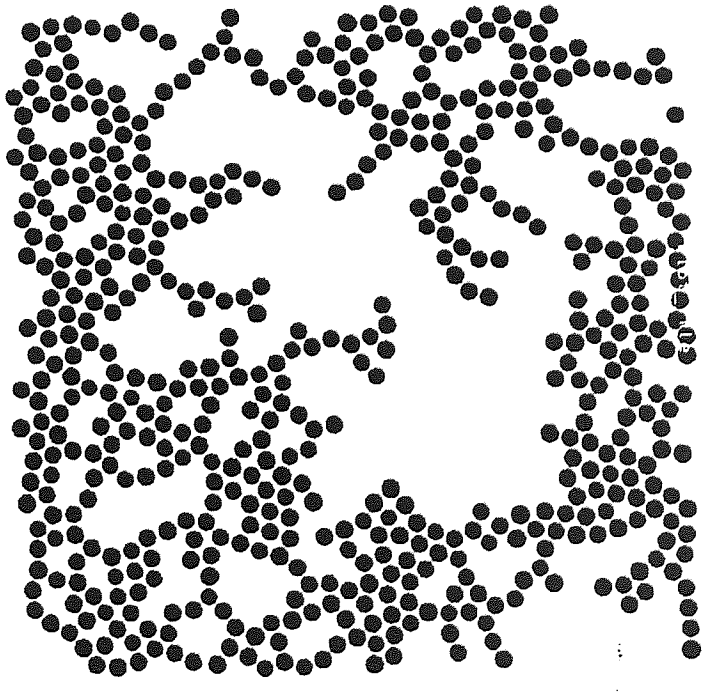

Figure B.14 Percolating cluster at p_g for 100% hard assembly.;

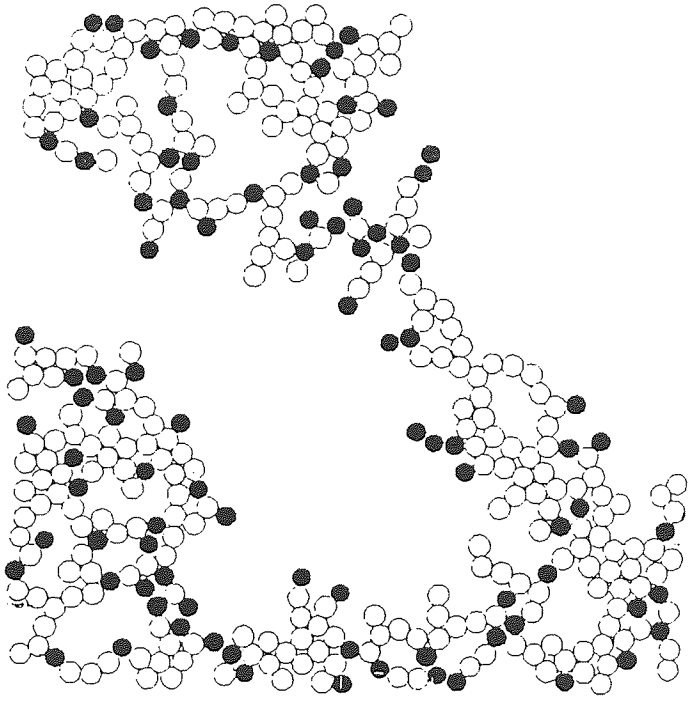

Figure B.15 Assembly backbone at p_e for 25% hard assembly.;

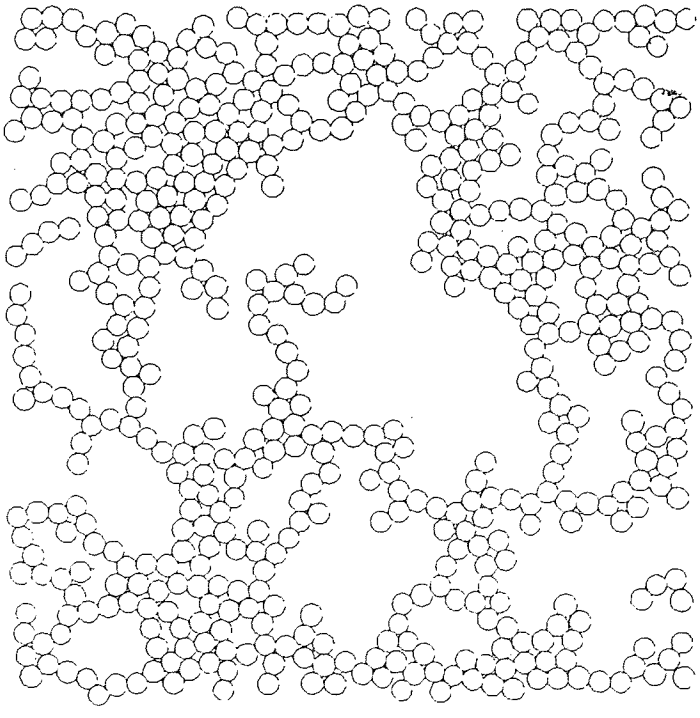

Figure B.16 Assembly backbone at p_e for 0% hard assembly.;

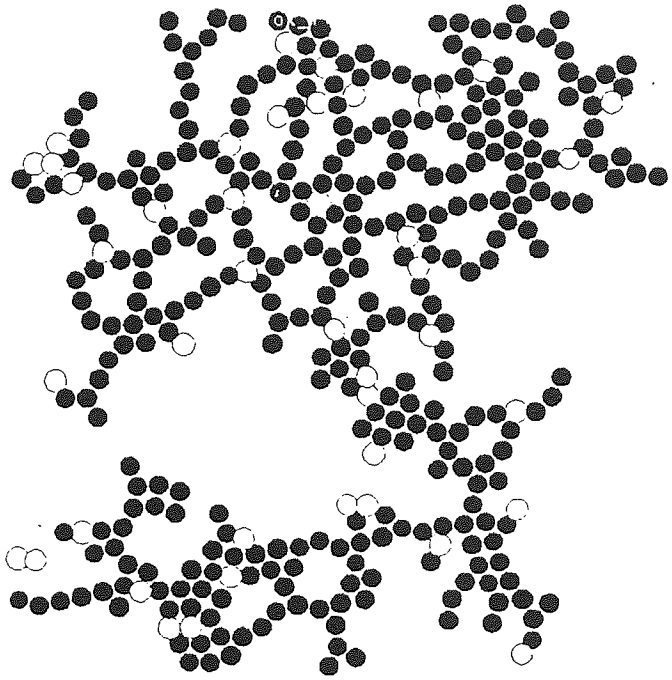

Figure B.17 Assembly backbone at p_c for 75% hard assembly.;

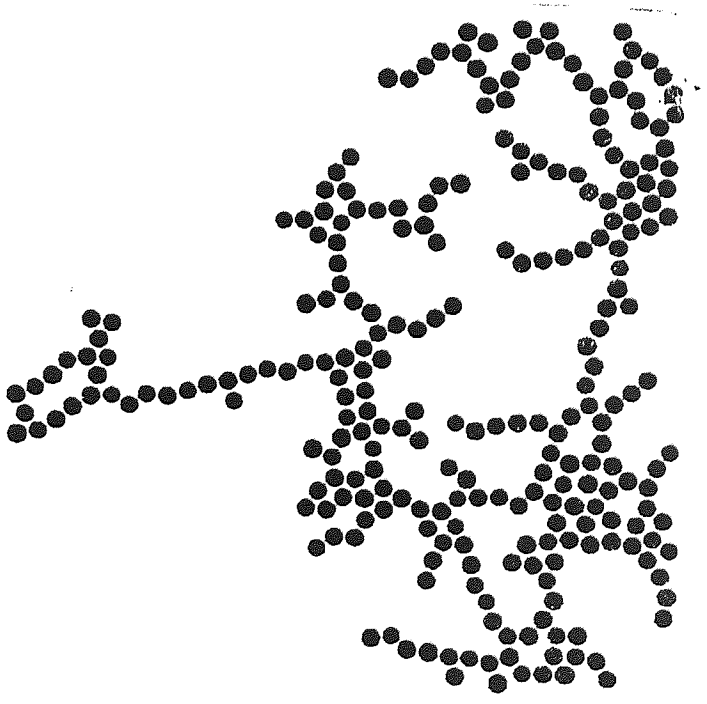

Figure B.18 Assembly backbone at p_c for 100% hard assembly.;

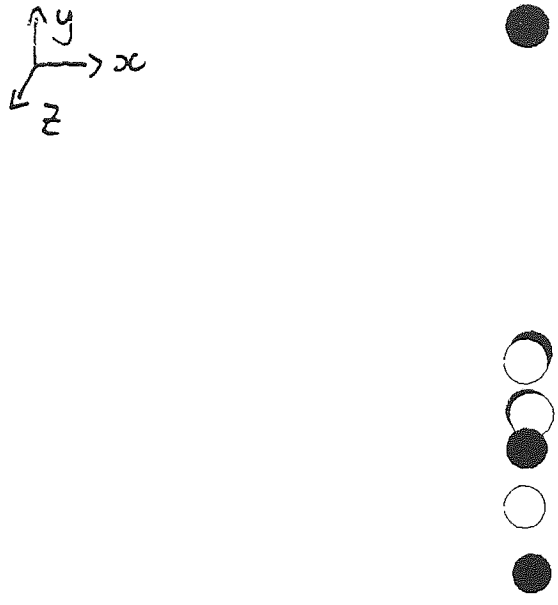

Figure B.19 Backbone section at x_{max} for 3D 50/50 assembly.;

Figure B.20 Backbone section at y_{max} for 3D 50/50 assembly.;

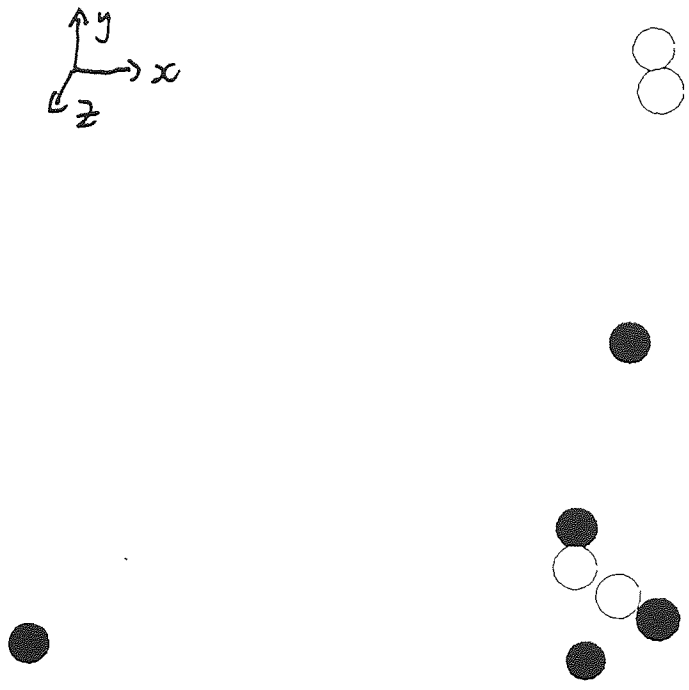

Figure B.21 Backbone section at z_{max} for 3D 50/50 assembly.;

Figure B.22 Backbone section at y_{min} for 3D 50/50 assembly.;

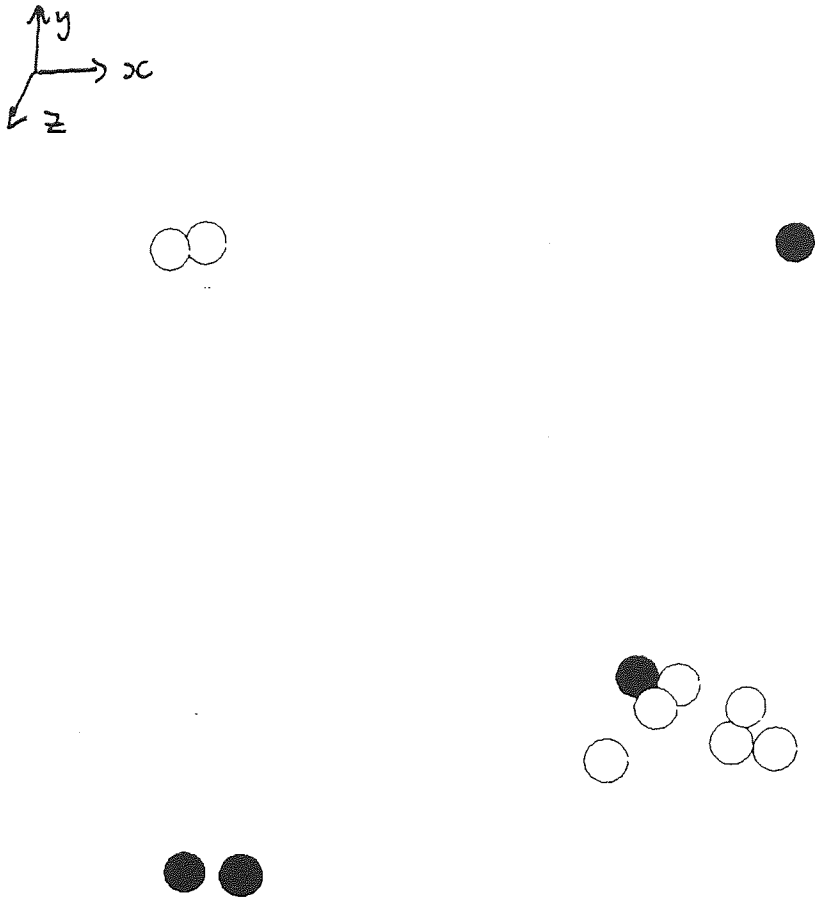

Figure B.23 Backbone section at z_{min} for 3D 50/50 assembly.;

Figure B.24 Backbone section at $x_{max}/2$ for 3D 50/50 assembly.;

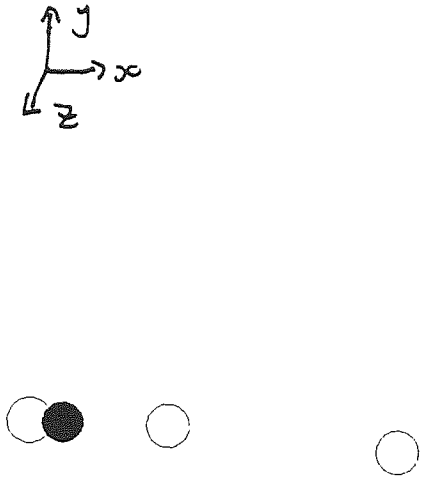

Figure B.25 Backbone section at $y_{max}/2$ for 3D 50/50 assembly.;

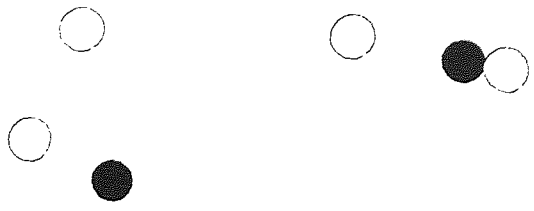

Figure B.26 Backbone section at $z_{max}/2$ for 3D 50/50 assembly.;

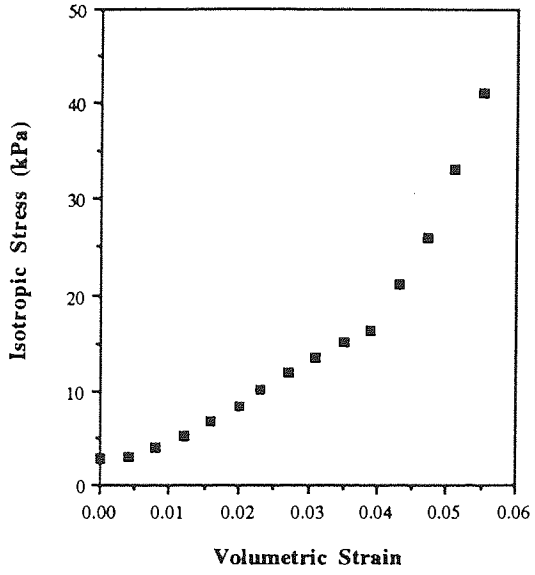

Figure B.27 Detection of elastic percolation threshold for 3D 0% hard assembly.;

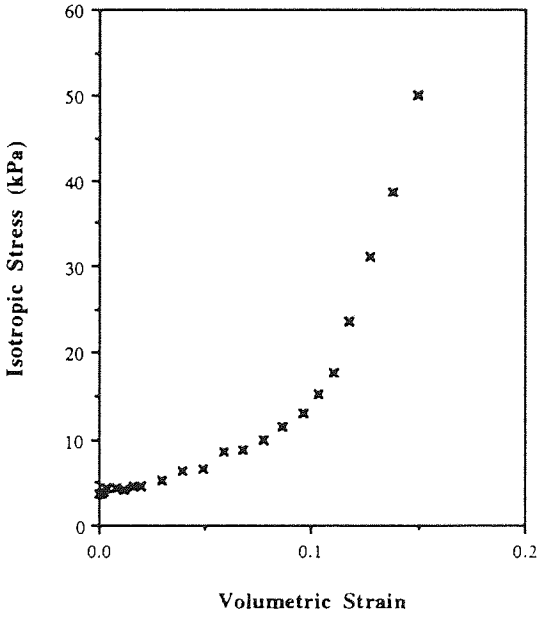

Figure B.28 Detection of elastic percolation threshold for 3D 25% hard assembly.;

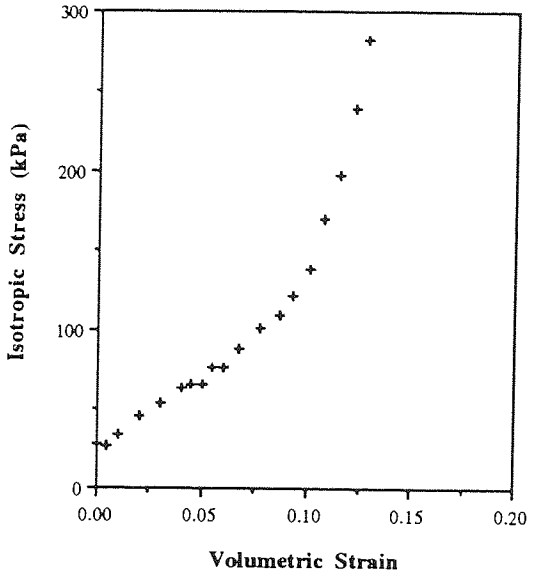

Figure B.29 Detection of elastic percolation threshold for 3D 75% hard assembly.;

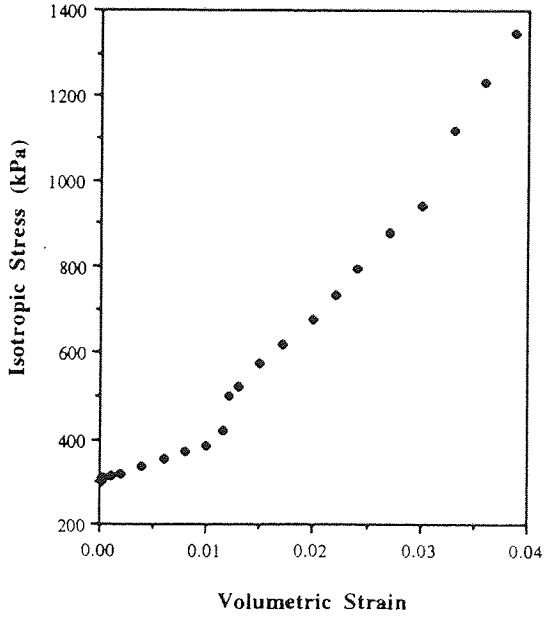

Figure B.30 Detection of elastic percolation threshold for 3D 100% hard assembly.;

Appendix C

Further test results from Chapter 6

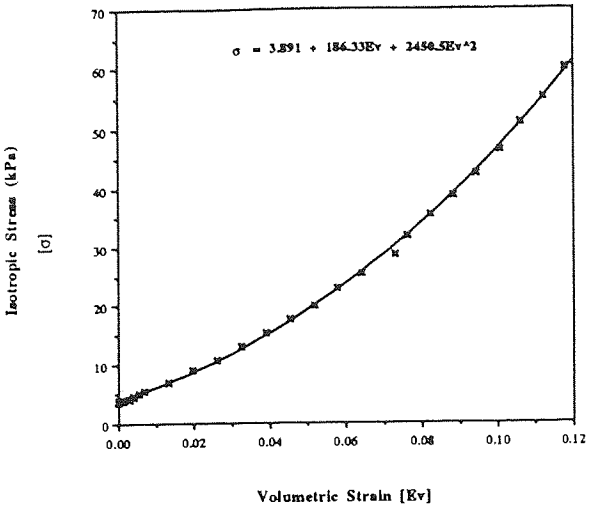

Figure C.1 Stress-strain curve for 25% hard assembly subject to quasi-static compression;

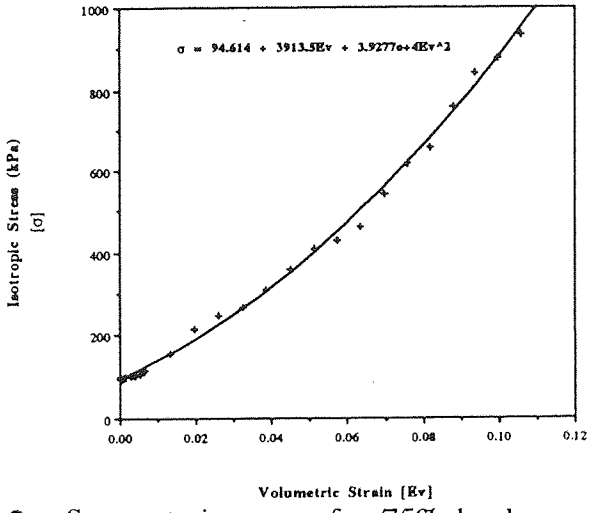

Figure C.2 Stress-strain curve for 75% hard assembly subject to quasi-static compression;

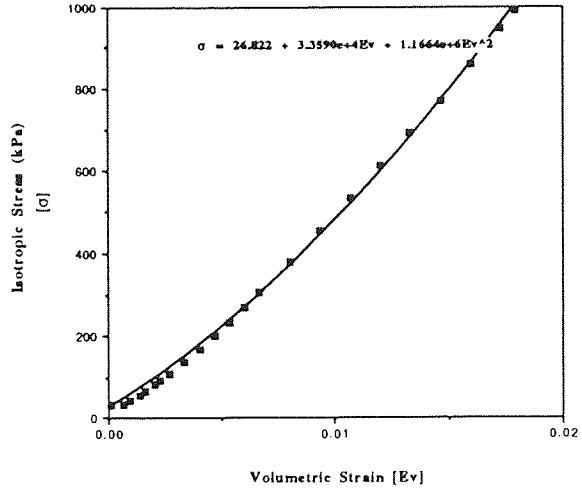

Figure C.3 Stress-strain curve for 90% hard assembly subject to quasi-static compression;

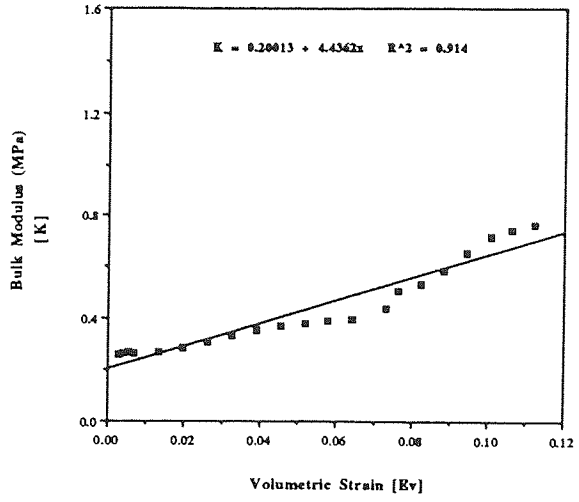

Figure C.4 Evolution of bulk modulus with strain for 25% hard assembly;

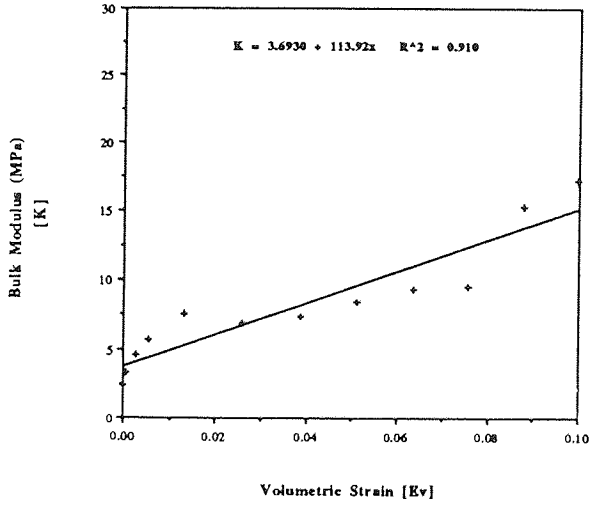

Figure C.5 Evolution of bulk modulus with strain for 75% hard assembly;

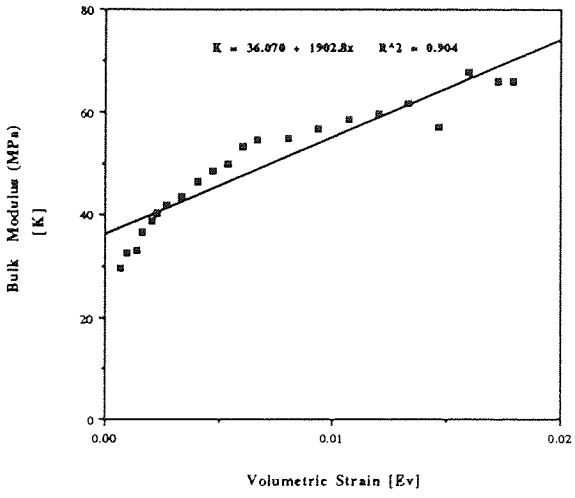

Figure C.6 Evolution of bulk modulus with strain for 90% hard assembly;

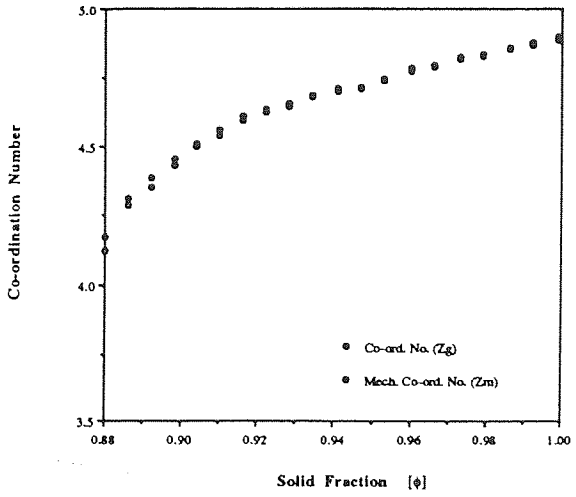

Figure C.7 Evolution of geometric (Z_g) and mechanical (Z_m) co-ordination numbers with solid fraction ϕ for the 25% hard assembly.

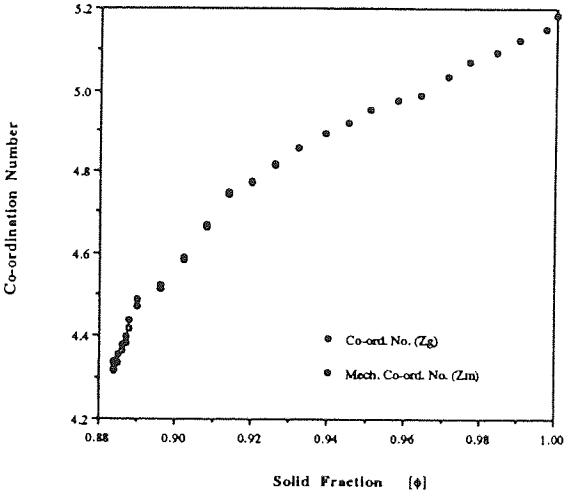

Figure C.8 Evolution of geometric (Z_g) and mechanical (Z_m) co-ordination numbers with solid fraction ϕ for the 75% hard assembly.

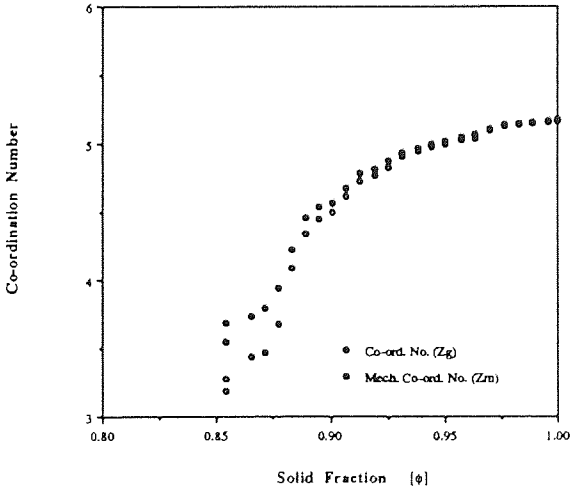

Figure C.9 Evolution of geometric (Z_g) and mechanical (Z_m) co-ordination numbers with solid fraction ϕ for the 90% hard assembly.

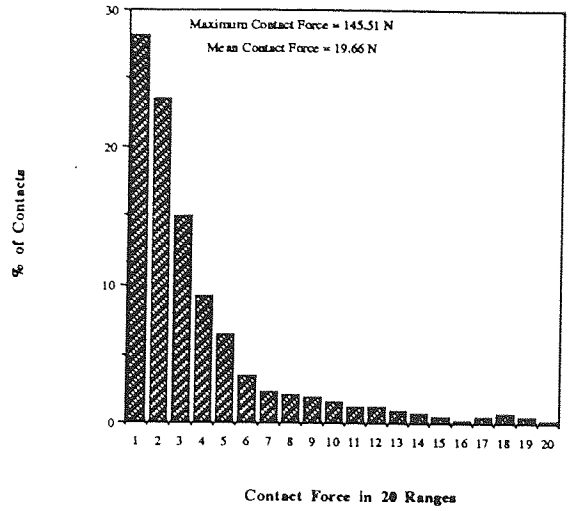

Figure C.10 Contact force distribution for the hard-hard particle contacts in the 50/50 assembly at $\sigma = 20$ kPa.;

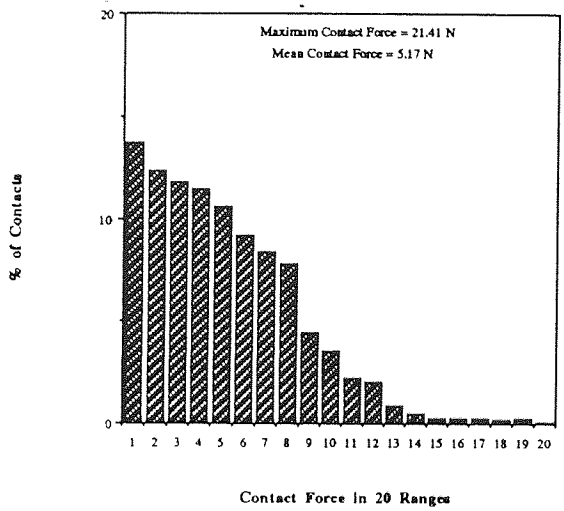

Figure C.11 Contact force distribution for the hard-soft particle contacts in the 50/50 assembly at $\sigma = 20$ kPa.;

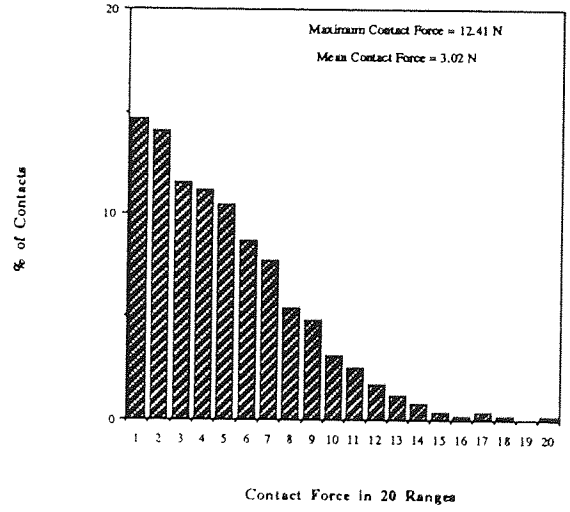

Figure C.12 Contact force distribution for the soft-soft particle contacts in the 50/50 assembly at $\sigma = 20$ kPa.;

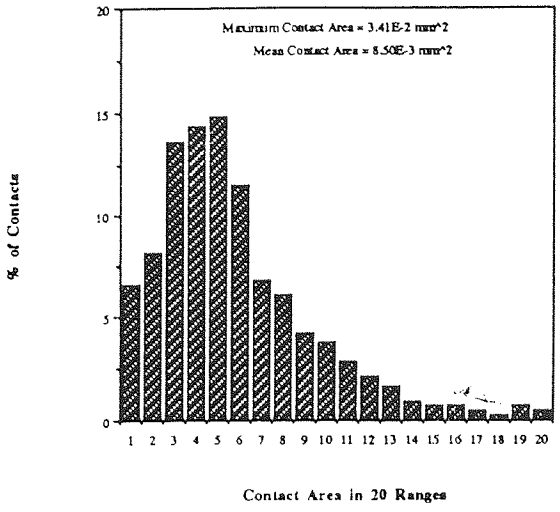

Figure C.13 Contact area distribution for the hard-hard particle contacts in the 50/50 assembly at $\sigma = 20$ kPa.;

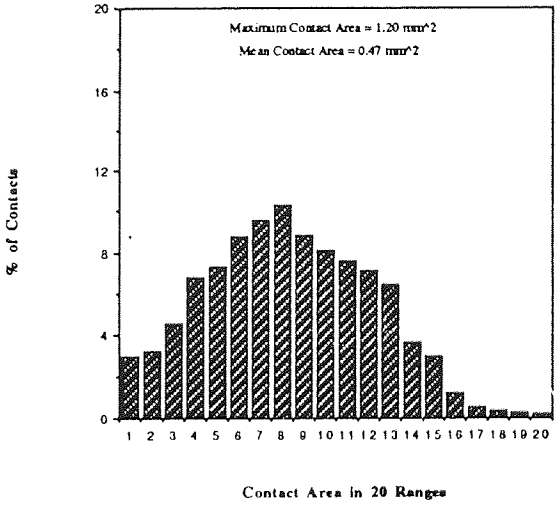

Figure C.14 Contact area distribution for the hard-soft particle contacts in the 50/50 assembly at $\sigma = 20$ kPa.;

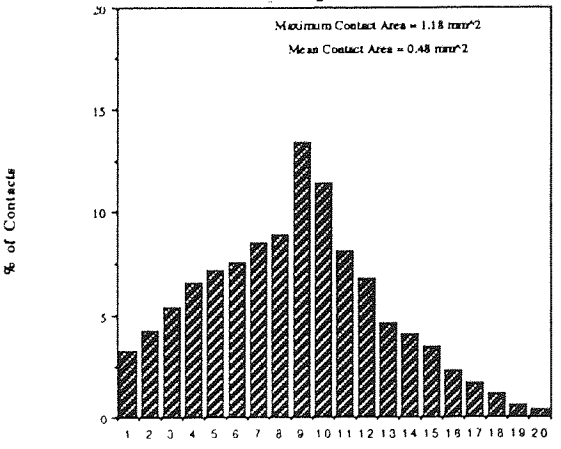

Figure C.15 Contact area distribution for the soft-soft particle contacts in the 50/50 assembly at $\sigma = 20$ kPa.;

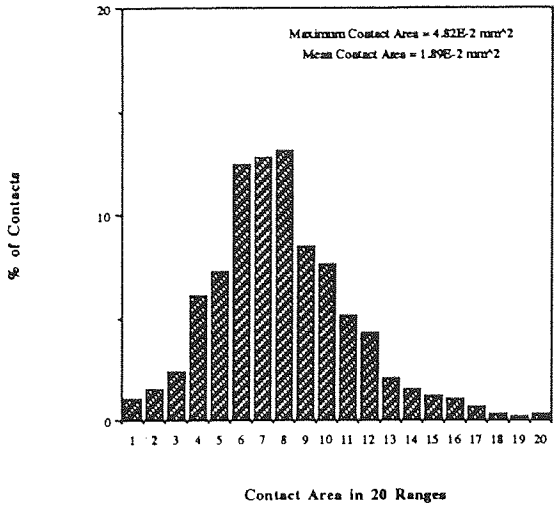

Figure C.16 Contact area distribution for the hard-hard particle contacts in the 50/50 assembly at $\sigma = 100$ kPa.;

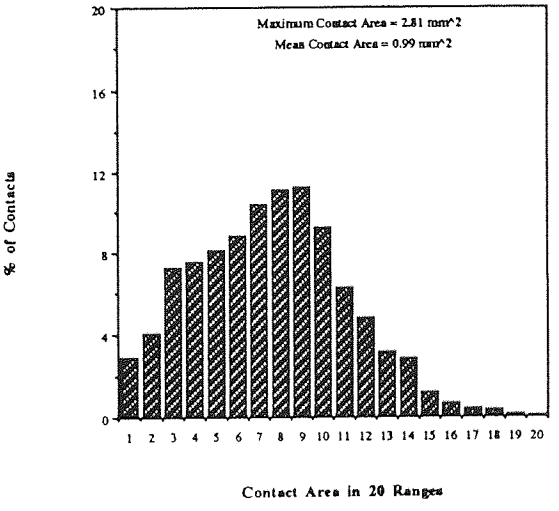

Figure C.17 Contact area distribution for the hard-soft particle contacts in the 50/50 assembly at $\sigma = 100$ kPa.;

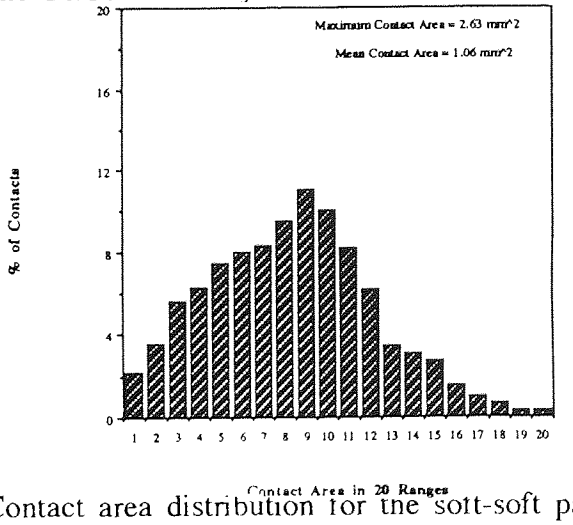

Figure C.18 Contact area distribution for the soft-soft particle contacts in the 50/50 assembly at $\sigma = 100$ kPa.;

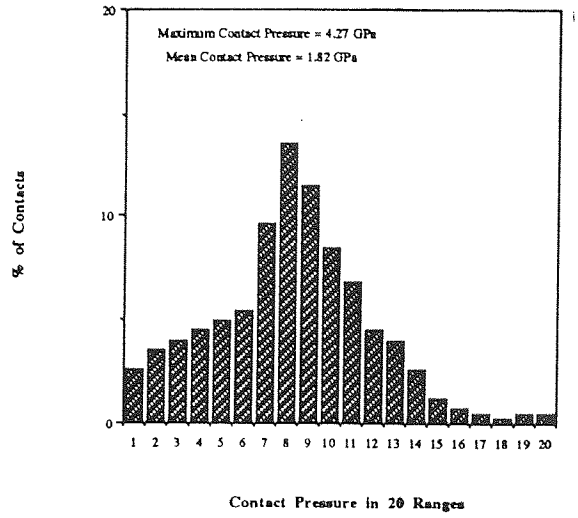

Figure C.19 Contact pressure distribution for the hard-hard particle contacts in the 50/50 assembly at $\sigma = 20$ kPa.;

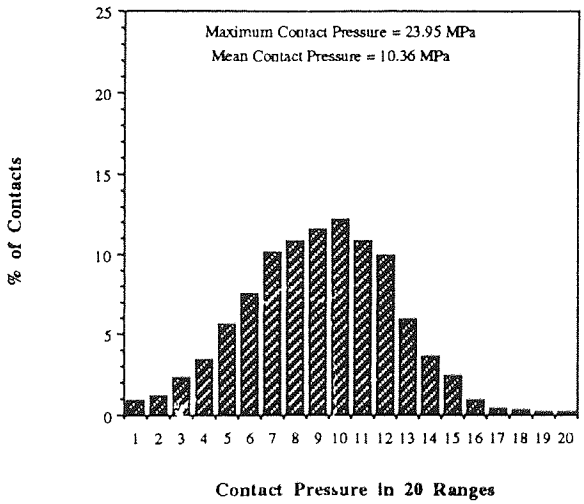

Figure C.20 Contact pressure distribution for the hard-soft particle contacts in the 50/50 assembly at $\sigma = 20$ kPa.;

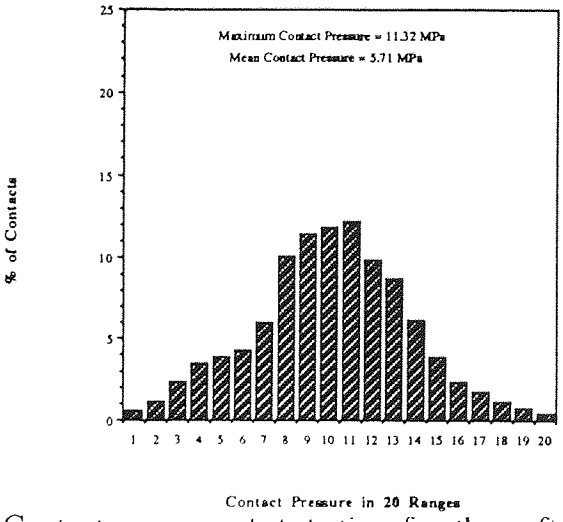

Figure C.21 Contact pressure distribution for the soft-soft particle contacts in the 50/50 assembly at $\sigma = 20$ kPa.;

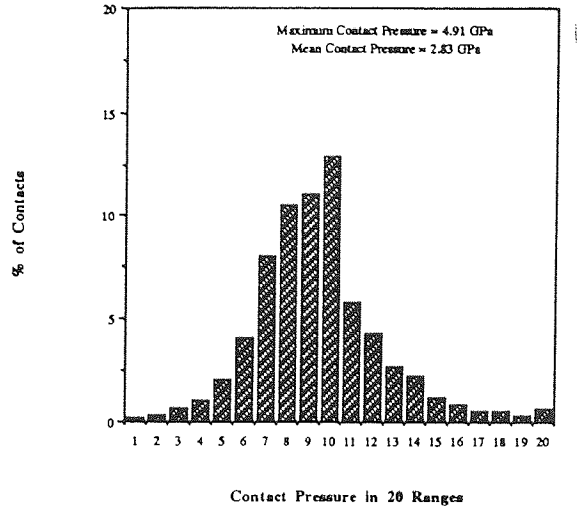

Figure C.22 Contact pressure distribution for the hard-hard particle contacts in the 50/50 assembly at $\sigma = 100$ kPa.;

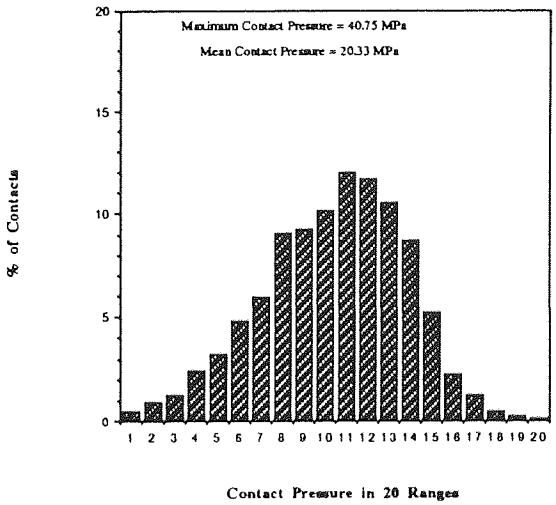

Figure C.23 Contact pressure distribution for the hard-soft particle contacts in the 50/50 assembly at $\sigma = 100$ kPa.;

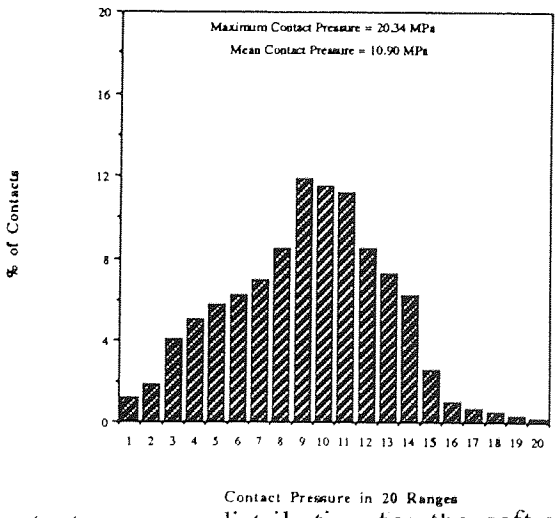

Figure C.24 Contact pressure distribution for the soft-soft particle contacts in the 50/50 assembly at $\sigma = 100$ kPa.;

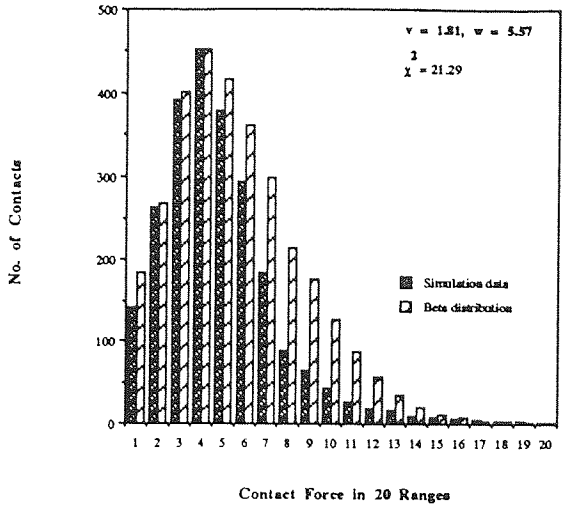

C.25 Beta contact force distribution for 25% hard assembly at $\sigma = 20$ kPa.;

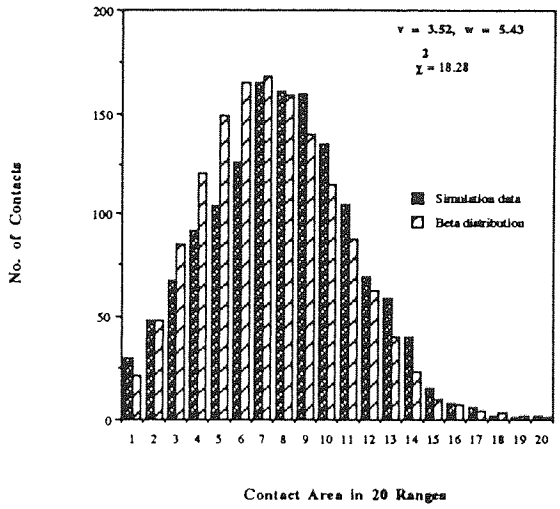

C.26 Beta contact area distribution for 100% hard assembly at $\sigma = 500$ kPa.;

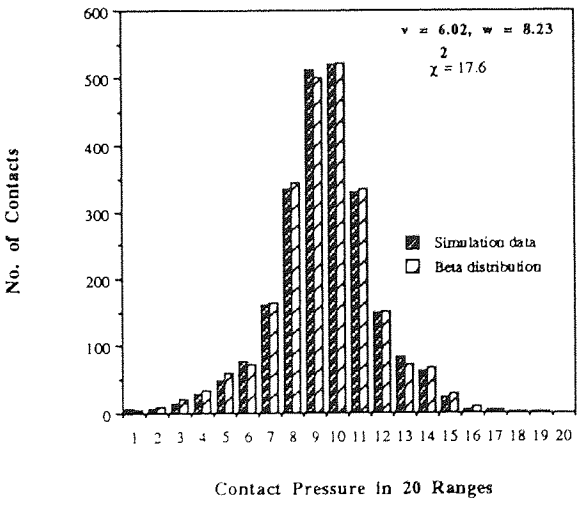

C.27 Beta contact pressure distribution for 0% hard assembly at $\sigma = 10$ kPa.;

Appendix D

Further test results from Chapter 7

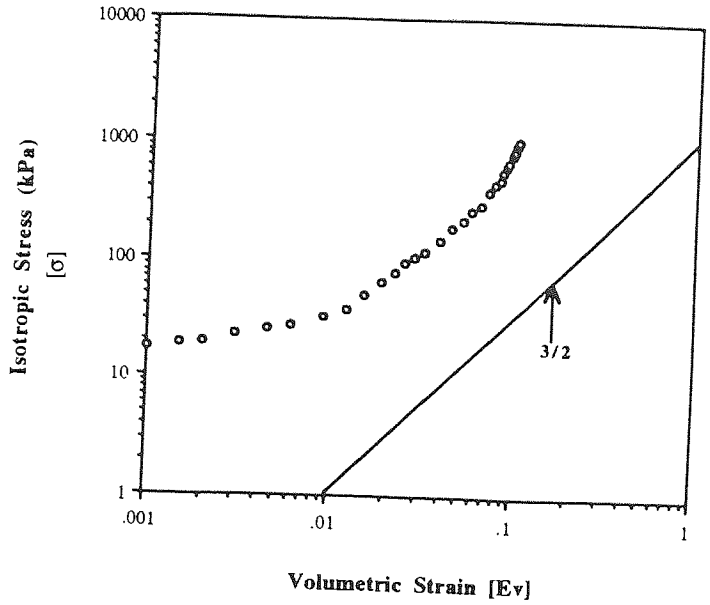

Figure D.1 Stress-strain curve for 2/1 hard/soft size ratio assembly (50% hard/soft mixture) subject to quasi-static compression.

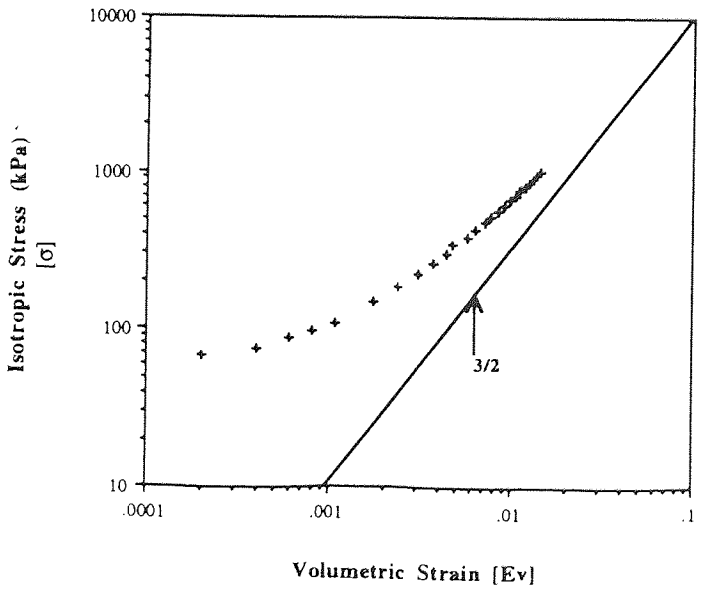

Figure D.2 Stress-strain curve for 2/1 hard/soft size ratio assembly, 75% hard/soft mixture, subject to quasi-static compression.

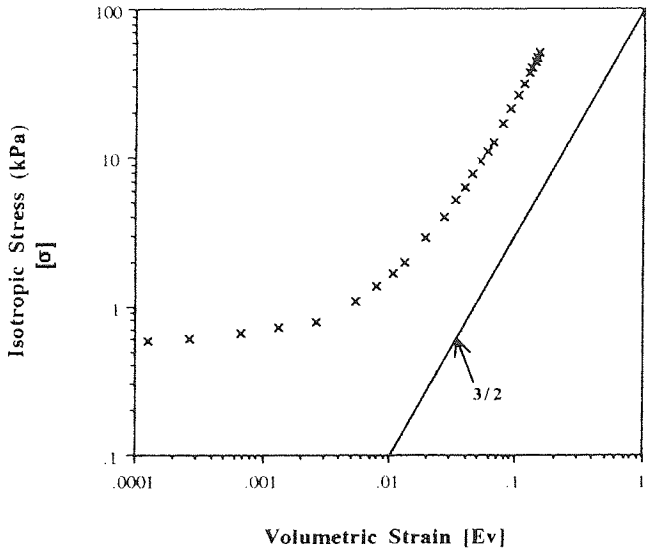

Figure D.3 Stress-strain curve for 2/1 soft/hard size ratio assembly, 25% hard/soft mixture, subject to quasi-static compression.

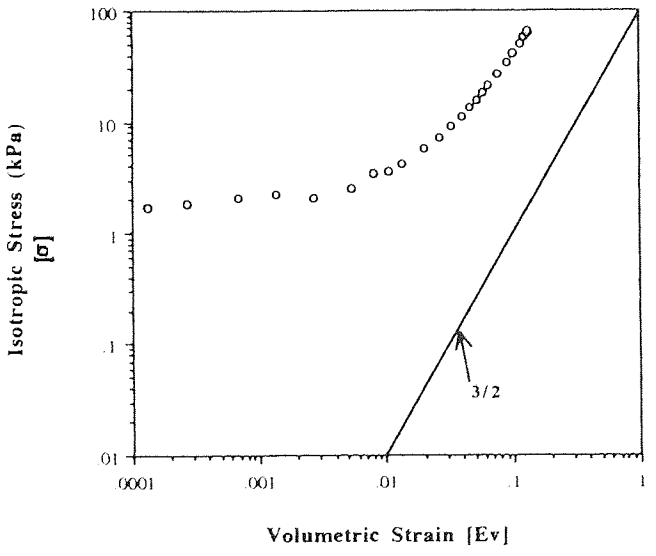

Figure D.4 Stress-strain curve for 2/1 soft/hard size ratio assembly, 50% hard/soft mixture, subject to quasi-static compression.

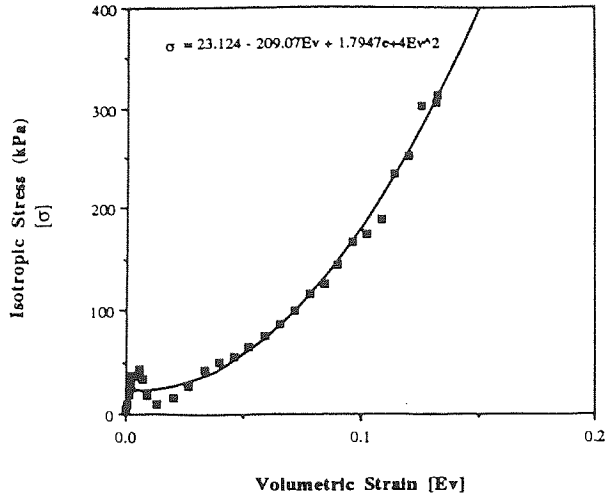

Figure D.5 Second order polynomial stress-strain relationship for 40% hard/soft mix, 2/1 hard/soft size ratio assembly subject to quasi-static compression;

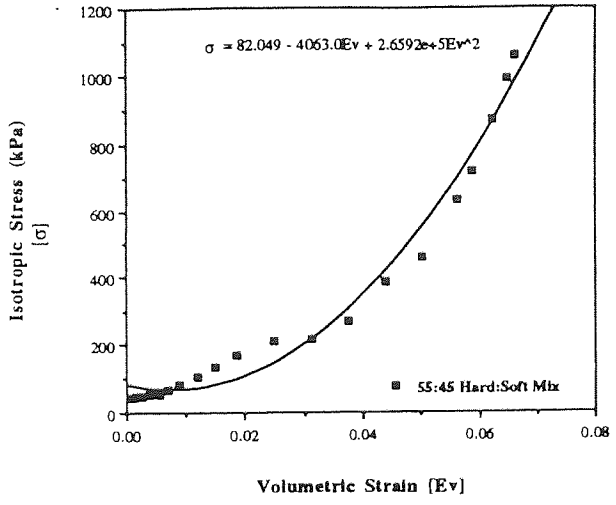

Figure D.6 Second order polynomial stress-strain relationship for 55% hard/soft mix, 2/1 hard/soft size ratio assembly subject to quasi-static compression;

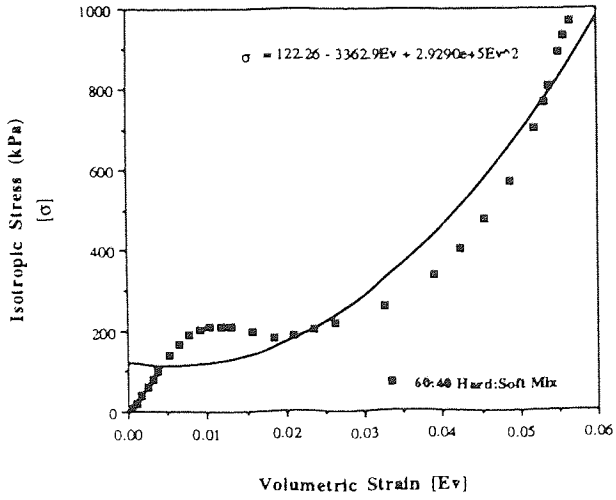

Figure D.7 Second order polynomial stress-strain relationship for 60% hard/soft mix, 2/1 hard/soft size ratio assembly subject to quasi-static compression;

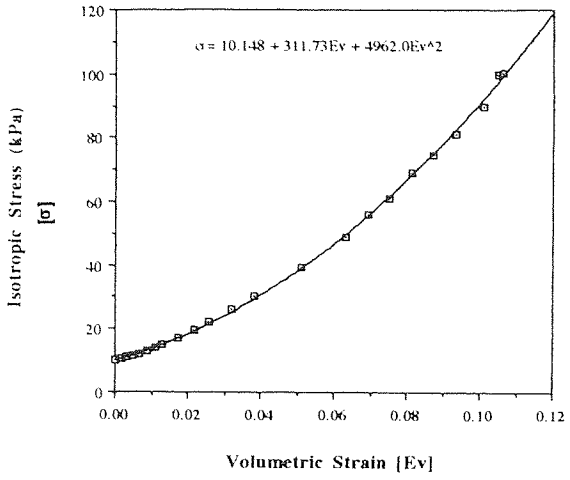

Figure D.8 Second order polynomial stress-strain relationship for 25% hard/soft mix, 2/1 hard/soft size ratio assembly at a stress level of $\sigma = 10$ kPa.

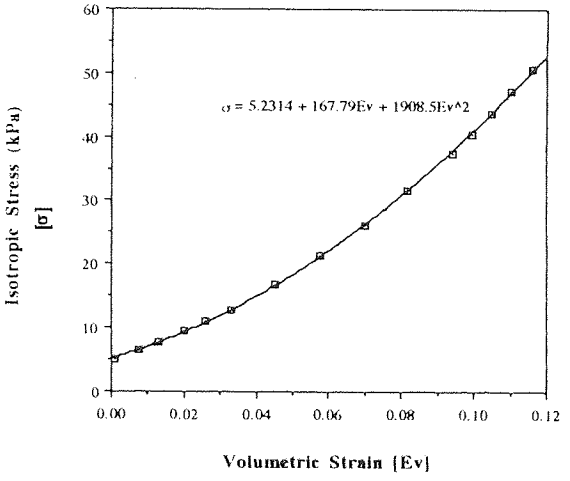

Figure D.9 Second order polynomial stress-strain relationship for 25% hard/soft mix, 2/1 soft/hard size ratio assembly at a stress level of $\sigma = 10$ kPa.

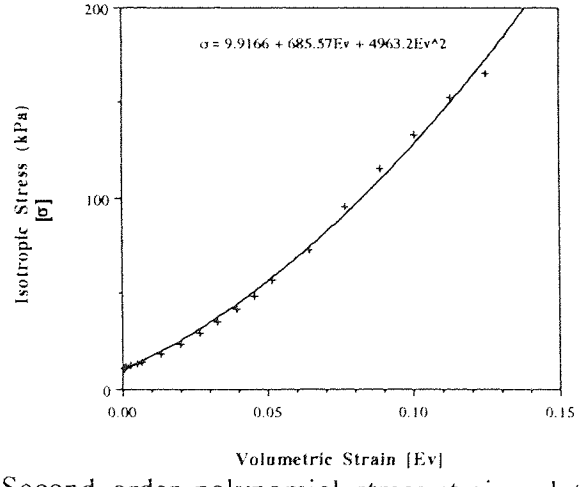

Figure D.10 Second order polynomial stress-strain relationship for 75% hard/soft mix, 2/1 soft/hard size ratio assembly at a stress level of $\sigma = 10$ kPa.

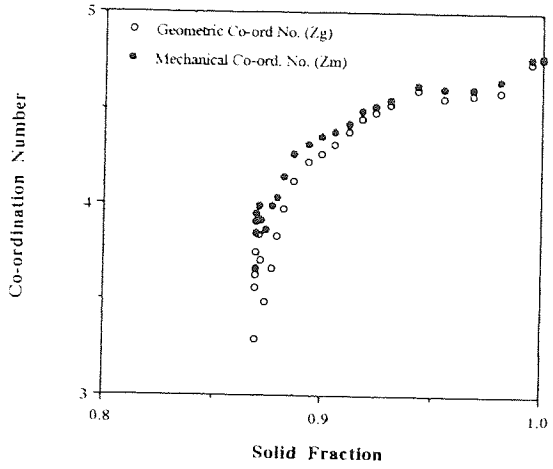

Figure D.11 The evolution of geometric (Zg) and mechanical (Zm) co-ordination numbers with solid fraction ϕ for 75% hard/soft mix, 2/1 soft/hard size ratio assembly.

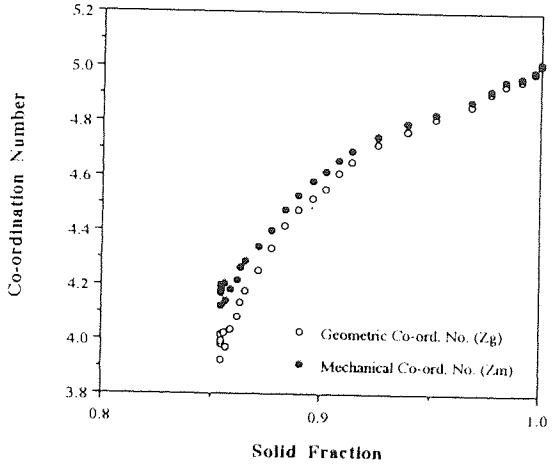

Figure D.12 The evolution of geometric (Zg) and mechanical (Zm) co-ordination numbers with solid fraction ϕ for 25% hard/soft mix, 2/1 soft/hard size ratio assembly.

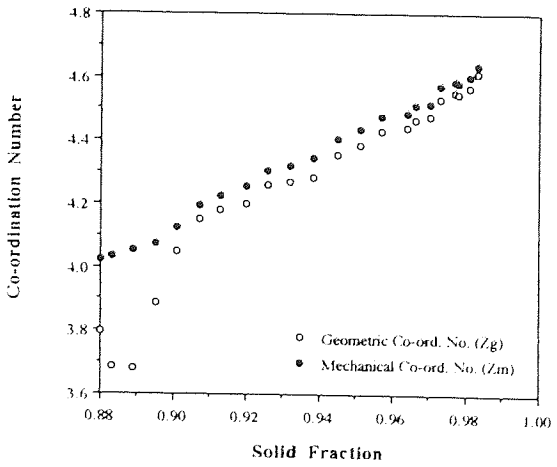

Figure D.13 The evolution of geometric (Zg) and mechanical (Zm) co-ordination numbers with solid fraction ϕ for 50% hard/soft mix, 2/1 hard/soft size ratio assembly.

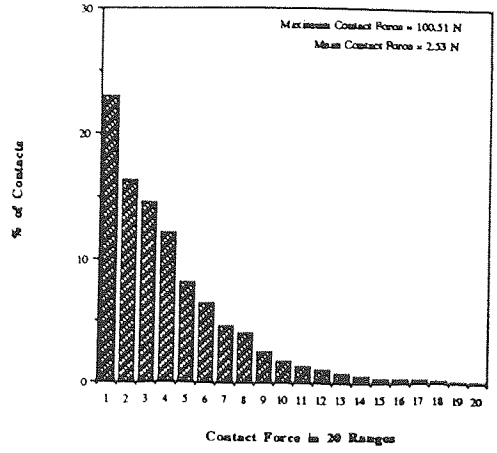

Figure D.14 Contact force distribution for 40% hard/soft mix, 2/1 hard/soft size ratio assembly at a stress level of $\sigma = 10$ kPa.

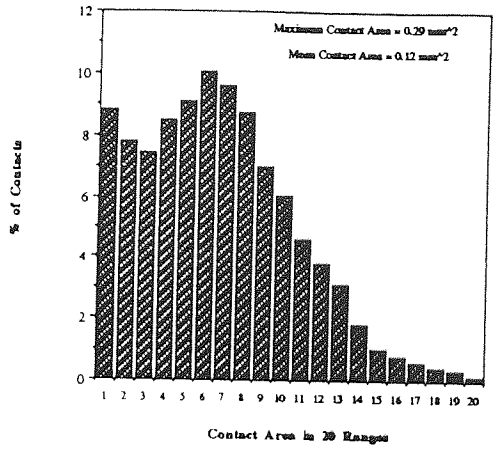

Figure D.15 Contact area distribution for 40% hard/soft mix, 2/1 hard/soft size ratio assembly at a stress level of $\sigma = 10$ kPa.

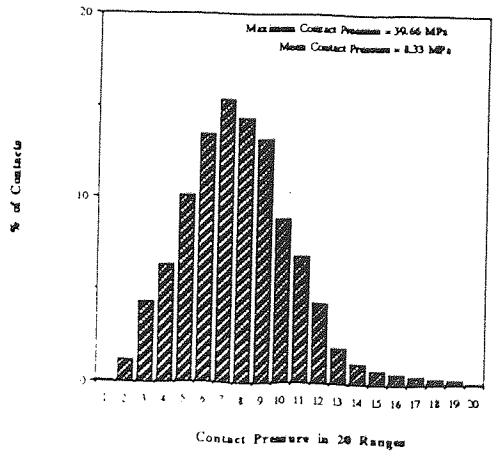

Figure D.16 Contact pressure distribution for 40% hard/soft mix, 2/1 hard/soft size ratio assembly at a stress level of $\sigma = 10$ kPa.

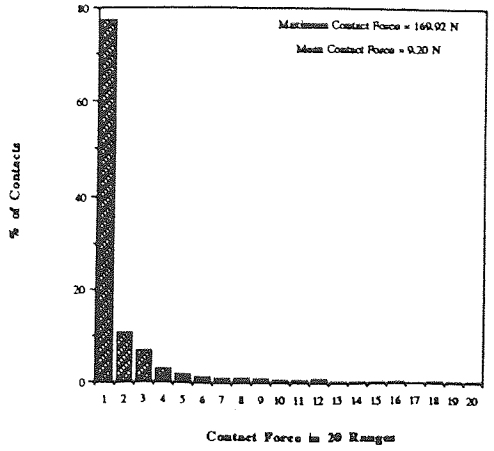

Figure D.17 Contact force distribution for 60% hard/soft mix, 2/1 hard/soft size ratio assembly at a stress level of $\sigma = 10$ kPa.

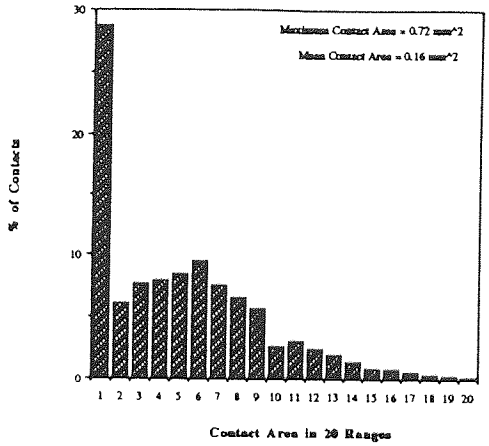

Figure D.18 Contact area distribution for 60% hard/soft mix, 2/1 hard/soft size ratio assembly at a stress level of $\sigma = 10$ kPa.

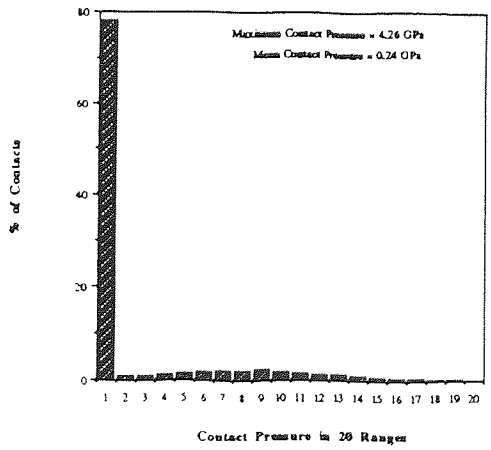

Figure D.19 Contact pressure distribution for 60% hard/soft mix, 2/1 hard/soft size ratio assembly at a stress level of $\sigma = 10$ kPa.

Appendix E

Further test results from Chapter 8

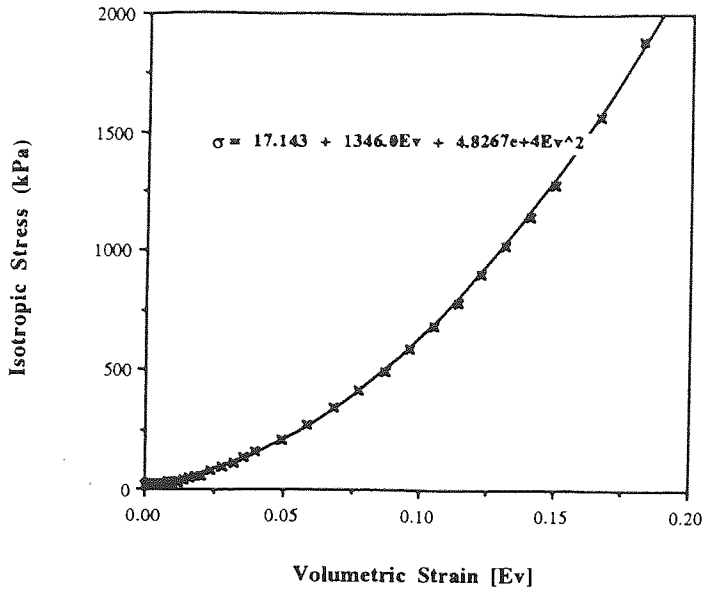

Figure E.1 Second order polynomial stress-strain relationship for 3D 25% hard/soft assembly subject to quasi-static compression.

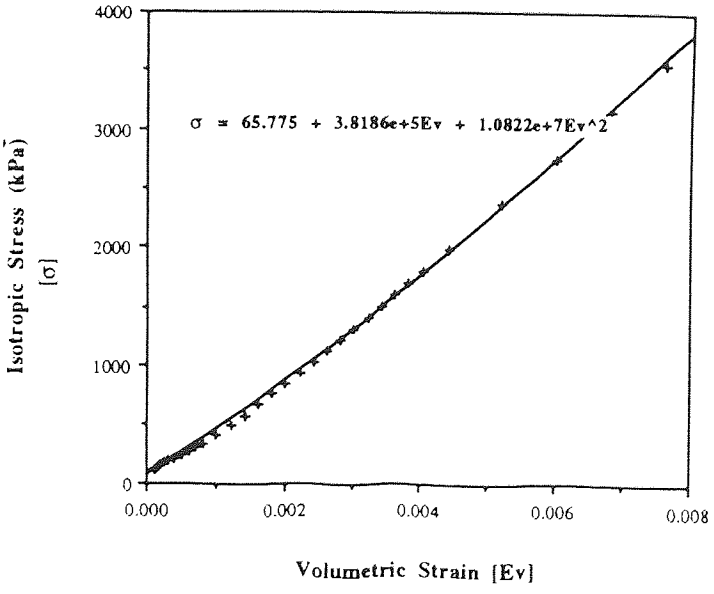

Figure E.2 Second order polynomial stress-strain relationship for 3D 75% hard/soft assembly subject to quasi-static compression.

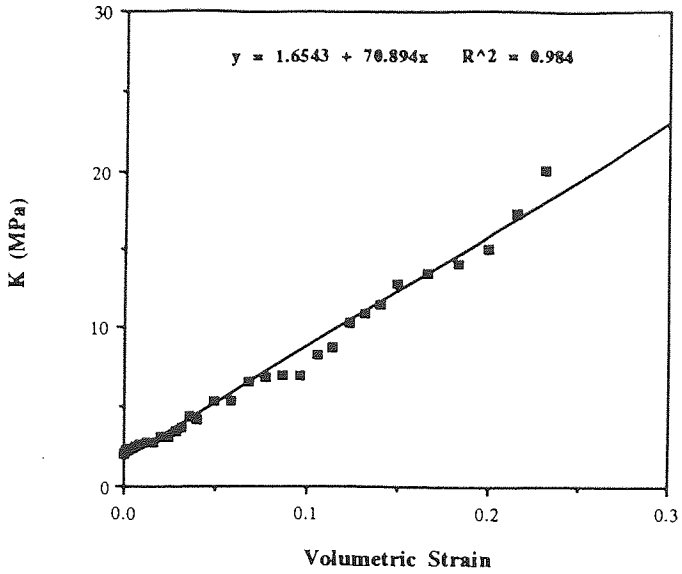

Figure E.3 The evolution of bulk modulus with volumetric strain for 3D 25% hard/soft mix subject to quasi-static compression.

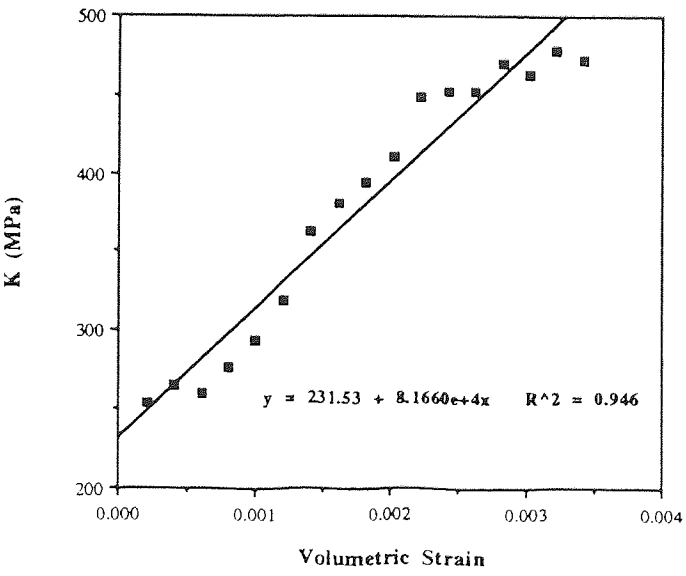

Figure E.4 The evolution of bulk modulus with volumetric strain for 3D 75% hard/soft mix subject to quasi-static compression.

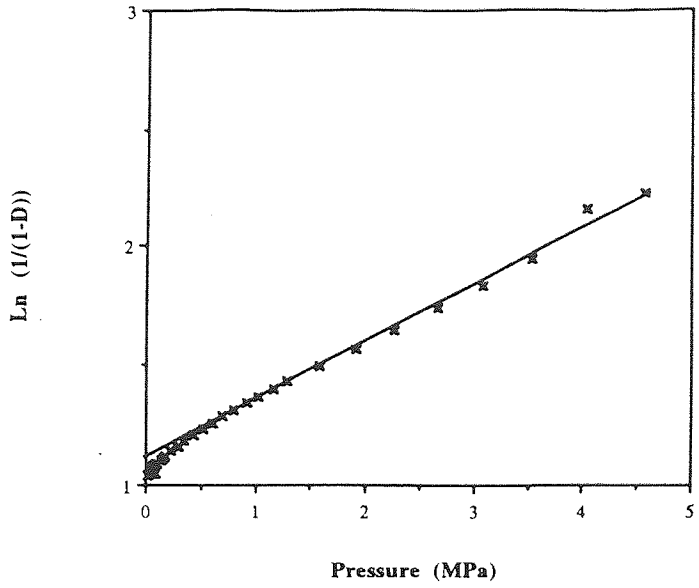

Figure E.5 Heckel relationship for 3D 25% hard/soft mix subject to quasi-static compression.;

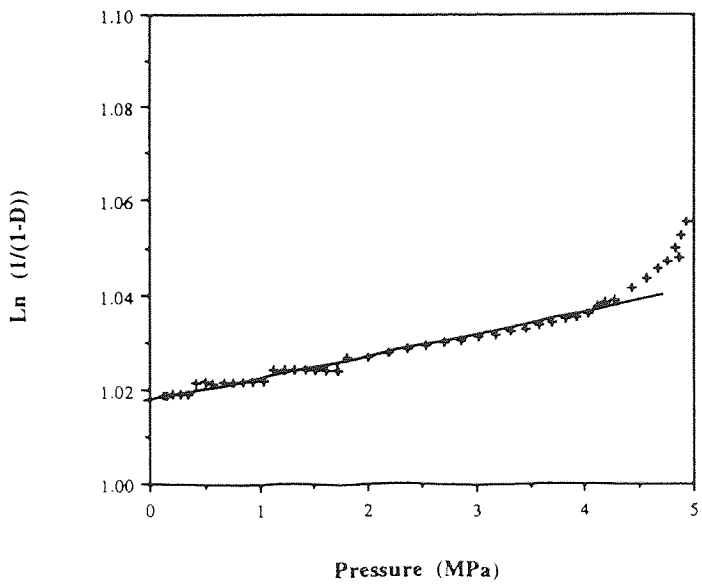

Figure E.6 Heckel relationship for 3D 75% hard/soft mix subject to quasi-static compression.

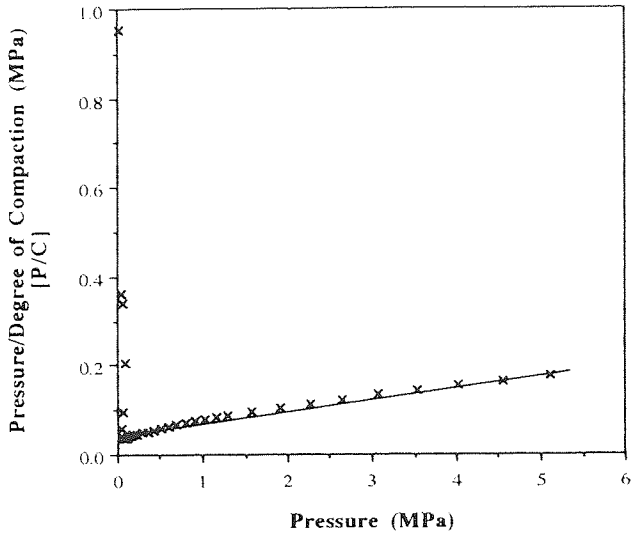

Figure E.7 Kawakita relationship for 3D 25% hard/soft mix subject to quasi-static compression.

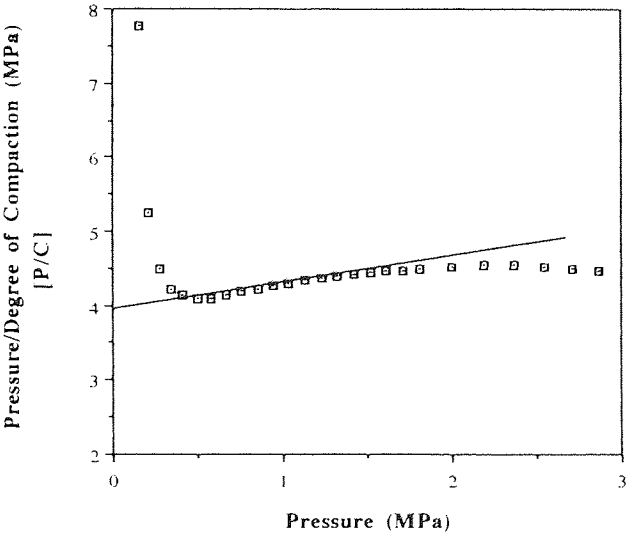

Figure E.8 Kawakita relationship for 3D 75% hard/soft mix subject to quasi-static compression.

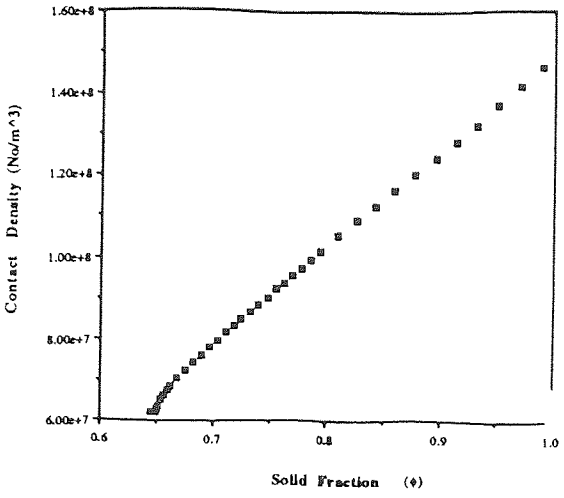

Figure E9 Evolution of contact density C with solid fraction ϕ for 3D 0% hard particle assembly subject to quasi-static compression.

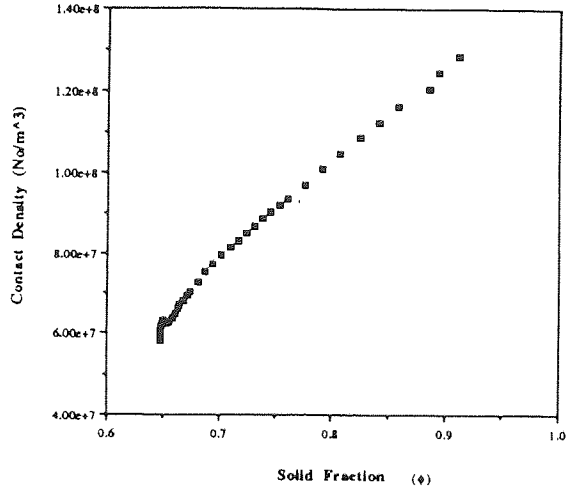

Figure E10 Evolution of contact density C with solid fraction ϕ for 3D 25% hard particle assembly subject to quasi-static compression.

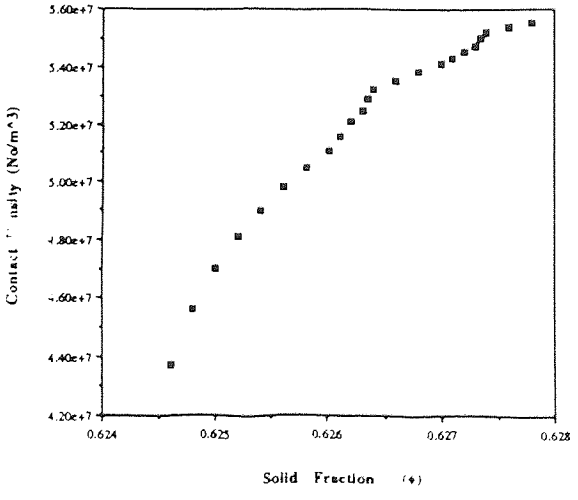

Figure E11 Evolution of contact density C with solid fraction ϕ for 3D 100% hard particle assembly subject to quasi-static compression.

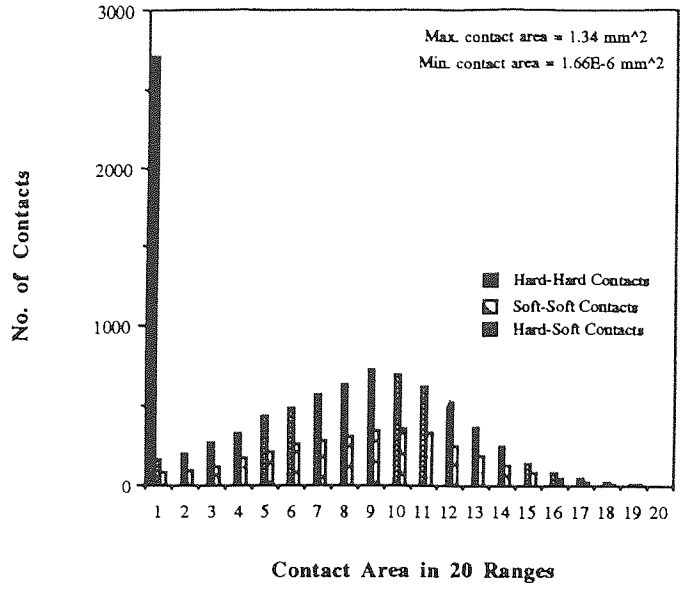

Figure E12 Contact-type specific, contact area distributions for 3D 50% hard particle assembly subject to quasi-static compaction.

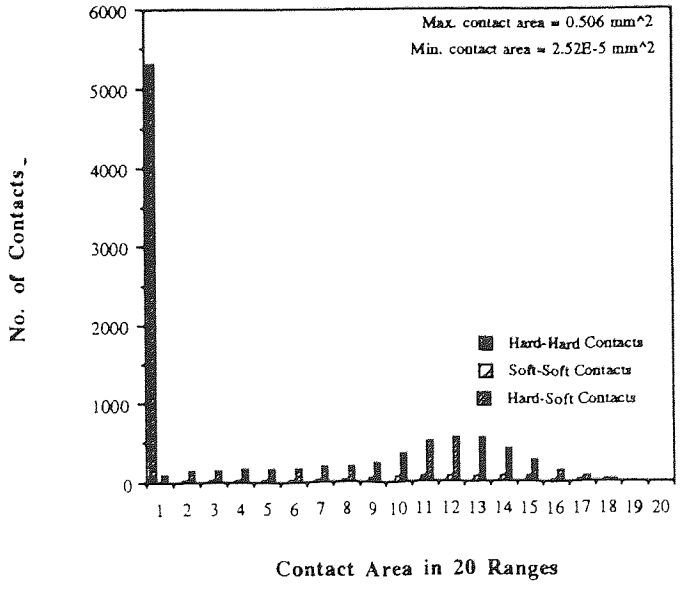

Figure E13 Contact-type specific, contact area distributions for 3D 75% hard particle assembly subject to quasi-static compaction.

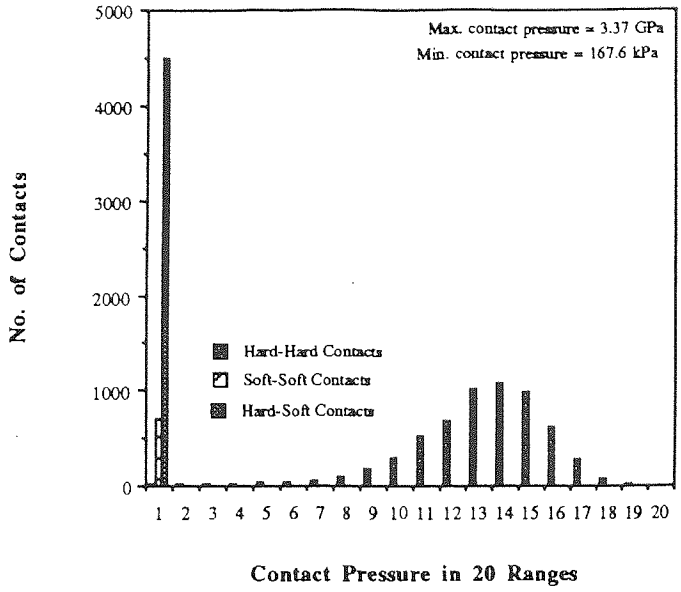

Figure E14 Contact-type specific, contact pressure distributions for 3D 50% hard particle assembly subject to quasi-static compaction.

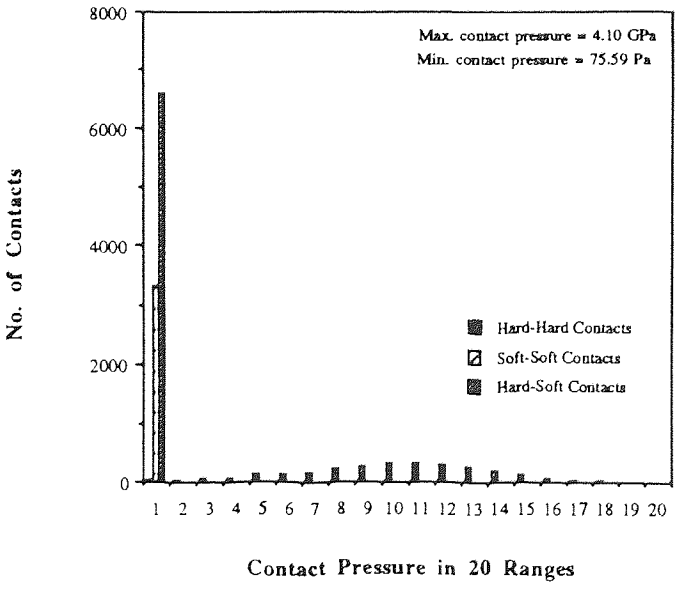

Figure E15 Contact-type specific, contact pressure distributions for 3D 75% hard particle assembly subject to quasi-static compaction.

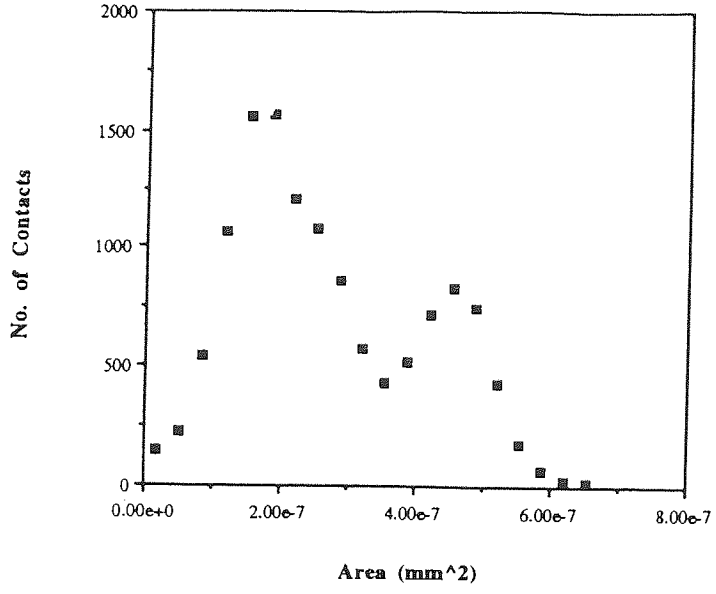

Figure E16 Multifractal contact area distribution for 0% hard particle assembly at a stress level of $\sigma = 100$ kPa

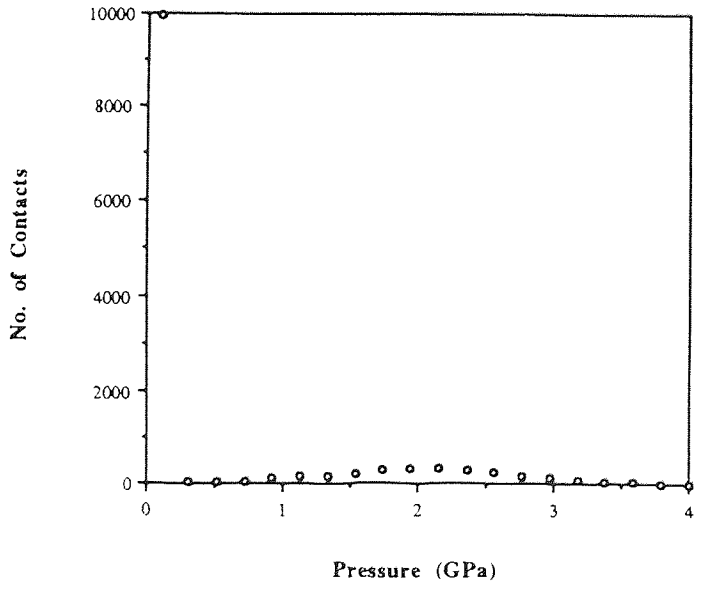

Figure E17 Multifractal contact pressure distribution for 50% hard particle assembly at a stress level of $\sigma = 1$ MPa.